Transport and magnetic exchange properties of spin-orbit coupled, anisotropic Dirac materials and Majorana nanowires

by

Ganesh C. Paul

PHYS07201404014

Institute of Physics, Bhubaneswar

A thesis submitted to the
Board of Studies in Physical Sciences
In partial fulfillment of requirements
for the Degree of

DOCTOR OF PHILOSOPHY

of

HOMI BHABHA NATIONAL INSTITUTE

June, 2020

Homi Bhabha National Institute

Recommendations of the Viva Voce Committee

As members of the Viva Voce Committee, we certify that we have read the dissertation prepared by Mr. Ganesh C. Paul entitled "Transport and magnetic exchange proper- ties of spin-orbit coupled, anisotropic Dirac materials and Majorana nanowires", and recommend that it may be accepted as fulfilling the dissertation requirement for the Degree of Doctor of Philosophy.

A M Jayannavar

Chairman - Prof. A. M. Jayannavar Date: 09/06/2020

Arijit Saha

Guide /Convener - Dr. Arijit Saha Date: 09/06/2020

Co-guide (if any) Date:

Arijit Kundu

Examiner - Dr. Arijit Kundu Date: 09/06/2020

Saptarshi Mandal

Member 1 - Dr. Saptarshi Mandal Date: 09/06/2020

Dinesh

Member 2 - Dr. Dinesh Topwal Date: 09/06/2020

Final approval and acceptance of this thesis is contingent upon the candidate's submission of the final copies of the dissertation to HBNI.

I hereby certify that I have read this thesis prepared under my direction and recommend that it may be accepted as fulfilling the thesis requirement.

Date: 09/06/2020

Place: IOP, Bhubaneswar

Arijit Saha

Co-guide (if applicable) **Guide**

STATEMENT BY AUTHOR

This dissertation has been submitted in partial fulfillment of requirements for an advanced degree at Homi Bhabha National Institute (HBNI) and is deposited in the Library to be made available to borrowers under rules of the HBNI.

Ganesh C. Paul

CERTIFICATE

This is to certify that the Ph.D. thesis titled "**Transport and magnetic exchange properties of spin-orbit coupled, anisotropic Dirac materials and Majorana nanowires**" submitted by Ganesh C. Paul, in partial fulfilment of the degree of Doctor of Philosophy in Physics of Homi Bhabha National Institute is a record of bona fide research work done under my supervision. It is further certified that the thesis represents independent work by the candidate and collaboration was necessitated by the nature and scope of the problems dealt with.

Date: **Arijit Saha**

(Guide)

DECLARATION

I, hereby declare that the investigation presented in the thesis has been carried out by me. The work is original and has not been submitted earlier as a whole or in part for a degree / diploma at this or any other Institution / University.

Ganesh C. Paul

List of Publications arising from the thesis

Journal

- Ganesh C. Paul, Sk Firoz Islam and Arijit Saha, Fingerprints of tilted Dirac cones on the RKKY exchange interaction in 8-Pmmn Borophene, *Phys. Rev. B* **99**, 155418 (2019)
- Ganesh C. Paul, Arijit Saha and Sourin Das, Spin-selective coupling to Majorana zero modes in mixed singlet and triplet superconducting nanowires, *Phys. Rev. B* **97**, 205446(2018)
- Ganesh C. Paul and Arijit Saha, Quantum charge pumping through resonant crossed Andreev reflection in superconducting hybrid junction of Silicene, *Phys. Rev. B* **95**, 045420 (2017)
- Ganesh C. Paul, Surajit Sarkar and Arijit Saha, Thermal conductance by Dirac fermions in a normal-insulator-superconductor junction of silicene, *Phys. Rev. B* **94**, 155453 (2016)

Conferences

- DAE Solid State Physics Symphosium 2016;
  KIIT University, Bhubaneswar, India; (Dec. 26-30, 2016)
- International Workshop on "Topological Aspects of Quantum Matter" (TAQM 2018);
  TIFR, India; (Dec. 17-20, 2018)
- International Workshop on "Bound states in superconductors and interfaces"(BOSSA 2019);
  MPIPKS, Dresden, Germany; (April 08-10, 2019)

Ganesh C. Paul

Dedicated to my father whom I have lost during my PhD

ACKNOWLEDGEMENTS

First, I would like to express my gratitude to my supervisor Dr. Arijit Saha for his constant support, guidance and encouragement during my doctoral study. Any words of appreciation will fall short of his actual contribution to my research works and this thesis. His expertise and deep analysing power have helped me in understanding the subject throughout my doctoral study. He has provided adequate freedom while choosing and solving a problem which enabled me to explore cracks and corners of the problem.

I am thankful to Prof. Sourin Das under whose mentorship I have completed one project. His elegant way of thinking, the expertise in tackling a problem has inspired me. I thank Dr. Arijit Kundu with whom I started a collaboration and I have learned a lot from him.

I would like to thank Prof. Arun M. Jayannavar with whom I have interacted from the very beginning of my research. The scientific discussions with Prof. S. D. Mahanti have been very fruitful for me. The keen to learn attitude even at his age has deeply motivated me and I am thankful to him.

I am fortunate to have many good collaborators : Dr. Paramita Dutta, Surajit Sarkar, Dr. Sk Firoz Islam and Arnob Kumar Ghosh. Working and discussing with them has always been a lot of fun and encouraging.

On a personal level, the doctoral study has given me some good friends to cherish for the years to come. I thank my seniors, friends, and juniors for making my stay in the hostel a memorable one.

I am thankful to my respected teachers of our school whose advice and encouragement has always been helpful in my life.

Finally, I am indebted to my parents, my sisters and their in-laws for supporting me throughout my life. My parents have always given me the freedom to choose my career path. It would not have been possible to come at this stage without their constant support and encouragement.

Contents

SUMMARY

Study of topological phases of matter has remained a central interest in modern condensed matter physics community for the last decade oweing to its own merit. The remarkable discoveries of graphene and topological insulator has boosted the invetigation in various other topological systems and two dimentional (2D) materials. Along this direction, many monolayer materials namely silicene, phosphorene, borophene, dichalcogenides etc. have been predicted theoretically exhibiting topological phases. Theye have been successfully synthesied on different substrates in experiments. Numerous novel topological phases *e.g.* topological superconductor, Weyl semimetal, Dirac semimetal etc. have also attracted immense interest both in theory and experiments not only from fundamental point of view but for their possible application in spintronics and topological quantum computation. Very recent addition, in this direction, is the discovery of higher order phases *i.e.,* higher order topological insulator and superconductor. Few of them have recently been synthesized in various experimental setups.

Transport signatures have played a crucial role to probe and distinguish the novel topological phases in various systems for a long time. Presence of any bound states, either in topological or trivial system, have also been predicted by studying various transport phenomena namely electrical and thermal conductance, shot noise, Joshephson current etc. Moreover, transport measurement can also indicate any topological phase transition that takes place in the system. Major part of the present thesis is devoted to study the transport signature of various novel topological phases and Majorana zero mode in hybrid junctions of low dimentional systems (2D spin-orbit coupled Dirac materials and 1D nanowire) using scattering matrix formalism. A part of the thesis also discusses the magnetic exchange interaction in monolayer of anisotropic Dirac material- borophene.

Silicene, a 2D allotrope of silicon, has Dirac-like band structure which is predicted to be tunable by an external electric field applied perpendicular to the silicene sheet. This tunable band gap arises due to the presence of spin-orbit coupling. This enables the possibility of realizing a rich variety of topological phases and Majorana fermion in it under suitable circumstances. This 2D material has been grown experimentally by successful deposition of silicene sheet on silver substrate. Our objective was to explore the transport properties of various hybrid junction of this new generation Dirac materials.

In this direction, the properties of thermal conductance in a normal-insulator-superconductor (NIS) junction of silicene have been studied for both thin and thick barrier limit of the insulating region. While thermal conductance, in this kind of junction of Dirac materials, displays the conventional exponential dependence on temperature, it manifests a nontrivial oscillatory dependence on the strength of the barrier region. We have explored the tunability of the thermal conductance by the interplay betwen external electric field and the induced superconducting gap. Moreover, the effect of doping concentration on thermal conductance has also been discussed. In the thin barrier limit, the period of oscillation of the thermal conductance as a function of the barrier strength comes out to be $\pi/2$ when doping concentration in the normal silicene region is small. On the other hand, the period gradually converts to π with the enhancement of the doping concentration. Such change of periodicity of the thermal response with doping can be a possible probe to identify the crossover from specular to retro Andreev reflection in Dirac materials. In the thick barrier limit, thermal conductance exhibits oscillatory behavior as a function of barrier thickness d and barrier height V_0 while the period of oscillation becomes V_0 dependent. However, amplitude of the oscillations, unlike in tunneling conductance, gradually decays with the increase of barrier thickness for arbitrary height V_0 in the highly doped regime. We have discussed experimental relevance of our findings.

Adiabatic quantum pumping is a transport phenomenon in which low-frequency periodic modulations of at least two system parameters with a phase difference lead to a zero bias finite dc current in meso- and nanoscale systems. Such zero-bias current is a consequence of the time variation of the parameters of the quantum system which explicitly breaks time-reversal symmetry. We have theoretically investigated the phenomena of adiabatic quantum charge pumping through a normal-insulator-superconductor-insulator-normal (NISIN) setup of silicene within the scattering matrix formalism. Assuming thin barrier limit of the insulating region, we have considered the strength of the two barriers (χ_1 and χ_2) as the pumping parameters in the adiabatic regime. Within this geometry, we have obtained crossed Andreev reflection (CAR) with probability unity in the χ_1-χ_2 plane without the unwanted concomitant elastic cotunneling (CT). Tunability of the band gap at the Dirac point by appyling an external electric field perpendicular to the silicene sheet and variation of the chemical potential at the normal silicene region, open up the possibility of achieving novel perfect CAR process through our setup. This resonant behavior arises periodically in the plane of the barrier strengths. The behavior of the pumped charge through the NISIN structure as a function of the pumping strength

and angles of the incident electrons have been analyzed. We have predicted that almost quantized pumped charge can be obtained through our geometry when the pumping contour encloses the CAR or transmission resonance in the pumping parameter space. We have mentioned possible experimental feasibility of our theoretical predictions.

Majorana zero mode, in condensed matter system, is an emmergent quasi-particle of self-conjugate nature and is predicted to be building block of fault tolerant topological quantum computation. Topological superconductor, in 3D (2D), supports this zero energy Majorana modes at its vortex (edge). Zero bias peak (ZBP) in the differential conductance in hybrid superconductor-semiconductor systems as an indirect signature of Majorana zero modes was earlier predicted theoretically and then confirmed experimentally. We have looked into the transport properties of a quasi one dimensional ferromagnet-noncentrosymmetric superconductor (F-NCS) junction using scattering matrix formalism. We have shown that the relative orientation of the stoner field ($\tilde{\mathbf{h}}$) in the ferromagnetic lead and the $\mathbf{d}$ vector of the superconductor acts like a on-off switch for the zero bias conductance of the device. In the regime, where triplet pairing amplitude dominates over the singlet counterpart (topological phase), a pair of Majorana zero modes appear at each end of the superconducting part of the nanowire. The presence of the two kinds of pairing gaps gives rise to a pair of Majorana modes instead of a lone one at each end. When $\tilde{\mathbf{h}}$ is parallel or anti-parallel to the $\mathbf{d}$ vector, transport gets completely blocked due to blockage in pairing while, when $\tilde{\mathbf{h}}$ and $\mathbf{d}$ are perpendicular to each other, the zero energy two terminal differential conductance spectra exhibits sharp transition from $4e^2/h$ to $2e^2/h$ as the magnetization strength in the lead becomes larger than the chemical potential indicating the spin selective coupling of pair of Majorana zero modes to the lead. For a canted angle between $\tilde{\mathbf{h}}$ and $\mathbf{d}$, a zero bias dip emmerges out instead of a peak, in the tunneling conductance giving birth to a possible novel probe of the zero modes in the transport measurements.

Ruderman-Kittel-Kasuya-Yosida (RKKY) exchange interaction is an indirect exchange coupling between two magnetic impurities being mediated by the conduction electrons of the host material. Since the RKKY exchange interaction is directly related to the susceptibility of the host material, it has been used as a probe in electronic systems. We have theoretically investigated the indirect signatures of the tilted anisotropic Dirac cones on RKKY exchange interaction in 8-Pmmn borophene, a two dimensional polymorph of boron atoms. The 8-Pmmn borophene is one of the most recent

2D polymorph of boron atoms, which has been predicted to host tilted Dirac cones where the tilting direction around the Dirac cones are opposite to each other. Unlike the case of isotropic non-tilted Dirac material-graphene, here we have observed that the tilting of the Dirac cones exhibits a significant impact on the RKKY exchange interaction in terms of the suppression of oscillation frequency. The reason can be attributed to the behavior of the Fermi level and the corresponding density of states with respect to the tilting parameter. When the two impurities are located perpendicular to the tilt axis, interference between the Dirac fermions from different valleys do not contribute to the oscillation frequency and the period of oscillation increases as one enhances the value of the tilt parameter. This change of oscillation frequency may be a possible way to indirectly probe the degree of tilting of the Dirac cone present in anisotropic Dirac materials such as 8-Pmmn borophene. On the other hand, for the separation of the two impurities being along the tilt axis, interference among the Dirac cones plays a dominant role in determining the period of oscillation and the tilt parameter exhibits a negligible effect on the corresponding period. We have derived the direction dependent analytical expressions of the RKKY exchange interaction, in terms of Meijer G-function. Behavior of RKKY exchange interaction is also investigated numerically for two spatially separated magnetic impurities in the x-y plane of the 2D borophene sheet.

We have concluded the thesis with a summary and possible future directions.

List of Figures

List of Tables

CHAPTER 1

2D Dirac Materials

1.1 Introduction

Graphene, till date, is the most well known two dimensional (2D) Dirac material [7]. The remarkable discovery of Graphene took place in 2004 by Novoselov and Geim [8]. A year later, topological insulator was predicted in Graphene by Kane and Mele [9], but it was later realised that the spin-orbit coupling, which is mandatory to realize QSHE, is too small to get any reasonable signature of the same in experiments. Topological insulator, with insulating bulk and conducting counter propagating edges, was predicted theoretically in 2006 by Bernevig, Hughes and Zhang in HgTe quantum well [10, 11] and was later experimentally verified by König *et al.* in 2007 [12].

Along this direction, many monolayer materials namely silicene [13], phosphorene [14], borophene [15], transition metal dichalcogenides [16] etc. have been predicted theoretically exhibiting topological phases [17, 18, 19, 20]. They have been successfully synthesized on different substrates in experiments [21, 22, 23, 24]. Numerous novel topological phases *e.g.* topological superconductor, Weyl semimetal, Dirac semimetal etc. have also attracted immense interest both in theory and experiments not only from fundamental point of view but for their possible applications in various sectors ranging from spintronics [25] to topological quantum computation [26].

We begin with discussing basic properties of graphene in Sec. 1.2. Then we discuss the model

Hamiltonian of silicene, its topological properties alongwith the experimental evidence of silicene in Sec. 1.3. We then present basic features of borophene and its experimental evidence in Sec. 1.4.

1.2 Graphene

Graphene can be described by the simplest tight-binding model on a honeycomb lattice [5],

$$\hat{H}_0 = -t \sum_{\langle i,j\rangle\alpha} c^{\dagger}_{i\alpha} c_{j\alpha}, \tag{1.1}$$

where $c^{\dagger}_{i\alpha}$ ($c_{i\alpha}$) creates (annihilates) an electron with spin orientation $\alpha = \uparrow\downarrow$ at site i on sublattice A (equivalently for sublattice B); $\langle i, j\rangle$ runs over all the nearest neighbor hopping sites, and t is the hopping amplitude. Graphene lattice structure is demonstrated in Fig. 1.1(a) .

We can rewrite Eq. (1.1) in momentum space as

$$\hat{H}_0 = t \sum_{\alpha} \int d^2k \left(c^{\dagger}_{\mathrm{A}\alpha}, c^{\dagger}_{\mathrm{B}\alpha}\right) \begin{pmatrix} 0 & f(\mathbf{k}) \\ f^*(\mathbf{k}) & 0 \end{pmatrix} \begin{pmatrix} c_{\mathrm{A}\alpha} \\ c_{\mathrm{B}\alpha} \end{pmatrix} \tag{1.2}$$

with

$$f(\mathbf{k}) = e^{-iak_y/\sqrt{3}} + 2e^{iak_y/2\sqrt{3}} \cos\frac{ak_x}{2}. \tag{1.3}$$

Here, a is the lattice constant. The energy spectrum, obtained from this Hamiltonian, is

$$E(\mathbf{k}) = t\sqrt{1 + 4\cos\frac{ak_x}{2}\cos\frac{\sqrt{3}ak_y}{2} + 4\cos^2\frac{ak_x}{2}}. \tag{1.4}$$

The spectrum is depicted in Fig. 1.1(b). From Eq.(1.4), we can see that the band gap closes at the K_η point defined by

$$K_\eta = \frac{1}{a}\left(\eta\frac{4\pi}{3}, 0\right) \qquad \text{with} \qquad \eta = \pm. \tag{1.5}$$

The K_+ and K_- points are sometimes referred as K and K' points, respectively. We are particularly interested in deriving the relevant low energy effective Hamiltonian of graphene near its Fermi energy. We see that the dispersion relation is linear for $k_i \simeq 0$ *i.e.,* near the Fermi energy. The cones are thus called the Dirac cones and the points where the band gap closes as Dirac points .

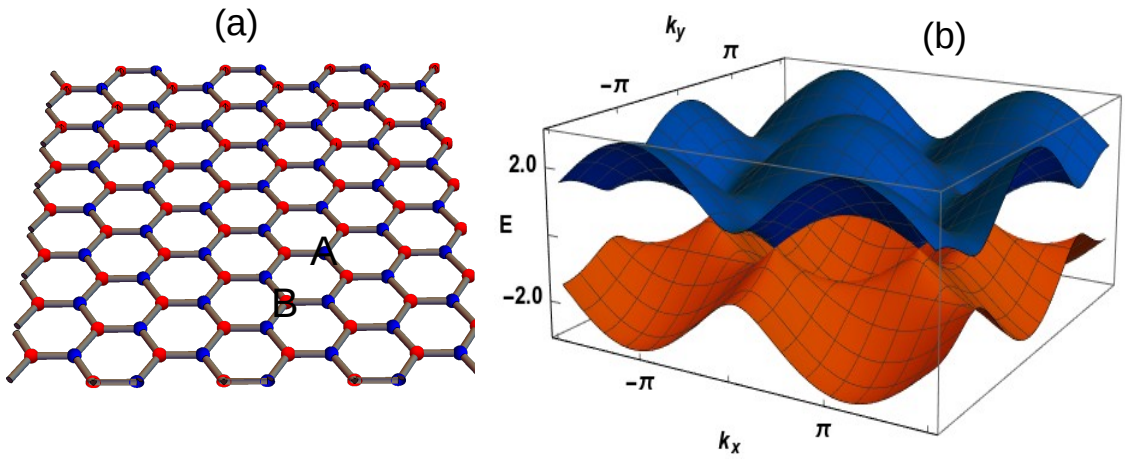

Figure 1.1: Graphene lattice structure is presented in panel (a). A and B sublattices are shown by blue and red circles respectively. Band spectrum of graphene is depicted in panel (b).

In the close vicinity of the K_η point, the Hamiltonian can be approximated by

$$\hat{H}_\eta = \sum_\alpha \int d^2k (c^{\eta\dagger}_{\mathrm{A}\alpha}, c^{\eta\dagger}_{\mathrm{B}\alpha}) H^\alpha_\eta \begin{pmatrix} c^\eta_{\mathrm{A}\alpha} \\ c^\eta_{\mathrm{B}\alpha} \end{pmatrix}, \tag{1.6}$$

with

$$H^\alpha_\eta = \hbar v_{\mathrm{F}} \begin{pmatrix} 0 & \eta k_x + i k_y \\ \eta k_x - i k_y & 0 \end{pmatrix} = \hbar v_{\mathrm{F}} \left(\eta k_x \tau_x - k_y \tau_y \right) \tag{1.7}$$

where $\tau = (\tau_x, \tau_y, \tau_z)$ is the Pauli matrix which acts on the sublattice space, and $v_{\mathrm{F}} = \frac{\sqrt{3}}{2\hbar} at$ is the Fermi velocity. The dispersion relation is linear for $k_i \simeq 0$. H^s_η is mentioned as the Dirac Hamiltonian at the Dirac point K_η.

1.3 Silicene

The silicon analog of graphene was first mentioned in 1994 in a theoretical study by Takeda and Shiraishi [27] and later it was reinvestigated by Guzman-Verri et al. in 2007, who coined the term 'silicene' [28]. The basic features of silicene is similar to that of graphene. The two differences that leads silicene essentially different from graphene are the presence of the spin-orbit interaction, which makes silicene a topological insulator[29], and its buckled structure with a layer separation between the two sublattices. This freedom allows one to generate a potential difference between the two sublattices by applying an external electric field perpendicular to the silicene sheet [30].

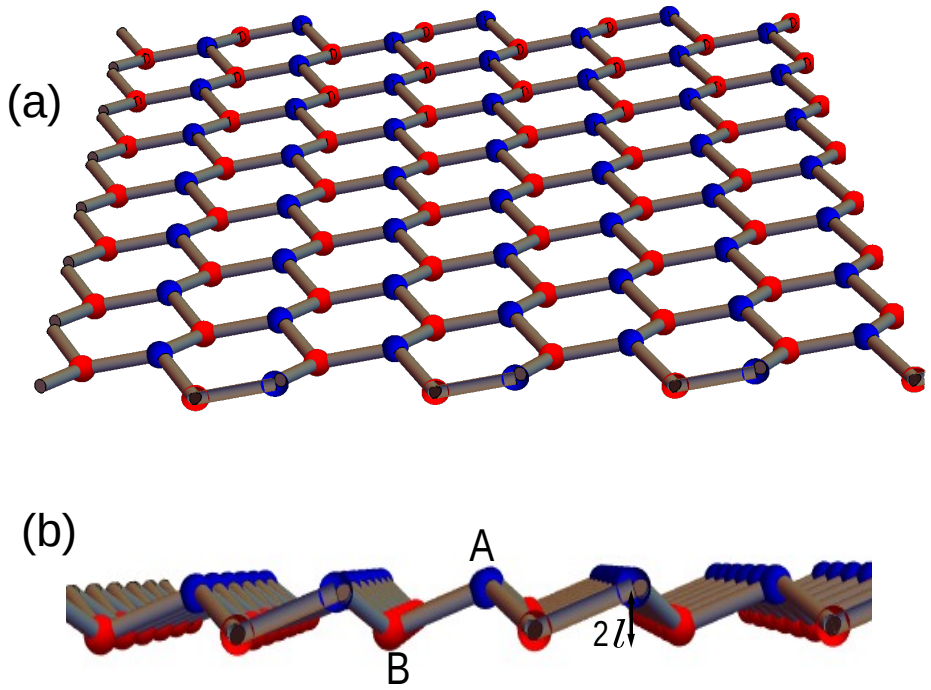

Figure 1.2: Schematic drawing of the lattice structure of silicene. Slightly canted top view is presented in panel (a) and the front view is shown in panel (b). Two types of sublattices are shown by blue (A) and red (B) circles which do not lie in the same plane thus giving rise to the buckled structure. The latter is prominent in the lower panel.

Spin-orbit coupling (SOC) term that couples electron with spin degrees of freedom can be written as,

$$H_{so} = \frac{\hbar}{4m_0^2c^2}\left(\nabla V \times \vec{p}\right)\cdot\vec{\alpha} = -\frac{\hbar}{4m_0^2c^2}\left(\vec{F}\times\vec{p}\right)\cdot\vec{\alpha}, \tag{1.8}$$

where V is the potential energy, $\vec{F}$ is the force, $\vec{p}$ is momentum, $\vec{\sigma}$ is the vector of Pauli matrices, $\hbar$ is Plank's constant, c is velocity of light, and m_0 denotes the mass of a free electron.

The nearest neighbor (NN) SOC, in graphene comes out to be zero due to its mirror symmetry with respective to an arbitrary bond, while the next nearest neighbor (NNN) SOC can be nonzero. However, the value of the NNN SOC is small and can be taken to be zero for all practical purposes. In case of silicene, the nearest neighbour SOC is zero (following the same mirror symmetry argument), while the NNN SOC is nonzero. This SOC has two components : parallel and perpendicular to the plane according to the two components of the electric field force. The perpendicular component arises because of the buckling structure *i.e.,* sublattices A and B being noncoplanar.

The force parallel with the plane gives rise to the parallel component of SOC term in Silicene

which reads

$$H_{so1} = i\gamma_2 \left(\vec{F}_{\parallel} \times \vec{d}_{ij}\right) \cdot \vec{\alpha} \equiv it_2 \nu_{ij} \alpha_z. \tag{1.9}$$

where $\nu_{ij} = \frac{\vec{d}_i \times \vec{d}_j}{|\vec{d}_i \times \vec{d}_j|}$, $\vec{d}_i$ and $\vec{d}_j$ are two nearest bonds connecting the next nearest neighbor $\vec{d}_{ij}$. Here, γ_2 and t_2 are undetermined parameters.

The second component of SOC comes from the force perpendicular to the plane and is given by

$$H_{so2} = i\gamma_1 \left(\vec{\sigma} \times \vec{d}^{0}_{ij}\right) \cdot F_{\perp} \vec{e}_z \equiv it_1 \mu_{ij} \left(\vec{\sigma} \times \vec{d}^{0}_{ij}\right)_z, \tag{1.10}$$

where $\vec{d}^{0}_{ij} = \vec{d}_{ij}/|\vec{d}_{ij}|$, γ_1 and t_1 are undetermined parameters, $\mu_{ij} = \pm 1$ for the A (B) sublattice.

When external electric field E_z is applied perpendicular to silicene, the tight-binding Hamiltonian with NN and NNN hopping can be written as

$$\begin{aligned} H \;=\; & -t \sum_{<i,j>\alpha} \hat{c}^{\dagger}_{i\alpha}\, \hat{c}_{j\alpha} + i\frac{\lambda_{SO}}{3\sqrt{3}} \sum_{<<i,j>>\alpha\beta} \nu_{ij} \hat{c}^{\dagger}_{i\alpha} \sigma^{z}_{\alpha\beta}\, \hat{c}_{j\beta} \\ & -i\frac{2}{3}\lambda_R \sum_{<<i,j>>\alpha\beta} \mu_{ij} \hat{c}^{\dagger}_{i\alpha} (\vec{\sigma} \times \hat{d}_{ij})^{z}_{\alpha\beta}\, \hat{c}_{j\beta} \\ & +el \sum_{i\alpha} \zeta_i E^{i}_{z} \hat{c}^{\dagger}_{i\alpha}\, \hat{c}_{i\alpha} \; - \mu \sum_{i\alpha} \hat{c}^{\dagger}_{i\alpha}\, \hat{c}_{i\alpha}\,. \end{aligned} \tag{1.11}$$

The operator $\hat{c}^{\dagger}_{i\alpha}$ creates an electron at site i with spin polarization α while the operator $\hat{c}_{i\alpha}$ annihilates it. The first term describes the nearest-neighbor hopping of amplitude t on honeycomb lattice, where $< i, j >$ denotes the nearest-neighbor sites. The second term is for the effective SOC with $\lambda_{SO} \sim 4$ meV [30], where $\vec{\sigma} = (\sigma^x, \sigma^y, \sigma^z)$ is the pauli spin matrices. This is the first component of SOC mentioned above. The sum $<< i, j >>$ is over the next nearest-neighboring sites. The third term is the Rashba SOC of amplitude λ_R arising from perpendicular component of the electric field force. The fourth term represents the staggered sublattice potential, where $\zeta_i = \pm 1$ for the A(B) sites. This Hamiltonian describes the basic features of germanene and stanene as well whereas the main difference lies in the fact that Rashba SOC is in these two materials are strong compared to silicene and hence can't be neglected as we did for silicene. It is worth to note that, the Hamiltonian written above for silicene is similar to the famous Kane-Mele model [9] where they considered both mirror symmetry conserved spin-orbit interaction and mirror symmetry broken Rashba like spin-orbit interaction.

	t(eV)	v_F	a(Å)	$\lambda_{\rm SO}$ (meV)	$\lambda_{\rm R}$ (meV)	ℓ(Å)	θ (degree)
Graphene	2.8	9.8	2.46	10^{-3}	0	0	90
Silicene	1.6	5.5	3.86	3.9	0.7	0.23	101.7
Germanene	1.3	4.6	4.02	43	10.7	0.33	106.5
Stanene	1.3	4.9	4.70	43	9.5	0.33	107.1

Table 1.1: The system parameters obtained from first principle calculation, characterizing graphene, silicene, germanene and stanene are presented. Here, $v_{\rm F}$ is in the unit of 10^5m/s, ℓ is the buckle height and θ is the bond angle. This table is adapted from Ref. [5, 6].

Here also we are interested to obtain the low-energy effective Hamiltonain near the Fermi energy, which is constructed similar to the case of graphene. Rewriting the Hamiltonian (1.11) in the form of (1.6), we obtain the Dirac Hamiltonian which is given by

$$H_\eta^s = \begin{pmatrix} \Delta_\alpha^\eta & \hbar v_{\rm F}(\eta k_x + i k_y) \\ \hbar v_{\rm F}(\eta k_x - i k_y) & -\Delta_\alpha^\eta \end{pmatrix}, \tag{1.12}$$

where

$$\Delta_\alpha^\eta = \ell E_z - \eta\alpha\lambda_{\rm SO} \equiv \ell(E_z - \eta\alpha E_{\rm cr}), \tag{1.13}$$

and

$$E_{\rm cr} \equiv \lambda_{\rm SO}/\ell. \tag{1.14}$$

The term Δ_α^η can be termed as the Dirac mass. We have shown the derivation of the low energy effective Hamiltonian of Silicene from the full lattice Hamiltonian in Appendix A. The energy spectrum is found to be

$$E(\mathbf{k}) = \pm\sqrt{(\hbar v_{\rm F} k)^2 + (\Delta_\alpha^\eta)^2}. \tag{1.15}$$

The band structure of silicene is shown in Fig. 1.3(a). The band gap, near the Dirac point K_η, is given by $2|\Delta_\alpha^\eta| = 2\ell|E_z - \eta\alpha E_{\rm cr}|$. In Fig. 1.3(b), we demonstrate the low-energy nature of the band structure near the Dirac point. One can notice the hexagonal Brillouin zone (BZ) and the Dirac like dispersion near the Fermi level. Although the BZ has six corners, only two of them are inequivalent which are marked by K and $K^{'}$.

Note that, the band gap is tunable by controlling external electric field E_z as shown in Fig. 1.4. The gap is open in absence of electric field. As $|E_z|$ increases, the gap becomes smaller, and it closes at $E_z = \eta\alpha E_{\rm cr}$. In this situation, silicene is semimetallic akin to graphene. With the further enhance-

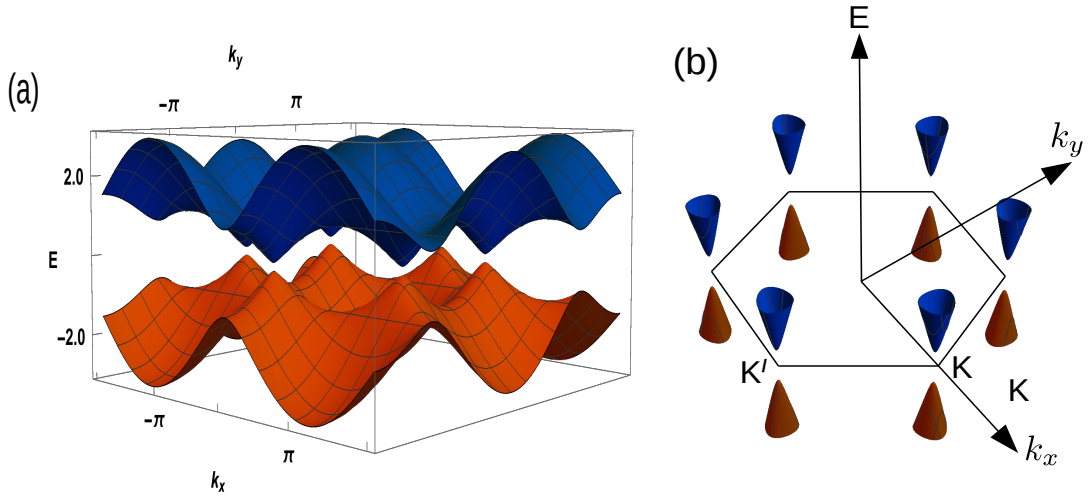

Figure 1.3: The band dispersion of a monolayer silicene is shown as a function of k_x and k_y in panel (a). The band dispersion near the Fermi energy is presented in panel (b) where low energy effective band dispersion exhibits Dirac like nature. There are six corners of the Brillouin zone and the two inequivalent points K and $K^{'}$ are indicated.

ment of $|E_z|$, the gap opens again. This feature signifies the bulk-boundary correspondance. Fig. 1.4 dictates the electric field tunability of the topological phase transition.

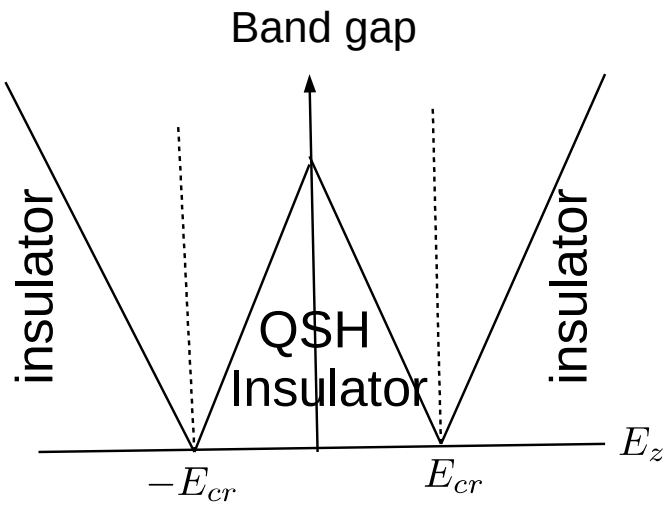

Figure 1.4: Band gap is shown as a function of electric field. Topological phase transition takes place from quantum spin hall insulating phase to band insulating phase with the rise the E_z. E_{cr} is the critical electric field at which the band gap closes.

To better understand the topological phase transition and the boundary edge modes that appear in monolayer silicene, we demonstrate nanoribbon bandstructure in Fig.(1.5). The band structure is shown as a function of momentum along x direction while in the other direction we have taken finite size ($N_y = 40$). We see that in absence of the electric field *i.e.*, $E_z = 0$, nanoribbon posses edge states

and the system is in topological insulating phase. This feature is depicted in Fig. 1.5(a) where counter propagating edge modes are clearly visible. As E_z increases, the band gap decreases and gets closed for $E_z = E_{\text{cr}}$. The edge state vanishes for electric field crossing critical value which is demonstrated in Fig. 1.5(b).

There are other possible way to control band gap in silicene namely by photo-irradiation [31], antiferromagnetic exchange interaction etc [5]. We neglect those effects and only consider the effect of perpendicular electric field to understand the topological phase transition for simplicity.

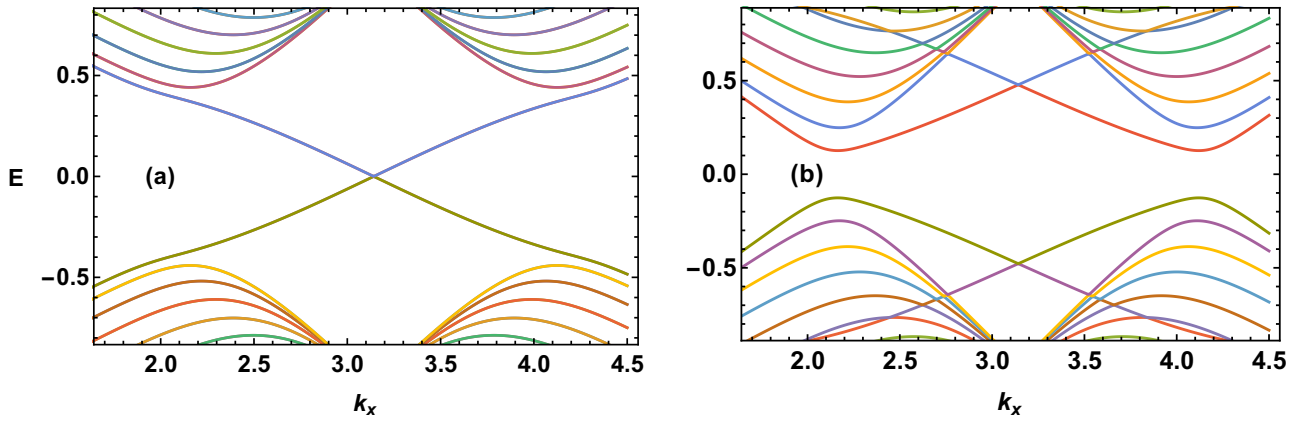

Figure 1.5: Band structure of Silicene nanoribbon is depicted. The chosen parameters are : $\lambda_{\text{SO}} = 0.4$; (a) E_z=0 and (b) E_z=0.5 . All of them are normalized with the hopping parameter t. The edge states are clearly visible in (a) indicating the topological insulating phase while they are absent in (b) characterizing the band insulating phase.

1.3.1 Chern number and Topological phase transition

We now present the Chern number which is a topological invarient being used to distinguish different phases that may appear in 2D Dirac materials. For any Bloch state $|\psi(\mathbf{k})\rangle$ we can define a "gauge potential" in the momentum space by

$$A_j(\mathbf{k}) = -i \left\langle \psi(\mathbf{k}) | \frac{\partial}{\partial k_j} | \psi(\mathbf{k}) \right\rangle \tag{1.16}$$

which is known as the Berry connection. Subsequently using Stokes theorem, we can define the Berry curvature $F(\mathbf{k})$ which is given by

$$F(\mathbf{k}) = \frac{\partial}{\partial k_x} A_y(\mathbf{k}) - \frac{\partial}{\partial k_y} A_x(\mathbf{k}) . \tag{1.17}$$

$F(\mathbf{k})$ is analogous to the magnetic field in momentum space. The Chern number can now be obtained by integrating the Berry curvature $F\left(\mathbf{k}\right)$.

$$\mathcal{C} = \frac{1}{2\pi}\int d^2k\, F\left(\mathbf{k}\right). \tag{1.18}$$

We now calculate the Berry curvature, with the Hamiltonian of Eq. (1.12) for each valley, which is given by

$$F_s^{\eta}\left(\mathbf{k}\right) = -\eta\frac{\Delta_\alpha^\eta}{2\left(\left(\hbar v_{\mathrm{F}}k\right)^2 + \left(\Delta_\alpha^\eta\right)^2\right)^{3/2}}. \tag{1.19}$$

Corresponding Chern number is found to be

$$\mathcal{C}_\alpha^\eta = -\frac{\eta}{2}\mathrm{sgn}(\Delta_\alpha^\eta), \tag{1.20}$$

The Chern number is quantized and is given by $\mathcal{C}_\alpha^\eta = \pm\frac{1}{2}$. This quantization does not depend on deformation of the band structure provided that the band-gap is not zero. The Chern number is integer when the Berry curvature is integrated over a closed region (first Brillouin zone). Here we consider a continuum model where the integral is over all momenta ranging from 0 to ∞. The region close to the Dirac point contributes $1/2$ of the total contribution to the Chern number. Thus we obtain only half integer value of the Chern number.

It changes its sign when the Dirac mass Δ_α^η changes its sign, which obviously goes through vanishing of the band gap. This quantity, thus, is a topological charge and the insulating phase is indexed by a set of four Chern numbers $\mathcal{C}_\alpha^\eta$ which can be used to construct the total Chern number $\mathcal{C}$, the spin Chern number $\mathcal{C}_s$[32, 33, 34], the valley Chern number[35, 17] and the spin-valley Chern number[36, 5], in the following way

$$\mathcal{C} = \mathcal{C}_\uparrow^K + \mathcal{C}_\uparrow^{K'} + \mathcal{C}_\downarrow^K + \mathcal{C}_\downarrow^{K'}, \tag{1.21}$$

$$\mathcal{C}_s = \frac{1}{2}(\mathcal{C}_\uparrow^K + \mathcal{C}_\uparrow^{K'} - \mathcal{C}_\downarrow^K - \mathcal{C}_\downarrow^{K'}), \tag{1.22}$$

$$\mathcal{C}_v = \mathcal{C}_\uparrow^K - \mathcal{C}_\uparrow^{K'} + \mathcal{C}_\downarrow^K - \mathcal{C}_\downarrow^{K'}, \tag{1.23}$$

$$\mathcal{C}_{sv} = \frac{1}{2}(\mathcal{C}_\uparrow^K - \mathcal{C}_\uparrow^{K'} - \mathcal{C}_\downarrow^K + \mathcal{C}_\downarrow^{K'}). \tag{1.24}$$

It is worth to note that, the valley Chern number and the spin-valley Chern number are meaningfull only in case of Dirac theory and they are ill defined in the tight-binding model. A topological phase transition takes place depending on the sign change of the Dirac mass Δ_α^η. This motivates one to study silicene as a electric field tunable topological insulator.

1.3.2 Experimental Evidence of Silicene

There is no solid phase of silicon similar to graphite. Hence, pure 2D silicene layers cannot be generated by exfoliation methods as initially was successfully done in the case of graphene [8]. More sophisticated and advanced methods have been used for the growth and synthesis of silicene.

In this direction, Vogt *et al.* have studied one-atom-thick Si sheets formed on the Ag(111) surface [1] under ultrahigh vacuum conditions. Si was deposited by evaporation from a Si source, and the Ag sample was kept at temperatures between $\approx$ 220–260° C. Omicron VT-STM with an electrochemically etched tungsten tip was used for scanning tunneling microscope (STM) measurements which were performed at room temperature in constant-current mode. Angular-resolved photoelectron spectroscopy (ARPES) measurements were also carried out to study the electron-energy distribution .

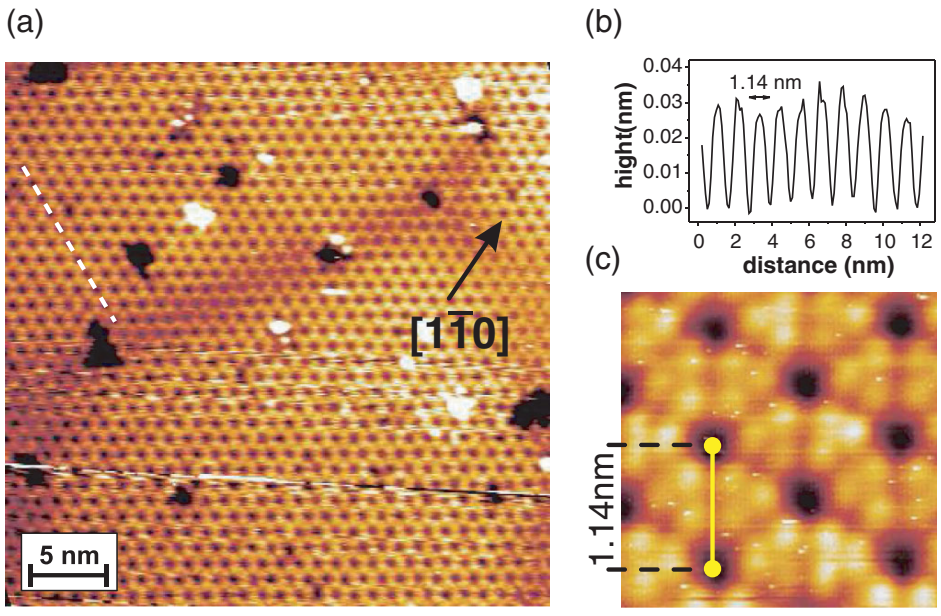

Figure 1.6: (a) Filled-states STM image of a 2D Si layer deposited on silver substrate [Ag(111)] where honeycomblike structure is clearly visible. (b) Line profile, along the dashed white line shown in panel (a), indicating the buckled structure. (c) High-resolution STM topograph of the Si layer exhibiting the honeycomb structure. This figure is adapted from Ref. [1]

Filled-states STM image of the Silicene layer is shown in Fig. 1.6(a), while the line profile along the dashed white line given in Fig. 1.6(a) is depicted in Fig. 1.6(b). It reveals that the dark centers in the STM micrograph have distance of 1.14 nm on average which is 4 times the surface Ag(111) lattice constant, and thus corresponds to the (4×4) symmetry. Buckled nature of silicene is clearly visible in Fig. 1.6(b). The high resolution STM image shown in Fig. 1.6(c) is measured at a sample bias of $U_{bias} = -1.3V$. The 2D Si adlayer gives rise to triangular structures, each of which consists of three bright protrusions and they are separated by 0.4 nm with respect to each other. These triangles are situated hexagonally around the dark centers, which are separated by 4 Ag lattice constants. STM images have been recorded at other sample biases giving rise to the same outcome.

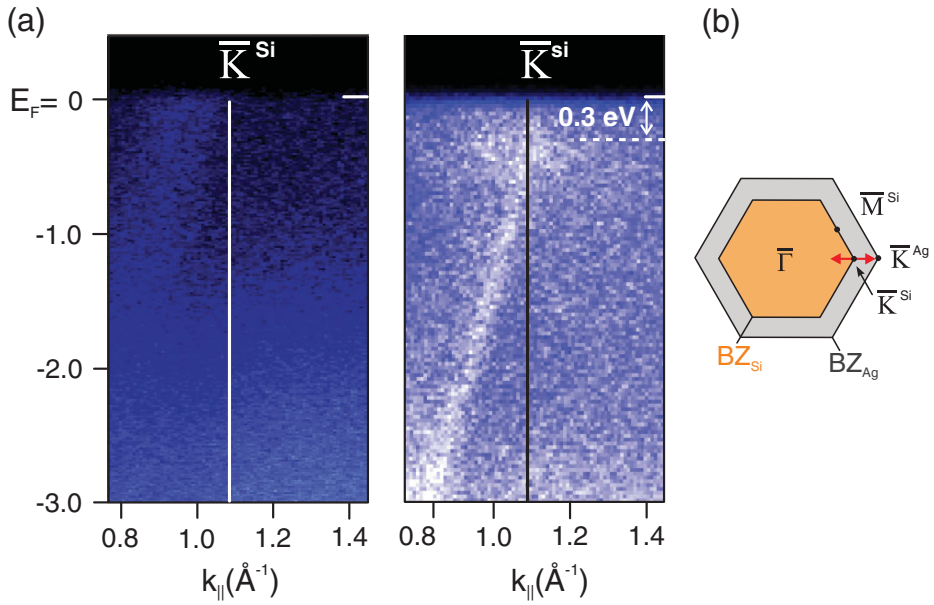

Figure 1.7: ARPES intensity map along the Ag $\overline{\Gamma}$-$\overline{K}$ direction for the clean Ag surface in shown in left panel whereas after formation of the 2D Si adlayer is given in the right panel. (b) Brillouin-zone (BZ) of the 2D Si layer with respect to the Ag(111)-(1×1) surface is shown. The red arrow dictates the ARPES measurement direction. This figure is adapted from Ref.[1] .

ARPES data recorded at a photon energy of $h\nu = 126eV$ is depicted in Fig. 1.7(a) which identify a Dirac like linear dispersion of honeycomb Si bands (right figure). This dispersion is similar to that of graphene, indicating the existence of Dirac fermions in silicene. The linear dispersion can be described by $E \propto \hbar v_F k$, where v_F is the Fermi velocity. The Fermi velocity for the silicene layer is found to be of $1.3 \times 10^6 m/s$, which is comparable to the graphene Fermi velocity. Similar to the case of graphene, only a single dispersing branch of the "Dirac cone" is visible in the $\bar{\Gamma} - \bar{K}$ direction [Fig. 1.7(b) red arrow] which can be attributed to a photoemission interference effect. Left image of Fig. 1.7(a) is the ARPES result for clean Ag surface *i.e.,* before the deposition of Si and this does not

show any Dirac like dispersion. The direction along which the ARPES measurement is done is shown in Fig. 1.7(b) where Brillouin zone of 2D Silicene is demonstrated.

Silicene sheet has been grown on other substrate as well *e.g.* Fleurence *et al.* have reported the formation of two-dimensional epitaxial silicene through surface segregation on zirconium diboride thin films grown on Si wafers [37]. They have confirmed the presence of buckling in silicene. However, they have obtained a buckling induced band gap opening at the Γ point which may also originate from the electronic coupling with the substrate.

1.4 Borophene

A thin layer of boron atoms called borophene is one of the latest addition to the famility of Dirac materials. As Boron has one less electron than carbon, it's honeycomb structure is unstable. However, stabilization is possible by adding extra boron atoms in the honeycomb lattice. First principle calculations have predicted that depending on the arrangements of the extra boron atoms, various stable monolayer-boron structures, such as α sheet, β sheet, are possible [15, 23, 38]. One of the most stable predicted structure among these is 8-$Pmmn$ borophene.

The $Pmmn$ space group is generated by the translations of the vectors $(a, 0, 0)$, $(0, b, 0)$, and $(0, 0, c)$ (the latter is not present for the two-dimensional structure), inversion $\mathcal{I}$, reflection σ_{v}, rotation $\mathcal{C}_2$, and the n-glide plane consisting of the $(a/2, b/2, 0)$ translation and the $z \to -z$ reflection. Here, a, b, c are the lattice spacings. We do not consider the spin-orbit coupling which may be present in the material. The Hilbert space is then split into two subspaces of the n-symmetric and the n-antisymmetric wave functions. Then the Hamiltonian $H(k_x, k_y)$, which follows the $Pmmn$ space group symmetry, can be written in the block-diagonal form with the blocks H_{S} and H_{A}. The Bloch waves corresponding to both the subspaces then correspond to the smaller effective unit cell and doubled first Brillouin zone .

8-$Pmmn$ borophene has 8 atoms per unit cell. There is another possible structure obeying $Pmmn$ space group symmetry : 2-$Pmmn$ borophene, which has 2 atoms per unit cell. We are interested only in the former one as this hosts Dirac fermions. There are two inequivalent atoms in the lattice of 8-$Pmmn$ borophene which are termed, using the terminology of Ref. [39], as : inner atoms and ridge atoms. These two kinds of atoms are not situated on the same plane and thus borophene is

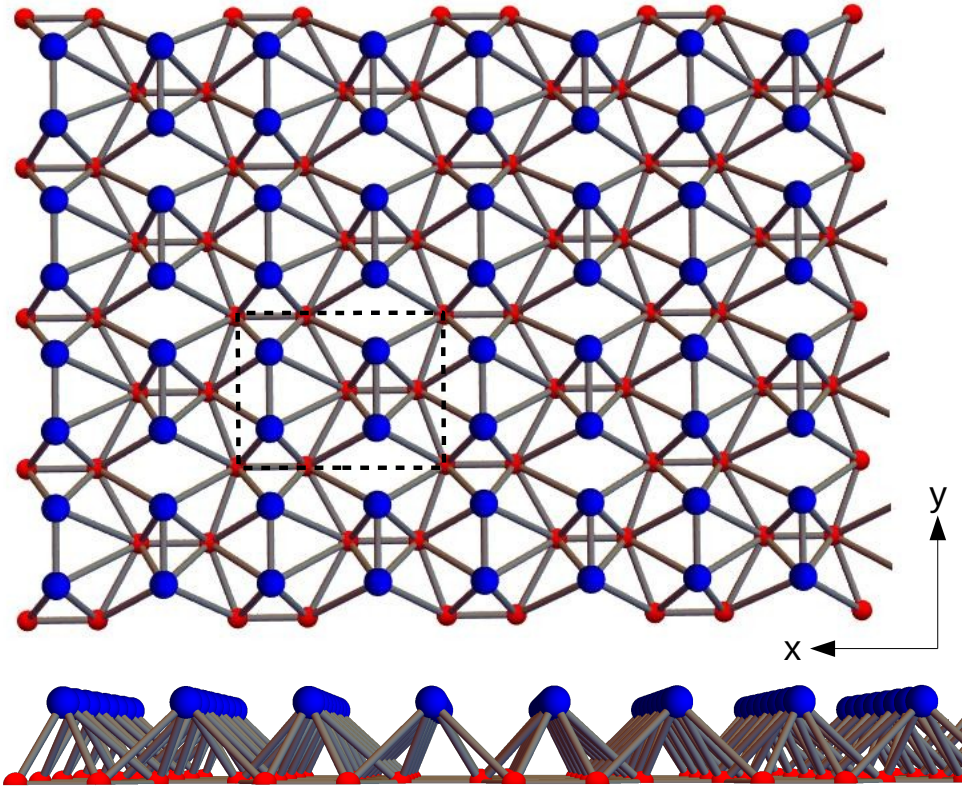

Figure 1.8: Schematic sketch of the lattice structure of 8-Pmmn borophene. Big blue (dark gray) circles and small red (light gray) circles indicate two types of nonequivalent atoms B_R (ridge atom) and B_I (inner atom) respectively. Upper panel dictates the frontview of borophene lattice structure. The unit cell, comprising of 8 atoms, is shown by dashed black rectangle. Lower panel presents the sideview of borophene lattice structure.

not flat $2D$ like graphene. The lattice is identified by the following parameters [40]: $a = 0.452$ nm, $b = 0.326$ nm, and the coordinates of two inequivalent atoms are $(a/2, 0.247b, 0.109$ nm) (ridge atom) and $(0.185a, b/2, 0.040$ nm) (inner atom), and the coordinates of other atoms are obtained via proper symmetry operations.

The resulting tight-binding model, which is a 16 band model (originating from 8 atoms), yields good agreement with the first principle Density Functional Theory (DFT) results of [39]. The resulting energy dispersion near the Fermi energy exhibits tilted anisotropic Dirac cone like structure at $\mathbf{k}_{\rm D} = (0, k_{\rm D})$ and $-\mathbf{k}_{\rm D}$, where $k_{\rm D} = 0.290 \times 2\pi/b$ [40].

A low energy effective Hamiltonian for 8-$Pmmn$ borophene has been recently put forwarded by Zabolotskiy and Lozovic [41] using symmetry consideration. A general low energy two band effective Hamiltonian for 2D Dirac materials associated with the anisotropic Dirac cone can be written as (near the Dirac points $\mathbf{q} = \pm\mathbf{k_D}$)

$$H_D = \xi(v_x\sigma_x q_x + v_y\sigma_y q_y + v_t\sigma_0 q_y) \ , \tag{1.25}$$

where σ_x, σ_y are the Pauli matrices in the atomic basis and σ_0 is a 2×2 unit matrix. We have chosen $\hbar = 1$. Here, $\xi = \pm 1$ is the valley index and v_i $(i = x, y)$ correspond to the velocities along $i^{\rm th}$ direction, while v_t denotes the velocity scale associated with the tilted Dirac cones. Note that the tilting is along the y-direction. The different velocity parameters are given by $\{v_x, v_y\} = \{0.86, 0.69\}$ and $v_t = 0.32$ in units of 10^6 m/sec [39, 41]. The major differences of this Hamiltonian from that of graphene (given in Eq.1.7) is the presence of the tilting term *i.e.,* $v_t\sigma_0 q_y$ and assymetry in the Fermi velocities along x and y directions. The corresponding energy dispersion is given by [42]

$$E(\mathbf{q_x}, \mathbf{q_y}) = q_y v_{\rm t} \pm \sqrt{q_x^2 v_x^2 + q_y^2 v_y^2}. \tag{1.26}$$

The Fermi energy has been set at charge neutrality point *i.e.,* at the Dirac point. The band structure near the Dirac point $\mathbf{q} = \mathbf{q_D}$ is shown in Fig. 6.1. The band is tilted only along y direction and is symmetric along the x axis which can be understood from Eq. (1.26). The band dispersion around the other valley $\mathbf{q} = -\mathbf{q_D}$ has opposite chirality *i.e.,* along the y axis, bands are oppositely tilted. It is important to note that the tilting breaks particle-hole symmetry in borophene [39, 41].

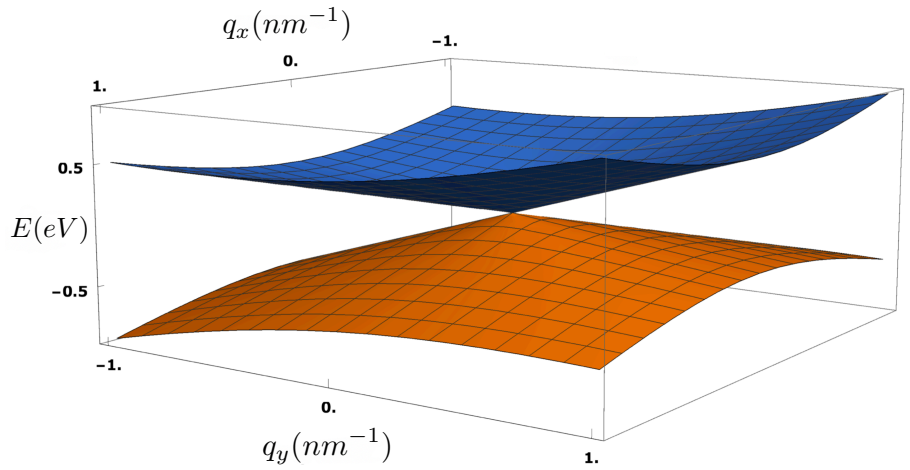

Figure 1.9: A tilted, anisotropic Dirac cone of 8-Pmmn borophene, in the close vicinity of Dirac point $\mathbf{q_D}$, is shown in the q_x-q_y plane.

1.4.1 Experimental Evidence of Borophene

In recent years several monolayer boron structures have been experimentally realized on silver substrate [Ag(111)] following their theoretical predictions. In this direction, Manix *et al.* [43] synthesized atomically thin and crystalline sheets of boron atom on silver substrate under ultrahigh-vacuum conditions using solid boron atomic source. In situ scanning tunneling microscopy (STM) images have shown the growth of planar structures with anisotropic behavior, which is consistent with first-principles calculation. They have further verified the planar, chemically distinct, and atomically thin nature of these sheets using characterization techniques. Scanning tunneling spectroscopy revealed that borophene sheets are metallic with highly anisotropic electronic properties which was predicted earlier theoretically.

Feng *et al.* have confirmed that two-dimensional boron sheets can be grown epitaxially on a Ag(111) substrate [44]. They have observed two kinds of boron sheet, a β_{12} sheet and a χ_3 sheet by scanning tunnelling microscopy. Both of them are shown to exhibit a triangular lattice but with different arrangements of periodic holes.

In another work, Feng *et al.* have investigated the electronic structure of β_{12} phase of a monolayer boron sheet both theoretically and experimentally [2]. The β_{12}-sheet, the lone phase found from low-energy electron diffraction (LEED) measurement, exhibits a rectangular structure which is different from the hexagonal structure of Ag(111) but they have obtained sub-domains with three equivalent domains which are related by 120° rotations. A schematic scetch of the BZ of Ag(111) with the three

domain orientations is depicted in Fig. 1.10 where the measured Fermi surface is also shown. The band structure from the monolayer sheet exhibits solo Fermi pocket centered at the S point of the β_{12}-sheet and a couple of Fermi pockets centered at the $\overline{\mathrm{M}}$ point of Ag(111), as shown by the red and black arrows, respectively. Note that, S and $\overline{\mathrm{M}}$ points are the high symmetry points as depicted in Fig. 1.10(a).

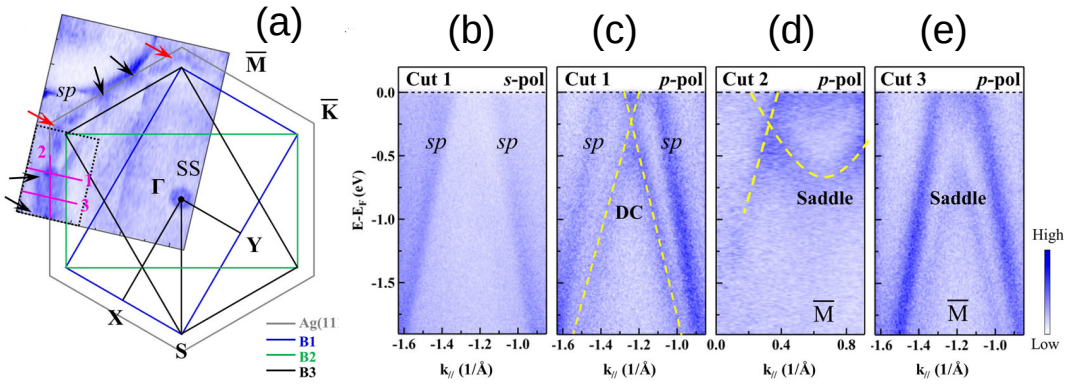

Figure 1.10: (a) The Fermi surface of the β_{12}-boron sheet on Ag(111) is illustrated. The black, green, and blue rectangles refer to the BZ of three equivalent domains, while the BZ of Ag(111) is shown by grey hexagon. The black and red arrows indicate the bands of the boron layer. The surface state (SS) and bulk *sp* band of Ag(111) are visible. The pink lines refer to the cuts $1-3$ where the ARPES intensity plots in (b)-(e) were measured. (b) ARPES intensity plot measured along cut 1 is shown using *s* polarized light. (c)-(e) ARPES intensity plots measured with *p* polarized light along cut 1 to cut 3, respectively. The Dirac cones (DC) are visible which are indicated by the yellow dashed lines. All the ARPES data in (a)-(e) corresponds to a photon energy of 80 eV. This figure is adapted from Ref.[2]

The band structure measured via ARPES technique along different directions in the momentum space (the purple lines in Fig. 1.10) is shown in Figs. 1.10(c-f). Polarized light with its electric field being parallel to the plane of incidence is denoted as p-polarized, while light whose electric field is perpendicular to the plane of incidence is termed as s-polarized. Both *s* and *p* polarized light have been used to investigate the nature of the band structure. In general, the s-polarized light mainly probes the in-plane p_x and p_y orbitals, whereas the p-polarized light probes both the in-plane (p_x and p_y) and the out-of-plane (p_z) orbitals. The measurements of cut 1 using *p* polarized light [Fig. 1.10(c)] exhibit a Dirac cone of boron sheet as well as the bulk *sp* band of Ag(111). There is no energy gap (within the limit of experimental resolution) at the Dirac point which signals the nature of the quasiparticles being massless Dirac fermions and the sheet to be semi-metallic. The Fermi velocities calculated from Fig. 1.10(c) are approximately 9.24×10^5 m/s and 1.06×10^6 m/s for the left and

right branches of the Dirac cone, respectively. While these values are close to the Fermi velocity of graphene ($\sim$ 1.0×10^6 m/s), the difference arises due to the anisotropy of the Dirac cones which is also predicted theoretically [41]. In Fig. 1.10(d), the band structure along the $\overline{\mathrm{K}}$-$\overline{\mathrm{M}}$-$\overline{\mathrm{K}}$ direction is shown where a pair of Dirac cones are visible (shown by the yellow dashed lines) although due to limitation of the experimental configuration the one on the right side is not fully visible. The band structure along the $\overline{\Gamma}$-$\overline{\mathrm{M}}$ is shown in Fig. 1.10(e). However, ARPES measurement shows that *s* polarized light does not produce any Dirac like dispersion as can be seen from Fig. 1.10(b).

CHAPTER 2

Majorana Zero Mode in 1D Systems

2.1 Introduction

Dirac equation is a relativistic wave equation derived by Paul Dirac in 1928. This celebrated equation, which combined special theory of relativity with quantum mechanics, is given by

$$i\hbar\frac{\partial}{\partial t}\Psi = H_{Dirac}\Psi = (c\boldsymbol{\alpha}.\mathbf{p} + \beta mc^2)\Psi. \tag{2.1}$$

where, $\boldsymbol{\alpha}$ and β do not commute. Dirac proposed the following form of the 4×4 matrices:

$$\alpha_i \equiv \sigma_x \otimes \sigma_i = \begin{pmatrix} 0 & \sigma_i \\ \sigma_i & 0 \end{pmatrix}, \beta \equiv \sigma_z \otimes \mathbb{I} = \begin{pmatrix} \mathbb{I} & 0 \\ 0 & -\mathbb{I} \end{pmatrix} \tag{2.2}$$

where σ_i are the Pauli matrices. This equation can also be written in Lorentz covariant form using 4 component gamma matrices $\gamma^\mu \equiv (\beta; \beta\boldsymbol{\alpha})$:

$$(i\gamma^\mu\partial_\mu - m)\Psi = 0. \tag{2.3}$$

with the standard notation $\partial_\mu \equiv \frac{\partial}{\partial x^\mu}$ and considering $\hbar = c = 1$. The gamma matrices follow the Clifford algebra $\{\gamma^\mu, \gamma^\nu\} = 2\eta^{\mu\nu}$, where $\eta^{\mu\nu}$ is the Minkowski metric.

In 1937, Majorana [45] considered the following set of purely imaginary gamma matrices: $\tilde{\gamma}^0 = \sigma_2 \otimes \sigma_1$, $\tilde{\gamma}^1 = i\sigma_1 \otimes \mathbb{I}$,$\tilde{\gamma}^2 = i\sigma_3 \otimes \mathbb{I}$ and $\tilde{\gamma}^3 = i\sigma_2 \otimes \sigma_2$ in the Dirac equation. Consequently the equation Eq.(2.3) becomes:

$$(i\tilde{\gamma}^\mu \partial_\mu - mc)\tilde{\Psi} = 0. \tag{2.4}$$

which leads to the condition on the field :

$$\tilde{\Psi} = \tilde{\Psi}^*. \tag{2.5}$$

This implies that the particles, which follow Majorana equation (2.4), are their self conjugate *i.e.,* they are their own anti-particle. For more than 60 years, this elusive particle is hunted by different communities of high energy physics : elementary particle physics, nuclear physics, astrophysics, and cosmology. For the last few years search for Majorana reaches a new territory : condensed matter physics [46].

In condensed matter physics, Majorana fermions are not elementary particles, rather they are *emergent quasiparticles*. Moreover, they don't follow the usual fermionic statistics; rather they satisfy non-abelian exchange statistics [26, 47]. Thus, they are non-abelian anyons : particle exchanges are non-trivial operations which do not commute in general. This is fundamentally different from other types of particle where an exchange operation merely multiplys the wavefunction by +1 (for bosons) or -1 (for fermions) or $e^{i\phi}$ (for abelian anyons). Furthermore, a Majorana fermion is in a sense half of a normal fermion, meaning that a fermionic state can be obtained as a superposition of two of them. We term it as 'Majorana zero mode' (MZM) instead of calling it a fermion and the reason behind calling it a 'zero mode' becomes clear in the next section.

Being its own antiparticle means that a MZM must be an equal superposition of an electron and a hole state. It is, thus, obvious to hunt for such excitations in superconductors, where the wavefunctions of Boguliubov quasiparticles have equal portion of an electron and a hole component due to the particle-hole symmetry. In second quantized language, the annihilation operator of a Boguliubov quasiparticle in the natural s-wave superconductor has the form $b = uc^\dagger_\uparrow + vc_\downarrow$, where c_σ annihilates a fermion with spin orientation $\sigma = \uparrow, \downarrow$. Here u and v are in general momentum dependent but for

this discussion, momentum is irrelevant here and therefore omitted for simplicity. The operator b can never be written in the form of a Hermitian operator due to the different spins of c and $c^\dagger$. We can write annihilation operator for MZM, following Hermitian condition, as : $\gamma = uc_\sigma^\dagger + u^* c_\sigma$ and therefore the creation operator, $\gamma^\dagger = \gamma$. The major difference from the s-wave Boguliubov quasiparticle operator is that the MZM have equal spin projections. Such equal spin pairing do not occur in most types of naturally found superconductors and were first predicted to occur in the $\nu = 5/2$ fractional quantum Hall state [48].

The search for MZMs took a big step forward in 2008 with the seminal paper by Fu and Kane [49] where they showed that $p_x \pm ip_y$-wave-like pairing can be engineered in the surface states of a strong topological insulator when brought into close proximity to a s-wave superconductor and a ferromagnetic insulator (giving rise to proximity-induced superconductivity [50, 51] in the surface of a topological insulator). The necessary ingredient is the strong spin-orbit coupling of the topological insulator which leads to the band splitting with momentum-dependent spin directions. When the topological insulator is coupled to a magnetic insulator, the unwanted Kramer's degeneracy is lifted by the induced Zeeman splitting and an effectively spinless regime can be achieved. After a couple of years, two remarkable works by Lutchyn *et al.* and Oreg *et al.* [52, 53] proposed a realistic way to obtain MZMs in one dimensional (1D) semiconducting nanowires which we discuss in Sec. 2.3 in details. There have also been proposals to create MZMs in magnetic spin chain on top of a s-wave superconductor [54].

We first discuss Kitaev toy model for Majorana states in a spinless p-wave superconductor in Sec. 2.2. Then we discuss realistic model and present the results for hunt of MZM in 1D systems in Sec. 2.3. The experimental detection of MZM, till date, based on 1D semiconductor nanowire is summarized in Sec. 2.4.

2.2 Majorana zero mode in Kitaev Chain

Kitaev in his seminal paper [55] considered a 1D tight-binding chain with p-wave superconducting pairing. The Hamiltonian of the lattice chain is given by

$$\mathcal{H}_{\text{chain}} = -\mu \sum_{i=1}^{N} n_i - \sum_{i=1}^{N-1} \left(t c_i^\dagger c_{i+1} + \Delta c_i c_{i+1} + h.c. \right), \tag{2.6}$$

where $h.c.$ refers to hermitian conjugate, μ is the chemical potential, $c_i(c_i^\dagger)$ is the electron annihilation (creation) operator for site i, and $n_i = c_i^\dagger c_i$ is the corresponding number operator. Here Δ and t denote the superconducting pairing gap and nearest neighbour hopping respectively. The chemical potential μ is assumed to be homogeneous throughout the chain. For simplicity, the superconducting phase ϕ can be taken to be zero, such that $\Delta = |\Delta|$. The time-reversal symmetry ($\mathcal{T}$) is broken in Eq. (2.6) since only one kind of the spin projection is considered, i.e., effectively spinless electrons are considered in the model (the spin label is thus omitted). Note that, the superconducting pairing is non-standard since it couples electrons with the same spin (whereas in standard s-wave pairing, electron couples only with opposite spin projection). Moreover, electrons are paired only with the neighboring sites in contrast to the s-wave pairing which is onsite.

We now rewrite Eq. (2.6) in terms of Majorana operators. Fermionic operators can always be decomposed as a linear combination of two Majorana operators :

$$c_i = \frac{1}{2} \left(\gamma_{i,1} + i \gamma_{i,2} \right), \tag{2.7}$$

$$c_i^\dagger = \frac{1}{2} \left(\gamma_{i,1} - i \gamma_{i,2} \right), \tag{2.8}$$

where $\gamma_{i,1}$ and $\gamma_{i,2}$ are two Majorana operators on lattice site i. By inverting the above equations, we obtain

$$\gamma_{i,1} = c_i^\dagger + c_i, \tag{2.9}$$

$$\gamma_{i,2} = i \left(c_i^\dagger - c_i \right), \tag{2.10}$$

Hence, these Majorana operatos are hermitian as expected. Figure 2.1 shows a schematic sketch of Kitaev's chain with Majorana decomposition. The upper panel dictates that two Majoranas are

coupled on each site to form a fermion operator as given by Eq. (2.7). These new Majorana operators satisfy the following algebra:

$$\{\gamma_{i,1}, \gamma_{j,1}\} = 2\delta_{ij}, \quad \{\gamma_{i,1}, \gamma_{j,2}\} = 0 \tag{2.11}$$

$$\gamma_i = \gamma_i^\dagger, \quad \gamma_i^2 = 1 \tag{2.12}$$

Writing Eq. (2.6) in terms of the Majorana operators, we obtain

$$\mathcal{H}_{\text{chain}} = -\frac{\mu}{2}\sum_{i=1}^{N}(1 + i\gamma_{i,2}\gamma_{i,1}) - \frac{i}{2}\sum_{i=1}^{N-1}[(\Delta + t)\gamma_{i,2}\gamma_{i+1,1} + (\Delta - t)\gamma_{i,1}\gamma_{i+1,2}]. \tag{2.13}$$

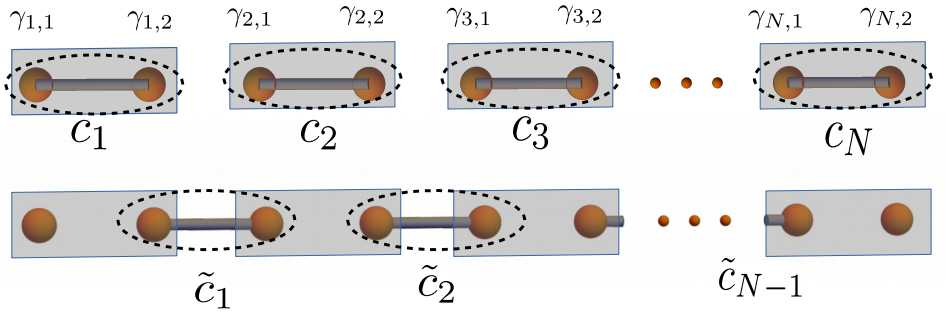

Figure 2.1: Schematic sketch of Kitaev's 1D p-wave superconducting tight binding chain. Upper panel refers to the trivial phase of the Kitaev chain where two Majoranas are coupled on each site to form fermion operator. Lower panel describes topological phase of the Kitaev chain in which Majoranas couple each other from adjacent sites and form normal fermions. This leaves one unpaired Majorana at each end of the chain.

In the regime, $\mu < 0$ and $t = \Delta = 0$, the chain resides in the topologically trivial phase. In this limit, the only surviving term is the coupling between Majorana modes $\gamma_{i,1}$ and $\gamma_{i,2}$ at the same lattice site as shown in the upper panel of Fig. 2.1. Clearly the spectrum is gapped since introducing an extra spinless fermion into the chain costs a finite energy $|\mu|$. It is important to note that the system remains in trivial phase even when the parameters are away from this fine-tuned limit provided that the gap persists.

The other limit is especially interesting when $\mu = 0$, $t = \Delta$, where topological phase can be achieved. In this case, the Hamiltonian becomes

$$\mathcal{H}_{\text{chain}} = -it\sum_{i=1}^{N-1}\gamma_{i,2}\gamma_{i+1,1}. \tag{2.14}$$

Here two Majorana operators from the adjacent sites couple to form a normal fermion and thus leaving behind one unpaired Majorana at each end of the chain. We can construct a new fermion operator, $\tilde{c}_i$, by combining Majorana operators from neighboring sites

$$\tilde{c}_i = (\gamma_{i+1,1} + i\gamma_{i,2})/2. \tag{2.15}$$

This pairing is shown in the lower panel of Fig. 2.1. In terms of these new fermion operators we can rewrite Eq. (2.13) as

$$\mathcal{H}_{\text{chain}} = 2t \sum_{i=1}^{N-1} \tilde{c}_i^\dagger \tilde{c}_i. \tag{2.16}$$

The sum is over $N-1$ electrons and the energy cost of adding an electron is $2t$. The Majorana operators $\gamma_{N,2}$ and $\gamma_{1,1}$, which are situated at the two ends of the chain, are completely missing from Eq. (2.14)! We can now form a single fermionic non-local state composed from these two 'unpaired' Majorana modes as

$$\tilde{c}_M = (\gamma_{N,2} + i\gamma_{1,1})/2. \tag{2.17}$$

This is a highly non-local fermionic state since $\gamma_{N,2}$ and $\gamma_{1,1}$ are localized at the opposite ends of the chain. Moreover, since this fermionic operator is absent from the Hamiltonian, occupying the corresponding state does not cost any energy. In "normal" superconductors the ground state is non-degenerate and consists of a superposition of even number of particle states (condensate of Cooper pairs), while odd number of quasiparticles are allowed in the Hamiltonian (2.6) without any extra energy cost. The ground state, therefore, is two-fold degenerate corresponding to having an even or odd number of total electrons in the superconductor. This even or oddness, also termed as parity, refers to the eigenvalue of the number operator of the zero-energy fermion, $n_M = \tilde{c}_M^\dagger \tilde{c}_M = 1(0)$ for odd (even) parity.

Although we have considered limiting case $\Delta = t$ and $\mu = 0$, it can be shown that the MZMs remain unpaired at the end of the chain as long as the chemical potential lies within the gap ($|\mu| < 2t$) [55] . In the general case, the MZMs are not completely localized only at the two ends of the chain, rather they decay exponentially away from the edges. The overlap of these unpaired Majorana

wavefunctions results in a splitting between the degenerate states by an energy that scales as $e^{-L/\xi}$, where L is the length of the chain and ξ is the coherence length. So, the MZMs remain prestine at zero energy only if the wire is long enough such that their overlap is negligible.

2.3 Majorana zero mode in one dimensional semiconducting nanowire

Although Kitaev's ingenious idea was a big step to find MZMs in condensed matter systems especially in 1D wires, the toy model was hard to realize in experimental setups due to unavailability of natural p-wave superconductors. Two seminal works by Lutchyn *et al.* [52] and Oreg *et al.* [53] showed that it is indeed possible to engineer the topological superconducting phase in 1D nanowire system (mimicing Kitaev's toy model) by judiciously combining three naturally available ingredients: 1D wire with strong spin-orbit coupling, a standard s-wave superconductor, and an external magnetic field. Figure 2.2 dictates the schematic sketch of the model with the required ingrdients mentioned before. Thus, the model Hamiltonian for the wire reads

$$H = H_{\text{wire}} + H_{\Delta} \tag{2.18}$$

$$H_{\text{wire}} = \int dx \psi_{\sigma}^{\dagger} \left(-\frac{\partial_x^2}{2m} - \mu - i\alpha\sigma^y\partial_x + h\sigma^z \right) \psi_{\sigma} \tag{2.19}$$

$$H_{\Delta} = \int dx \Delta(\psi_{\uparrow}\psi_{\downarrow} + H.c.). \tag{2.20}$$

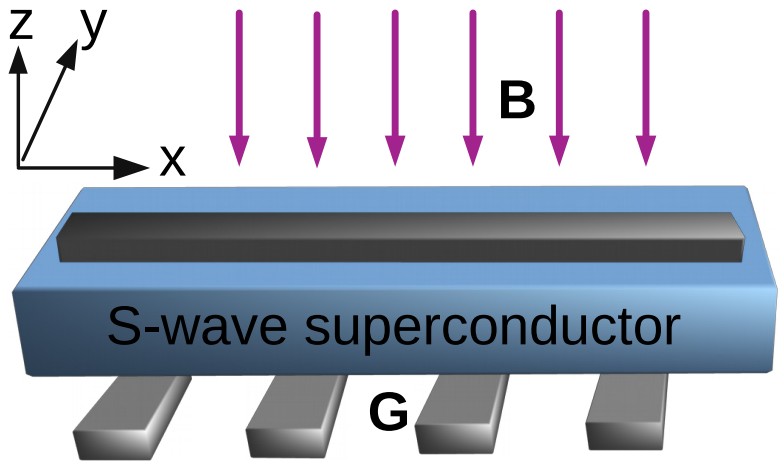

Figure 2.2: Schematic sketch of a 1D spin–orbit coupled nanowire (dark grey) in close proximity to a s-wave superconductor. Big arrows indicate perpendicularly applied magnetic field B. The back gates (grey) are connected to control the chemical potential in the nanowire.

Here $\psi_{\sigma}^{\dagger}$ creats an electron with effective mass m, chemical potential μ, and spin σ in the wire. α

refers to the strength of the spin-orbit coupling in the wire; and h denotes the Zeeman energy originated from a magnetic field applied along the z axis whereas the wire lies along the x axis. The precise direction of spin-orbit coupling and magnetic field axes are unimportant provided they are perpendicular to each other as well as to the wire direction. For realistic situation, one can conceive $H_{\rm wire}$ to be described by an electron-doped semiconducting nanowire such as InAs/InSb with strong Rashba like spin-orbit coupling [56]. The pairing term H_Δ refers to the proximity effect of the s-wave superconductor on the wire. The chemical potential (onsite energy) of the wire is controlled by a set of gate electrodes (see Fig. 2.2). The wire is assumed to be long enough such that the size quantization can be ignored along the wire direction so that MZM do not overlap with each other and thin enough that the 1D subbands are well separated compared to the relevant energy scales.

First we consider $\Delta = 0$ case and examine the Hamiltonian $H_{\rm wire}$. In absence of any spin-orbit coupling and magnetic field *i.e.,* $\alpha = h = 0$, the electrons exhibit parabolic dispersion ($E \propto k^2$) having spin degeneracy. With spin-orbit coupling, parabolic bands get shifted depending on their spin orientation along the axis of the spin–orbit field as shown by the blue and red parabolas in Fig. 2.3(a). The 'spinless' regime is *not* possible here; the spectrum always supports an *even* number of pairs of Fermi points for any Fermi energy. As the magnetic field is turned on, Zeeman gap pops up at $k = 0$ which splits the bands and the corresponding band energies are given by

$$\epsilon_\pm(k) = \frac{k^2}{2m} - \mu \pm \sqrt{(\alpha k)^2 + h^2} \tag{2.21}$$

These bands are depicted by the solid black curves in Fig. 2.3(b). When the Fermi level resides within this magnetic field-induced gap (μ shown in the figure), the effective 'spinless' regime in the wire can be obtained.

Now we switch on proximity induced superconductivity *i.e.,* $\Delta > 0$ and investigate the resulting band structure. To intuitively understand the underlying physics, we project out the upper unoccupied band and only consider the lower, which is legitimate for $\Delta \ll h$. The spins of electrons in the lower band (which is of our interest) are partially polarised because of competition between spin-orbit coupling and the magnetic field. It is important to note that, without the momentum dependence of the spin direction, it is impossible to induce superconductivity by proximity with a s-wave superconductor because the s-wave pairing only couples the electrons with oppsoite spins. The spin orientations

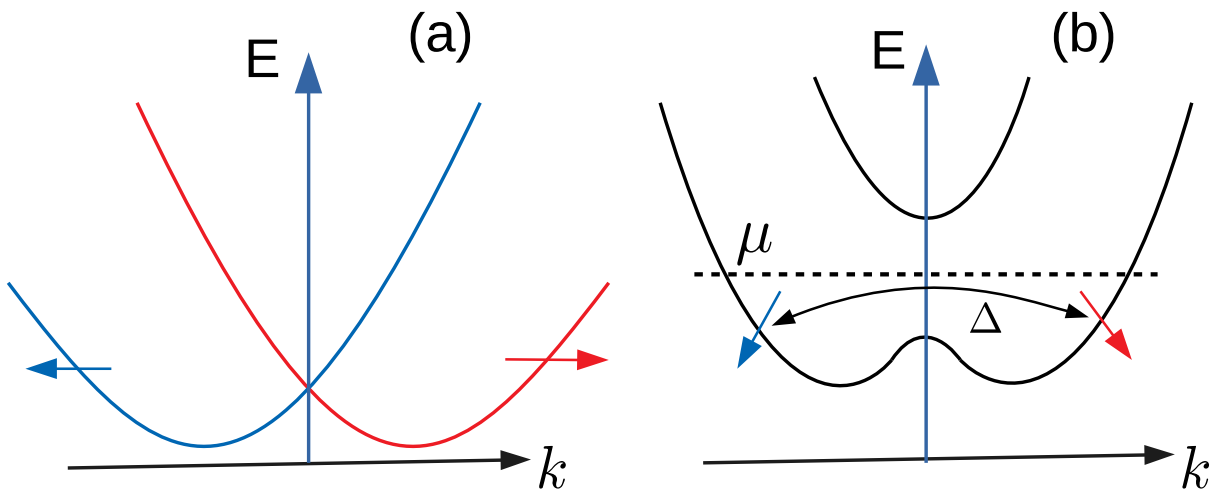

Figure 2.3: Band dispersion is shown for the rashba nanowire in absence of the magnetic field (red and blue curves in (a)) and in presence of the magnetic field (black curves in (b)). The chemical potential is indiacted by the dashed black line and when it lies within the magnetic field-induced Zeeman gap at $k = 0$, the wire appears 'spinless'. Δ refers to the proximity induced superconducting gap in the wire.

are shown by blue and red arrow in Fig. 2.3(b). With the enhancement of the magnetic field, the gap between the bands increases which helps in orienting the spins of the electrons in the same direction and effectively 'spinless' regime can be achieved similar to the Kitaev's toy model. A strong magnetic field, nonetheless, is not suitable as it hinders superconducting pairing to be induced and this is why a fine-tuning among the parameters is required. In proximity to the superconductor, electrons living near k_F and $-k_F$ get coupled which gives rise to effective p-wave pairing because of 'spinless' character. When Δ is weak compared to h, the wire hosts topological superconducting state which can be connected smoothly to the weak-pairing phase of Kitaev's toy model [55, 57].

The presence of superconductivity, because of particle-hole symmetry, doubles the number of bands as shown in Fig. 2.4. We analyze various gaps that open up for $\Delta \neq 0$ as a result of the pairings in Eq. (2.24). The gaps near $k = 0$ and near the Fermi momenta are denoted as Δ_0 and Δ_F, respectively. The BdG spectrum of the system becomes (see Fig. 2.4)

$$E_{\pm}^2(k) = (\frac{\hbar^2 k^2}{2m} - \mu)^2 + \alpha^2 k^2 + h^2 + \Delta^2 \pm 2\sqrt{h^2\Delta^2 + (\frac{\hbar^2 k^2}{2m} - \mu)^2(h^2 + \alpha^2 k^2)}. \tag{2.22}$$

Δ_0 is cruical to understand the emergence of topological superconductivity. There are two kinds of gapping mechanisms at low momentum (near $k = 0$) namely h and Δ. Due to their competition,

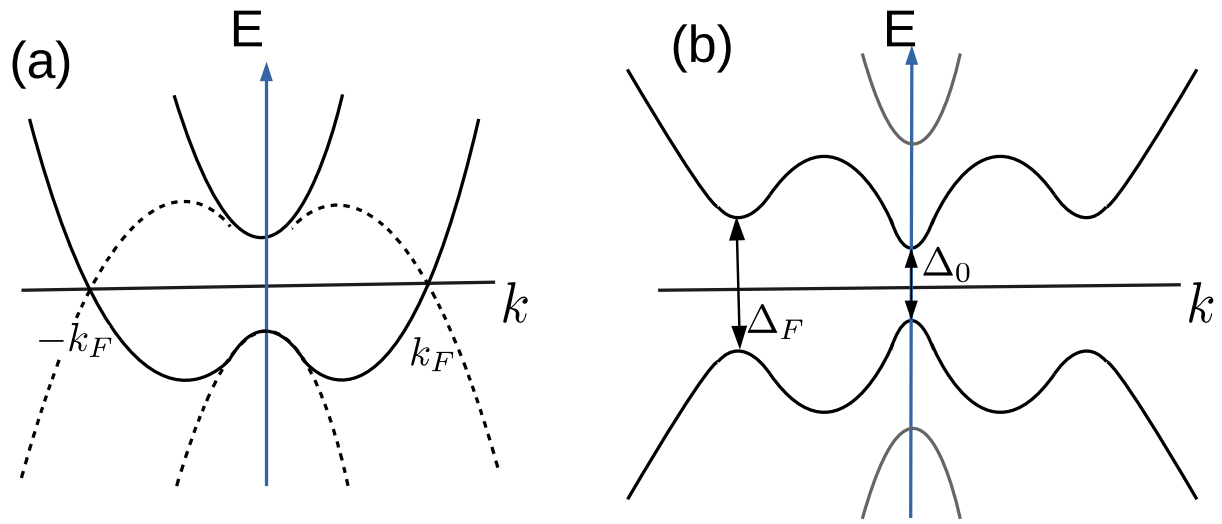

Figure 2.4: Bogoliubov-de Gennes spectrum of the Rashba nanowire. (a) $\Delta = 0$: electron (solid lines) and hole (dashed lines) bands cross each other at finite energies (interband crossings) and at the Fermi energy (intraband crossings). (b) A finite $\Delta \neq 0$ leads to both intraband and interband pairings, Eq. (2.24), and open a gap Δ_F at the Fermi points k_F, and modify the Zeeman gap at $k = 0$. This gap Δ_0 is determined by the competition between h and Δ. This gap closes and reopens with the increase of h, giving rise to a topological phase transition.

the gap Δ_0 can be closed, which is an indication of a topological phase transition. There is a critical Zeeman field

$$h^c \equiv \sqrt{\Delta^2 + \mu^2}, \tag{2.23}$$

for which the low momentum gap Δ_0 vanishes. When $h > h^c$, the gap reopens again but is now Zeeman-dominated and the system becomes a topological superconductor. The other gap Δ_F, in contrast to Δ_0, never closes and, for strong spin-orbit coupling, remains roughly constant $\Delta_F \sim \Delta$. The phase diagram of the nanowire is shown in Fig. 2.5.

The appearance of topological superconductivity in the Rashba nanowire can be intuitively understood by writing the Hamiltonian in helical basis. By projecting out the upper band and considering only one band (lower one), we obtain s-wave pairing term in the helical basis as:

$$H = \int \frac{dk}{(2\pi)} \frac{\Delta_-^p}{2} \{\psi_-^\dagger(k)\psi_-^\dagger(-k) + H.c.\}$$

with the emergent gap

$$\Delta_{-}^{p}(k) = \frac{i\alpha k\Delta}{2\sqrt{h^2+\alpha^2k^2}}. \tag{2.24}$$

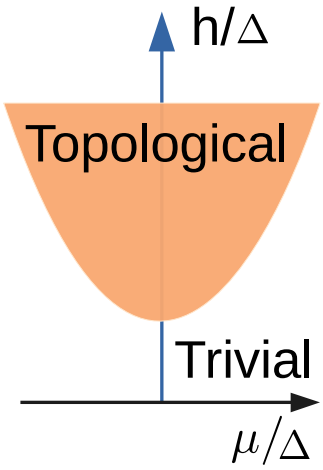

Figure 2.5: Phase diagram of the proximitized nanowire which becomes a one-dimensional topological superconductor for $h > \sqrt{\mu^2+\Delta^2}$.

This indicates that even in the proximity to a conventional s-wave pairing, the projection of the pairing onto the helical bands gives rise to an effective p-wave pairing which is of intraband nature in this case. We have given a detailed derivation of this emmergent p-wave pairing in Appendix B. Actually, when both upper and lower bands are taken into account, effective pairing, in the helical bands, consists of both s-wave (interband pairing) as well as p-wave (intraband pairing) components. Similar physics appears in case of three dimensional topological insulator in close proximity to s-wave superconductor where Fu and Kane showed that $p_x + ip_y$ like pairing emmerges out, giving rise to Majorana mode at the vortex core [49].

2.4 Experimental Signature of Majorana zero mode

Till date, there has been many sucssesful experiments that could infer the existance of MZM in Rashba nanowire. Upsurge activity from experimetal side came after the prediction of MZM in Rashba nanowire by Lutchyn *et al.* and Oreg *et al.* in 2010. Clear and direct probes of MZM have been carried out in three different classes of experiments : tunneing experiment, Josephson current mea-

surement and interferometry. We shall only focus on the outcome of tunneing experiments.

This platform of rashba nanowire has attracted enormous attention mainly because all the necessary ingredients : nanowire with strong spin orbit coupling, superconductor and magnetic field are easily available in present day laboratories. In the topological superconducting phase, as described earlier, MZM appears at each end of the wire. Emmergence of such zero modes takes place with the concomitant topological phase transition. The observation of the closing and reopening of the bulk bandgap is a strong evidence of the topological phase transition.

InAs [58] and InSb nanowires [59] have strong spin-orbit interaction of strength $\alpha_R = 10$ meVnm and $\alpha_R = 20$ meVnm respectively which helps in shifting the bands of different spins. They also posses large g factor of $g \approx 15$ and $g \approx 50$ respectively[58, 59]. When this nanowire is kept in close proximity to an s-wave superconductor, the large g-factors allow for weak magnetic field to open a relatively large Zeeman gap which drive the wire into a topological superconductor hosting MZMs. The strong spin-orbit coupling is shown to enforce the topological superconducting state to possess a relatively large gap which remains robust against disorder [60].

The first succsessful experiment in the direction of probing the transport signal of MZM was reported by Mourik *et al.* [3]. They used an InSb semiconductor quasi-one-dimensional wire with strong spin-orbit coupling which is partially deposited on a silicon substrate and kept in contact with superconducting (niobium titanium nitride) and normal metal electrodes as demosnstrated in Fig. 2.6(a).

A tunnel barrier is created in the nanowire by applying a negative voltage to the narrow area (tunnel barrier) in between normal (N) and superconducting (S) part of the nanowire. This tunnel barrier further localize the zero mode at the wire ends and preventsthe Majorana wave-functions to leak into the normal side. A bias voltage is applied externally between the N and S contacts and it drops almost completely across the tunnel barrier. The differential conductance dI/dV at voltage V and current I, in this setup, is proportional to the density of states at energy $E = eV$ measured from Fermi level. Magnetic field dependent dI/dV vs V is shown in Fig. 2.6(b) for increasing B fields in 10 mT steps from 0 to 490 mT. The two peaks at ± 250 meV signify the peaks in the quasi-particle density of states

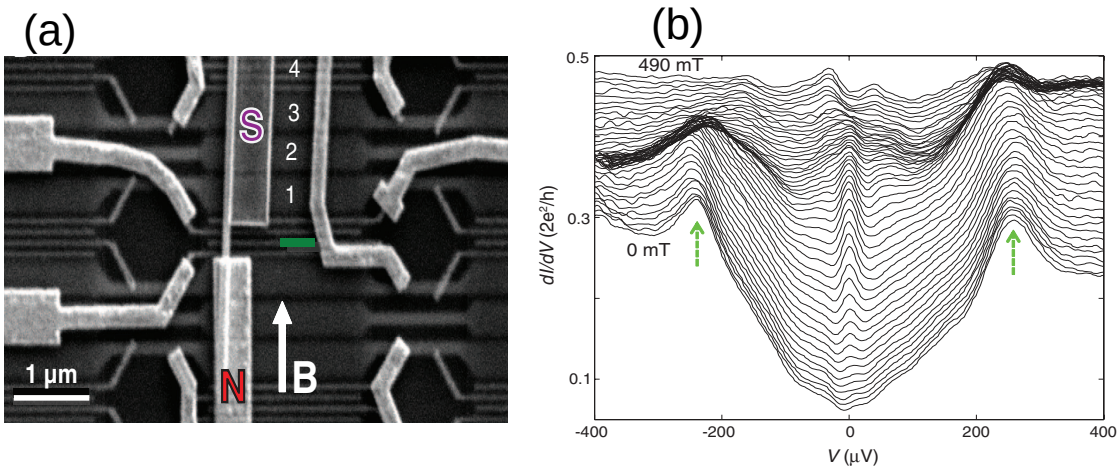

Figure 2.6: (a): Experimental set up of the semiconductor-superconductor heterostructure is shown. (b): Magnetic field–dependent dI/dV is measured as a function bias voltage V at temperature 70 mK for magnetic fields ranging from 0 to 490 mT in 10-mT steps. This figure is adapted from Ref. [3]

of the superconducting wire. The induced gap in the wire, thus, is $\Delta \approx 250meV$.

When electron arising from normal side is reflected as a hole (process called Andreev reflection), the conductance is given by $G = (2e^2/h)T_A$, where the factor of 2 appears because the Andreev reflection of an electron into a hole doubles the current and T_A is the Andreev reflection probability [61]. K. T. Law *et al.* showed that the Majorana induced Andreev reflection is always of unit proability and thus tunneling conductance dI/dV at zero energy is 0 $(2e^2/h)$ depending on absence (presence) of Majorana state at the end of superconducting region [62]. Furthermore, this zero bias conductance is independent of the precise tunnelling strength. The Majorana nature of this perfect Andreev reflection is a direct consequence of the well-known Majorana symmetry property where particle is same as its own antiparticle.

When magnetic field strength is between $\sim$ 100 and 400 mT along the nanowire axis, a peak has been observed at $V = 0$. The peak has an amplitude up to $\sim 0.05 \times 2e^2/h$ which is much lower compared to the theoretical prediction of $2e^2/h$ at zero temperature. This discrepancy was suspected as a result of thermal averaging, but this suspection is ruled out when the peak width exceeds the thermal broadening ($\sim 3.5k_BT$). Other averaging mechanisms, such as dissipation [63], have been taken into consideration where the main source of dissipation is 'soft gap' problem which is the presence of finite quasiparticle density-of-states within the superconducting gap. Substantial improvement could be achieved in hardening the gap by enhancing the quality of materials, eliminating the possible dis-

order, smoothening the interface between the wire and the superconductor [64, 65], and better control during device processing [66, 67].

Several groups have reported the experimental observations of zero-bias peak at non-zero magnetic field revealing the existence of Majorana bound states [58, 68, 69]. The obtained ZBP in transport measurement, however, were also predicted to be mimicked by other effects, such as owing to Kondo physics [70], smooth confinement [71, 72], weak antilocalization [73], disorder [74, 75], parity crossings of Andreev levels [76].

Investigation of concrete evidence of MZM in nanowire has been, thus, carried out extensively by various groups [77, 78, 79]. Addressing all the dissipation and disorder issues mentioned above, very recently, Zhang *et al.* have reported the quantized zero bias conductance peak in semiconductor-superconductor heterostructure [4]. A micrograph of a fabricated device and schematic of the measurement set-up is shown in Fig. 2.7(a) where an InSb nanowire is partially covered by a thin superconducting aluminium shell to create superconducting portion. The tunnel-gates are used to induce and control a tunnel barrier in segment between the normal and superconducting regime. The chemical potential in the region covered with Al can be tuned by using super-gates connected to that segment.

The magnetic field dependancy of dI/dV is depicted in Fig. 2.7(b). The ZBP remains quantized with the value $2e^2/h$ for a considerable value of magnetic field B which indicates the robustnace of ZBP against the applied B field. Experimental outcome matches qualitatively with theoretical prediction which is shown in Fig. 2.7(d). 'Soft gap' problem still sustains as can be seen in Fig. 2.7(c) left panel and is denoted by the black curve. ZBP attains its maximum value of $2e^2/h$ for $B = 0.88T$ which matches with the theory [see right panel of Fig. 2.7(c)] to a considerable extent.

This seminal paper has also shown the tunnel-gate voltage dependance of the ZBP. It is clear from Fig. 2.8(a) and (b) that the tunneling conductance is almost robust for tunnel gate voltage being -8.0 or more positive when bias voltage $V = 0$. However, for more negative tunnel-gate voltage, ZBP gets splitted and dI/dV approaches zero which can be attributed to the overlap of Majorana wavefunctions [72]. The above-gap conductance measured at $V = 0.2$ meV varies with tunnel-gate voltage as shown in Fig. 2.8(c) which is expected as this transport is carried by quasi-particles above

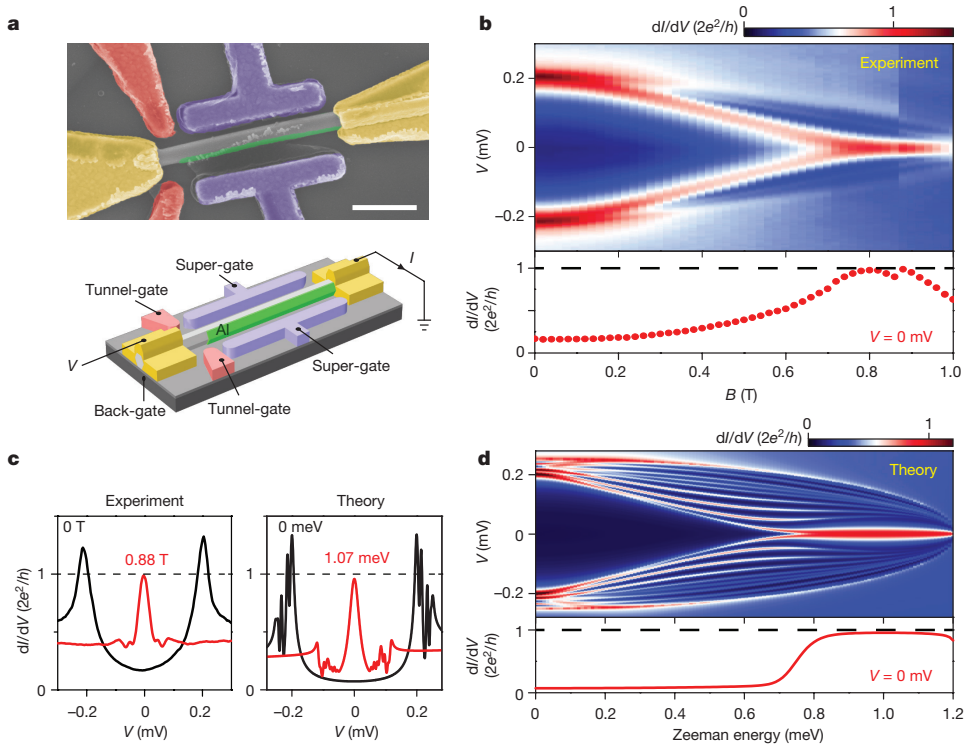

Figure 2.7: Scanning electron micrograph of the experimental device is shown in upper panel and its schematic sketch in lower panel of (a). The two tunnel-gates are shorted externally, as are the two super-gates. (b) Magnetic field dependence of the quantized ZBP is depicted in upper panel while the line cut along the zero-bias is presented in the lower panel. Magnetic field direction is aligned with the nanowire axis for all measurements. Super-gate and tunnel-gate voltages are fixed at -6.5V and -7.7V respectively, while the back-gate is kept grounded. Measurement is carried out at 20 mK. (c) Comparison between experiment and theory is shown : left (right) panel dictates the vertical line-cuts from b (d) at 0 T and 0.88 T (1.07 meV). (d) Theoretical results of dI/dV obtained from simulation is shown, with chemical potential $\mu = 0.3$ meV. This figure is adapted from Ref. [4] .

the superconducting gap. All of these observations match very well with the results from theoretical side which are shown in Fig. 2.8(d). They have also varied chemical potential, super-gate voltage and temperature, and have established the robustness of MZM against all of these parameters (local perturbations).

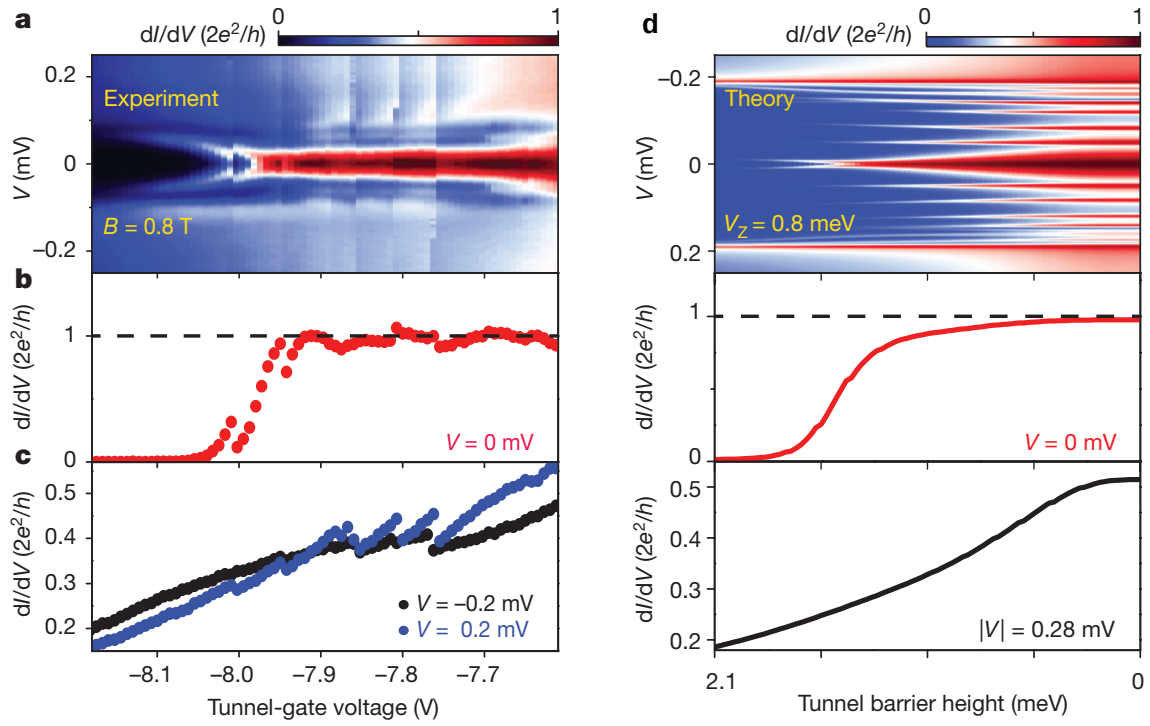

Figure 2.8: (a) : Tunnel-gate dependence of the quantized ZBP at B=0.8T while super-gate and back-gate voltages are fixed at -6.5V and $0V$, respectively. (b), (c) : Horizontal line-cuts from (a), revealing zero-bias conductance and above-gap conductance, respectively. The zero-bias conductance shows a quantized plateau for a range of tunnel-gate voltage. (d) : Theoretical results using Majorana simulation is shown describing the tunnel-gate dependence of dI/dV. The Zeeman field is chosen at 0.8 meV and chemical potential at 0.6 meV. This figure is adapted from Ref. [4] .

There is finite possibility of arising Andreev bound state (ABS) near the tunnel barrier region, which can mimic the ZBP of $2e^2/h$ in tunnelling conductance as predicted by Liu *et al.* [80]. However, these trivial ABS are not robust against tunnel-gate voltage as confirmed by Zhang *et al.* [4]. They concluded that while the temperature alone cannot differentiate the MZM origin from ABS, a stable quantized tunnel-conductance plateau which is robust against variations in all gate voltages and magnetic field strength, can be an unique identification of a topological MZM in tunnelling spectroscopy. Although the search for smoking gun signal of MZM is still under active research pathway.

CHAPTER 3

Thermal Conductance in Superconducting Hybrid Junction of Silicene

3.1 Chapter Summary

We have explored the the properties of thermal conductance in a normal-insulator-superconductor (NIS) junction of silicene for both thin and thick barrier limit of the insulating region. While thermal conductance, in this kind of junction of Dirac materials, displays the conventional exponential dependence on temperature, it manifests a nontrivial oscillatory dependence on the strength of the barrier region. We have explored the tunability of the thermal conductance by the interplay betwen external electric field and the induced superconducting gap. Moreover, the effect of doping concentration on thermal conductance has also been discussed. In the thin barrier limit, the period of oscillation of the thermal conductance as a function of the barrier strength comes out to be $\pi/2$ when doping concentration in the normal silicene region is small. On the other hand, the period gradually converts to π with the enhancement of the doping concentration. Such change of periodicity of the thermal response with doping can be a possible probe to identify the crossover from specular to retro Andreev reflection in Dirac materials. In the thick barrier limit, thermal conductance exhibits oscillatory behavior as a function of barrier thickness d and barrier height V_0 while the period of oscillation becomes V_0 dependent. However, amplitude of the oscillations, unlike in tunneling conductance, gradually decays

with the increase of barrier thickness for arbitrary height V_0 in the highly doped regime. We have discussed experimental relevance of our findings.

3.2 Introduction

With the discovery of graphene [81, 7] and topological insulator [82, 83], the study of Dirac fermions in condensed matter systems has become one of the most active field of reseach over the last decade. The low energy band spectrum of these materials exhibits massless Dirac equation. Hence, relativistic electronic band structure leads to upsurge research interest in terms of possible application as well as fundamental physics point of view.

In recent years, a silicon analogue of graphene, silicene [6, 13, 5, 84] consisting of a monolayer honeycomb structure of silicon atoms, has attracted an immense amount of research interest both theoretically [5, 6] and experimentally [21, 85, 1, 86]. This two-dimensional (2D) material has been grown experimentally by successful deposition of silicene sheet on silver substrate [21, 85, 1]. Also the interest in silicene soared due to the possibility of its various future applications ranging from spintronics [87, 88, 89, 90, 91], valleytronics [92, 17, 93, 94, 95] to silicon based transistor [96] at room temperature.

Very recently, it has been reported that low energy excitations in silicene follows relativistic Dirac equation akin to graphene [5, 30]. In fact, silicene shares almost all remarkable properties with graphene viz. hexagonal honeycomb structure, Dirac cones etc. However, due to large ionic radius of silicon atom, contrary to graphene, silicene does not possess a planar structure, rather it has a periodically buckled structure. Not only that, silicene has spin-orbit coupling (~ 1.55 meV) [6] which is significantly large compared to Graphene. Consequently, a band gap appears at the Dirac points $\mathbf{K}$ and $\mathbf{K}'$ resulting Dirac fermions to be massive. Due to the buckled structure the two sublattices in silicene respond differently to an externally applied electric field which can tune the band gap at the Dirac points [97, 98, 30]. Such tunability opens up the possibility to undergo a topological phase transition from topologically non-trivial state to a trivial state depending on whether the applied electric field is less or more than the critical value at which the band gap closes. Thus a rich varity of topological phases can be realised in silicene [29, 99, 92, 18, 100] under suitable circumstances.

On the other hand, proximity induced superconductivity in Dirac materials has attracted a great deal of attention in recent times [101, 82]. Very recently superconducting proximity effect in silicene has been investigated in Ref. [102] in which the authors have theoretically studied the behavior of electrical conductance in a normal-superconductor (NS) junction of silicene. Up to now, no exper-

iment has been carried out in the context of proximity effect in silicene. On the other hand, heat transport in Dirac systems [103, 104] and superconducting hybrid structures also has become an active field of research over the past decade [105, 106, 107]. Thermal conductance (TC) has been investigated in graphene based hybrid junctions in Ref. [108, 109, 110, 111] where due to low-energy relativistic nature of Dirac fermions in graphene, TC exhibits oscillatory behavior with respect to the barrier strength. Such oscillatory behavior of TC is in sharp contrast to that of the conventional NS junction [112, 113] where TC decays with the barrier strength. However, study of TC in silicene based normal-insulator-superconductor (NIS) hybrid junction is still unexplored to the best of our knowledge. The extra tunability of the band gap by an external electric field also allows one to control the TC by the same. Also, TC in silicene NIS junction for both thin and thick (arbitrary barrier thickness) insulating barrier limit with different doping concentrations is worth to explore.

Motivated by the above mentioned facts, in this chapter, we discuss TC in silicene NIS junction for both thin and thick insulating barrier as well as with various doping concentration in the normal silicene regime. In our analysis, we consider only the electronic part of the TC and neglect the phonon contribution at low temperature. We find that TC has an exponential dependance on temperature which is due to the s-wave symmetry of the superconductor. As the thermal transport is carried by the low-energy Dirac fermions like graphene, TC is shown to be oscillatory as a function of barrier strength. In moderate doped regime, where chemical potential is of the same order of band gap at the Dirac points, TC shows non-trivial nature due to interplay of chemical potenial, gap and temperature. TC is also controllable by the external electric field applied perpendicular to the silicene sheet. The period of oscillations of TC as a function of barrier strength depend on the doping concentration. In the thin barrier limit, the period of oscillation changes from $\pi/2$ to π as we go across from undoped to highly doped regime. In the thick barrier limit, oscillations persist in TC as a function of barrier thickness and barrier height but the period and amplitude of oscillations become functions of the barrier height. More strikingly, amplitude of oscillations of TC diminishes after a certain barrier thickness and height in the highly doped regime which is in contrast to the tunneling conductance [114].

The remainder of the chapter is organised as follows. In Sec. 3.3, we describe our model and method. Sec. 3.4 is devoted to the thin barrier regime where results are presented for three different doping concentrations. Features of the thick barrier limit are discussed in Sec. 3.5. Finally, we summerize and conclude in Sec. 3.6.

3.3 Model and Method

We consider a monolayer of silicene consisting of two sublattices A and B. Two sublattice planes are separted by a distance $2l$ due to the buckled structure. When an electric field is applied perpendicular to the silicene sheet, a staggered potential is generated between the two sublattices A and B as discussed earlier.

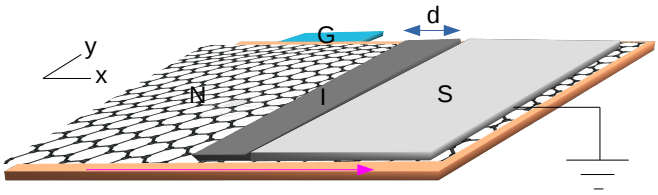

Figure 3.1: A schematic sketch of our silicene NIS set-up. Silicene sheet with hexagonal lattice structure is deposited on a substrate (orange, light grey). Here N indicates the normal region, I denotes the insulating barrier region of width d (grey). A bulk superconducting material denoted by S (light grey) is placed in close proximity to the silicene sheet to induce superconductivity in it. A gate (blue, light grey) is connected to the silicene sheet to tune the chemical potential (doping) in the normal region. The magenta (light grey) line indicates the direction of the heat transport in response to a temperature gradient δT between the normal and the superconducting side.

The low energy effective Hamiltonian of silicene, which is derived from lattice Hamiltonian in the Appendix A, near the Dirac points $k_\eta, \eta = \pm 1$ reads [30]

$$H_\eta = \hbar v_f(\eta k_x \hat{\tau}_x - k_y \hat{\tau}_y) + (elE_z - \eta\sigma\lambda_{SO})\hat{\tau}_z - \mu\hat{1}\ . \tag{3.1}$$

where v_f is the fermi velocity of the electrons, μ is the chemical potential and E_z is the external electric field. $\eta = \pm 1$ corresponds to the $\mathbf{K}$ and $\mathbf{K}'$ valley. In Eq. (3.1), σ is the spin index and $\hat{\tau}$ correspond to the Pauli matrices in the sublattice space and $\hat{1}$ is the 2×2 identity operator.

In this chapter we consider a normal-insulator-superconductor (NIS) set-up of silicene in $x - y$ plane as depicted in Fig. 3.1 with normal region (N) being in $x \leq -d$. The insulating region (I) with width d has $-d \leq x \leq 0$ while the superconducting region (S) occupies $x \geq 0$ for all y. The insulating region has a barrier potential which can be implemented by an external gate voltage. Also the chemical potential can be tuned by a gate voltage connected to the silicene sheet (see. Fig. 3.1). Superconductivity in silicene is induced via the proximity effect of a bulk s-wave superconductor placed close to the silicene sheet in the region $x \geq 0$.

Silicene NIS junction can be described by the Dirac Bogoliubov-de Gennes (DBdG) equation of the form [102]

$$\begin{bmatrix} \hat{H}_\eta & \Delta\hat{1} \\ \Delta^\dagger\hat{1} & -\hat{H}_\eta \end{bmatrix} \Psi = E\Psi \ . \tag{3.2}$$

where E is the excitation energy, Δ is the proximity induced superconducting pairing gap and H_η is given by Eq.(3.1). Here we have assumed that the induced superconducting pairing gap does not have spatial structure inside the superconducting region *i.e.,* $\Delta(x) = \Delta$ for $x \geq 0$ while $\Delta(x) = 0$ for $x < 0$. The schematic band diagram of the silicene NIS set-up is shown in Fig. 3.2. In silicene, the pairing occurs between $\eta = 1$, $\sigma = 1$ and $\eta = -1$, $\sigma = -1$ as well as $\eta = 1$, $\sigma = -1$ and $\eta = -1$, $\sigma = 1$ for a s-wave superconductor.

Solving Eq.(3.2) we find the wave functions in three different regions. The wave functions for the electrons and holes moving in $\pm x$ direction in normal silicene region reads

$$\psi_N^{e\pm} = \frac{1}{A}\begin{bmatrix} \frac{\pm\eta k_1^e e^{\pm i\eta\alpha_e}}{\tau_1^e} \\ 1 \\ 0 \\ 0 \end{bmatrix} \exp[i(\pm k_{1_x}^e x + k_{1_y}^e y)] \ ,$$

$$\psi_N^{h\pm} = \frac{1}{B}\begin{bmatrix} 0 \\ 0 \\ \frac{\mp\eta k_1^h e^{\pm i\eta\alpha_h}}{\tau_1^h} \\ 1 \end{bmatrix} \exp[i(\pm k_{1_x}^h x + k_{1_y}^h y)] \ . \tag{3.3}$$

where the normalization factors are given by $A = \sqrt{\frac{2(E+\mu_N)}{\tau_1^e}}$, $B = \sqrt{\frac{2(E-\mu_N)}{\tau_1^h}}$ and

$$k_1^{e(h)} = \sqrt{\left(k_{1_x}^{e(h)}\right)^2 + \left(k_{1_y}^{e(h)}\right)^2} \ , \tag{3.4}$$

$$k_{1_x}^{e(h)} = \sqrt{(E \pm \mu_N)^2 - (elE_z - \eta\sigma\lambda_{SO})^2 - \left(k_{1_y}^{e(h)}\right)^2} \,. \tag{3.5}$$

$$\tau_1^{e(h)} \;=\; E \pm \mu_N \mp (elE_z - \eta\sigma\lambda_{SO}) \,. \tag{3.6}$$

Here μ_N is the chemical potential in the normal silicene region.

Due to translational invariance in the y-direction, corresponding momentum $k_{1_y}^{e(h)}$ is conserved. The angle of incidence α_e and the Andreev reflection (AR) angle α_h are related via the relation

$$k_1^h \sin(\alpha_h) = k_1^e \sin(\alpha_e) \,. \tag{3.7}$$

AR is a process where electron is converted as a hole at the interface. For the rest of the chapter, we have denoted the band gap $(elE_z - \lambda_{SO})/\Delta$ at $\mathbf{K}$ valley by λ and the gap $(elE_z + \lambda_{SO})/\Delta$ at $\mathbf{K}'$ valley by λ'. In the Insulating region wave functions can be found from normal region wave functions (Eq.(3.3)) by replacing $\mu_N \to \mu_N - V_0$.

In the superconducting region the wave functions of DBdG quasiparticles are given by,

$$\begin{aligned}
\psi_S^e &= \frac{1}{\sqrt{2}} \begin{bmatrix} u_1 \\ \eta u_1 e^{i\eta\theta_e} \\ u_2 \\ \eta u_2 e^{i\eta\theta_e} \end{bmatrix} \exp[(i\mu_S - \kappa)x + iq_y^e y] \,, \\
\psi_S^h &= \frac{1}{\sqrt{2}} \begin{bmatrix} u_2 \\ -\eta u_2 e^{-i\eta\theta_h} \\ u_1 \\ -\eta u_1 e^{-i\eta\theta_e} \end{bmatrix} \exp[(-i\mu_S - \kappa)x + iq_y^h y] \,.
\end{aligned} \tag{3.8}$$

Here, $u_{1(2)} = \left[\frac{1}{2} \pm \frac{\sqrt{E^2-\Delta^2}}{2E}\right]^{\frac{1}{2}}$ and $\kappa = \sqrt{\Delta^2 - E^2}$. The transmission angles for electron-like and

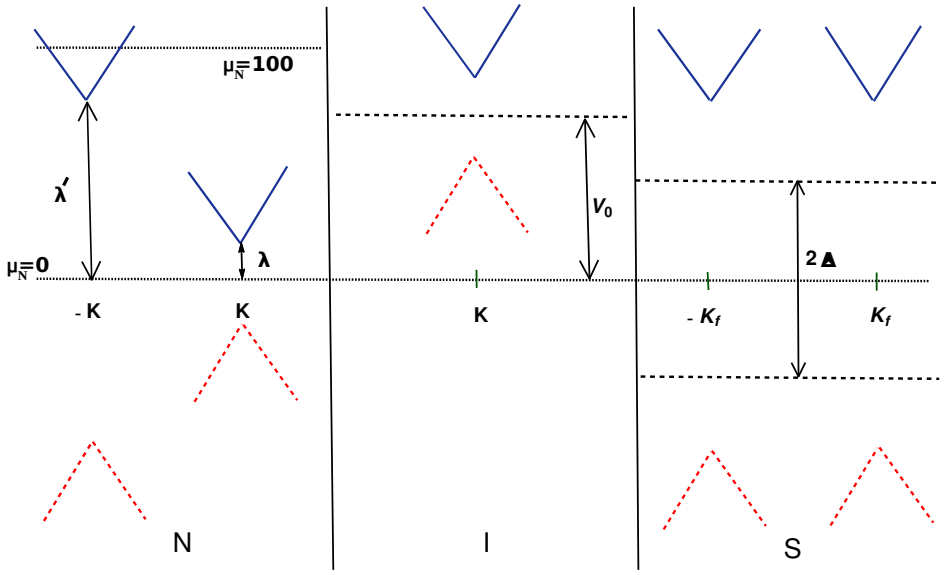

Figure 3.2: A schematic band diagram of our silicene NIS geometry. While in the normal (N) silicene and superconducting (S) silicene region both $\mathbf{K}$ and $\mathbf{K}'$ valleys are depicted, in the insulating (I) barrier region only $\mathbf{K}$ valley is shown for simplicity. Blue solid line indicates conduction band while valence bands are represented by the red dashed lines. Dot-dashed line and dot-dot-dashed line represent $\mu_N = 0$ and $\mu_N = 100\Delta$ respectively.

hole-like quasi-particles are given by,

$$q^{\alpha} \sin\theta_{\alpha} = k_1^e \sin\alpha_e \ . \tag{3.9}$$

for $\alpha = e, h$. The quasiparticle momentums can be written as

$$q^{e(h)} = \mu_S \pm \sqrt{E^2 - \Delta^2} \ . \tag{3.10}$$

where $\mu_S = \mu_N + U_0$ and U_0 is the gate potential applied in the superconducting region to tune the Fermi surface mismatch. The requirement for the mean-field treatment of superconductivity is that $\mu_S \gg \Delta$ [115, 101].

We consider electrons with energy E incident at the interface of our NIS junction of a silicene sheet. Considering both normal reflection and Andreev reflection from the interface, we can write the wave functions in three different regions of the junction as

$$
\begin{aligned}
\Psi_N &= \psi_N^{e+} + r\psi_N^{e-} + r_A\psi_N^{h-} \,, \\
\Psi_I &= p\psi_I^{e+} + q\psi_I^{e-} + m\psi_I^{h+} + n\psi_I^{h-} \,, \\
\Psi_S &= t_e\psi_S^{e} + t_h\psi_S^{h} \,.
\end{aligned} \tag{3.11}
$$

where r and r_A are the amplitudes of normal reflection and Andreev reflection (AR) in the N region respectively. t_e and t_h denote the amplitudes of transmitted electron like and hole like quasi-particles in the S region. Using boundary conditions at the two interfaces, we can write

$$
\Psi_N|_{x=-d} = \Psi_I|_{x=-d}, \quad \Psi_I|_{x=0} = \Psi_S|_{x=0} \,. \tag{3.12}
$$

From these equations we can find the reflection and AR amplitudes r and r_A, required for evaluating the electronic contribution of TC. For the NIS junction, normalized thermal conductance κ is given by [116, 108]

$$
\begin{aligned}
\kappa &= \int_0^{\infty}\int_{-\frac{\pi}{2}}^{\frac{\pi}{2}} dE d\alpha_e \left[1 - R_e - R_h\frac{\cos(\alpha_h)}{\cos(\alpha_e)}\right] \\
&\quad \cos(\alpha_e)\left[\frac{E^2}{4T^2\cosh^2(\frac{E}{2T})}\right] \,.
\end{aligned} \tag{3.13}
$$

Here, R_e and R_h are reflection and AR probability respectively. From current conservation, we obtain [102]

$$
\begin{aligned}
R_e &= |r|^2 \,, \\
R_h &= \frac{k_{1_x}^h}{k_{1_x}^e}\left[\frac{2(E+\mu_N)(E-\mu_N-\lambda)}{|\eta k_{1_x}^h - ik_{1_y}^e|^2 + (E-\mu_N-\lambda)^2}\right]|r_A|^2 \,.
\end{aligned} \tag{3.14}
$$

The derivation of Eq.(3.13) using BTK formalism [61] is given in the Appendix C.

3.4 Thin barrier

In this section, we present our numerical results based on Eq.(3.13) for the thin barrier limit. In this particular limit of insulating barrier, we consider $d \to 0$ and $V_0 \to \infty$, such that $k_I^e d, k_I^h d \to \chi$ where k_I^e, k_I^h are the electron and hole momentum inside the insulating barrier respectively. χ is defined as the barrier strength of the insulating region. Such limit has been considered before in Ref. [117, 118] for the analysis of tunneling conductance in graphene and silicene.

We take U_0 to be very large compared to the superconducting pairing potential Δ. For simplicity, we consider $\theta_e = 0$ and $\theta_h = 0$ in Eq.(4.10) and Eq.(3.10). Due to significant chemical potential imbalance between the normal and superconducting sides, there is a large mismatch of Fermi wavelengths in these two sides resulting in interesting behavior in TC.

Before proceeding to present our numerical results, here we illustrate whether both valleys contribute to TC at all doping conentrations or not. For silicene, the band gap at $\mathbf{K}'$ valley satisfies $\lambda' \gg \mu_N/\Delta$ for the undoped and moderately doped regime. In general, doping concentration can be controlled by applying external gate voltage in silicene. Consequently, $\mathbf{K}'$ valley does not contribute to TC in these two regimes. Nevertheless, in highly doped regime, $\mu_N \sim 100\Delta$ which is much larger than both the band gaps λ and λ' at $\mathbf{K}$ and $\mathbf{K}'$ valley respectively (see Fig. 3.2). Hence, we consider contribution for both the valleys while calculating TC for the highly doped regime. Therefore, we can write $\kappa = \kappa_{\mathbf{K}} + \kappa_{\mathbf{K}'}$ in this case. On the other hand, $\kappa = \kappa_{\mathbf{K}}$ for the undoped and moderately doped regime.

3.4.1 Undoped regime ($\mu_N = 0$)

In this subsection we present our results when the normal region of the silicene sheet is undoped *i.e.,* $\mu_N = 0$. In Fig. 3.3((a)-(d)) we show the behavior of TC as a function of T/T_c for λ ranging from 0 to 0.8. In silicene λ can be tuned by just the external electric field E_z. We choose various barrier strengths. Here, T_c is the transition temperature of the superconducting silicene. The exponential fall of TC (κ) when the temperature is below the transition temperature T_c results because of spherical symmetry of the s-wave superconductor [108]. This behavior is similar to that of conventional no-

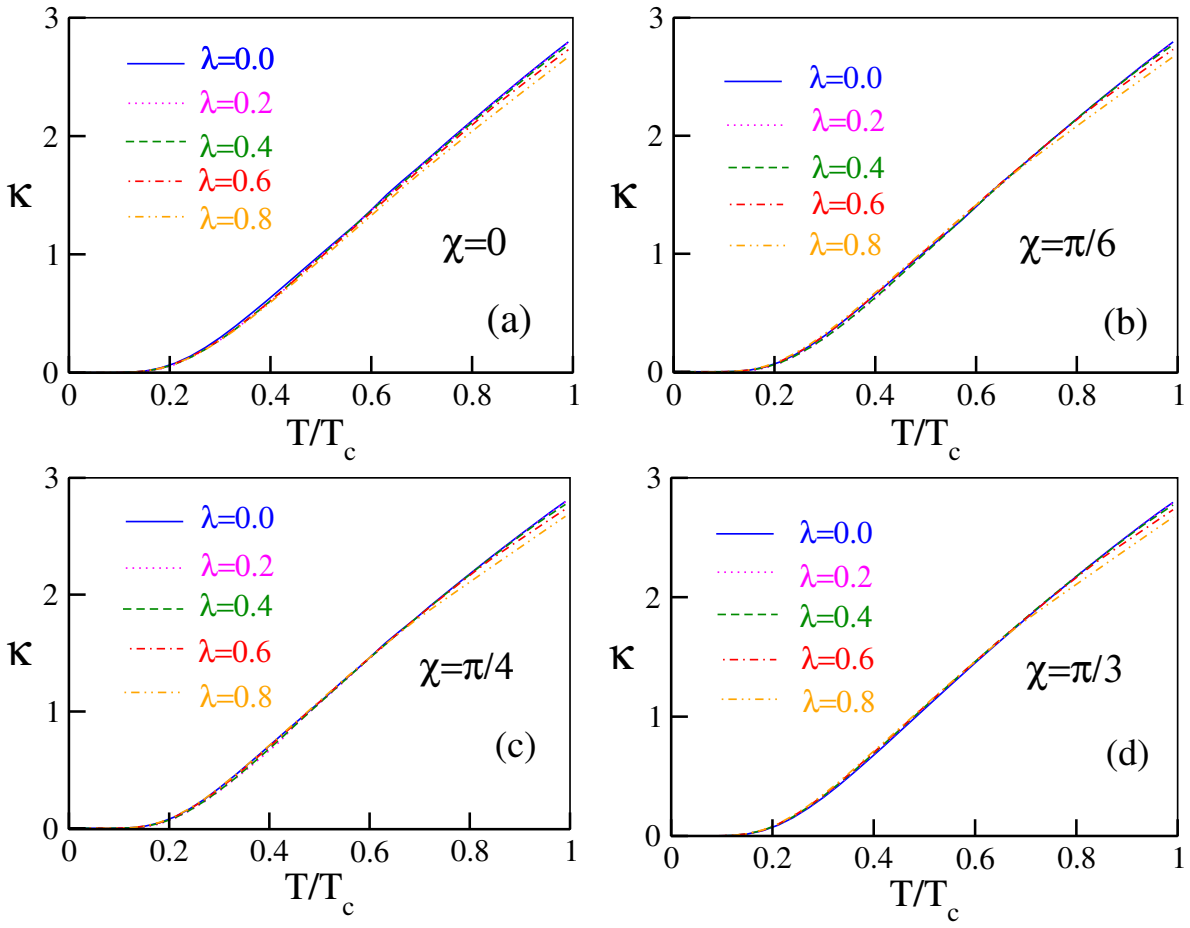

Figure 3.3: Thermal conductance is shown as a function of temperature T/T_C with $U = 100\Delta$ and λ ranging from 0 to 0.8 for the undoped regime ($\mu_N = 0$).

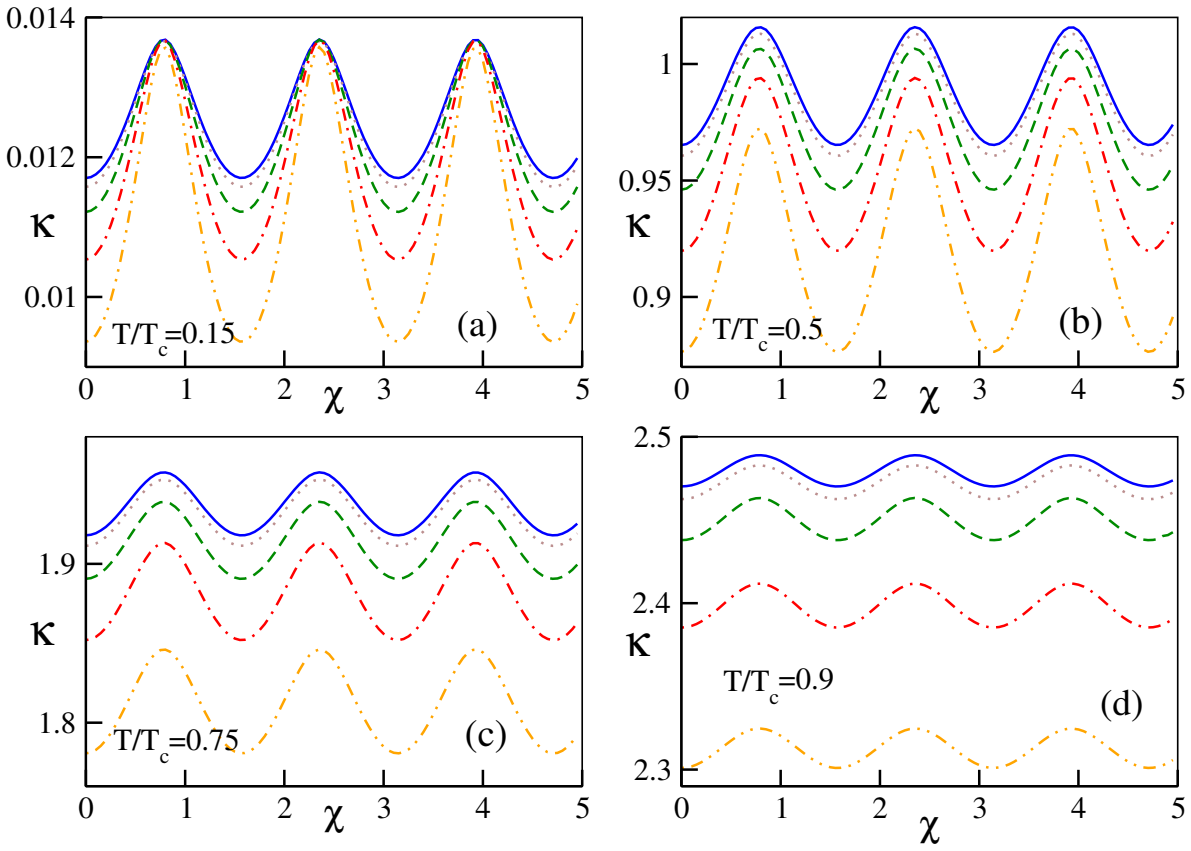

Figure 3.4: Thermal conductance is depicted as a function of the barrier strength χ with $U = 100\Delta$ and λ ranging from 0 to 0.8 for the undoped regime ($\mu_N = 0$). Blue (solid), magenta (dotted), green (dashed), red (dash-dotted) and orange (dash-dot-dotted) curves indicate λ values 0.0, 0.2, 0.4, 0.6 and 0.8 respectively.

mal metal-superconductor junction [113]. As we increase λ by suitably adjusting the perpendicular electric field E_z, TC decreases monotonically. As λ *i.e.,* band gap increases, the available propagating states through which thermal transport takes place reduces and as a consequence TC decreases monotonically with λ. However, as carriers with all energies contribute to the thermal transport, quantitative value of κ is hardly affected by change of band gap at Dirac points which is less than the induced superconducting gap in magnitude. This we can see from formula of κ (see Eq.(3.13)).

In Fig. 3.4((a)-(d)) we demonstrate the bahavior of TC with respect to the barrier strength χ. We choose different temperatures below the transition temperature T_c. TC exhibits a periodic behavior with periodicity $\pi/2$ as shown in Fig. 3.4. Such periodic behavior of TC is entirely different from conventional NS junction where TC always decays with the barrier strength. This periodic behavior is also the manifestation of Dirac fermions in silicene.

The oscillatory behavior of the conductance can be understood as the following way : nonrelativistic free electrons with energy E passing through a potential barrier V are described by the wave function of the form e^{ikx} where $k \sim \sqrt{E-V}$. For $E < V$, the wave function decreases exponentially inside the barrier. On the contrary, relativistic free electrons have a dispersion $k \sim (E-V)$ and the corresponding wave functions do not decay inside the barrier region for arbitrary large potential barrier. Instead, the transmittance across the junction displays an oscillatory behavior as a function of the energy of incident particle E. In general, for the kinetic energy of a free electron being given by k^α leads to a complex momentum $k \sim (E-V)^{1/\alpha}$ inside the tunneling barrier region and hence the wave function has exponentially damped oscillatory behavior. Only relativistic massless fermions whose kinetic energy is directly proportional to the momentum are unique in a sense that their momentum is real inside the barrier region. Therefore, the undamped oscillatory behavior at subgap energies is a direct manifestation of the presence of relativistic low-energy Dirac fermions.

When temperature T is very small compared to T_c, the quantitative value of κ is vanishingly small which can also be seen from Fig. 3.3 focusing at small T/T_c region. Also, the $\pi/2$ periodicity of TC is independent of T/T_c value. Moreover, for the $\mu_N = 0$ regime, the major contribution in TC originates from the unusual specular Andreev reflection (SAR) [115] process due to the pecularity of 2D Dirac systems. When a hole is reflected back along the path of the incident electron the process is known as

retro Andreev reflection. On the other hand, the process is called specular Andreev reflection when the refected path of hole follows mirror like reflection from the interface. This unusual process of specular Andreev reflection was first predicted in graphene by Beenakker [115] and experimentally verified recently by Efetov *et al.* [119]. In general, in SAR process, an electron in the conduction band is reflected as a hole in the valence band while in the usual case of RAR, electron and hole both lie in the conduction band. Thus, for the undoped regime, electron from conduction band is always reflected from valence band and thus transport in the junction occurs primarily due to SAR process.

Effect of λ is more prominent near the transition temperature T_c because superconducting gap decreases as $T \to T_c$ resulting the band gap in the normal region to overcome the superconducting pairing gap. As a result normal reflection probability enhances rusulting in reduction in κ. Note that, the maxima of the peaks of κ for different λ are same for $T = 0.15T_c$ which is unique behavior at very low temperature ($T \ll T_c$). On the contrary, peak heights of κ gets reduced due to the evanescent modes as long as T approaches T_c.

The oscillatory behavior of the TC can be explained as follows. Nonrelativistic free electrons with energy E incident on a potential barrier with height V_0 are described by an exponentially decaying (non-oscillatory) wave function inside the barrier region if $E < V_0$, since the dispersion relation is $k \sim \sqrt{E - V_0}$. On the contrary, relativistic free electrons satisfies a dispersion $k \sim (E - V_0)$, consequesntly corresponding wave functions do not decay inside the barrier region [120]. Instead, the transmittance of the junction displays an oscillatory behavior as a function of the strength of the barrier. Hence, the undamped oscillatory behavior of TC at $T < T_c$ is a direct manifestation of the relativistic low-energy Dirac fermions in silicene.

3.4.2 Moderately doped regime ($\mu_N \neq 0$)

In this subsection, we present our results for the moderate doping case where chemical potential in the normal part of the silicene sheet is 0.5Δ. This regime is qualitatively different from the undoped one because the doping concentration has now almost same order of magnitude with λ. So it is interesting to analyse whether non-trivial behavior of TC emerges out due to the interplay between doping and band gap at the two valleys. In Fig. 3.5((a)-(d)), TC is shown as a function of temperature with

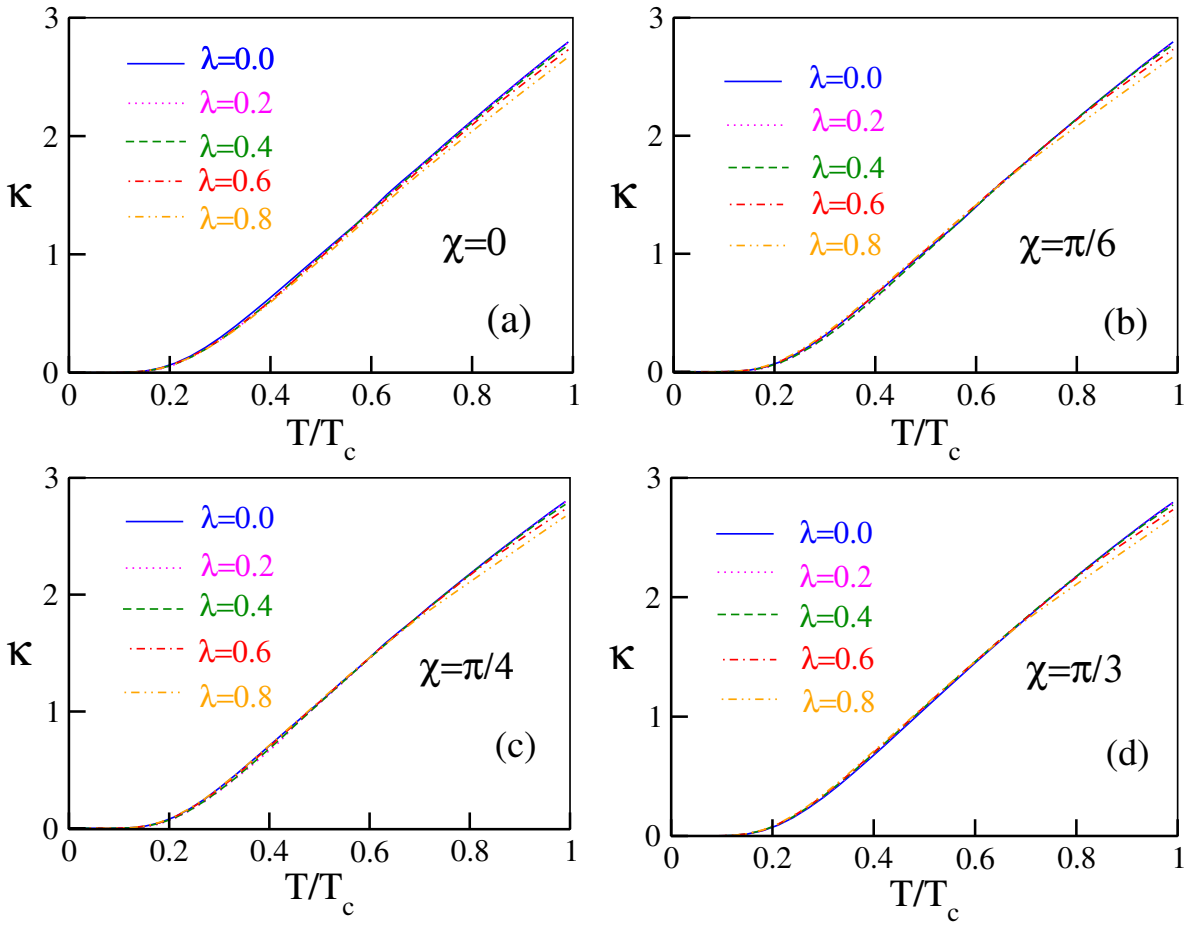

Figure 3.5: Thermal conductance is shown as a function of temperature T/T_C with $U = 100\Delta$ and λ ranging from 0 to 0.8 for moderate doping ($\mu_N = 0.5\Delta$).

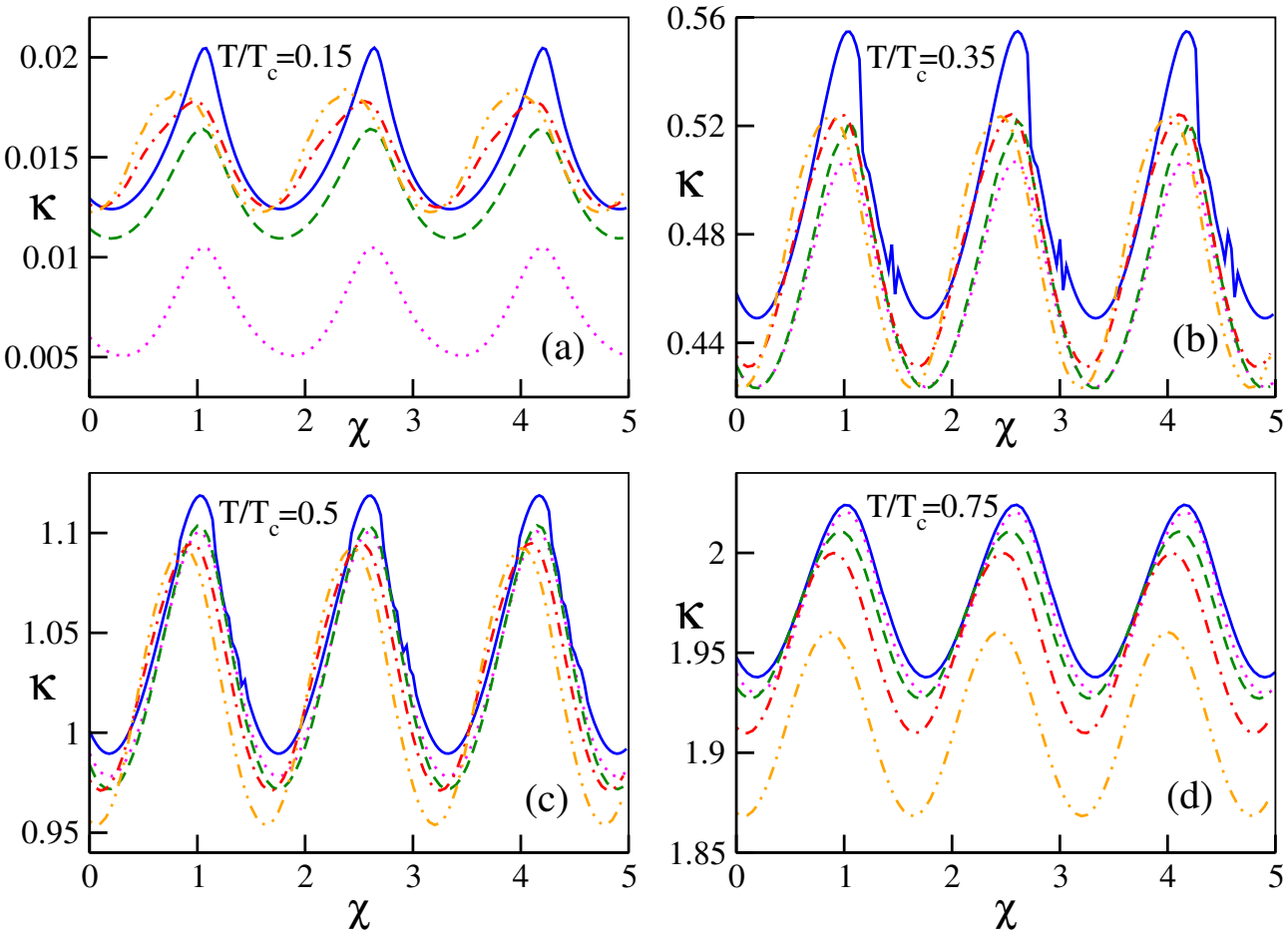

Figure 3.6: We show the thermal conductance as a function of the barrier strength χ with $U = 100\Delta$ and λ ranging from 0 to 0.8 for moderate doping ($\mu_N = 0.5\Delta$). Specification of λ is same as in Fig. 3.4.

different λ and for various barrier strength χ. The striking difference from the undoped case is that κ does not show monotonic behavior with λ. When $T \ll T_c$, κ decreases with increasing λ value by E_z from 0 to 0.4. Then κ further increases as λ crosses μ_N value. At temperaure close to T_c, κ decreases monotonically with increasing λ similar to the undoped case. Note that, κ decreases in the $T \ll T_c$ regime due to the evanescent modes present between the energy range $|\mu_N - \lambda|$ to $|\mu_N + \lambda|$. Then κ start increasing in the subgapped regime when $\mu_N \sim \lambda$ resulting in the non-monotonic behavior. As long as $T \to T_c$ it again decreases due to the silicene band gap like the $\mu_N = 0$ case.

Transition from non-monotonic to monotonic behavior of TC takes place at $T \sim 0.6T_c$ independent of χ value. This non-monotonic characteristics is more promiment in Fig. 3.6((a)-(b)) where oscillatory nature of κ with barrier strength is presented for different values of T/T_c. For a fixed T/T_c, such non-monotonic characteristics of κ can be tuned by the external electric field E_z which is unique in silicene. Here also the periodicity of oscillations remains $\pi/2$ independent of temperature and contribution in κ originates from both specular Andreev reflection (SAR) and retro Andreev reflection (RAR).

3.4.3 Highly doped regime ($\mu_N \sim 100\Delta$)

Here in this subsection we present the features of TC while normal portion of silicene is highly doped ($\mu_N \sim 100\Delta$). In this case the mean-field condition: $\mu_N + U \gg \Delta$ [115] can be satisfied by assuming $U \ll \Delta$ or taking $U \gg \Delta$ as before. Former one does not exhibit any Fermi surface mismatch between the normal and superconducting regions. On the other hand, the latter one contributes to large density mismatch between the two sides. We have numerically calculated κ for $U = 0 \ll \mu_N$, $U = 100\Delta \simeq \mu_N$ and $U = 10000\Delta \gg \mu_N$ regime. The corresponding results are presented in Fig. 3.7 and Fig. 3.8. Here also, similar to the undoped and moderately doped regime, κ has exponential dependance on temperature which is a universal feature in thermal transport. The only difference from the previous two cases lies in the fact that we consider the separate contribution of both the valleys $\mathbf{K}$ and $\mathbf{K}'$ when $\mu_N \gg \Delta$ (see Fig. 3.2).

From analytical expressions of the superconducting wave functions (see Eq.(4.10) and Eq.(3.10)), we notice that the change in wave functions due to the variation of λ and λ' is negligible because $\mu_N \sim 100\Delta \gg \lambda, \lambda'$. Hence, in this regime κ comes out to be independent of the applied electric field

E_z which is depicted in Fig. 3.7. The corresponding behavior is independent of U also. Nevertheless, the quantitative value of κ is enhanced by a factor of "2" compared to the previous two cases due to the contribution coming from both the valleys.

The oscillatory behavior of TC with respect to the barrier strength χ persists in the highly doped regime as well (see Fig. 3.8((a)-(d))). However, now the periodicity changes with the U value. As long as $U \gg \mu_N$, period remains $\pi/2$ but it increases gradually to π as U decreases towards $U \ll \mu_N$. Both for $U = 0$ and $U = 100\Delta$, periodicity of κ remains same at π but the spread of the curve decreases as U decreases as depicted in Fig. 3.8(a,c). This change of behavior with variation of U can be qualitatively understood from Fermi surface mismatch between the normal and superconducting sides. For large Fermi wavelengths mismatch between the normal and superconducting regions, period of oscillations remains $\pi/2$ which is similar to the undoped and moderately doped regimes. However, as the Fermi wavelengths mismatch becomes vanishingly small in the highly doped regime, periodicity of oscillation converts to π. Here also, λ as well as λ' have neglizible effect on the thermal transport as μ_N is the dominant energy scale in this particular regime. Similar periodicity of π in the behavior of tunneling conductance in graphene for the highly doped regime was reported earlier in Ref. [117].

Note that, for the highly doped regime, major contribution in κ originates from the retro AR in contrast to SAR in the undoped regime. Also the periodicity of κ changes from $\pi/2$ to π as long as $U \approxeq \mu_N$. Such change of periodicity with doping, in the behavior of thermal conductance in the thin barrier limit, can be an indirect way to identify the crossover from SAR to retro AR in Dirac materials. Although, it is not apparent to compute separately the individual contribution of retro AR and SAR to κ when $\mu_N \neq 0$. This is because within our scattering matrix formalism we have to average over all values of energy (see Eq.(3.13)). Hence, the change of periodicity of κ from $\pi/2$ to π may not be a strong justification (smoking gun signal) for the crossover phenomenon from SAR to retro AR as the periodicity again can change from π to $\pi/2$ due to Fermi wavelengths mismatch between the normal and superconducting regions even if $\mu_N \sim 100\Delta$ where the major contribution to κ arising from retro AR (see Fig. 3.8(b)). However, to observe the latter change, one has to enhance the doping concentration in the superconducting side also.

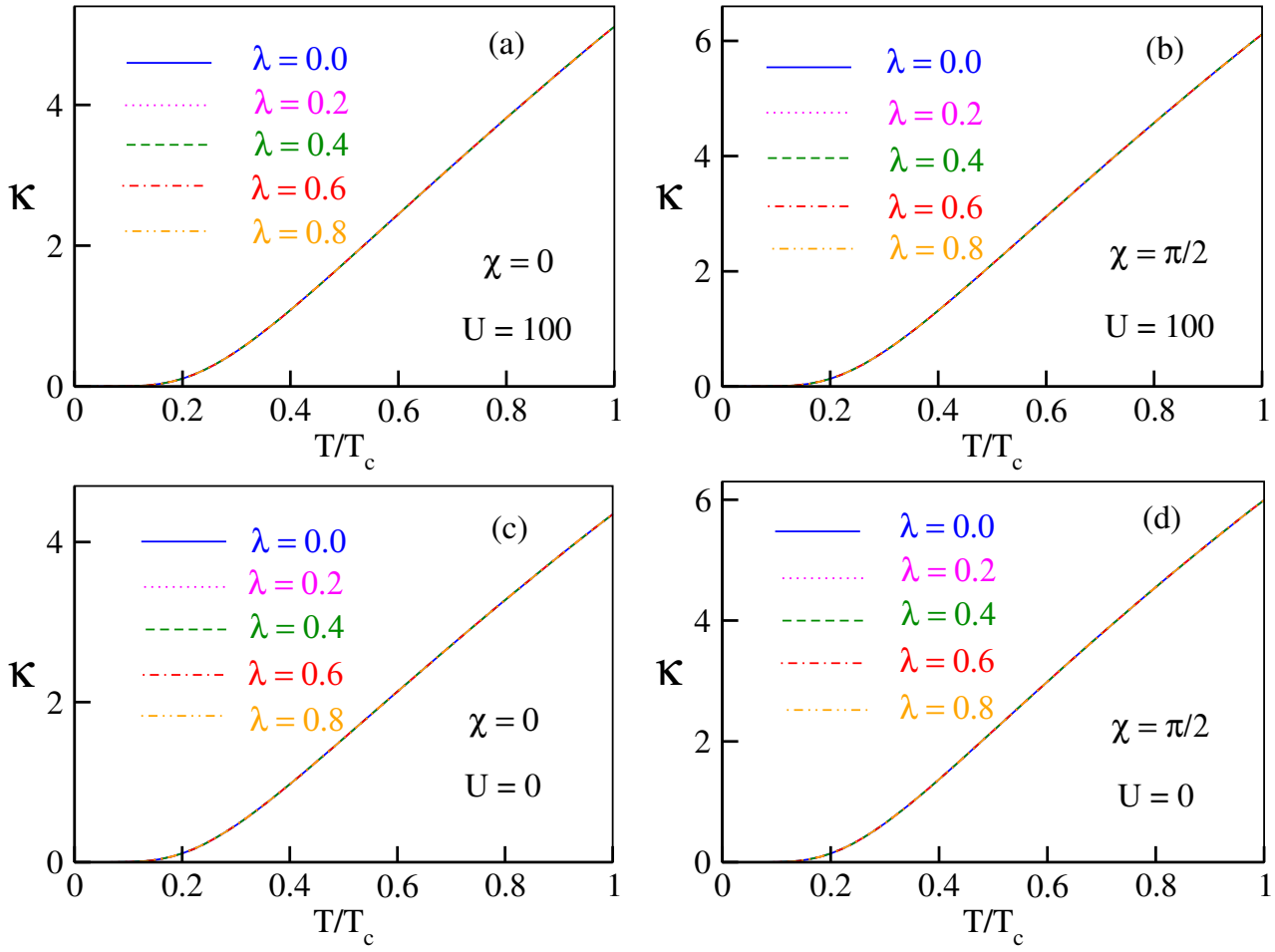

Figure 3.7: Thermal conductance is shown as a function of temperature T/T_C with λ ranging from 0 to 0.8 and λ' ranging from 40 to 40.8 for the highly doped ($\mu_N \sim 100\Delta$) regime.

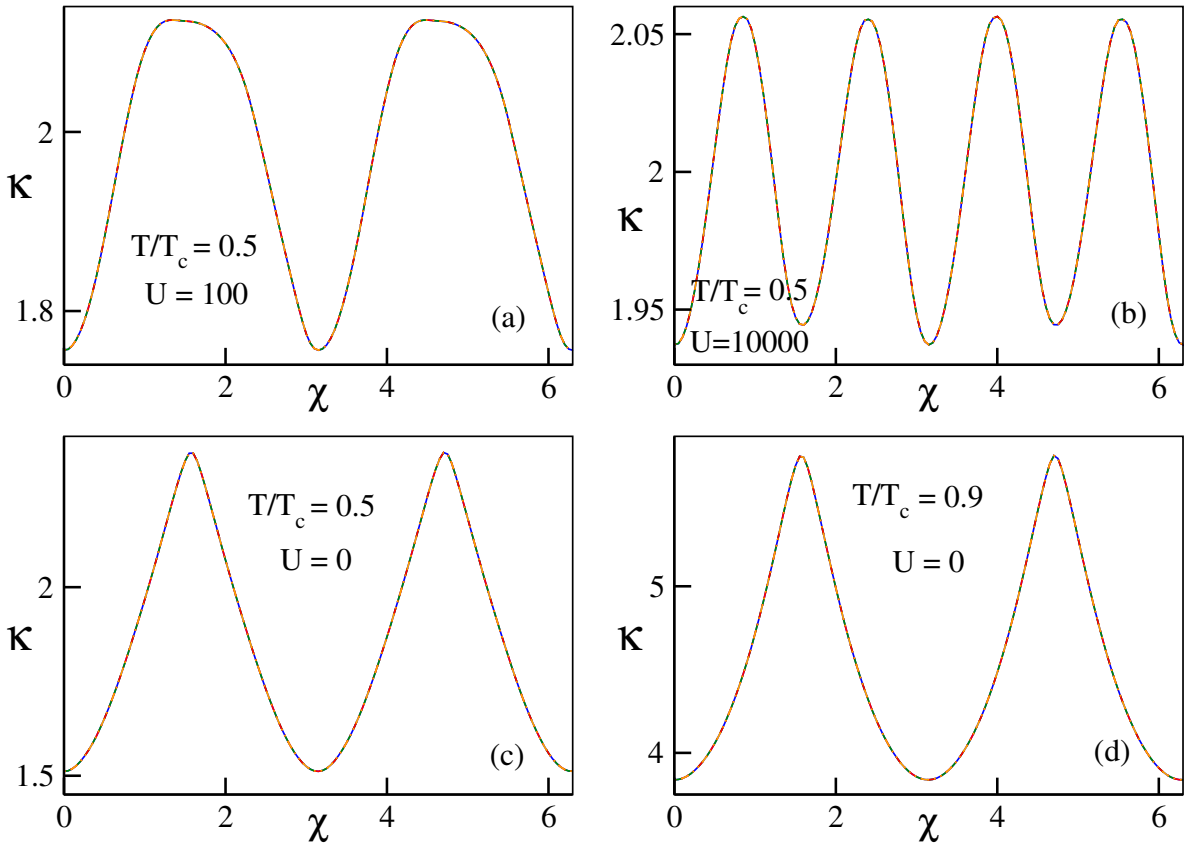

Figure 3.8: Thermal conductance is shown as a function of the barrier strength χ with λ ranging from 0 to 0.8 for high doping ($\mu_N \sim 100\Delta$) condition. Specification for λ' remains same as mentioned in Fig. 3.7.

3.5 Thick barrier

In this section we examine TC in the thick barrier limit where we consider a barrier of width d and height V_0. The height of the barrier can be tuned by applying an additional gate voltage in the insulating region [114]. We emphasize on the role being played by the barrier height V_0 as well as thickness d. We show κ manifests osscillatory behavior with respect to both d and V_0. However, the period of oscillation is no longer universal as in the thin barrier limit but beocmes a function of applied voltage V_0 and width d. Similar feature is found earlier in graphene NIS junction [114] where tunneling conductance is shown to have oscillation whose period depends on V_0.

Note that, in the thick barrier limit, extended BTK formalism [61] is valid for our model of NIS junction if $d \leq \xi$ where $\xi = \hbar v_F/\pi\Delta$ which is the phase coherence length in the superconducting side. Fermi wavelength is given by, $\lambda_F = 2\pi/k_F$ where $k_F = \mu_N/\hbar v_F$ being the Fermi wave vector. So λ_F and ξ are related by, $\lambda_F = 2\pi^2\Delta\ \xi/\mu_N$. We notice that undoped regime is not valid in the thick barrier limit becuase Fermi wavelength diverges in that regime. In the moderately doped regime, choosing $\mu_N = 0.5\Delta$ as before, we obtain $d/\lambda_F \leq 1/4\pi^2 \sim 0.025$.

3.5.1 Moderately doped regime ($\mu_N \neq 0$)

When the doping concentration is moderate ($\mu_N = 0.5\Delta$) in the normal silicene regime, TC exhibits similar features as in the thin barrier limit. Here we illustrate the behavior of TC as a function of barrier height V_0 and thickness d in Fig. 3.9 and Fig. 3.10 for $\lambda = 0.3$ and $\lambda = 0.7$ respectively. We note the following features. (i) When $d \to 0$, TC is unaffected by the barrier height V_0. This is true for arbitray bandgap λ as we can see from Fig. 3.9 and Fig. 3.10. Nonetheless, V_0 affects TC as d increases. Qualitatively we understand that as U is chosen to be large $\sim\ 100\Delta$, small barrier height V_0 has negligible effect on TC. (ii) As barrier height dominates U, TC exhibits oscillatory behavior as a function of d and such oscillation persists even for very large values of V_0. Similarly oscillation is present as V_0 changes even for $d \sim 0.025\lambda_F$. However, the period of oscillation does not show any universal periodicity of $\pi/2$ like in the thin barrier case. The period of oscillation of κ depends on both d and V_0. Similar feature was found earlier in case of tunneling conductance in graphene NIS junction [114]. (iii) The external electric field E_z does not change the qualitative behavior of κ as shown in Fig. 3.9 and Fig. 3.10. Although it changes the quantitative value of κ. As λ increases by tuning E_z, TC reduces monotonically with both d and V_0 similar to the thin barrier case when

$T/T_c = 0.8$.

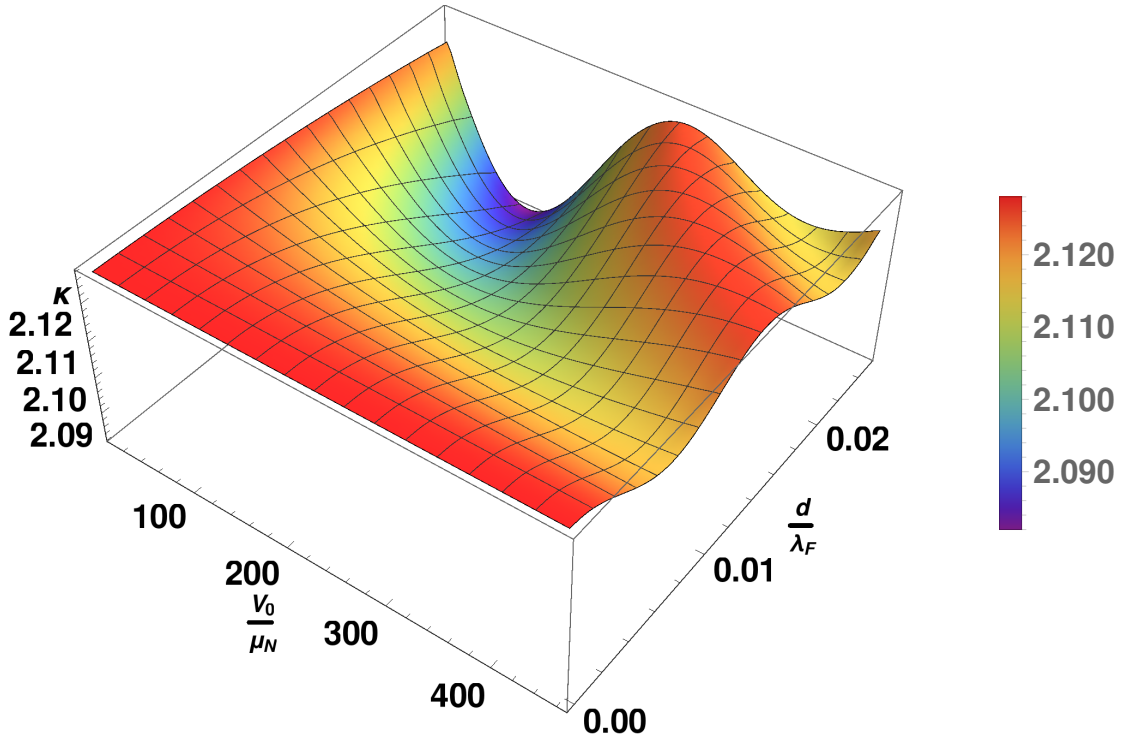

Figure 3.9: Plot of thermal conductance as a function of the barrier height V_0 and barrier thickness d for $T/T_c = 0.8$, $\lambda = 0.3$, $U = 100\Delta$ and $\mu_N = 0.5\Delta$.

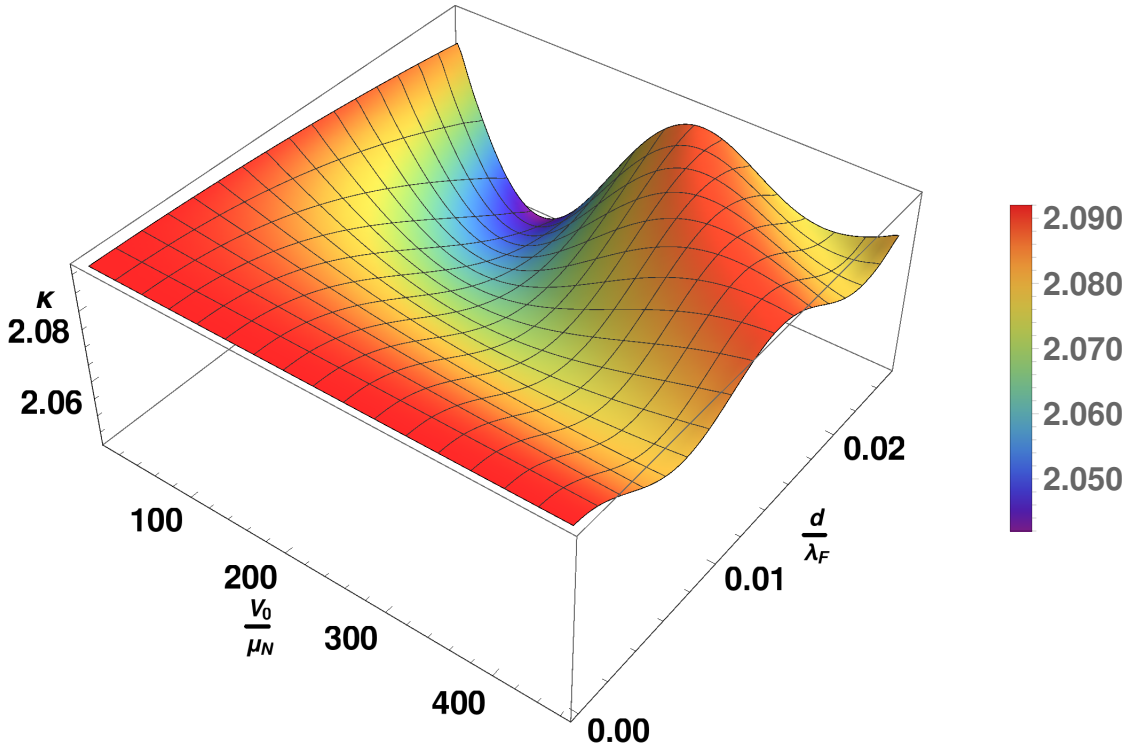

Figure 3.10: Thermal conductance is shown as a function of the barrier height V_0 and barrier thickness d. Here $\lambda = 0.7$ and the value of the other parameters are chosen to be the same as in Fig. 3.9.

3.5.2 Highly doped regime ($\mu_N \sim 100$)

Here, we present the behavior of TC as a function of d and V_0 with high doping concentration where $\mu_N \sim 100\Delta$. We choose $U = 0$ only. Hence, there is no Fermi wavelength mismatch between the normal and superconducting side of the silicene sheet. Thus the effect of applied gate voltage V_0 across the insulating region can be investigated prominently in this regime due to $U = 0$. Also, as we have already pointed out in thin barrier limit that λ and λ' has negligible effect on κ when $\mu_N/\Delta \gg \lambda, \lambda'$, hence we consider $\lambda = 0$ and $\lambda' = 40$.

Fig. 3.11 represents TC as a function of d and V_0 for $\lambda = 0$ and $T/T_c = 0.8$. We choose V_0 value to be much larger than μ_N in order to investigate the effect of applied gate voltage or barrier height on TC. We note that κ exhibits oscillation with respect to V_0 even for very small barrier thickness d. The period of these oscillations is entirely dependent on V_0. As mentioned earlier, such oscillations of κ at very small d does not appear at moderate doping concentration unless and until V_0 exceeds U. Note that, the enhancement in the quantitative value of κ compared to the previous case arises due to both $\mathbf{K}$ and $\mathbf{K}'$ valley contribution. Also in the highly doped regime, the amplitudes of oscillations of κ decay after a certain value of barrier thickness ($d \sim 0.4\lambda_F$) for arbitrary barrier height V_0. This can be understood from the Fermi wave-length mismatch between the barrier and the normal silicene region for high value of d and V_0. This feature of TC is in sharp contrast to the tunneling conductance in graphene which is oscillatory for arbitrary d and V_0 [114].

3.6 Summary and conclusions

To summerize, in this chapter, we investigate thermal conductance κ by Dirac fermions in silicene NIS junction where superconductivity is induced in silciene sheet via the proximity effect. We study the behavior of TC in this set-up both for thin and thick insulating barrier limit. We show that TC exhibits $\pi/2$ periodic oscillation with respect to the barrier strength in thin barrier limit for undoped ($\mu_N = 0$) and moderately doped ($0 < \mu_N \leq \Delta$) regime where the Fermi surface mismatch between the normal and superconducting sides is significant. The oscillation becomes π periodic as a function of barrier strength in the highly doped ($\mu_N \gg \Delta$) regime where Fermi surfaces in the two sides are almost aligned. This change of periodicity ($\pi/2$ to π) in thermal response with the variation of doping concentration can be an indirect probe to identify the crossover from SAR to retro AR.

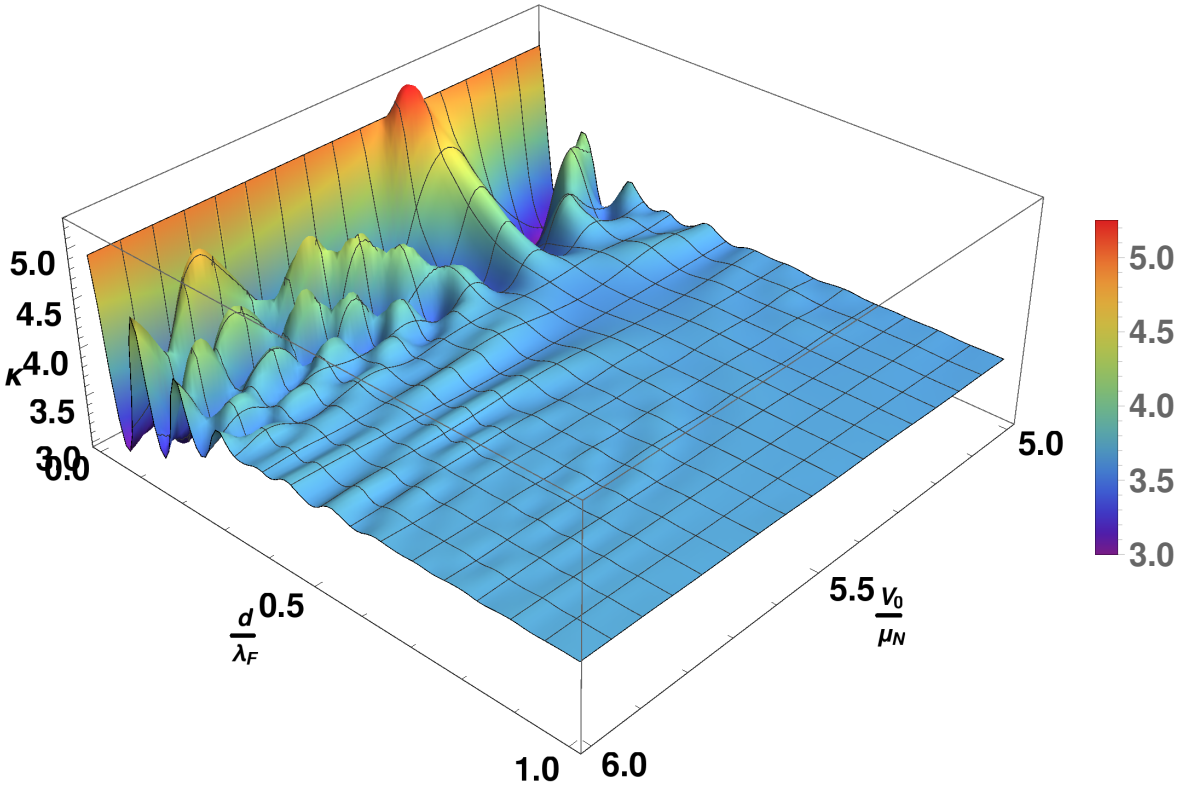

Figure 3.11: Thermal conductance is depicted as a function of barrier height V_0 and thickness d with $\lambda = 0$, $\lambda' = 40$, $U = 0$ and $T/T_c = 0.8$ for the highly doped ($\mu_N \sim 100\Delta$) regime.

Nonetheless, TC shows conventional exponential dependence on temperature independent of doping concentration and barrier characteristics. The external electric field reduces TC monotonically in the undoped regime. However, a non-trivial interplay between band gap at Dirac points and doping concentration appears in the moderately doped case. Consequently, electric field can tune TC in the later regime. On the other hand, electric field has negligible effect on TC when $\mu_N/\Delta \gg \lambda$.

In the thick barrier limit, oscillation of TC persists both as a fucntion of barrier thickness d as well as barrier height V_0. The latter can be tuned by an additional gate voltage appled at the insulating region. However, we show that the periodicity of TC no longer remains constant, rather becomes functions of both d and V_0. Also after a certain barrier thickness ($d \sim 0.4\lambda_F$), amplitude of oscillations in TC decays for arbitrary V_0 in the highly doped regime.

In our analysis, we consider only the electronic contribution in TC and neglect the phonon contribution at small temperatures ($T < T_c$). Very recently, nanoscale control of phonon excitation in graphene has been reported [121]. Hence, such nanoscale control of phonon excitation in silicene and the effect of electron-phonon interaction on TC will be presented elsewhere.

As far as experimental realization of our silicene NIS set up is concerned, superconductivity in

silicene can be induced by s-wave superconductor like Al [122, 123]. In recent years, proximity induced superconductivity has been observed in other 2D materials such as graphene [122, 123, 124] and transition metal dichalcogenides [125]. Once such superconducting proximity effect is realized in silicene, fabrication of silicene NIS junction can be feasible. Typical spin-orbit energy in silicene is $\lambda_{\rm SO} \sim 4$ meV while the buckling parameter $l \approx 0.23$ Å [6, 5]. Considering Ref. [122], typical induced superconducting gap in silicene would be ~ 0.2 meV. For such induced gap, choosing $\mu_N \sim 100\Delta \sim 20$ meV, we obtain $\lambda_F \sim 130$ nm. Hence, a barrier of thickness $\sim 10 - 15$ nm may be considered as thin barrier and the gate voltage $V_0 \sim 500$ meV can therefore meet the demands of our silicene NIS setup. For the thick barrier limit, thickness can be varied arbitrarily (satisfying $d \leq \lambda_F \sim 100$ nm), with the gate voltage $V_0 \sim 100 - 200$ meV.

However, the effects of external electric field might not be visible in the above regime as envisaged by our theoretical calculation. To realize non-trivial effects due to the electric field on TC, chemical potential in the normal silicene region can be $\mu_N \sim 80 - 120$ μeV and the external electric field E_z can be within the range $E_z \sim 170 - 180$ eV/μm. In this moderately doped regime ($0 < \mu_N \leq \Delta$), the criterion for d and V_0 can be similar to the highly doped regime as mentioned before.

Note that, in our analysis, we have considered a bulk silicene material following Ref. [102]. The bulk-boundary correspondence has not been taken into account within our scattering matrix formalism where the effect of edge mode can't be taken into account. So, we cannot distinguish between the topological phase or the band insulating phase within our formalism even if we tune the electric field E_z in our calculation. Hence, in our analysis, the contribution in the thermal conductance is arising from the bulk states only.

We expect our results to be analogous to the recently discovered 2D materials like germenene, stanene [126, 127]. Although the effect of Rashba SOC λ_R in these materials can be more important than silicene [6, 5]. For silicene, λ_R is small compared to λ_{SO} [30]. The low energy spectrum of silicene is independent of λ_R only at the Dirac point [30]. Inclusion of small λ_R breaks the spin symmetry and spin is no longer a good quantum number. Qualitatively, from scattering point of view, presence of small λ_R introduces spin flip scattering processes from the normal-superconductor (NS) interface. Apart from spin conserving reflection and AR processes, the reflection and AR processes with spin flip also contribute to κ. Nevertheless, as λ_R is small, the amplitudes of those additional scattering processes will also be small. Hence, after averaging over all the energy values while computing κ, the contribution arising from these two extra scattering processes on the resulting thermal

conductance will be vanishingly small. Thus, to our expectation, the qualitative feature of κ as a function of T/T_c or χ will remain similar even one includes small λ_R into account.

CHAPTER 4

Quantum Charge Pumping in Superconducting Hybrid Junction of Silicene

4.1 Chapter Summary

Adiabatic quantum pumping is a transport phenomenon in which low-frequency periodic modulations of at least two system parameters with a phase difference lead to a zero bias finite dc current in meso- and nanoscale systems. Such zero-bias current is a consequence of the time variation of the parameters of the quantum system which explicitly breaks time-reversal symmetry. We have theoretically investigated the phenomena of adiabatic quantum charge pumping through a normal-insulator-superconductor-insulator-normal (NISIN) setup of silicene within the scattering matrix formalism. Assuming thin barrier limit of the insulating region, we have considered the strength of the two barriers (χ_1 and χ_2) as the pumping parameters in the adiabatic regime. Within this geometry, we have obtained crossed Andreev reflection (CAR) with probability unity in the χ_1-χ_2 plane without the unwanted concomitant elastic cotunneling (CT). Tunability of the band gap at the Dirac point by appyling an external electric field perpendicular to the silicene sheet and variation of the chemical potential at the normal silicene region, open up the possibility of achieving novel perfect CAR process through our setup. This resonant behavior arises periodically in the plane of the barrier strengths. The behavior of the pumped charge through the NISIN structure as a function of the pumping strength

and angles of the incident electrons have been analyzed. We have predicted that almost quantized pumped charge can be obtained through our geometry when the pumping contour encloses the CAR or transmission resonance in the pumping parameter space. We have mentioned possible experimental feasibility of our theoretical predictions.

4.2 Introduction

In recent years, a close cousin to graphene [81, 7], silicene [6, 13, 5, 84, 128, 21, 85, 1, 86] consisting of a monolayer honeycomb structure of silicon atoms, has attracted a lot of research interest in condensed matter community due to its unique Dirac like band structure which allows one to realize a rich varity of topological phases [29, 99, 92, 18, 100, 129] and Majorana fermion [100] in it under suitable circumstances. Moreover, this band structure is shown to be tunable by an external electric field applied perpendicular to the silicene sheet [98, 30]. Dirac fermions, in turn, becomes massive at the two valleys $\mathbf{K}$ and $\mathbf{K}'$ in this material. These properties have enable silicene to be a promising candidate for realizing spintronics [87, 89, 90, 88, 91], valleytronics [92, 17, 94, 95] devices as well as silicon based transistor [96] at room temperature.

An intriguing phenomenon occurs in case of a normal metal-superconductor material-normal metal (NSN) junction in which an electron incident from one of the normal metal leads forms a pair with another electron from the other normal metal lead and enters into the superconductor forming a Cooper pair. Such non-local process is called crossed Andreev reflection (CAR) [130, 131] whose signature has been verified in various experiments [132, 133, 134]. From the practical point of view, superconducting hybrid structures can be designed by placing a bulk superconducting material in close proximity to a normal metal system [132, 133] and superconducting correlation is actually induced into the non superconducting region via the proximity effect. Very recently, superconducting proximity effect in silicene has been investigated theoretically in Ref.[102, 135, 118]. Although, up to now, no experiment has been put forwarded in the context of proximity effect in silicene. In Ref.[102], a unique possibility of acquiring pure crossed Andreev reflection (CAR) without any contamination from normal transmission/co-tunneling (CT) has been reported in normal-superconductor-normal (NSN) junction of silicene where elastic cotunneling as well as Andreev reflection can be suppressed to zero by properly tuning the chemical potential and band gap at the two normal sides. However, in such NSN junction, maximum value of CAR probability does not reach 100% because normal reflection does not vanish. This naturally motivates us to study a normal-insulator-superconductor-insulator-normal (NISIN) junction of silicene and explore whether incorporating an insulating barrier at each NS interface can give rise to resonant CAR in such setup. CAR can be used to produce non

local entangled electron pairs [136, 137] and thus obtaining 100% CAR process in engineered system has been searched for a long time.

On the other hand, adiabatic quantum pumping, is a transport phenomena in which low-frequency periodic modulations of at least two system parameters [138, 139, 140, 141] with a phase difference lead to a zero bias finite dc current in meso and nanoscale systems. Such zero-bias current is obtained as a consequence of the time variation of the parameters of the quantum system, which explicitly breaks time-reversal symmetry [142, 143, 144]. It is necessary to break time-reversal symmetry in order to get net pumped charge, but it is not a sufficient condition. Indeed, in order to obtain a finite net pumped charge, parity or spatial symmetry must also be broken. Finally, to reach the adiabatic limit, the required condition to satisfy is that the period T of the oscillatory driving signals has to be much larger than the dwell time $\tau_{dwell} \simeq L/v_F$ of the electrons inside the scattering region of length L, *i.e.,* , $T = 2\pi/\omega \gg \tau_{dwell}$ [140]. In this limit, the pumped charge in a unit cycle becomes independent of the pumping frequency. This is referred to as "adiabatic quantum charge pumping" [140].

During the past decades, quantum charge and spin pumping has been studied extensively in mesoscopic setups including quantum dots and quantum wires both at the theoretical [145, 145, 146, 147, 142, 143, 148, 149, 150, 151, 152, 153, 154, 155, 156, 157, 158, 159] as well as experimental [160, 161, 162, 163, 164, 165] level with focus on both the adiabatic and nonadiabatic regime. In recent times, quantum pumping has been explored in Dirac systems like graphene [157, 166, 156, 144, 167] and topological insulator [168, 169]. However, the possible quantization of pumped charge [170] during a cycle through non-interacting open quantum systems has been investigated so far based on the resonant transmission process [171, 149, 144, 172]. In more recent times, quantized behavior of pumped charge has been predicted in superconducting wires with Majorana fermions [173], fractional fermions [172] and topological insulators in enlarged parameter spaces [174]. Although, till date, quantum pumping phenomena through resonant CAR process has not been investigated to the best of our knowledge.

Motivated by the above mentioned facts, in this chapter, we study adiabatic quantum charge pumping either through resonant CAR process or resonant transmission process, under suitable circumstances, in silicene NISIN junction [175]. We model our pump setup within the scattering matrix

formalism [139, 140] and consider the strength of the two barriers (in the thin barrier limit) as our pumping parameters. We show that CAR probability can be unity in the pumping parameter space. Moreover, resonant CAR is periodic in the pumping parameter space due to the relativistic nature of the Dirac fermions. Similar periodicity is present, in case of resonant tunneling process as well, under suitable condition. Adiabatic quantum pumping through these processes, with the modulation of two barrier strengths, can lead to large pumped charge from one reservoir to the other. We investigate the nature of pumped charge through NISIN structure as a function of the pumping strength and angle of incidence of incoming electrons choosing different types of pumping contours (circular, elliptic, lemniscate [172] etc.).

The remainder of the chapter is organized as follows. In Sec. 4.3, we describe our pump setup based on the silicene NISIN junction and the formula for computing pumped charge within the scattering matrix framework. Sec. 4.4 is devoted to the numerical results obtained for the pumped charge as a function of various parameters of the systems. Finally, we summarize our results and conclude in Sec. 4.5.

4.3 Model and Method

In this section we describe our quantum pump setup in which we consider a normal-insulator-superconductor-insulator-normal (NISIN) structure of silicene in $x-y$ plane as depicted in Fig. 4.1. Here, the superconducting region being located between $0 < x < L$, while the insulating barriers are situated on its left, $-d < x < 0$, and on its right, $L < x < L + d$. The normal region of silicene occupies at the extreme left *i.e.,* , $x < -d$ and extreme right ends, $x > L + d$. Here, superconductivity is assumed to be induced in the silicene sheet via the proximity effect, where a bulk s-wave superconductor is placed in close proximity to the sheet in the region $0 < x < L$. The two insulating regions in silicene have gate tunable barriers of strength χ_1 and χ_2 in the thin barrier limit [135, 176]. Two additional gate voltages G_1 and G_2 can tune the chemical potential in the left and right normal silicene regions respectively.

The silicene NISIN junction can be described by the Dirac Bogoliubov-de Gennes (DBdG) equation of the form [102, 135]

$$\begin{bmatrix} \hat{H}_{\tilde{\eta}} & \Delta\hat{1} \\ \Delta^{\dagger}\hat{1} & -\hat{H}_{\tilde{\eta}} \end{bmatrix} \Psi = E\Psi \ . \tag{4.1}$$

where E is the excitation energy, Δ is the proximity induced superconducting pairing gap. The Hamiltonian $H_{\tilde{\eta}}$ describes the low energy physics close to each $\mathbf{K}$ and $\mathbf{K}'$ Dirac points and reads as [30]

$$H_{\tilde{\eta}} = \hbar v_f(\tilde{\eta}k_x\hat{\tau}_x - k_y\hat{\tau}_y) + (elE_z - \tilde{\eta}\sigma\lambda_{SO})\hat{\tau}_z - \mu\hat{1} \ . \tag{4.2}$$

where v_f is the Fermi velocity of the electrons, μ is the chemical potential, λ_{SO} is the spin-orbit term and E_z is the external electric field applied perpendicular to the silicene sheet. Here $\tilde{\eta} = \pm 1$ denotes the $\mathbf{K}$ and $\mathbf{K}'$ valley. In Eq. (4.2), σ is the spin index and $\hat{\tau}$ correspond to the Pauli matrices acting on the sub-lattices A and B where $\hat{1}$ is the 2×2 identity operator.

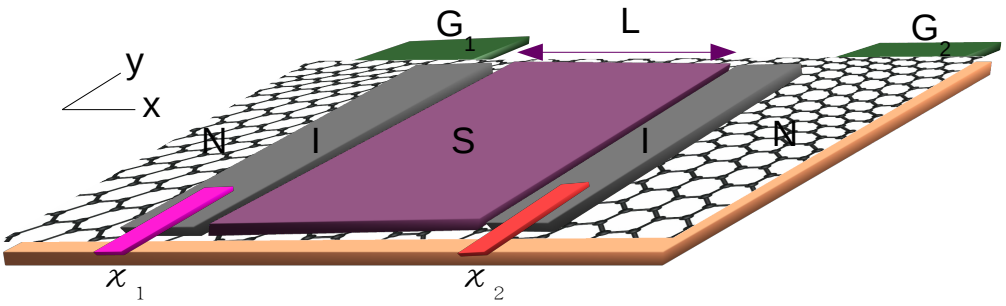

Figure 4.1: A schematic sketch of our silicene NISIN set-up. Silicene sheet with hexagonal lattice structure is deposited on a substrate (orange, light grey). Here N indicates the normal region, I denotes the thin insulating barrier region (grey, light grey). A bulk superconducting material of length L, denoted by S (pink, light grey), is placed in close proximity to the silicene sheet to induce superconducting correlation in it. Two gates G_1 and G_2 (dark green, dark grey) are connected to the two normal regions (N) of the silicene sheet to tune the chemical potential (doping) there. Two extra gates (blue and red, light grey) indicated by χ_1 and χ_2 are symbolically denoted to modulate the barrier strengths.

The potential energy term elE_z in the low energy Hamiltonian $H_{\tilde{\eta}}$ originates due to the buckled structure of silicene in which the A and B sublattices are non-coplanar (separated by a distance of length l) and therefore acquire a potential difference when an external electric field E_z is applied perpendicular to the plane. It turns out that at a critical electric field $E_z^c = \lambda_{SO}/el$, the band gap at each of the valleys become zero with the gapless modes of one of the valley being up-spin polarized and

the other being down-spin polarised [98, 30]. Away from the critical field, the bands (corresponding to $H_{\tilde{\eta}}$) at each of the valleys $\mathbf{K}$ and $\mathbf{K}'$ split into two conduction and valence bands with the band gap being $|elE_z - \tilde{\eta}\sigma\lambda_{SO}|$. Note that, in silicene, the pairing occurs between $\tilde{\eta} = 1$, $\sigma = 1$ and $\tilde{\eta} = -1$, $\sigma = -1$ as well as $\tilde{\eta} = 1$, $\sigma = -1$ and $\tilde{\eta} = -1$, $\sigma = 1$ for a s-wave superconductor.

Here we set up the equations to analyze the quantum pumping phenomena through our NISIN structure. Solving Eq.(4.1) we find the wave functions in three different regions. The wave functions for the electrons (e) and holes (h) moving in $\pm x$ direction in left or right normal silicene region N reads

$$\psi^{e\pm}_{Nm} = \frac{1}{A}\begin{bmatrix} \frac{\pm\tilde{\eta}k^{e}_{1m}e^{\pm i\tilde{\eta}\alpha_{em}}}{\tau^{e}_{1m}} \\ 1 \\ 0 \\ 0 \end{bmatrix} \exp[i(\pm k^{e}_{1_x m}x + k^{e}_{1_y}y)]\,,$$

$$\psi^{h\pm}_{Nm} = \frac{1}{B}\begin{bmatrix} 0 \\ 0 \\ \frac{\mp\tilde{\eta}k^{h}_{1m}e^{\pm i\tilde{\eta}\alpha_{hm}}}{\tau^{h}_{1m}} \\ 1 \end{bmatrix} \exp[i(\pm k^{h}_{1_x m}x + k^{h}_{1_y}y)]\,. \tag{4.3}$$

where the index $m = \mathrm{L/R}$ stands for the left or right normal silicene region and we use this symbol for the rest of the chapter. In Eq.(4.3) the normalization factors are given by $A = \sqrt{\frac{2(E+\mu_m)}{\tau^{e}_{1m}}}$, $B = \sqrt{\frac{2(E-\mu_m)}{\tau^{h}_{1m}}}$ and

$$k^{e(h)}_{1m} = \sqrt{\left(k^{e(h)}_{1_x m}\right)^2 + \left(k^{e(h)}_{1_y}\right)^2}\,, \tag{4.4}$$

$$k^{e(h)}_{1_x m} = \sqrt{(E\pm\mu_m)^2 - (elE_{zm} - \tilde{\eta}\sigma\lambda_{SO})^2 - \left(k^{e(h)}_{1_y}\right)^2}\,. \tag{4.5}$$

$$\tau_{1m}^{e(h)} \;=\; E \pm \mu_m \mp (elE_{zm} - \tilde{\eta}\sigma\lambda_{SO}) \; . \tag{4.6}$$

Here μ_m indicates the chemical potential in the left (μ_L) or right (μ_R) normal silicene region. E is the energy of the incident particle.

Due to the translational invariance in the y-direction, corresponding momentum $k_{1_y}^{e(h)}$ is conserved. Hence, the angle of incidence α_{em} and the Andreev reflection (AR) angle α_{hm} are related via the relation

$$k_{1m}^{h} \sin(\alpha_{hm}) = k_{1m}^{e} \sin(\alpha_{em}) \; . \tag{4.7}$$

In the insulating region I, the corresponding wave functions can be inferred from normal region wave functions (Eq.(4.3)) by replacing $\mu_m \rightarrow \mu_m - V_0(V_0')$ where V_0 and V_0' are the applied gate voltages at the left and right insulating regions respectively. We define dimensionless barrier strengths [135, 176] $\chi_1 = V_0 d/\hbar v_F$ and $\chi_2 = V_0' d/\hbar v_F$ which we use as pumping parameters for our analysis. Here d is the width of the insulating barriers assumed to be the same for both of them.

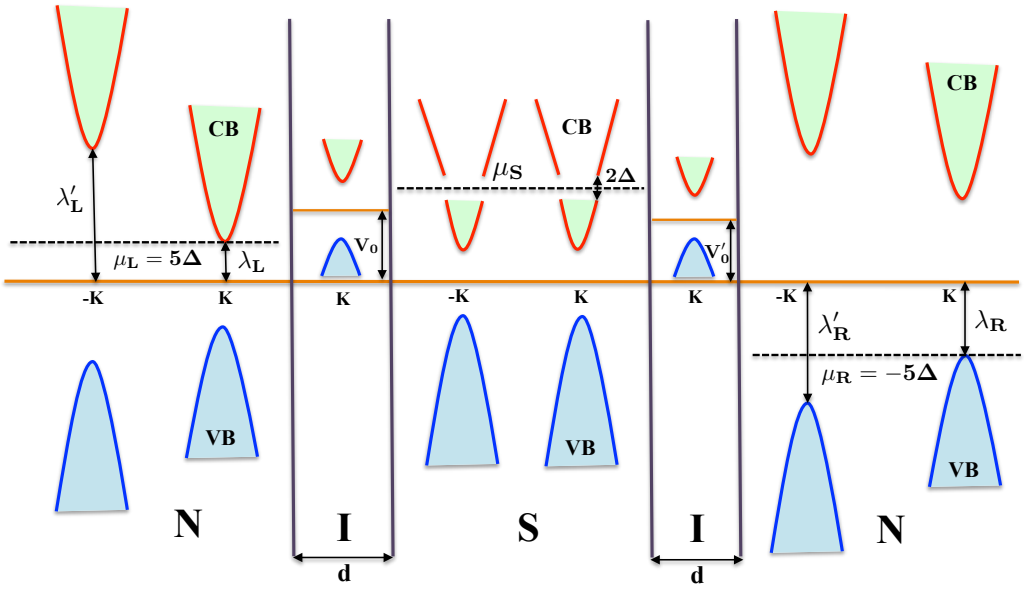

Figure 4.2: A schematic sketch of the band structure of our silicene NISIN setup is depicted. For the normal regions of silicene (N) as well as superconducting (S) silicene region, both $\mathbf{K}$ and $\mathbf{K}'$ valleys are presented. In contrast, only $\mathbf{K}$ valley is shown for both the insulating regions (I) for simplicity. Conduction band is denoted by CB while the valence bands are marked as VB. At the left normal silicene side, the chemical potential is kept at the bottom of the CB ($\mu_L = 5\Delta$, dashed line) while at the right normal silicene side, the chemical potential is set at the top of the valance band ($\mu_R = -5\Delta$, dashed line) to obtain resonant CAR process.

In the superconducting region S, the wave functions of DBdG quasiparticles are given by,

$$\psi_S^{e\pm} = \frac{1}{\sqrt{2}} \begin{bmatrix} u_1 \\ \pm\tilde{\eta}u_1 e^{i\tilde{\eta}\theta_e} \\ u_2 \\ \pm\tilde{\eta}u_2 e^{i\tilde{\eta}\theta_e} \end{bmatrix} \exp[\pm(i\mu_S - \kappa)x + iq_y^e y] \, ,$$

$$\psi_S^{h\mp} = \frac{1}{\sqrt{2}} \begin{bmatrix} u_2 \\ \mp\tilde{\eta}u_2 e^{-i\tilde{\eta}\theta_h} \\ u_1 \\ \mp\tilde{\eta}u_1 e^{-i\tilde{\eta}\theta_e} \end{bmatrix} \exp[\pm(-i\mu_S - \kappa)x + iq_y^h y] \, . \tag{4.8}$$

Here the coherence factors are given by,

$$u_{1(2)} = \left[\frac{1}{2} \pm \frac{\sqrt{E^2 - \Delta^2}}{2E}\right]^{\frac{1}{2}} \text{and} \quad \kappa = \sqrt{\Delta^2 - E^2}. \tag{4.9}$$

As before, the translational invariance along the y direction relates the transmission angles for the electron-like and hole-like quasi-particles via the following relation given by,

$$q^\beta \sin\theta_\beta = k_{1m}^e \sin\alpha_{em} \, . \tag{4.10}$$

for $\beta = e, h$. The quasi-particle momentum can be written as

$$q^{e(h)} = \mu_S \pm \sqrt{E^2 - \Delta^2} \, . \tag{4.11}$$

where $\mu_S = \mu_m + U_0$, and U_0 is the gate potential applied to the superconducting region in order to tune the Fermi wave-length mismatch [115] between the normal and superconducting regions. The requirement for the mean-field treatment of superconductivity is justified in our model as we have taken $\mu_S \gg \Delta$ [115, 101] throughout our calculation.

We consider electrons with energy E incident from the left normal region of the silicene sheet in the subgapped regime ($E < \Delta$). Considering normal reflection, Andreev reflection, cotunneling (normal transmission) and crossed Andreev reflection from the interface, we can write the wave functions in five different regions of the junction as

$$
\begin{aligned}
\Psi_N^L &= \psi_{NL}^{e+} + r_e\psi_{NL}^{e-} + r_A\psi_{NL}^{h-} \,, \\
\Psi_I^L &= p_1\psi_{IL}^{e+} + q_1\psi_{IL}^{e-} + m_1\psi_{IL}^{h+} + n_1\psi_{IL}^{h-} \,, \\
\Psi_S &= t_1\psi_S^{e+} + t_2\psi_S^{e-} + t_3\psi_S^{h+} + t_4\psi_S^{h-} \,, \\
\Psi_I^R &= p_2\psi_{IR}^{e+} + q_2\psi_{IR}^{e-} + m_2\psi_{IR}^{h+} + n_2\psi_{IR}^{h-} \,, \\
\Psi_N^R &= t_e\psi_{NR}^{e+} + t_A\psi_{NR}^{h+} \,.
\end{aligned} \tag{4.12}
$$

where r_e, r_A, t_e, t_A correspond to the amplitudes of normal reflection, AR, transmission and CAR in the N silicene regions, respectively. The transmission amplitudes t_1, t_2, t_3 and t_4 denote the electron like and hole like quasi-particles in the S region. Using the boundary conditions at the four interfaces, we can write

$$
\begin{aligned}
\Psi_N^L|_{x=-d} &= \Psi_I^L|_{x=-d}, \quad \Psi_I^L|_{x=0} = \Psi_S|_{x=0} \,, \\
\Psi_S|_{x=L} &= \Psi_I^R|_{x=L}, \quad \Psi_I^R|_{x=L+d} = \Psi_N^R|_{x=L+d} \,.
\end{aligned} \tag{4.13}
$$

which yields a set of sixteen linearly independent equations. Solving these equations numerically, we obtain r_e, r_A, t_e, t_A which are required for the computation of pumped charge through our setup.

In order to carry out our analysis for the pumped charge in silicene NISIN structure, we choose the two dimensionless insulating barrier strengths χ_1 and χ_2 as our pumping parameters. They evolve in time either as (off-set circular contours)

$$
\begin{aligned}
\chi_1 &= \chi_0 + P\cos(\omega t - \eta) \,, \\
\chi_2 &= \chi_0 + P\cos(\omega t + \eta) \,,
\end{aligned} \tag{4.14}
$$

or as (“lemniscate” contours),

$$\chi_1 = \chi_{1_0} + P_L\Big(\cos\theta\cos\omega t - \frac{1}{2}\sin\theta\sin 2\omega t\Big)/(1+\sin^2\omega t)\ ,$$
$$\chi_2 = \chi_{2_0} + P_L\Big(\cos\theta\cos\omega t + \frac{1}{2}\sin\theta\sin 2\omega t\Big)/(1+\sin^2\omega t)\ , \tag{4.15}$$

respectively. In the circular contours χ_0 and in the lemniscate contours χ_{1_0}, χ_{2_0} correspond to the mean value of the amplitude respectively, around which the two pumping parameters are modulated with time. P and P_L are called the pumping strengths for the two types of contours respectively. Furthermore, 2η and θ represent the phase offset between the two pumping signals for the circular and lemniscate contours, respectively. Here ω is the frequency of oscillation of the pumping parameters.

We, in our analysis, only consider the adiabatic limit of quantum pumping where time period of the pumping parameters $T = 2\pi/\omega$ is much longer than the dwell time $\tau_{dwell} \simeq L/v_F$ of the Dirac fermions inside the proximity induced superconducting region.

To calculate the pumped charge, we employ Brouwer's formula [140] which relies on the knowledge of the parametric derivatives of the S-matrix elements. Following Ref.[177], S-matrix for the NISIN structure of silicene for an incident electron with energy E, can be written as

$$S = \begin{bmatrix} |r_e|e^{i\gamma_e} & |r_A|e^{i\gamma_h} & |t_e|e^{i\delta_e} & |t_A|e^{i\delta_h} \\ |r_A|e^{i\gamma_h} & |r_e|e^{i\gamma_e} & |t_A|e^{i\delta_h} & |t_e|e^{i\delta_e} \\ |t_e|e^{i\delta_e} & |t_A|e^{i\delta_h} & |r_e|e^{i\gamma_e} & |r_A|e^{i\gamma_h} \\ |t_A|e^{i\delta_h} & |t_e|e^{i\delta_e} & |r_A|e^{i\gamma_h} & |r_e|e^{i\gamma_e} \end{bmatrix}\ , \tag{4.16}$$

We write here the complex S-matrix elements S_{ij} in polar form, with modulus and phase explicitly shown, since the phase is going to play a major role in the determination of the pumped charge. For a single channel S-matrix, the formula for the pumped charge becomes [177]

$$\begin{aligned} Q = \frac{e}{2\pi}\int_0^T dt[\ &- |r_A|^2(\dot\gamma_h\cos\alpha_{hL} + \dot\gamma_e\cos\alpha_{eL}) \\ &- |t_A|^2(\dot\delta_h\cos\alpha_{hR} + \dot\gamma_e\cos\alpha_{eL}) \\ &+ |t_e|^2(\dot\delta_e\cos\alpha_{eR} - \dot\gamma_e\cos\alpha_{eL}) \\ &+ \dot\gamma_e\cos\alpha_{eL}]\ , \end{aligned} \tag{4.17}$$

The derivation of this working formula following Ref. [140] is given in Appendix D . Here, we have redefined the complex scattering amplitudes r_A and t_A to satisfy the conservation of probability current [102]. On the other hand, the other two scattering amplitudes r_e and t_e remain unchanged. Hence, the redefined scattering probabilities $|r_A|^2$ and $|t_A|^2$ become

$$\begin{aligned} |r_A|^2 &\equiv \frac{k^h_{1_x}}{k^e_{1_x}}\left[\frac{2(E+\mu_L)(E-\mu_L-\lambda_L)}{|\eta k^h_{1_x}-ik^e_{1_y}|^2+(E-\mu_L-\lambda_L)^2}\right]|r_A|^2\,, \\ |t_A|^2 &\equiv \frac{k^h_{1_x}}{k^e_{1_x}}\left[\frac{(E+\mu_L)}{(E-\mu_R)}\right]|t_A|^2\,. \end{aligned} \tag{4.18}$$

Furthermore, γ_e, γ_h, δ_e, δ_h are the phases of redefined r_e, r_A, t_e and t_A respectively. Here, α_{eL}, α_{eR} correspond to the incident and transmitted angles of electrons while α_{hL}, α_{hR} represent the reflected and transmitted angles of holes respectively. Note that, if $\alpha_{eL}=0$, then the last term of Eq.(4.17) consisting of the time derivative of reflection phase is called "*topological part*" [152] while the rest is termed as "*dissipative part*" [152]. The last term is called "topological" becuase for $\alpha_{eL}=0$, it has to return to itself after the full period. Hence, the only possible change in γ_e in a period can be integer multiples of 2π *i.e.,* $\gamma_e(T)\rightarrow\gamma_e(0)+2\pi n$. On the other hand, the rest of the terms in Eq.(4.17) are together called "dissipative" since their cumulative contribution prevents the perfect quantization of pumped charge.

4.4 Numerical Results

In this section we present and discuss our numerical results for the pumped charge based on Eq.(4.17). The quantum mechanical scattering amplitudes are all functions of the incident electron energy E, length of the superconducting silicene region L, the strengths χ_1, χ_2 of the two thin insulating barriers, chemical potential μ_m ($m=\mathrm{L/R}$) of the left and right normal silicene region, external electric field E_{zm} ($m=\mathrm{L/R}$) and spin orbit coupling λ_{SO}. We denote the band gaps at the left and right normal silicene side as $2\lambda_L$ and $2\lambda_R$ respectively (see Fig. 4.2) where $\lambda_m=(elE_{zm}-\tilde{\eta}\sigma\lambda_{SO})$. In addition, we have set $\hbar=1$ throughout our analysis.

For clarity, we divide this section into two subsections. In the first one, we discuss quantum pumping via resonant CAR process with unit probability in the χ_1-χ_2 plane. The second one is devoted to the discussion of the same via the perfect transmission/CT process.

4.4.1 Pumping via CAR in the χ_1-χ_2 plane

Silicene is a material where a large value of non-local CAR process can be obtained due to its unique band structure [102]. The band gaps and Fermi level (chemical potential) in silicene can be tuned by applying electric fields only. By tuning the both, very recently, Linder *et al.* in Ref.[102] showed that one can completely block elastic cotunneling in silicene NSN junction in the subgapped regime. Consequently, pure CAR process is possible for a broad range of energies. However, maximum probability of CAR found in Ref.[102] was $\sim 96.2\%$ while the rest was normal reflection probability.

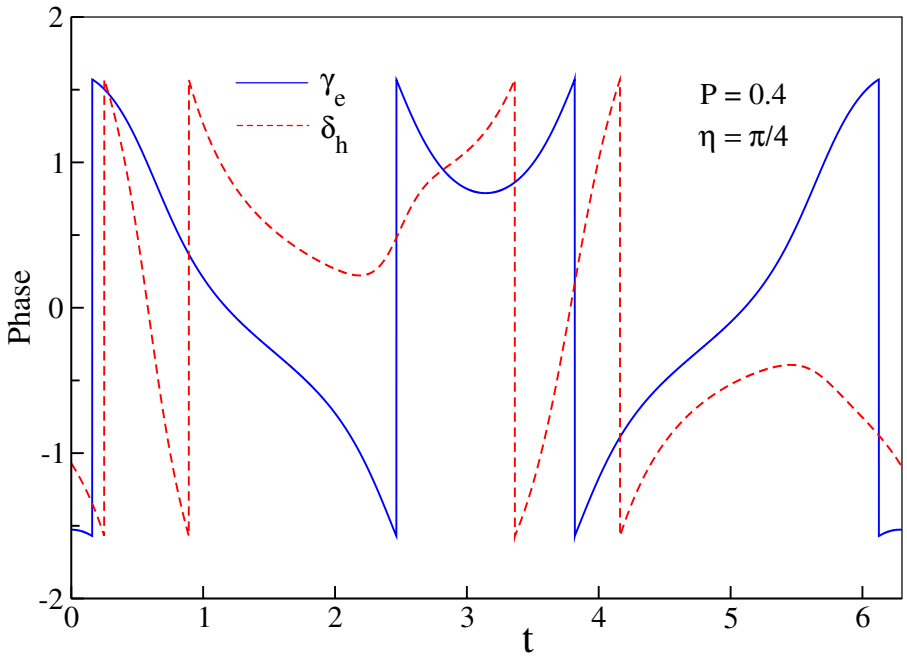

Figure 4.3: The plot shows the variation of the normal reflection phase γ_e and CAR phase δ_h, with time t, along a chosen pumping contour in the χ_1 - χ_2 plane.

The probability of non-local CAR process can be enhanced to unity (100%) (see Fig. 4.4) by introducing two insulating barriers at each NS interfaces. We have considered $\mu_L = 5\Delta$, $\mu_R = -5\Delta$ and $\lambda_L = \lambda_R = 5\Delta$ which reflects the fact that the Fermi level touches the bottom of the conduction band in the left normal silicene side while it touches the top of the valance band in right normal silicene side. This is illustrated in Fig. 4.2. The superconducting silicene side is doped with $\mu_S = 20\Delta$ to satisfy mean field condition for superconductivity $\mu_S \gg \Delta$ [102]. The band gaps λ_L and λ_R at the two normal sides can be adjusted by the external electric field E_{zm} (m=L/R). The chosen value of the band gaps and doping levels permits one to neglect the contribution from the other valley ($\mathbf{K}'$) which has much higher band gap compared to the other energy scales in the system (see Fig. 4.2). Under such circumstances, we obtain pure CAR in this setup choosing length of the superconducting side,

$L = 2.1\xi$ ($\xi = \hbar v_F/\pi\Delta$ is the phase coherence length of the superconductor) and incident electron energy, $E = 0.9\Delta$. Note that, for our analysis, we choose the same parameter values as used in Ref.[102].

The reason behind obtaining pure CAR process in our NISIN set-up is as follows. As there is a band gap $2\lambda_L = 2(elE_{zL} - \tilde{\eta}\sigma\lambda_{SO}) > \Delta$ in the left normal silicene side, probability for AR to take place is vanishingly small [102, 176]. On the other hand, $2\lambda_R = 2(elE_{zR} - \tilde{\eta}\sigma\lambda_{SO})$ is the energy gap between the conduction band and valance band in the right (R) normal silicene region as illustrated in Fig. 2. Moreover, the chemical potential μ_R in the right (R) normal silicene is chosen to be at the top of the valence band. Hence, only hole states are available in the right normal side. Therefore, an electron incident from the conduction band of the left normal silicene region encounters a gap and unavailability of electronic states to tunnel into the right normal region which essentially block the co-tunneling (CT) probability. Hence, the only possible scattering processes remain are normal reflection and CAR. This allows our system to possess completely pure CAR process with probability one in $\chi_1 - \chi_2$ plane as shown in Fig. 4.4. These resonant CAR peaks are $\pi/2$ periodic in nature and they appear in pairs. Such periodic nature and the fact that resonaces appear in pairs, affect the pumped charge behavior which will be discussed later. The oscillatory behavior of the CAR resonance can be explained as follows. Non-relativistic free electrons with energy E incident on a potential barrier with height V_0 are described by an exponentially decaying (non-oscillatory) wave function inside the barrier region if $E < V_0$, since the dispersion relation is $k \sim \sqrt{E - V_0}$. On the contrary, relativistic free electrons satisfies a dispersion $k \sim (E - V_0)$, consequently corresponding wave functions do not decay inside the barrier region [120, 117, 135]. Instead, the transmittance of the junction displays an oscillatory behavior as a function of the strength of the barrier. Hence, the undamped oscillatory behavior of CAR is a direct manifestation of the relativistic low-energy Dirac fermions in silicene. The periodicity depends on the Fermi wave-length mismatch between the normal and superconducting region [135, 176].

Note that, the Fermi energy (chemical potential) need neither necessarily exactly touch valance band maxima or conduction band minima nor they need to have same magnitude at the two normal regions to obtain resonant CAR. A small deviation, from the numerical values that we have taken, also leads to the resonant CAR probability to take place within the subgapped regime. Previously, possibility of obtaining CAR was also reported in p-n junction of graphene [178] at a specific value of the parameters. However, a small deviation from that leads to CT along with CAR contaminating

that possibility.

As phases of the scattering amplitudes play a major role in the determination of the pumped charge, we show the behavior of phases of normal reflection and CAR amplitudes (γ_e and δ_h respectively) as a function of time for one full cycle in Fig. 4.3. We observe that both γ_e and δ_h exhibit four abrupt jumps for a full period of time (along a chosen contour). These jumps play a significant role in determining the pumped charge which we emphasis later. In addition, throughout our analysis, we have considered incident electrons to be normal to the interface *i.e.,* $\alpha_{eL} = 0$ for simplicity. Later for completeness, we demonstrate angle dependence of the pumped charge.

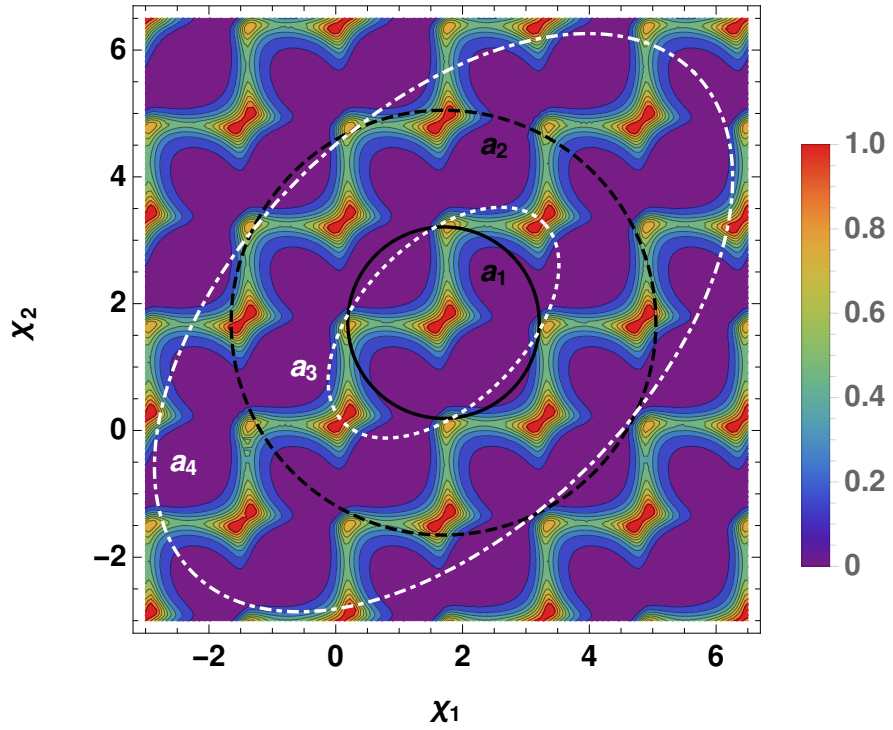

Figure 4.4: Plot of CAR probability $|t_A|^2$ in χ_1-χ_2 plane. The contours a_1, a_2 represents $\eta = \pi/4$ and $P = 1.51$, $P = 3.35$ respectively. On the other hand, the contours a_3, a_4 are for $\eta = \pi/6$ and $P = 1.82$, $P = 4.56$ respectively. The value of the other parameters are chosen to be $L = 2.1\xi$, $E = 0.9\Delta$, $\omega = 1$, $\chi_0 = 1.7$, $\mu_L = 5\Delta$, $\mu_R = -5\Delta$, $\mu_S = 20\Delta$ and $\lambda_L = \lambda_R = 5\Delta$.

Under such scenario where the only possible scattering processes are normal reflection and CAR, Eq.(4.17) simplifies to

$$Q = \frac{e}{2\pi}\int_0^T dt[\quad - \quad |t_A|^2(\dot{\delta}_h \cos\alpha_{hR} + \dot{\gamma}_e \cos\alpha_{eL}) \\ + \quad \dot{\gamma}_e \cos\alpha_{eL}] \,, \tag{4.19}$$

The behavior of pumped charge Q as a function of the pumping strength P is shown in Fig. 4.5

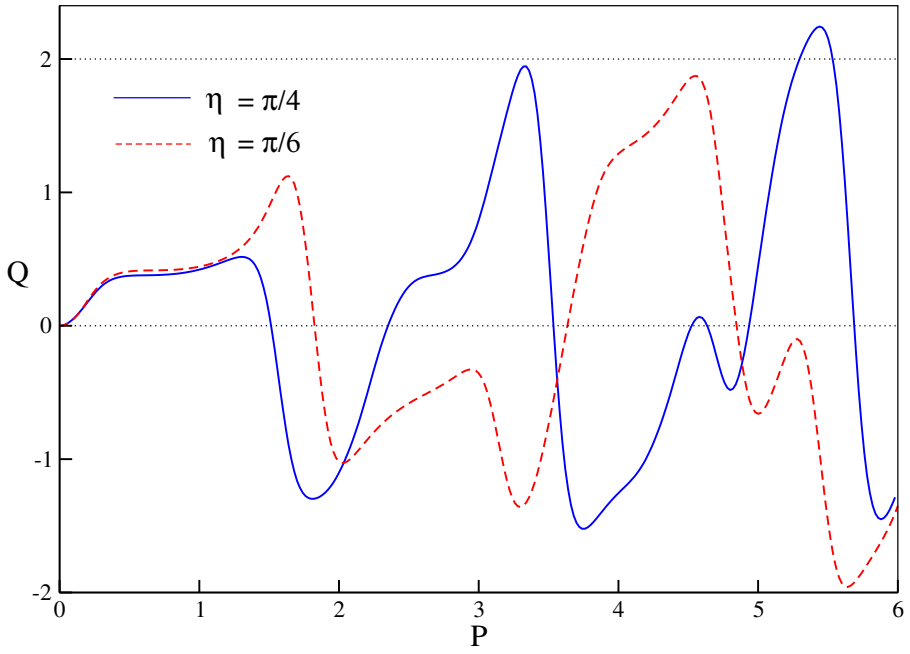

Figure 4.5: The pumped charge Q in units of the electron charge e, for pumping in the χ_1-χ_2 plane, is shown as a function of the pumping strength P for circular and elliptic contours. The value of the other parameters are chosen to be the same as mentioned in Fig. 4.4.

for $\eta = \pi/4, \pi/6$ which correspond to circular and elliptic contour respectively. The features of Q, depicted in Fig. 4.5, can be understood from the behavior of CAR probability $|t_A|^2$ in the χ_1-χ_2 plane. For small values of P, pumped charge Q becomes vanishingly small in magnitude as the pumping contours do not enclose any $|t_A|^2 = 1$ point. When a pumping contour encloses one of the resonant peaks of $|t_A|^2$, topological part of the pumped charge gives rise to ne (n is the winding number) due to the integration around a singular point. At this point the reflection phase γ_e becomes ill-defined. However, the dissipative part nullifies the topological part resulting in small values of Q (see Eq.(4.17)) for both $\eta = \pi/4, \pi/6$. On the other hand, when a contour encloses both $|t_A|^2$ resonances, the relative integration direction around the two singular points plays an important role. Namely, when two resonances are enclosed in a path with the same orientation, then the two contributions have opposite sign and tend to cancel each other. For *e.g.* when $\eta = \pi/4$ (black circular contours a_1 and a_2), the pumped charge is zero for $P = 1.51$ (see Fig. 4.5) as the contour a_1 encloses both the peaks resulting in zero pumped charge. Similar feature was found in case of resonant transmission in Ref.[171, 149, 153, 172] where pumped charge was found to be zero when the pumping contour encloses both the resonances. Q approaches almost quantized value $2e$ for $P = 3.35$ and the corresponding contour a_2 encloses even number of resonance pairs in the same orientation. Hence the topological part of pumped charge is almost zero and the contribution to Q arises from the dissipative

part. The large contribution from the dissipative part arises due to the total drop of the CAR phase δ_h by a factor of 4π during its time evolution along the contour a_2 (see Fig. 4.3). Similarly, when $\eta = \pi/6$, Q is zero at $P = 1.82$ which corresponds to the a_3 contour which encloses four peaks (two pairs) in total, resulting in zero contribution from the topological part. On the other hand, pumped charge reaches its maximum when $P = 4.56$ (a_4 contour) where also the entire contribution originates from the dissipative part (see Fig. 4.5). Pumped charge Q exceeds the value $+2e$ as pumping strength P increases (see Fig. 4.5) for both $\eta = \pi/4$ and $\pi/6$. Physically, the contribution of the dissipative part in pumped charge increases non-monotonically with the pumping strength. Hence, as the pumping contour encloses more number of pairs of resonant CAR peaks, due to the enhancement of dissipative part, pumped charge can exceed +2e with further increase of P. Pumped charge can change sign depending on the sense of enclosing of the resonances *i.e.,* whether it is clock-wise or anti-clockwise.

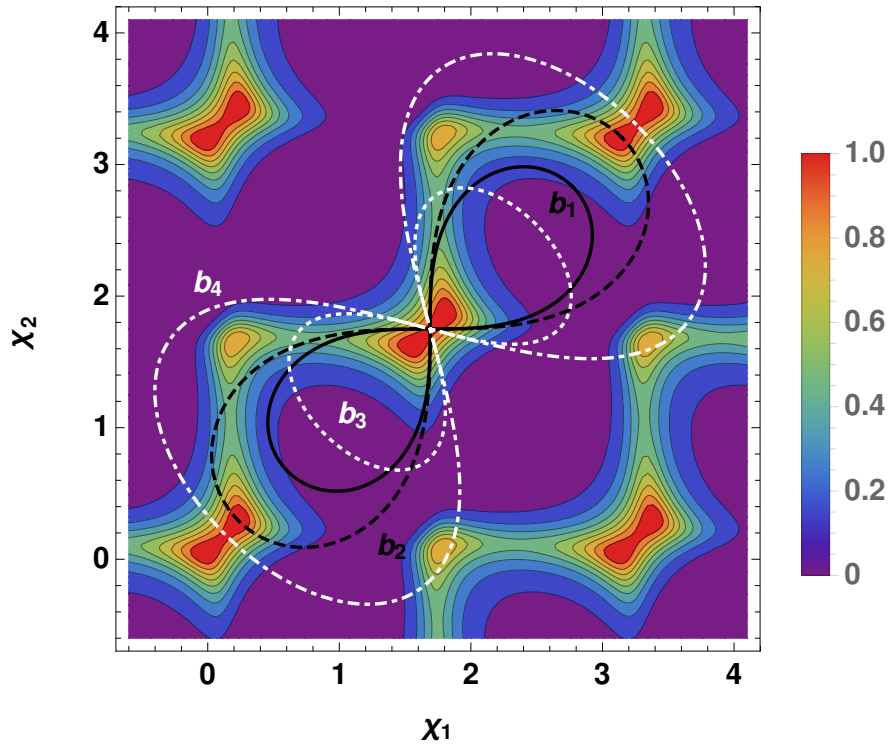

Figure 4.6: Plot of CAR probability $|t_A|^2$ along with lemniscate contours are shown in the χ_1-χ_2 plane. The contours b_1, b_2 represents $\theta = \pi/4$ and the contours corresponding to $\theta = \pi/3$ are b_3, b_4. We have chosen the mean values $\chi_{1_0} = 1.69$ and $\chi_{2_0} = 1.75$. The value of the other parameters are chosen to be the same as mentioned in Fig. 4.4.

The behavior of pumped charge Q with respect to the pumping strength P_L for lemniscate contours with $\theta = \pi/4$ and $\pi/3$ is presented in Fig. 4.7 and the corresponding contours are shown in Fig. 4.6. The pumped charge is small for small values of P_L where the contribution from topological part is

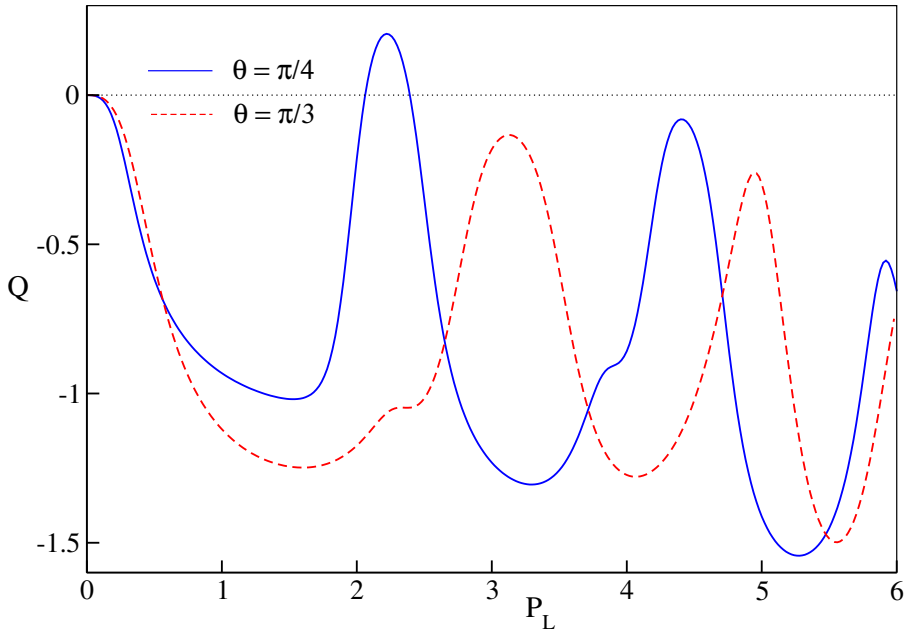

Figure 4.7: Pumped charge Q in unit of electon charge e, for pumping in the χ_1-χ_2 plane, is shown as a function of the pumping strength P_L for the lemniscate contours. All other parameters are identical to those used in Fig. 4.4.

cancelled by the dissipative part. As P_L increases, the corresponding pumping contour encloses both the $|t_A|^2$ peaks within opposite integration orientations and as a consequence, the two contributions for the pumped charge sum up. This is exactly the reason that motivates us to choose the lemniscate contours. However, the dissipative part effectively reduces the total pumped charge. Such feature arises for lemniscate contours of the type b_1 and b_3. Moreover, we observe that the pumped charge becomes zero for $P_L = 2.06$ at $\theta = \pi/4$, where both the bubbles of the b_2 contour enclose two $|t_A|^2$ peaks from the two adjacent resonances in the χ_1-χ_2 plane and hence their combined contribution to pumped charge get cancelled for each bubble separately. The qualitative behavior of Q remains similar for $\theta = \pi/3$ where maximum value of Q is achieved when each bubble of the lemniscate contour of type b_4 encloses odd number of resonance pairs while Q tends to zero as even number of pairs are enclosed by each bubble of the contour.

4.4.2 Pumping via transmission/CT in the χ_1-χ_2 plane

In this subsection we present our numerical results for the adiabatic quantum pumping through pure CT *i.e.,* resonant transmission process. The latter can be achieved by tuning the Fermi level (chemical potential) at the bottom of the conduction band in both the normal silicene regions (see Fig. 4.2). The numerical values of all the parameters are identical to those used before except now $\mu_R = 5\Delta$,

$L = 2.2\,\xi$ and $E = 0.93\Delta$.

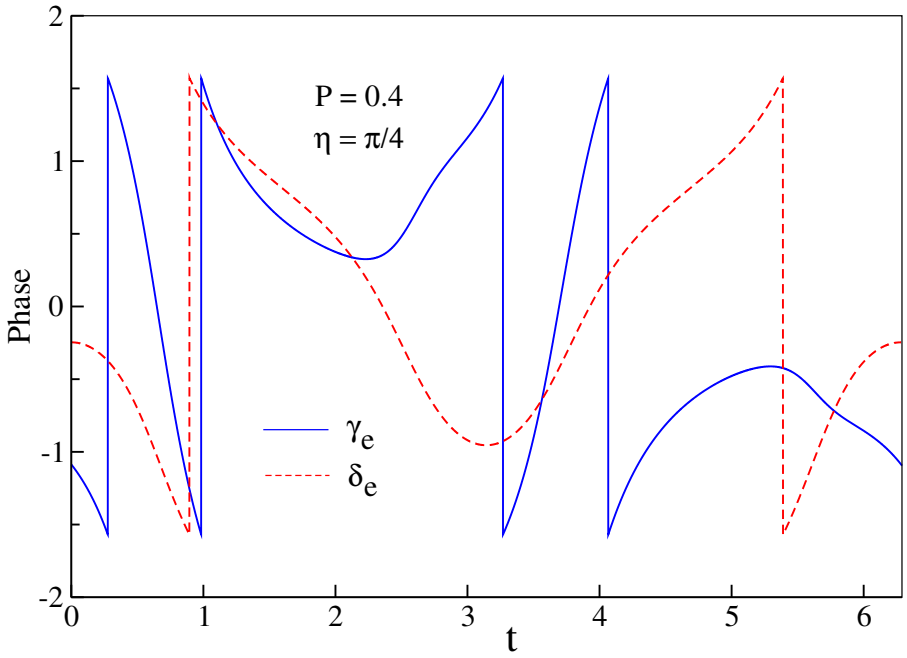

Figure 4.8: The variation of the normal reflection phase γ_e and transmission phase δ_e, with time t, is shown along a chosen pumping contour in the χ_1 - χ_2 plane.

As before, due to the presence of a gap ($2\lambda_L > \Delta$) in the left normal side, AR is forbidden while CAR cannot take place because of the unavailability of the hole states in the right normal region in the low energy limit. An incident electron thus only encounters two scattering processes which are normal reflection and transmission. The presence of insulating barriers between the NS interfaces allows both these scattering probabilities to be oscillatory as a function of the dimensionless barrier strengths χ_1 and χ_2 which is depicted in Fig. 4.9.

In this regime, as AR and CAR probabilities are always zero, hence Eq.(4.17) reduces to

$$\begin{aligned} Q &= \frac{e}{2\pi}\int_0^T dt[|t_e|^2(\dot{\delta}_e \cos\alpha_{eR} - \dot{\gamma}_e \cos\alpha_{eL}) \\ &+ \dot{\gamma}_e \cos\alpha_{eL}]\,, \end{aligned} \tag{4.20}$$

In Fig. 4.10, pumped charge Q is presented as a function of pumping strength P for $\eta = \pi/4$ (circular contour) and $\pi/6$ (elliptic contour). To understand the behavior of the pumped charge, we also investigate the transmission probability $|t_e|^2$ in $\chi_1 - \chi_2$ plane (see Fig. 4.9). We observe qualitatively similar features of the pumped charge as depicted in the previous subsection. Here also topological part of pumped charge becomes zero when pumping contour encloses even number of

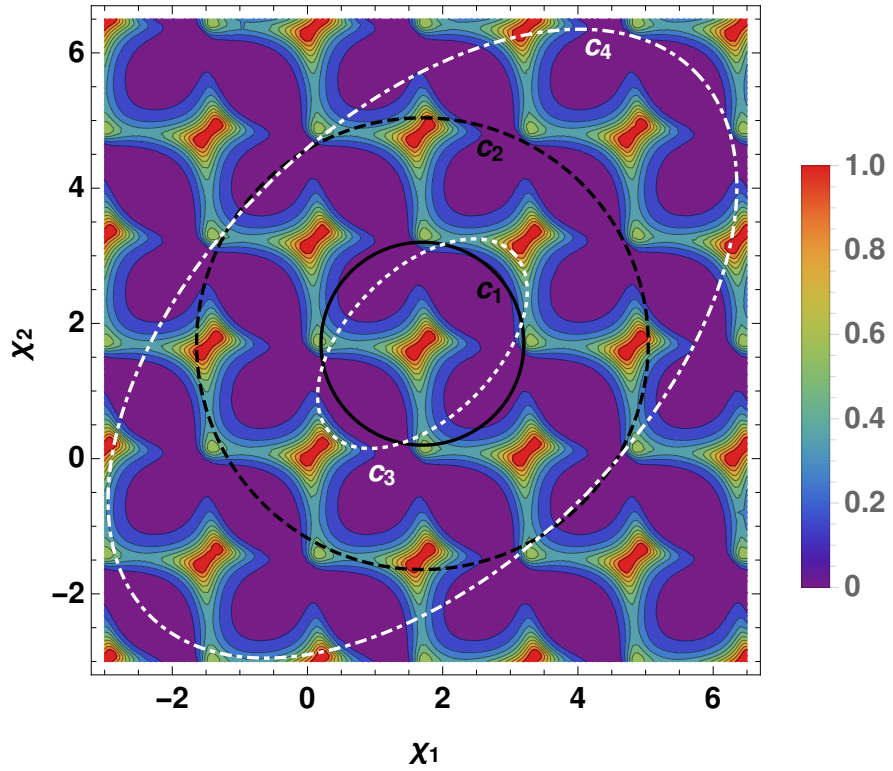

Figure 4.9: Transmission probability $|t_e|^2$ along with circular and elliptic contours are shown in χ_1-χ_2 plane. The contours c_1, c_2 represent $\eta = \pi/4$ and $P = 1.5$, $P = 3.34$ respectively. On the other hand, the contours c_3, c_4 correspond to $\eta = \pi/6$ and $P = 1.55$, $P = 4.65$ respectively. The value of the other parameters are chosen to be $L = 2.2\xi$, $E = 0.93\Delta$, $\omega = 1$, $\chi_0 = 1.7$, $\mu_L = 5\Delta$, $\mu_R = 5\Delta$, $\mu_S = 20\Delta$ and $\lambda_L = \lambda_R = 5\Delta$.

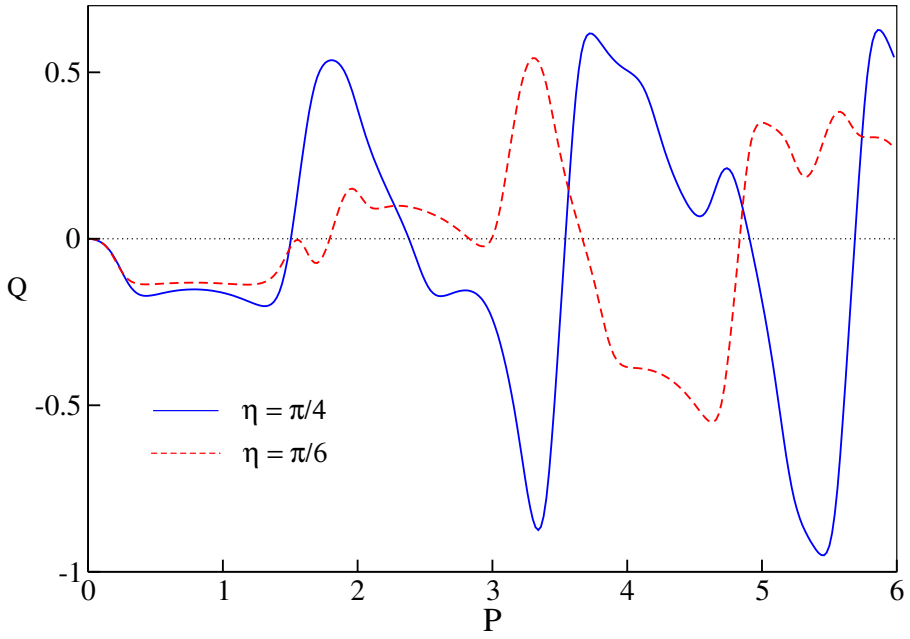

Figure 4.10: Pumped charge Q in unit of electron charge e, for pumping in the χ_1-χ_2 plane, is shown as a function of the pumping strength P for the circular and elliptic contours. We choose the same values of the other parameters as mentioned in Fig. 4.9.

resonance pairs in the same orientation. Finite contribution from dissipative part, in Q, emerges due to the total jump of the transmission phase δ_e by a factor of 2π during its time evolution along the contour c_2 (see Fig. 4.8). On the other hand, for contour c_1, dissipative part vanishes because over a full period of time, reflection and transmission phases γ_e and δ_e respectively cancell each other (see Eq.(4.20)). Although, Q approaches to $-e$ for pumping via resonant CT process compared to $2e$ via the resonant CAR process.

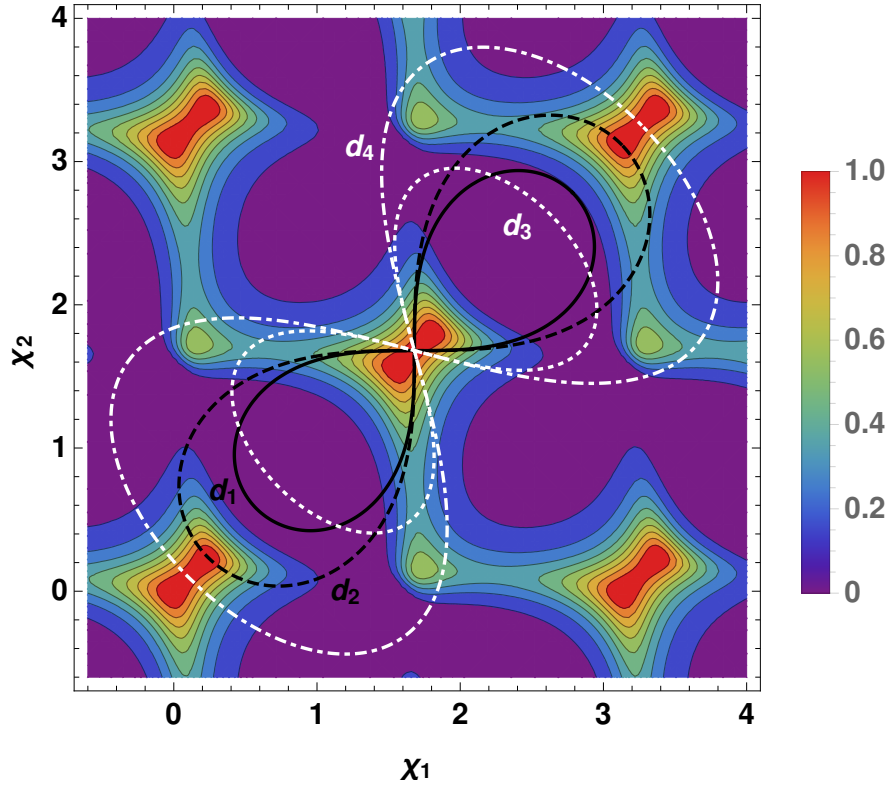

Figure 4.11: Transmission probability $|t_e|^2$ together with different lemniscate contours are shown in the χ_1-χ_2 plane. The contours d_1, d_2 represents $\theta = \pi/4$ and the contours d_3, d_4 corresponds to $\theta = \pi/3$. We choose the values of χ_{1_0} and χ_{2_0} as $\chi_{1_0} = \chi_{2_0} = 1.68$. All other parameters are identical to those used in Fig. 4.9.

In Fig. 4.12, we show the behavior of pumped charge Q as a function of the pumping strength P_L with lemniscate contours. To understand the corresponding behavior of Q, we also show $|t_e|^2$ in the χ_1-χ_2 plane along with different lemniscate contours (see Fig. 4.11). Here also the features of Q remains similar as previous subsection for both $\theta = \pi/4$ and $\pi/3$.

As we mention earlier, the above mentioned results are valid for normal incidence of the incoming electron *i.e.,* $\alpha_{eL} = 0$. Here, we explore the dependence of the pumped charge on the angle of incident electrons. In Fig. 4.13, pumped charge Q as a function of incident angle α_{eL} is presented when either CAR probability $|t_A|^2$ or transmission probability $|t_e|^2$ is enclosed by the circular pumping

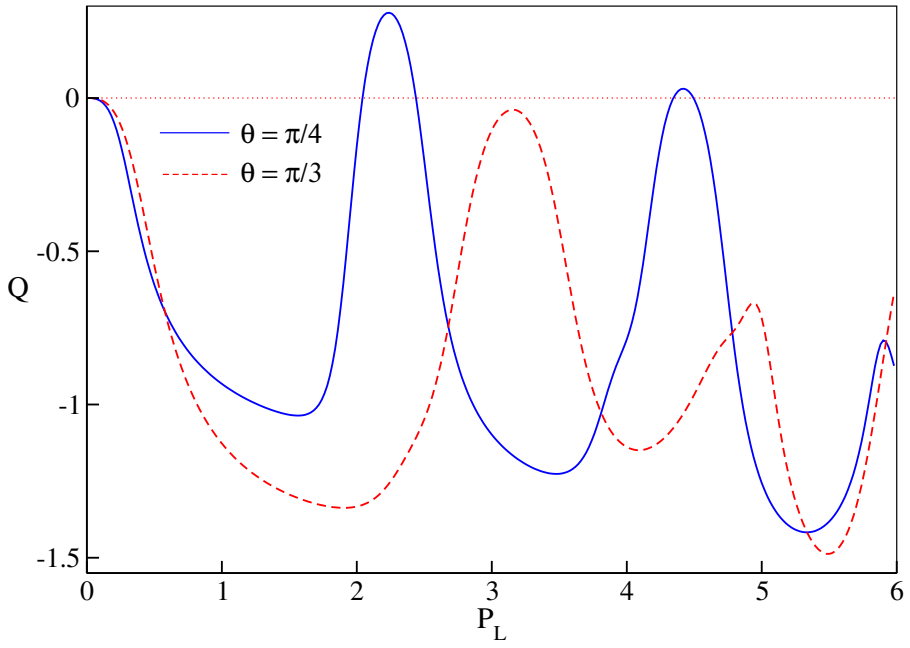

Figure 4.12: Pumped charge Q, in unit of electron charge e, is depicted as a function of the pumping strength P_L for the lemniscate contours. All other parameters are identical to those used in Fig. 4.9.

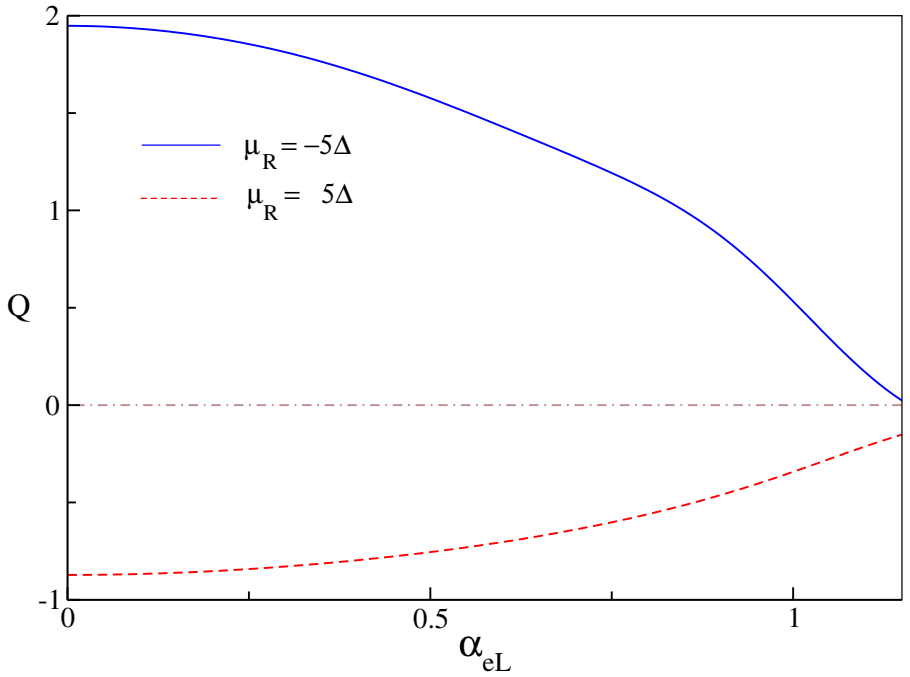

Figure 4.13: Pumped charge Q, in unit of electron charge e, is shown as a function of the incident angle α_{eL} for both $\mu_R = -5\Delta$ and $\mu_R = 5\Delta$. Here we choose $\eta = \pi/4$, $P = 3.35$ for $\mu_R = -5\Delta$ and $P = 3.34$ for $\mu_R = 5\Delta$ respectively.

contour. The α_{eL} dependence is shown upto the critical angle α_c. Above α_c, AR and CAR processes cannot take place [115]. Rather, normal reflection is the dominating scattering mechanism above α_c. It is evident from Fig. 4.13 that as the angle of incidence α_{eL} increases, Q decreases monotonically for enclosing $|t_A|^2$ or $|t_e|^2$ in either cases. The reason can be attributed to the fact that both $|t_A|^2$ and $|t_e|^2$ in the two different scenarios, acquire the maximum value at normal incidence *i.e.,* $\alpha_{eL} = 0$ and decreases slowly with the increase of α_{eL}. Also, for $0 < \alpha_{eL} < \alpha_c$, normal reflection probability $|r_e|^2$ also contributes to Eq.(4.17) and the interplay between all the quantum mechanical amplitudes and their phases results in smaller value of pumped charge. Note that, in case of pumping via CAR resonance process in $\chi_1 - \chi_2$ plane, Q approaches zero as α_{eL} proceeds towards α_c. However, Q is finite even at α_c in case of pumping via resonant transmission in the same parameter space, This is because at α_c, $|t_A|^2$ vanishes while $|t_e|^2$ still has small probability which gives rise to small pumped charge arising from the dissipative part (see Eq.(4.20)).

4.5 Summary and conclusions

To summarize, in this chapter, we have investigated the possibility of enhancing the CAR probability $|t_A|^2$ in silicene NSN set up by introducing thin insulating barrier [135, 176] I at each NS interface. We show that, for electrons with normal incidence, resonant CAR can be obtained in our setup by tuning the band gap in both the normal silicene regions by applying an external electric field as well as adjusting the chemical potential by additional gate voltages. We also show that $|t_A|^2$ is periodic in χ_1-χ_2 plane due to relativistic nature of Dirac fermions. On the other hand, it is also possible to attain transmission probability $|t_e|^2$ of magnitude unity in silicene NISIN junction under suitable circumstances. Owing to Dirac nature of particles, $|t_e|^2$ also exhibits periodic behavior in the space of barrier strengths χ_1 and χ_2.

We then explore adiabatic quantum charge pumping through our NISIN setup and show that the behavior of pumped charge as a function of the pumping strength P is closely related to the features of CAR probability $|t_A|^2$ or transmission probability $|t_e|^2$ in the pumping parameter space. For electrons with normal incidence, large pumped charge with value close to $Q \sim 2e$ can be obtained when particular circular or elliptic pumping contour encloses the resonant CAR in χ_1-χ_2 plane. Although the major contribution to Q, in this case, arises from the dissipative part. On the other hand, large pumped charge can also be obtained with lemniscate contour when odd number of $|t_A|^2$ peaks are

enclosed by each of its bubble. In contrast, pumped charge approaches to $Q \sim -e$ when various pumping contours enclose $|t_e|^2$ resonance in the same parameter space. However, pumped charge decreases monotonically as we increase the angle of incidence of the incoming electron. In experimental situation, the measurable quantity should be the angle averaged pumped charge analogous to angle averaged conductance [179]. From our analysis, we expect that the qualitative nature of angle averaged pumped charge as a function of the pumping strength will remain similar to the $\alpha_{eL} = 0$ case. Although the quantitative value of Q will be smaller than the angle resolved case as Q decreases monotonically with α_{eL}.

Note that, our calculation is valid for zero temperature. Nevertheless, in our case, temperature T_p must be smaller than the proximity induced superconducting gap Δ. We expect that the qualitative features of our results for the pumped charge will survive in the presence of low temperatures. For non-zero yet small temperatures, $T_p \ll \Delta$, the pairs of resonant peaks in the parameters space will have a slight broadening due to thermal smearing. Therefore, we believe that the qualitative features of pumped charge Q with respect to the pumping strength P will still be captured in our model. Although there can be quantitative change in Q. On the other hand, if $T_p > \Delta$, then CAR process from the interface will decay and pumped charge will become vanishingly small due to thermal fluctuation.

As far as practical realization of our silicene NISIN quantum pumping set up is concerned, superconductivity in silicene may be possible to induce by proximity coupled to a s-wave superconductor for *e.g.* Al, $NbSe_2$ analogous to graphene [122, 123, 179]. Once such proximity induced superconductivity in silicene is realized, fabrication of silicene NISIN junction can be feasible. The strength of the two oscillating barriers can be possible to tune by applying a.c gate voltages. Typical spin-orbit energy in silicene is $\lambda_{\rm SO} \sim 4$ meV and the buckling parameter is $l \approx 0.23$ Å [6, 5]. Considering Ref. [122, 124], typical proximity induced superconducting gap in silicene would be $\Delta \sim 0.2$ meV. For such induced superconducting gap, chemical potential is $\mu_S \sim 20\Delta \sim 4$ meV and we obtain $\xi \sim 580$ nm and length of the superconducting region $L \sim 1.2$ μm. Hence, an insulating barrier of thickness $d \sim 10 - 20$ nm may be considered as thin barrier and the gate voltage $V_0 \sim 500$ meV can therefore justify the needs of our model [135]. To achieve both the resonances, $\lambda_L = \lambda_R = 5\Delta \sim 1$ meV which can be tuned by an external electric field $E_{zL} = E_{zR} \sim 200$ V/μm. For both resonant processes, typical dwell time of the electrons inside the superconducting region is ~ 2.2 fs while the time period of the oscillating barriers is $T \sim 30$ ps and the corresponding frequency of modulation parameters turns out to be ~ 230 GHz. Thus the dwell time τ_{dwell} is much smaller than

the time period T of the modulation parameters, hence satisfying the adiabatic condition of quantum pump. Pumped current through our setup should be in the range of $\sim 10 - 15\,\mathrm{nA}$ which can be measurable in modern day experiment.

CHAPTER 5

Majorana Zero Modes in Mixed Singlet and Triplet Superconducting Nanowire

5.1 Chapter Summary

Majorana zero mode, in condensed matter system, is an emmergent quasi-particle of self-conjugate nature and is predicted to be building block of fault tolerant topological quantum computation. Topological superconductor, in 3D (2D), supports this zero energy Majorana modes at its vortex (edge). We have studied the transport properties of a quasi one dimensional (1D) ferromagnet-noncentrosymmetric superconductor (F-NCS) junction using scattering matrix formalism. We have shown that the relative orientation of the stoner field ($\tilde{\mathbf{h}}$) in the ferromagnetic lead and the $\mathbf{d}$ vector of the superconductor acts like a on-off switch for the zero bias conductance of the device. In the regime, where triplet pairing amplitude dominates over the singlet counterpart (topological phase), a pair of Majorana zero modes appear at each end of the superconducting part of the nanowire. The presence of the two kinds of pairing gaps gives rise to a pair of Majorana modes instead of a lone one at each end. When $\tilde{\mathbf{h}}$ is parallel or anti-parallel to the $\mathbf{d}$ vector, transport gets completely blocked due to blockage in pairing while, when $\tilde{\mathbf{h}}$ and $\mathbf{d}$ are perpendicular to each other, the zero energy two terminal differential conductance spectra exhibits sharp transition from $4e^2/h$ to $2e^2/h$ as the magnetization strength in the lead becomes larger than the chemical potential indicating the spin selective coupling of pair of

Majorana zero modes to the lead. For a canted angle between $\tilde{\mathbf{h}}$ and $\mathbf{d}$, a zero bias dip emmerges out instead of a peak, in the tunneling conductance giving birth to a possible novel probe of the zero modes in the transport measurements.

5.2 Introduction

Localized Majorana zero modes (MZMs) that appear at the end of one dimensional topological superconductor are anticipated to be the building blocks of future topological quantum computers [55, 26, 57, 180, 181]. Theoretical proposals [53, 52] to engineer such a topological superconductor from a semiconducting nanowire (NW) with Rashba spin-orbit coupling have stimulated a lot of recent exciting experiments (mentioned in Chapter 2) towards realizing this exotic phase hosting Majorana zero mode (MZM). The zero bias peak (ZBP) in the differential conductance was predicted [182, 62, 183, 184] in hybrid superconductor-semiconductor systems. However, the earler experimental findings [3, 58, 68, 69] were largely debated because of the possibility of ZBP appearing from coalescing Andreev levels [71], Kondo physics [70, 69], weak antilocalization [73], disorder [185] or multi band effects [75] etc. With the improved devices, more recent experiments [77, 186, 79] reveal more convincing signatures of MZMs. Nevertheless, the topological origin of ZBP is not ensured as the ZBP appearing from Andreev bound levels also mimic those of MZMs [80] and it is hard to distinguish them. Hence, newer probes of MZMs beyond ZBP is of great importance [187, 188, 189].

Noncentrosymmetric superconductors (NCS) [190, 191] are a class of superconductors in which inversion symmetry is broken. From theoretical perspective, the main interest is the fact that the lack of inversion symmetry results in the violation of the usual classification of superconductors into even-parity, spin singlet states and odd-parity, spin triplet states. The absence of inversion symmetry allows mixing between spin singlet and spin triplet pairs. As a result, the superconducting pairing can have a mixture of singlet and triplet states which do not break any additional symmetries of the system *e.g.* time reversal symmetry [192]. Physical origin of the parity mixing can be attributed to the presence of Rashba like antisymmetric spin-orbit coupling in the system which splits the Fermi surface and removes the spin degeneracy of electrons. The Fermi surface splitting can originate a mixing of spin-singlet and spin-triplet states in the superconducting condensate. There are many superconductors whose crystal structure lacks inversion centre and can be classified as noncentrosymmetric superconductors. Some of the examples are : $CePt_3Si$ [193], Mo_3Al_2C [194], $BiPd$ [195] etc.; and in general $CeTX_3$ series where T=transition metal, X=group IV element (*e.g.* $CeRhSi_3, CeIrSi_3$) [196].

From experimental point of view, thermal conductivity at low temperature [197], penetration depth measurement indicating power law behavior [198, 199], spin susceptibility measurement [200], point contact Andreev reflection (PCAR) spectroscopy [195] have been carried out to confirm the presence of both singlet and triplet type pairing structure in these materials.

In this chapter, we show that it is possible to use a ferromagnetic lead for probing MZM hosted in NCS [201]. Earlier zero energy peak in transport accross normal-metal-NCS junction was reported [202, 203] without establishing it's connection to the MZM. Effect of such zero energy peak in transport and shot noise phenomena across normal metal-NCS-normal metal has also been investigated [204, 205] without focusing on Majorana zero mode. Here we investigate the properties of two-terminal conductance of a quasi one dimensional ferromagnet-superconductor (FS) junction where the superconductor lacks inversion symmetry. We employ extended Blonder-Tinkham-Klapwijk (BTK) formalism [61] for our analysis. We show that in the topological phase, when triplet pairing dominates over the singlet one, the two terminal differential conductance at zero bias exhibits a sharp transition from $4e^2/h$ to $2e^2/h$ as the magnetization strength becomes larger than the chemical potential in the lead. We also observe a spin selective coupling of the ferromagnetic lead to the pair of MZMs as a function of the magnetization of the ferromagnet, with respect to the $\mathbf{d}$ vector in the topological regime.

The remainder of the chapter is organized as follows. In Sec. 5.3, we describe the model and briefly discuss the method. Sec. 5.4 is devoted for explaining our numerical results. Finally, we summarize our results and conclude in Sec. 5.5.

5.3 Model and Method

In Fig. 5.1, we present the schematic of our proposed FS set-up in which a part of the quasi one-dimensional (1D) NW is placed in close proximity to a ferromagnet and rest to a bulk superconducting material with broken inversion symmetry. Here ferromagnetism and superconductivity are induced in the NW via the proximity effect. It is assumed that both the strength and the direction of the induced magnetization vector in the NW can be controlled via the bulk ferromagnet [206]. The engineered FS structure is attached to a normal metal lead (not shown). The gate voltages (denoted by G) can tune

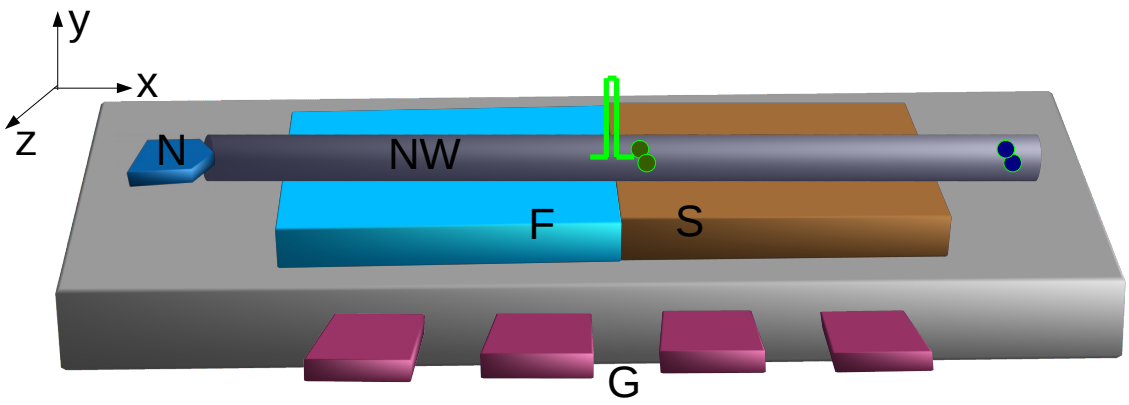

Figure 5.1: Schematic of our FS setup in which a quasi 1D NW (dark gray) is placed in close proximity to a ferromagnet F (light blue, light gray) and a bulk inversion symmetry broken superconductor S (brown, gray). Superconductivity is induced in the NW via the proximity effect. The gates G (maroon, light gray) control the chemical potential in different regions of the NW. A reservoir is attached with ferromagnetic portion of the nanaowire and is denoted by N. A δ-function barrier is symbolically depicted by the light green (light gray) rectangular barrier at the FS interface. Two pair of MZMs are shown by green (light gray) and dark blue (gray) circles at each end of the superconducting part of the NW.

the chemical potential in differnt parts of the NW.

We choose the x-axis along the axis of the NW. The interface of F and S regions of the NW is taken at $x = 0$ for simplicity. We consider an insulating barrier at the FS interface which is modeled by a δ-function potential given as $V(x) = (\hbar^2 k_F/m)Z\delta(x)$ where k_F is the Fermi wave vector in the lead, m denotes electron mass and Z is the dimensionless barrier strength. Chemical potential in F and S regions are μ and $\mu + U$ respectively where U is extra gate potential in the S region to tune the Fermi energy mismatch.

In the superconducting region, which is composed of both singlet and triplet pairing states, the pairing potential $\hat{\Delta}(\mathbf{k})$ (2×2 matrix), in general, can be written as $\hat{\Delta}(\mathbf{k}) = i[\Delta_s(\mathbf{k})\hat{\sigma}_0 + \sum_{j=1}^{3} d_j(\mathbf{k})\hat{\sigma}_j]\hat{\sigma}_2 e^{i\phi}$ [192]. Here, $\hat{\sigma}_{1,2,3}$ are Pauli spin matrices operating on spin space and ϕ is the superconducting phase. Throughout our analysis, we consider only the mean-field value of $\Delta_s(\mathbf{k})$ *i.e.,* $\Delta_s(\mathbf{k}) = \Delta_s$. In contrast, the triplet pairing potential is characterized by an odd vector function as $\mathbf{d}(\mathbf{k}) = -\mathbf{d}(-\mathbf{k})$. Following Burset *et al.* [203], we consider the chiral triplet state of the form, $\mathbf{d}(\mathbf{k}) = \Delta_p \frac{k_x + i\chi k_y}{|\mathbf{k}|}\hat{z} = \Delta_p e^{i\chi\theta}\hat{z}$, where Δ_p is the non-negative amplitude of the triplet pairing potential and $\chi = \pm$ denotes opposite chiralities. Here, χ determines the orientation of the angular momentum of the Cooper pairs and θ represents the relative phase between the singlet and triplet pairing states. The superconducting pairing preserves time reversal symmetry (TRS) either for $\theta = n\pi$ or for $\theta = n\pi/2$, with $n = 0, 1, \ldots$. For 1D case, depending on the value of θ, the Hamiltonian can be categorized to either in class C,

class D, or class DIII, according to the Altland-Zirnbauer symmetry classification [207, 208]. For the case with $\theta = 0$, the Hamiltonian belongs to the nontrivial DIII symmetry class if $\Delta_p > \Delta_s$ [209]. With this simplification, paring potential now takes the form, $\hat{\Delta}(\mathbf{k}) = i[\Delta_s\hat{\sigma}_0 + \Delta_p e^{i\chi\theta}\hat{\sigma}_3]\hat{\sigma}_2 e^{i\phi}$.

The FS junction can be described by the Bogoliubov-deGennes (BdG) equations as, $H(\mathbf{k})\Psi(\mathbf{k}) = \epsilon\Psi(\mathbf{k})$ where the Hamiltonian $H(\mathbf{k})$ can be written as

$$\begin{pmatrix} E(\mathbf{k}) - \tilde{h}\cos\psi & -\tilde{h}\sin\psi\, e^{-i\phi_F} & 0 & \Delta_+ \\ -\tilde{h}\sin\psi\, e^{i\phi_F} & E(\mathbf{k}) + \tilde{h}\cos\psi & -\Delta_- & 0 \\ 0 & \Delta_-^* & -E(-\mathbf{k}) + \tilde{h}\cos\psi & +\tilde{h}\sin\psi\, e^{-i\phi_F} \\ \Delta_+^* & 0 & \tilde{h}\sin\psi\, e^{i\phi_F} & -E(-\mathbf{k}) - \tilde{h}\cos\psi \end{pmatrix}$$

with $E(\mathbf{k}) = k^2/2 - \mu$ and $\Delta_\pm = [\Delta_s \pm \Delta_p e^{i\chi\theta}]e^{i\phi}$.

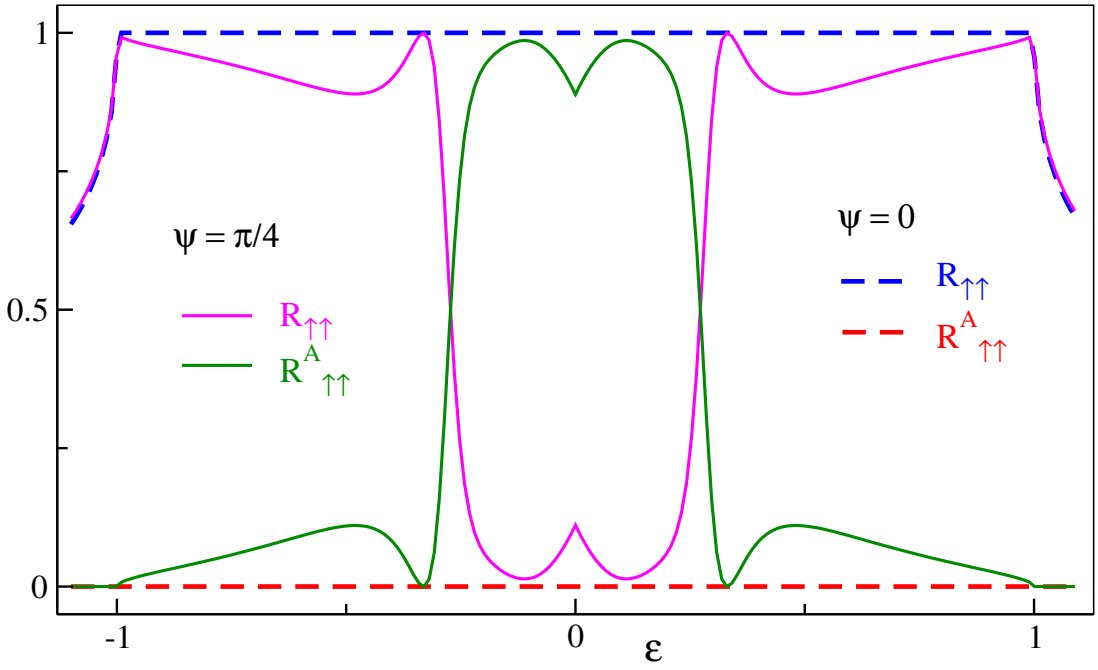

Figure 5.2: The behavior of reflection and SFAR scattering probabilities are shown as a function of incident electron energy (normalized by $(\Delta_p + \Delta_s)$) for two different angle of magnetization ψ of the ferromagnet. The value of the other parameters are chosen as $\tilde{h} = 1$, $\mu = 0$, $\Delta_s = 0$, $\Delta_p = 1$, $Z = 4$ and $U = 15$.

We consider the band energy $E(\pm\mathbf{k})$ of the NW as $E(\pm k_x)$ for a particular choice of k_y in the quasi 1D limit. We assume a situation where the transverse confining potential and the chemical potential in the NW are tuned such that only the lowest sub-band is participating ($k_y = 0$ mode) in transport and hence $\theta = 0$. $\theta \neq 0$ corresponds to different symmetry class. It is assumed that the

band energies for the electrons moving to the left and right are equal to each other. We define right movers by $\theta_+ = \theta$ and left movers by $\theta_- = \pi - \theta$ which reduces to $\theta_+ = 0$ and $\theta_- = \pi$ in our case. The effective pairing potential depends on different spin channels as well as the direction of motion. Right movers with spin $\uparrow$ and $\downarrow$ are effected by the pairing potential $\Delta_+(\theta_+)$ and $-\Delta_-(\theta_+)$ respectively while left movers sense $\Delta_+(\theta_-)$ and $-\Delta_-(\theta_-)$ corresponding to $\uparrow$ and $\downarrow$ spin channels respectively [203, 204].

The magnetization vector in the ferromagnetic region is considered to be

$$\tilde{\mathbf{h}} = \tilde{h}\{\sin\psi\cos\phi_F, \sin\psi\sin\phi_F, \cos\psi\} \tag{5.1}$$

Here, $\tilde{h}$ is the strength of the magnetization vector and ψ, ϕ_F are the polar and azimuthal orientation angle respectively. In the F region ($x < 0$), $\Delta_\pm = 0$. On the other hand, in the superconducting side ($x > 0$), $\tilde{h} = 0$. Wave functions inside the F region are given by

$$\begin{aligned}
\Psi^e_{F\uparrow} &= \{e^{-i\phi_F}\cos\psi/2, \sin\psi/2, 0, 0\}^T, \\
\Psi^e_{F\downarrow} &= \{-e^{-i\phi_F}\sin\psi/2, \cos\psi/2, 0, 0\}^T, \\
\Psi^h_{F\uparrow} &= \{0, 0, e^{i\phi_F}\cos\psi/2, \sin\psi/2\}^T, \\
\Psi^h_{F\downarrow} &= \{0, 0, -e^{i\phi_F}\sin\psi/2, \cos\psi/2\}^T .
\end{aligned} \tag{5.2}$$

For an incoming electron with spin σ, total wavefunction in F region becomes,

$$\Psi_F = \Psi^e_{F\sigma}\, e^{ik^e_{F\sigma}x} + r_{\sigma\sigma}\Psi^e_{F\sigma}\, e^{-ik^e_{F\sigma}x} + r_{\sigma,-\sigma}\Psi^e_{F-\sigma}\, e^{-ik^e_{F-\sigma}x} + r^A_{\sigma\sigma}\Psi^h_{F\sigma}\, e^{ik^h_{F\sigma}x} + r^A_{\sigma-\sigma}\Psi^h_{F-\sigma}\, e^{ik^h_{F-\sigma}x}. \tag{5.3}$$

Here $r^A_{\sigma-\sigma}$ and $r^A_{\sigma\sigma}$ denote the amplitudes for the conventional Andreev reflection (AR) and spin-flip Andreev reflection (SFAR) while $r_{\sigma\sigma}$ and $r_{\sigma-\sigma}$ correspond to the normal and spin flip reflection amplitudes respectively.

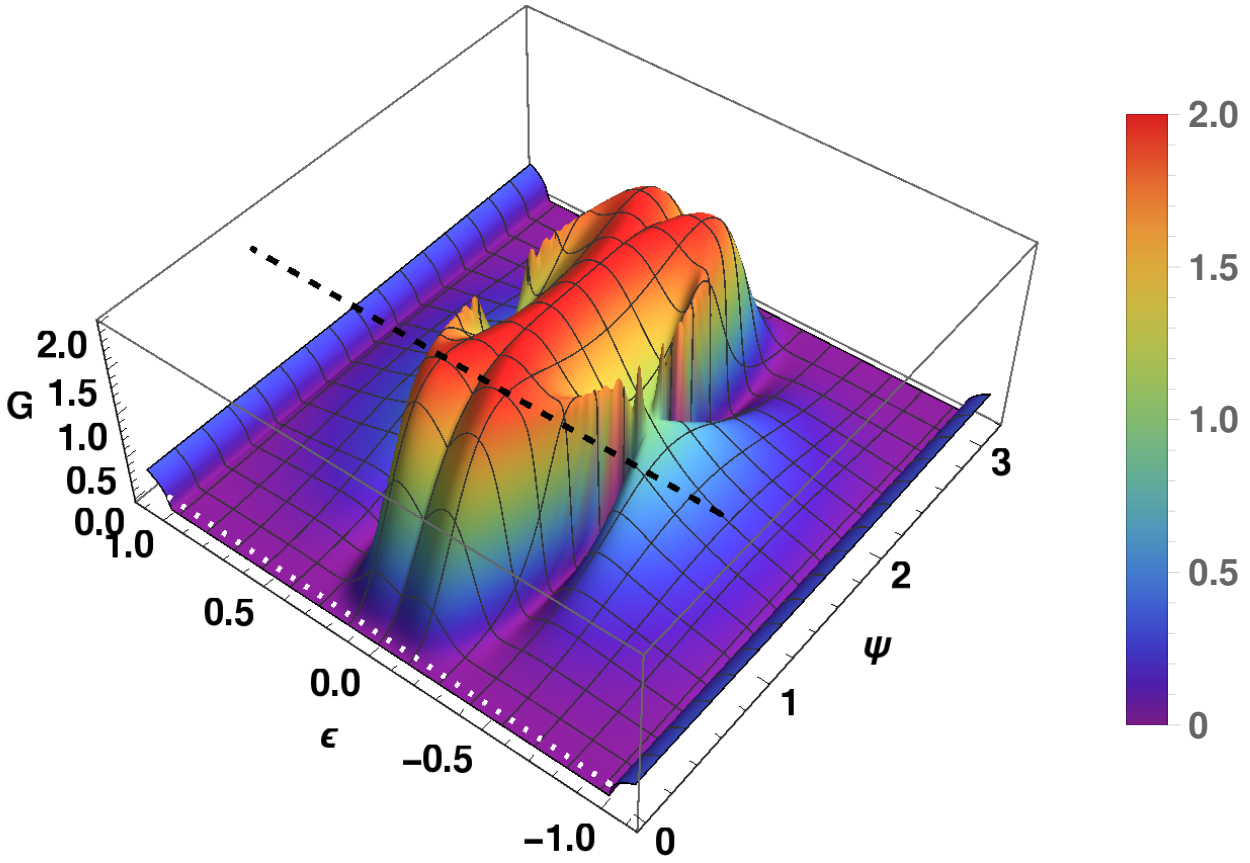

Figure 5.3: The behavior of differential conductance G (in unit of e^2/h) is displayed in the plane of incident electron energy (ϵ) and angle of magnetization (ψ). The values of the other parameters are chosen to be the same as mentioned in Fig. 5.2. Here, black dashed and white dotted lines correspond to the behavior of the same for $\psi = \pi/4$ and $\psi = 0$ respectively *i.e.,* they highlight G for Fig. 5.2.

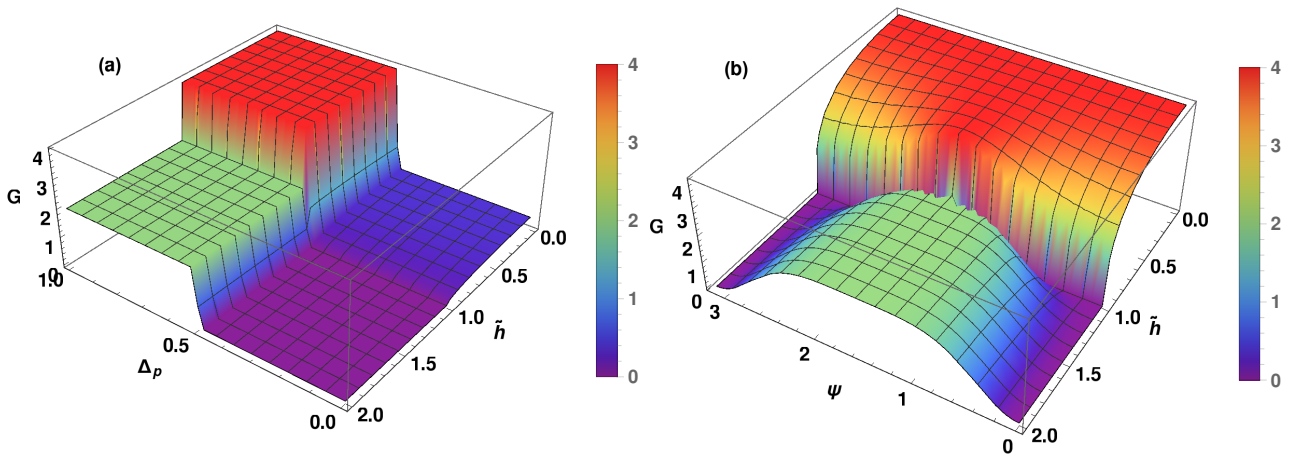

Figure 5.4: The features of differential conductance G (in unit of e^2/h), at $\epsilon = 0$, is demonstrated in $\tilde{h}-\Delta_p$ plane in panel (a) and $\tilde{h}-\psi$ plane in panel (b). We choose the values of the other parameters as $\psi = \pi/2$, $\mu = 1$, $\Delta_s = 1 - \Delta_p$, $Z = 4$, $U = 15$ for panel (a) and $\mu = 1$, $\Delta_s = 0$, $\Delta_p = 1$, $Z = 4$, $U = 15$ for panel (b).

On the other hand, the wave-function inside the S region can be written as,

$$\begin{aligned}\Psi_S &= c_1\, e^{ik^e_{S\uparrow}x}\{u_\uparrow(\theta_+)e^{i\phi_S},0,0,\eta^*_\uparrow(\theta_+)v_\uparrow(\theta_+)\}^T \\ &+c_2\, e^{ik^e_{S\downarrow}x}\{0,u_\downarrow(\theta_+)e^{i\phi_S},\eta^*_\downarrow(\theta_+)v_\downarrow(\theta_+),0\}^T \\ &+d_1\, e^{-ik^h_{S\uparrow}x}\{\eta^*_\uparrow(\theta_-)v_\uparrow(\theta_-),0,0,u_\uparrow(\theta_-)e^{-i\phi_S}\}^T \\ &+d_2\, e^{-ik^h_{S\downarrow}x}\{0,\eta^*_\downarrow(\theta_-)v_\downarrow(\theta_-),u_\downarrow(\theta_-)e^{-i\phi_S},0\}^T\,. \end{aligned} \tag{5.4}$$

with $\eta_\sigma(\theta_\alpha) = s_\sigma\Delta_\sigma(\theta_\alpha)/|\Delta_\sigma(\theta_\alpha)|$, $s_\sigma = (-1)^{\sigma-1}$ where $\sigma = \pm$ denotes the $\uparrow,\downarrow$ spin channels and $\alpha = \pm$ indicates the direction of motion. Momenta inside the F and S regions are given by: $k^{e/h}_{F\sigma} = \sqrt{2(\pm\epsilon+\mu+\sigma h)}$ and $k^{e/h}_{S\sigma} = \sqrt{2(\mu+U)\pm 2\sqrt{\epsilon^2-|\Delta_\sigma|^2}}$ respectively. Electron and hole components of the wave functions are given by

$$u_\sigma(\theta_\alpha) = \frac{1}{\sqrt{2}}\left(1+\frac{\sqrt{\epsilon^2-|\Delta_\sigma(\theta_\alpha)|^2}}{\epsilon}\right) \tag{5.5}$$

$$v_\sigma(\theta_\alpha) = \frac{1}{\sqrt{2}}\left(1-\frac{\sqrt{\epsilon^2-|\Delta_\sigma(\theta_\alpha)|^2}}{\epsilon}\right) \tag{5.6}$$

Now employing the appropriate boundary conditions, we find all the quantum mechanical scattering amplitudes from the FS interface. At zero temperature, following the BTK formalism [61], the differential conductance is given by,

$$G = G_0\sum_{\sigma=\uparrow,\downarrow}(1+R^A_{\sigma,\sigma}+R^A_{\sigma,-\sigma}-R_{\sigma,\sigma}-R_{\sigma,-\sigma}) \tag{5.7}$$

where $G_0 = \frac{2e^2}{h}D(\theta)$ is the normal state conductance and $D(\theta) = 4\cos^2\theta/(Z^2+4\cos^2\theta)$ [203, 204]. Here, $R_{\sigma,\pm\sigma}(R^A_{\sigma,\pm\sigma})$ are the reflection (AR) probability with conserved and flipped spin.

5.4 Results

The behavior of the scattering probabilities are shown in Fig. 5.2 as a function of the energy of the incident electron in the subgapped regime. Here, the ferromagnet part of the NW is effectively in the half-metalic regime as $\tilde{h} \gg \mu$. For simplicity, we have also chosen $\phi_F = 0$ throughout our analysis.

For $\psi = 0$, incoming electron spin is parallel to the $\mathbf{d}$ vector of the superconductor. This configu-

ration hinders the possibility of cooper pairing and therefore only possible process is normal reflection from the FS interface. Hence, the conductance vanishes in the subgapped regime. For $\psi \neq 0$, SFAR probability increases due to the dominance of p-wave pairing in the topological regime ($\Delta_p > \Delta_s$). Note that, the general condition for gap closing is $\Delta_s = \Delta_p \cos\theta$ which reduces to $\Delta_s = \Delta_p$ in our case. On the other hand, for $\psi = \pi/4$, an anti-resonance in SFAR probability is clearly visible in Fig. 5.2 at energy $\epsilon \sim 0.3$ in the topological regime. This anti-resonance can be attributed to an interesting interference between different spin channels when $\psi = \pi/4$. A simple derivation is given in the Appendix E to understand the appearance of the anti-resonance. Furthermore, in this parameter regime for any value of ψ, AR and spin flip reflections are prohibited due to the absence of other spin channel in the half metallic limit.

In Fig. 5.3, we show the behavior of differential conductance G (in unit of e^2/h) in the plane of incident electron energy (ϵ) and polarization angle ψ. We observe that G vanishes when incident electron spin is parallel (anti parallel) to the $\mathbf{d}$ vector *i.e.,* $\psi = 0\,(\psi = \pi)$. This is consistent with the slice of Fig. 5.3, denoted by the white dotted line and also depicted in Fig. 5.2. On the other hand, G reaches at its maximum value $2e^2/h$, at $\epsilon = 0$, when the polarization of the ferromagnet is perpendicular to the $\mathbf{d}$ vector of the superconductor *i.e.,* $\psi = \pm\pi/2$. This occurs as SFAR due to triplet cooper pairing becomes maximum with this orientation. This is indicative of a single MZM contributing resonantly to transport. Note that, a pair of MZMs appear at the two ends of the superconductor in the topological phase and above observation implies that only a specific linear combination of pair of MZMs is allowed to couple resonantly to the F region due to the spin selection rule while the other combination remains decoupled. Such SFAR induced by MZM was earlier studied theoretically [210] and recently confirmed experimentally [211]. Furthermore, when the incident electron energy is comparable to the superconducting gap ($\epsilon \sim 1$), reflection process dominates over AR. Hence, G becomes vanishingly small and independent of ψ as can be seen from Fig. 5.3. We also observe that the conductance peak splits as we move away from $\epsilon = 0$, for a wide range of ψ (see the highlighted black dashed line in Fig. 5.3). The ferromagnetic lead acts like a time-reversal breaking boundary perturbation to the pair of MZMs leading to their hybridization and hence resulting in split peaks.

The features of differential conductance G (in unit of e^2/h), at $\epsilon = 0$, is demonstrated in Fig. 5.4(a) in $\Delta_p - \tilde{h}$ plane for $\psi = \pi/2$. Note that, when $\tilde{h} = 0$ and $\Delta_p > \Delta_s$ (topological regime), G is $4e^2/h$ indicating two MZMs originating from the two different bands [203] contributing resonantly to conductance. On the other hand, when $\tilde{h} > \mu$ *i.e.,* spin polarized regime and $\Delta_p > \Delta_s$, G is

$2e^2/h$ indicating the fact that only one MZM participating in transport. Also, in the regime $\Delta_p > \Delta_s$, G manifests a sharp transition from $4e^2/h$ to $2e^2/h$ with the variation of $\tilde{h}$ *i.e.,* depending on the availibility of the spin channels. At $\epsilon = 0$, transport is being carried out solely by the subgapped MZMs and hence this sharp transition of G indicates the spin selective coupling of MZM to the ferromagnetic lead which is one of the main result of this chapter. Furthermore, in the trivial regime ($\Delta_s > \Delta_p$), singlet cooper pairing is not possible owing to the blockage of one spin channel ($\tilde{h} > \mu$) and as a consequence G vanishes. However, in the regime $\tilde{h} < \mu$, due to the availibility of both spin channels, normal AR gives rise to non-zero G.

The sensitivity of zero energy conductance on polarization angle ψ, in the topological superconducting regime, can be seen from Fig. 5.4(b). When the electron spin is perpendicular to the $\mathbf{d}$ vector *i.e.,* $\psi = \pi/2$, G is $2e^2/h$ for the entire $\tilde{h} > \mu$ regime due spin selective coupling to one MZM. Around $\tilde{h} = \mu$, G starts gradually increasing from $2e^2/h$ and finally reaches $4e^2/h$ for $\tilde{h} = 0$ *i.e.,* both MZMs are resonantly coupled to the lead. With the variation of ψ from $\pi/2$ (towards 0 or π), probability of SFAR decreases and hence G decreases monotonically and becomes zero when $\psi = 0$ and $\tilde{h} > \mu$. Hence, such spin dependent coupling of MZM, in the $\Delta_p > \Delta_s$ regime, explicitly depends on the polarization strength $\tilde{h}$ of the F regime and angle of magnetization ψ.

5.5 Summary and Conclusions

To summarize, in this chapter, we study two terminal differential conductance of a quasi 1D FS junction where the superconductor consists of mixed singlet and triplet pairings. When the superconducting part of the NW becomes topological and $\tilde{h}$ is parallel (anti-parallel) to $\mathbf{d}$ vector ($\psi = 0(\psi = \pi)$), transport is blocked through the junction due to the absence of SFAR. On the other hand, when $\tilde{h}$ is perpendicular to $\mathbf{d}$ ($\psi = \pi/2$) differential conductance splits away from $\epsilon = 0$ due to time-reversal breaking boundary perturbation. Moreover, zero energy conductance spectra exhibits sharp transition from $4e^2/h$ to $2e^2/h$ when $\tilde{h} > \mu$ *i.e.,* , as we move into the polarized regime. Such transition between quantized conductances at zero bias demonstrates an efficient spin dependent coupling to a single MZM from the pair of MZMs, using a ferromagnetic lead.

In systems having proximity induced conventional superconductivity (s wave), to realize MZMs at the two ends of a one-dimensional NW, the required ingredients are spin-orbit coupling in the NW and a magnetic field perpendicular to the spin-orbit field direction. The applied magnetic field and

the chemical potential have to be tuned appropriately to achieve topological phase in the NW [3, 58]. On the other hand, in our setup, we require neither spin-orbit coupling nor a Zeeman gap to achieve topological phase hosting MZMs at each end of the superconducting part of the NW. Essentially, the relative magnitude of the intrinsic spin singlet and triplet pairings of the unconventional superconductor gives rise to the topological phase hosting pair of MZMs at the ends of the superconducting part of the NW. This motivates us to consider an inversion symmetry broken NCS type superconductor with mixed singlet and triplet pairings [191] to study our model. The strength of the Stoner field $\tilde{h}$ in the ferromagnetic probe can be thought of as an efficient way to control time reversal breaking boundary perturbation, which leads to sharp transition of zero-bias differential conductance from the quantized value of $4e^2/h$ to $2e^2/h$ when the Stoner field $\tilde{h}$ in the ferromagnetic and the d vector of the superconductor are kept mutually perpendicular to each other.

As far as practical realization of our model is concerned, a NW may be possible to fabricate in close proximity to a ferromagnet for *e.g.* EuO and NCS superconductor for *e.g.* $\mathrm{Mo_3Al_2C}$, BiPd etc. [194, 195]. To validate our model, the orientation of the $\vec{d}$ vector of the spin-triplet component to be changed according to the direction of transport. Hence, the transport signatures (differential conductance G) must be measured in the plane orthogonal to the axis along which inversion symmetry broken spin-orbit coupling is present.

CHAPTER 6

RKKY Exchange Interaction in 8-Pmmn Borophene

6.1 Chapter Summary

Ruderman-Kittel-Kasuya-Yosida (RKKY) exchange interaction is an indirect exchange coupling between two magnetic impurities being mediated by the conduction electrons of the host material. We have theoretically investigated the indirect signatures of the tilted anisotropic Dirac cones via RKKY exchange interaction in 8-Pmmn borophene. The latter is a two dimensional polymorph of boron atoms. The 8-Pmmn borophene is one of the most recent 2D polymorph of boron atoms, which has been predicted to host tilted Dirac cones where the tilting direction around the Dirac cones are opposite to each other. Unlike the case of isotropic non-tilted Dirac material-graphene, here we have observed that the tilting of the Dirac cones exhibits a significant impact on the RKKY exchange interaction in terms of the suppression of oscillation frequency. The reason can be attributed to the behavior of the Fermi level and the corresponding density of states with respect to the tilting parameter. When the two impurities are located perpendicular to the tilt axis, interference between the Dirac fermions from different valleys do not contribute to the oscillation frequency and the period of oscillation increases as one enhances the value of the tilt parameter. This change of oscillation frequency may be a possible way to indirectly probe the degree of tilting of the Dirac cone present in anisotropic Dirac materials such as 8-Pmmn borophene. On the other hand, for the separation of the two impurities being along the tilt axis, interference among the Dirac cones plays a dominant

role in determining the period of oscillation and the tilt parameter exhibits a negligible effect on the corresponding period. We have derived the direction dependent analytical expressions of the RKKY exchange interaction, in terms of Meijer G-function. Behavior of RKKY exchange interaction is also investigated numerically for two spatially separated magnetic impurities in the $x - y$ plane of the 2D borophene sheet.

6.2 Introduction

With the advent of graphene [212, 7], monolayer materials with similar band structure have been under active consideration from the theoretical and experimental research point of view owing to their future application in nanoelectronics. Along this direction, a thin layer of boron atoms called borophene is the latest addition to the famility of Dirac materials. Having one less electron than carbon, boron's honeycomb structure is unstable. However, it can be stabilized by adding extra boron atoms in the honeycomb lattice. First principle calculations have predicted that depending on the arrangements of the extra boron atoms, various stable monolayer-boron structures, such as α sheet, β sheet, are possible [15, 23, 38]. In recent times, Mannix *et al.* reported a stable striped phase and a metastable homogeneous phase in two-dimensional (2D) boron silver substrate [43] while Feng *et al.* has experimentally confirmed the presence of Dirac fermions in this phase, named β_{12} sheet [2]. The 8-Pmmn borophene is one of the most recent 2D polymorph of boron atoms, which is predicted to host tilted Dirac cones [40]. In the community, it is an interesting question to investigate how to probe this degree of tilting.

The RKKY exchange interaction [213, 214, 215] is an indirect exchange coupling between two magnetic impurities being mediated by the conduction electrons of the host material. Since the RKKY exchange interaction is directly related to the susceptibility of the host material, it can be used as a probe to an electronic system. In recemt times, the physics of RKKY exchange interaction has been widely investigated in a variety of Dirac materials such as graphene [216, 217, 218, 219, 220, 221, 222], silicene [223], phosphorene [224, 225], topological insulator [226, 227, 228, 229], Dirac semimetal [230, 231] etc.

Formally, the magnitude of the RKKY exchange interaction is anticipated to be severely influenced by the position of the Fermi level and the corresponding density of states (DOS) in any host material. In this context, the tilting of the Dirac cone can modify DOS as well as Fermi level [223, 232] near the Dirac point in anisotropic Dirac materials. Hence, the features of the RKKY interaction can carry the signatures of the tilting nature of the Dirac cones. This issue has not been addressed so far to the best of our knowledge.

In this chapter, we explore the consequences of the tilted and anisotropic Dirac cones on the RKKY exchange interaction, considering 8-Pmmn borophene as a host material [233]. We obtain

semi-analytical results of the RKKY exchange interaction for two different spatial separation of the magnetic impurities: two impuries are located perpendicular to the tilt axis and parallel to the tilt axis. For the former case, interference between the Dirac fermions from different valleys do not contribute to the oscillation frequency and the period of oscillation increases as one enhances the value of the tilt parameter. This change of oscillation frequency may be a possible way to probe the degree of tilting of the Dirac cone present in anisotropic Dirac materials such as 8-Pmmn borophene. On the other hand, for the separation of the two impurities being along the tilt axis (along the y axis), interference among the Dirac cones plays a dominant role in determining the period of oscillation and tilting parameter exhibits negligible effect on the corresponding period. We also demonstrate the role of tilted and anistropic Dirac cone on Fermi level which in turn influences the RKKY exchange interaction. Behavior of RKKY exchange interaction is also investigated numerically for two spatially separated magnetic impurities in the x-y plane of the 2D borophene sheet.

The remainder of the chapter is structured as follows. In Sec. 6.3, we describe the model Hamiltonian for our setup and present a brief outline of the Green's function formalism to obtain the RKKY exchange interaction. The behavior of RKKY interaction, as a function of distance between the two magnetic impurities as well as tilting parameter, for different alignements of the impurities is presented in Sec. 6.4. Finally, we summarize our results and conclude in Sec. 6.5.

6.3 Model and Method

We begin with a general low energy two band effective Hamiltonian for 2D Dirac materials associated with anisotropic Dirac cone, which can be written as (near the Dirac points $\mathbf{q} = \pm\mathbf{q_D}$)

$$H_D = \xi(v_x\sigma_x q_x + v_y\sigma_y q_y + v_t\sigma_0 q_y) \,, \tag{6.1}$$

where σ_x, σ_y are the Pauli matrices in the atomic basis and σ_0 is a unit matrix. We have chosen $\hbar = 1$. Here, $\xi = \pm 1$ is the valley index and v_i $(i = x, y)$ corresponds to the velocities along $i^{\rm th}$ direction, while v_t denotes the velocity scale associated with the tilted Dirac cones. Note that the tilting lies along the y-direction. The different velocity parameters are given by $\{v_x, v_y\} = \{0.86, 0.69\}$ and

$v_t = 0.32$ in units of 10^6 m/sec [39, 41]. The above Hamiltonian can be further written as

$$H_D = \xi[v_t\sigma_0 q_y + v_F(\sigma_x\tilde{q}_x + \sigma_y\tilde{q}_y)] \ , \tag{6.2}$$

where $v_F = \sqrt{v_x v_y}$. The new renormalized momentum operators are given by $\tilde{q}_x = \sqrt{\frac{v_x}{v_y}}q_x$ and $\tilde{q}_y = \sqrt{\frac{v_y}{v_x}}q_y$ which satisfy the usual quantum mechanical commutation relation $[\tilde{q}_x, \tilde{q}_y] = 0$ and $[\tilde{x}, \tilde{q}_x] = i$, $[\tilde{y}, \tilde{q}_y] = i$ provided $\tilde{x} = \sqrt{\frac{v_y}{v_x}}x$ and $\tilde{y} = \sqrt{\frac{v_x}{v_y}}y$. The corresponding energy dispersion is given by [42]

$$E(\tilde{q}_x, \tilde{q}_y) = \xi v_t\sqrt{\frac{v_x}{v_y}}\tilde{q}_y + \lambda v_F \mid \tilde{q} \mid \ . \tag{6.3}$$

Here, $\lambda = \pm$ denotes band index. However, as we restrict ourself in the n-doped regime (conduction band), therefore λ is always positive in our analysis. The band structure near the Dirac point $\mathbf{q} = \mathbf{q_D}$ is shown in Fig. 6.1(a). The band dispersion around the other valley $\mathbf{q} = -\mathbf{q_D}$ has opposite chirality *i.e.,* tilting lies along the opposite direction. It is important to note that the tilting breaks particle-hole symmetry in borophene [39, 41].

Before proceeding further, we briefly examine how the tilting of the Dirac cones affects the Fermi energy and density of states (DOS). The Fermi energy (E_F) and DOS ($\rho(E)$) in a material, associated with tilted and anisotropic Dirac cone, depend on the tilting parameter v_t in the following way

$$E_F(v_t) = E_F^{(0)}\Big(1 - \frac{v_t^2}{v_F^2}\Big)^{\frac{3}{2}} \ , \tag{6.4}$$

$$\rho(E, v_t) = \rho^{(0)}(E)\Big(1 - \frac{v_t^2}{v_F^2}\Big)^{-\frac{3}{2}} \ , \tag{6.5}$$

where $E_F^{(0)}$ and $\rho^{(0)}(E)$ are the Fermi level and the DOS of a non-tilted isotropic Dirac material-*i.e.,* graphene, respectively and $v_F = \sqrt{v_x v_y}$ as mentioned earlier. Note that, with the enhancement of the tilting parameter v_t, the Fermi level decreases monotonically. On the other hand, DOS gets enhanced with v_t and the corresponding behavior of that, following the low energy spectrum (Eq.(6.3)), is shown as a function of energy in Fig. 6.1(b). At the Dirac point, $\rho(E)$ vanishes and increases linearly with energy similar to graphene [234, 235]. Impact of these phenomena on the period of oscillation of RKKY exchange interaction is explained in the next section.

Now we briefly discuss the theoretical formalism for investigating the RKKY exchange interaction in 2D electronic system. We consider two magnetic impurities (localized spins) at two different lattice

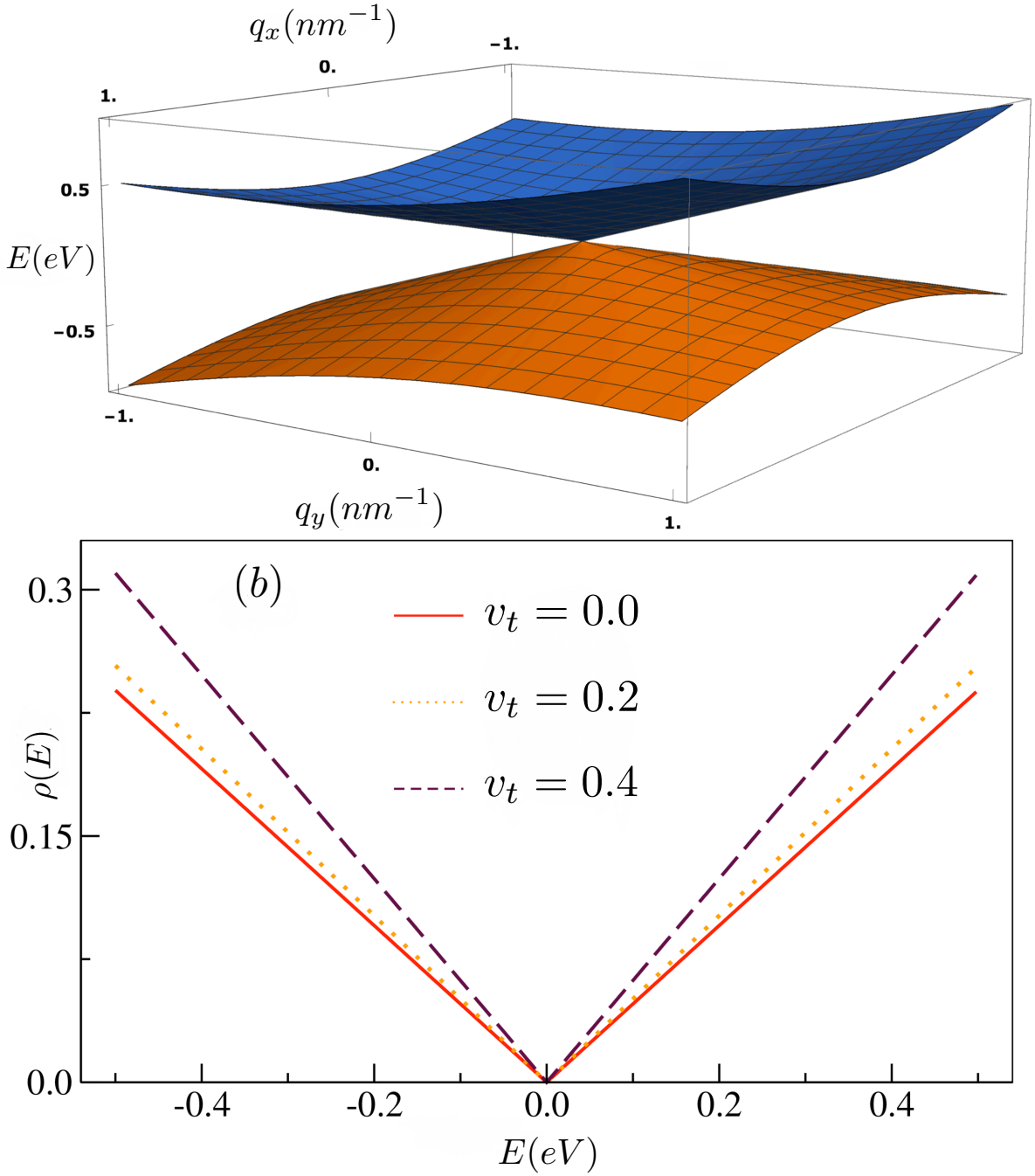

Figure 6.1: (a) A tilted, anisotropic Dirac cone of 8-Pmmn borophene, in the vicinity of Dirac point $\mathbf{k_D}$, is shown in the q_x-q_y plane. (b) The behavior of DOS (in arbitrary unit) is demonstrated near the Dirac point for different values of the tilt parameter v_t.

sites of the bulk 2D borophene sheet. The interaction term between the localized spins ($\mathbf{S}_i$) and the conduction electron spins ($\mathbf{s}_i$) is given by the Kondo Hamiltonian

$$H_{int} = J(\mathbf{S_1} \cdot \mathbf{s_1} + \mathbf{S_2} \cdot \mathbf{s_2}) \,, \tag{6.6}$$

where J is the bare exchange coupling strength. The microscopic origin of such model renders to Anderson impurity model [236, 237]. Using second order perturbation theory, the exchange interaction energy between the two localized spins can be written in the Heisenberg form as

$$E(\mathbf{r}) = J_{\alpha\beta}(\mathbf{r})\mathbf{S_1} \cdot \mathbf{S_2} \,, \tag{6.7}$$

where α, β indicate the atomic indices and $\mathbf{r}$ is the distance between the two impurities. Thus, the RKKY exchange interaction strength $J_{\alpha\beta}(\mathbf{r})$ is given by

$$J_{\alpha\beta}(\mathbf{r}) = \frac{J^2\hbar^2}{4}\chi_{\alpha\beta}(0, \mathbf{r}) \,. \tag{6.8}$$

where $\chi_{\alpha\beta}(0, \mathbf{r})$ is the susceptibility.

For a spin-degenerate system, susceptibility can be written in terms of the unperturbed retarded Green's functions as [221]

$$\chi(r_1, r_2) = -\frac{2}{\pi}\int_{-\infty}^{E_F} dE \, \mathrm{Im}[G^{(0)}_{\alpha\beta}(r_1, r_2, E)G^{(0)}_{\beta\alpha}(r_2, r_1, E)] \,, \tag{6.9}$$

To compute the susceptibility, which is directly proportional to RKKY exchange intercation, we need to evaluate the zeroth-order real space Green's functions. Since in the large distance, contribution to χ arises mainly from small momenta, one can extend the momentum cutoff to ∞ to obtain the real space Green's functions via the Fourier transform. We compute them in the linear band approximation and obtain

$$\begin{aligned} G^{(0)}_{\alpha\beta}(\mathbf{R}, 0, E) &= \frac{1}{\Omega_{BZ}}\int d^2\mathbf{k} \, e^{i\mathbf{k}\cdot\mathbf{R}} G^{(0)}_{\alpha\beta}(\mathbf{k}, E) \\ &= \frac{1}{\Omega_{BZ}}\int d^2\tilde{\mathbf{q}} \, e^{i\tilde{\mathbf{q}}\cdot\mathbf{R}}[e^{i\mathbf{K}\cdot\mathbf{R}} G^{(0)}_{\alpha\beta}(\tilde{\mathbf{q}} + \mathbf{K}, E) \\ &+ e^{i\mathbf{K'}\cdot\mathbf{R}} G^{(0)}_{\alpha\beta}(\tilde{\mathbf{q}} + \mathbf{K'}, E)] \,, \end{aligned} \tag{6.10}$$

where the integration is performed over the entire Brillouin zone Ω_{BZ}. Here, $\tilde{\mathbf{q}} = (\tilde{q}_x, \tilde{q}_y)$ is small momentum in the vicinity of the Dirac points, where the linear Dirac spectrum is valid. As $d\tilde{q}_x d\tilde{q}_y = dq_x dq_y$, we can replace $\tilde{q}$ by q without loss of generality.

We have also used the notation (x, y) in place of $(\tilde{x}, \tilde{y})$. The factor $\sqrt{\frac{v_x}{v_y}}$ in Eq.(6.3) has now been included in the tilting parameter v_t for simplicity. The unperturbed momentum space Green's function is given by,

$$\begin{aligned} G^{(0)}_{\alpha\beta}(\mathbf{k}, E) &= (E + i\eta - H_D)^{-1} \\ &= \frac{1}{D}\begin{bmatrix} E + i\eta - \xi v_t q_y & (q_x - iq_y)v_F \\ (q_x + iq_y)v_F & E + i\eta - \xi v_t q_y \end{bmatrix}, \end{aligned} \tag{6.11}$$

with $D = (E + i\eta - \xi v_t q_y)^2 - v_F^2 q^2$, $v_F = \sqrt{v_x v_y}$. Here, $\xi = \pm 1$ indicates the two Dirac points $\mathbf{K}$ and $\mathbf{K}'$.

6.4 Results

In this section we present our analytical as well as numerical results for different locations of the two magnetic impurities inside the bulk of the 2D borophene sheet. In general, it is a formidable task to obtain the analytical expressions for the susceptibility when the two impurities are arbitrarily located in the x-y plane. However, we manage to obtain the analytical form of RKKY exchange interaction for the two special cases: (A) when the two impurities are located perpendicular to the tilt axis and (B) parallel to the tilt axis. The schematic of the orientation of the impurities in the borophene lattice are shown in Fig.(6.2) . Here, we clarify our notations used for our analysis: χ_{11} denotes the susceptibility for the impurities being on same type of atoms and χ_{12} for the different types of atoms (one on ridge atom and the other on inner atom (see Fig. 6.2)). It is worthwhile to mention that when the impurities are on different atoms, they cannot be exactly along x or y axis. However, such small off-axis deviation along the tilt axis (y axis) or perpendicular to it (x axis), does not change our results qualitatively, in the continum limit.

Note that, RKKY exchange interaction strength is directly proportional to the susceptibility (see Eq.(6.8)). Hence, we express the susceptibility as a measure of RKKY interaction strength in units of $J^2\hbar^2/4$. Also, we normalize the distance between the two magnetic impurities by corresponding

lattice parameters *i.e.*, $R_x/a \to R_x$ and $R_y/b \to R_y$.

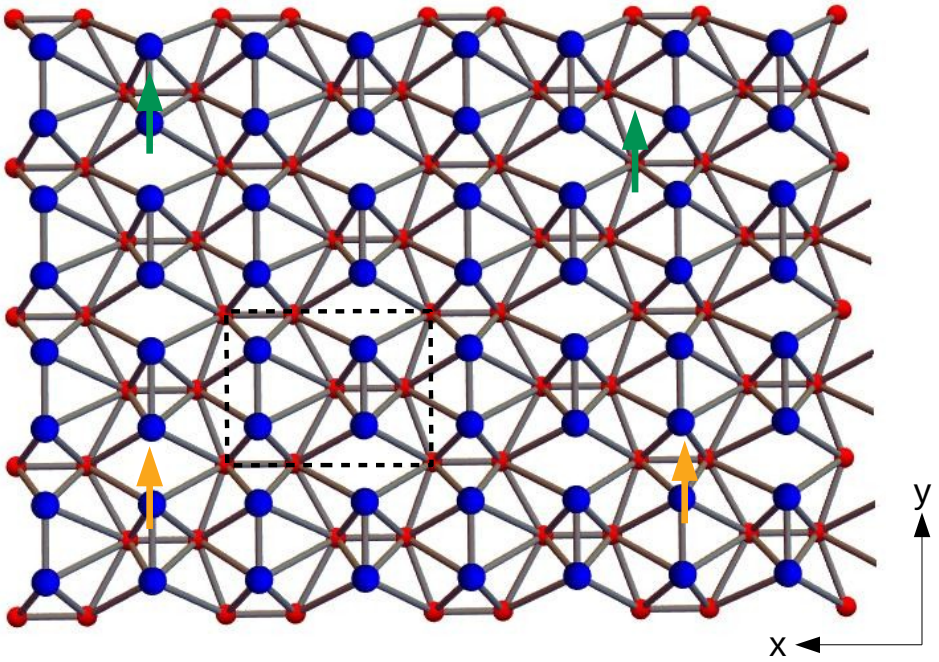

Figure 6.2: Schematic of the lattice structure of 8-Pmmn borophene. Big blue (dark gray) circles and small red (light gray) circles distinct two types of nonequivalent atoms B_R (ridge atom) and B_I (inner atom) respectively. The unit cell, comprising of 8 atoms, is shown by dashed black rectangle. Magnetic impurities are schematically shown by golden (light gray) and dark green (dark gray) arrows. Bottom (golden) arrows are aligned perpendicular to the tilt axis (x axis) while the left arrows (golden and dark green) are located along the tilt axis (y axis) inside the 2D sheet.

6.4.1 Impurities are located perpendicular to the tilt axis

When the two magnetic impurities reside perpendicular to the tilt axis (on the same atoms) of bulk borophene, the integral in Eq.(6.10) can be computed analytically for $R_y = 0$. This configuration has been indicated by golden arrows in Fig. 6.2. In this case, the zeroth-order real space Green's function reads as

$$\begin{aligned} & G_{11}^{(0)}(R_x, 0, E) \\ = \; & \frac{1}{\Omega_{BZ}} \int dq_x \, dq_y \frac{(E + i\eta - v_t q_y \xi) e^{iq_x R_x}}{(E + i\eta - v_t q_y \xi)^2 - v_F^2 (q_x^2 + q_y^2)} \\ = \; & \frac{-2\pi E}{v_F} \frac{(v_F^2 - 2v_t^2)}{(v_F^2 - v_t^2)^{\frac{3}{2}}} K_0(-i\tilde{\alpha}) (e^{i\mathbf{K}\cdot\mathbf{R}} + e^{i\mathbf{K}'\cdot\mathbf{R}}) \, , \end{aligned} \tag{6.12}$$

with $\tilde{\alpha} = ER_x/\sqrt{v_F^2 - v_t^2}$. Here, $K_0(x)$ are the modified Bessel function of first kind. In Ap-

pendix F, we provide the results of some standard integrals involving Bessel function which have been used throughout the calculation. Expressing the modified Bessel function in terms of Bessel and Neumann function, we obtain

$$\begin{aligned}\mathrm{Im}[\mathrm{G}_{11}^{(0)}(R_x,0,E)G_{11}^{(0)}(0,R_x,E)] &= \frac{4\pi^2E^2}{\Omega_{BZ}^2}\frac{v_F^2}{(v_F^2-v_t^2)^3}\\ \times\mathrm{Im}[(K_0(-i\tilde{\alpha}))]^2(2+2\cos\{(K_x-K_x^{'})R_x\})\ .&\end{aligned} \tag{6.13}$$

Henceforth, following the works of Saremi [216] and Sherafati *et al.* [220, 221], we separate the integration limit : $\int_{-\infty}^{E_F} = \int_{-\infty}^{0} + \int_{0}^{E_F}$. The first integral indicates the valence electrons (undoped case) and the second one is for the conduction electrons. While the latter integral involves Meijer G-function, former one does not converge. Following the standard procedure given in Ref. [216, 221], the integrand can be multiplied by a cutoff function $f(\tilde{\alpha},\tilde{\alpha}_0)$=$\exp(-\tilde{\alpha}/\tilde{\alpha}_0)$. Then one can perform the integral and takes limit $\tilde{\alpha}_0\to\infty$ at the end so that $f(\tilde{\alpha},\tilde{\alpha}_0)\to 1$. Thus, we arrive at the following form of the susceptibility:

$$\begin{aligned}\chi_{11} &= \frac{1}{\pi R_x^3}\frac{v_F^2}{(v_F^2-v_t^2)^{\frac{3}{2}}}[1+\cos\{(K_x-K_x^{\prime})R_x\}]\\ &\times\left[\frac{1}{16}-\frac{k_F^{'}R_x}{2\sqrt{\pi}}M(k_F^{'}R_x)\right],\end{aligned} \tag{6.14}$$

where, $k_F^{'} = E_F/\sqrt{v_F^2-v_t^2}$ and $M(k_F^{'}R_x)$=$G_{1,3}^{2,0}\left(\begin{smallmatrix}\frac{3}{2}\\ 1,1,1,-\frac{1}{2}\end{smallmatrix}\middle|\, {k_F^{'}}^2R_x^2\right)$ is the Meijer G-function. We have considered the first Brillouin zone area as $\Omega = 4\pi^2/ab$. Tilted anisotropic Dirac points are at $\vec{q}_D = (0,q_D)$ and $-\vec{q}_D$, $q_D = 0.29\times\frac{2\pi}{b}$ [41]. It is interesting to note that in case of borophene, the oscillatory factor $[1+\cos\{(K_x-K_x^{\prime})R_x\}] = 2$. Hence, the interference terms between the two Dirac points do not contribute to the RKKY exchange interaction which is evident from Eq.(6.14).

In Fig. 6.3, we demonstrate the behavior of susceptibility χ_{11} (when impurities are on the same atom) as a function of the distance R_x between the two magnetic impurities and tilt parameter v_t. The change in the periodicity of χ_{11}, with the enhancement of tilting parameter v_t, is evident from Fig. 6.3(a).

This feature can be understood from Eq.(6.14) in which the Meijer G-function is the entire source of the oscillation. As the period of oscillation is inversly proportional to the argument $k_F^{\prime}R_x$, it scales with v_t as $\tau(v_t) = \tau(0)/(1-x^2)$, where $x = v_t/v_F$ and $\tau(0)$ is the period of non-tilted and

isotropic Dirac cone *i.e.,* graphene. As the tilting parameter increases, period of oscillation increases monotonically. In the $v_t \to 0$ limit, $\tau(v_t)$ comes back to the untilted period $\tau(v_t = 0)$ as expected. On the other hand, for $v_t \to v_F$, the period diverges indicating flatness of exchange interaction. Hence, the internal band structure itself influences the RKKY exchange (Friedel oscillation) due to tilting and may be a way to probe the degree of tilting in anisotropic 2D Dirac materials. This is also one of the main results of this chapter.

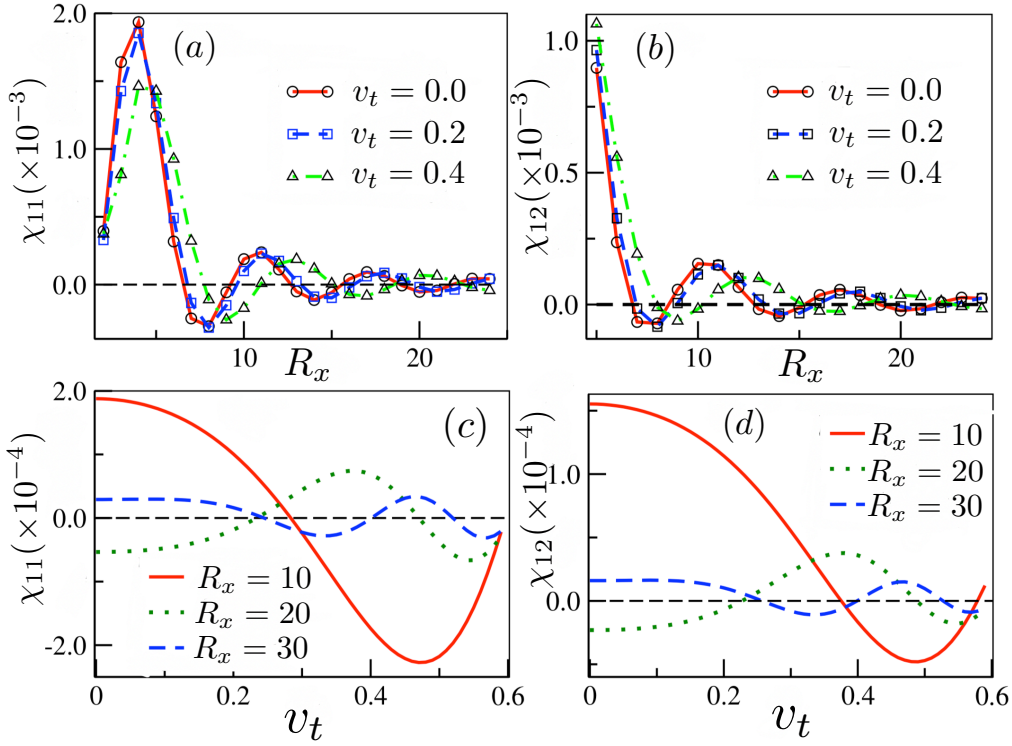

Figure 6.3: The behavior of the suscepibilities χ_{11} and χ_{12} is shown as a function of R_x in panels (a) and (b), and as a function of v_t in panels (c) and (d) respectively. We choose the other parameters as $v_F = 1.0$, $R_y = 0$, $E_F^{(0)} = 0.5$. Black dashed line indicates the null susceptibility.

We also observe that there is a reduction in the amplitude of χ_{11} as v_t increases (see Fig. 6.3(a)). The reason can be attributed to the presence of vanishingly small density of states near the Dirac point and lowering of Fermi level with the rise of tilting parameter v_t. Furthermore, we explore the long distance and very short distance limit of RKKY exchange interaction which can be figured out from the asympototic behavior of Meijer G-function. Using the standard tables [238, 239] and following Ref. [221], we obtain

$$\lim_{y\to 0} M(y) = \frac{4y^2[1 - 3\gamma - 3\ln(y/2)]}{9\sqrt{\pi}}, \tag{6.15}$$

$$\lim_{y\to \infty} M(y) = \frac{[2\cos(2y) + 8y\sin(2y) - \pi]}{8\sqrt{\pi}y}, \tag{6.16}$$

where $\gamma \approx 0.577$ is the Euler-Mascheroni constant. Therefore, we obtain the following form of the RKKY exchange interation in the long distance limit ($k_F^{'} R_x \gg 1$) as

$$\begin{aligned} \lim_{k_F^{'} R_x \to \infty} \chi_{11}(R_x) &= \frac{\chi_{11}^L}{R_x^3}[\pi - \cos(2k_F^{'} R_x) \\ &\quad -4k_F^{'} R_x \sin(2k_F^{'} R_x)] \,, \end{aligned} \tag{6.17}$$

where $\chi_{11}^L = v_F^2/8\pi^2(v_F^2 - v_t^2)^{3/2}$. On the other hand, our analytical results for the short distance limit ($k_F^{'} R_x \ll 1$) reads

$$\begin{aligned} \lim_{k_F^{'} R_x \to 0} \chi_{11}(R_x) &= \frac{\chi_{11}^S}{R_x^3}\Bigg[1 - \frac{32(k_F^{'} R_x)^3}{9\pi} \\ &\quad (1 - 3\gamma - 3\ln(k_F^{'} R_x/2))\Bigg] \,. \end{aligned} \tag{6.18}$$

where $\chi_{11}^S = v_F^2/16\pi(v_F^2 - v_t^2)^{\frac{3}{2}}$.

Here we present the results for the magnetic impurities located on different atoms. One can obtain the Green's function extending the momentum cutoff to ∞ as

$$\begin{aligned} & G_{12}^{(0)}(R_x, 0, E) \\ = \; & \frac{1}{\Omega_{BZ}} \int dq_x \, dq_y \frac{(q_x - iq_y)e^{iq_x R_x}}{(E + i\eta - v_t q_y \xi)^2 - v_F^2(q_x^2 + q_y^2)} \\ = \; & -\frac{2\pi E}{\Omega_{BZ}(v_F^2 - 2v_t^2)} K_1(-i\tilde{\alpha})(e^{i\mathbf{K}\cdot\mathbf{R}} + e^{i\mathbf{K'}\cdot\mathbf{R}}) \\ & -\frac{2i\xi v_t \pi E}{\Omega_{BZ}(v_F^2 - 2v_t^2)^{\frac{3}{2}}} K_0(-i\tilde{\alpha})(e^{i\mathbf{K}\cdot\mathbf{R}} - e^{i\mathbf{K'}\cdot\mathbf{R}}) \end{aligned} \tag{6.19}$$

Similar to χ_{11}, the integrand is multiplied by a cutoff function to evaluate the energy integral of the valence electrons. Finally we obtain

$$\begin{aligned} \chi_{12} = - \; & \frac{1}{2\pi R_x^3 \sqrt{v_F^2 - v_t^2}} \left(-\frac{3}{16} - \frac{k_F^{'} R_x}{2\sqrt{\pi}} \tilde{M}(k_F^{'} R_x) \right) \\ & \times [1 + \cos\{(K_x - K_x')R_x\}] \\ - \; & \frac{v_t^2}{2\pi R_x^3 (v_F^2 - v_t^2)^{\frac{3}{2}}} \left(\frac{1}{16} - \frac{k_F^{'} R_x}{2\sqrt{\pi}} M(k_F^{'} R_x) \right) \\ & \times [1 - \cos\{K_x - K_x')R_x\}] \,, \end{aligned} \tag{6.20}$$

where $\tilde{M}(k_F^{'}R_x) = G_{2,4}^{2,1}\left(\begin{smallmatrix}\frac{1}{2},\frac{3}{2}\\ 1,2,0,-\frac{1}{2}\end{smallmatrix}\middle| {k_F^{'}}^2 R_x^2\right)$. In Eq.(6.20), the second term vanishes for borophene ($K_x = K_x^{'} = 0$), while in the first term, again the interference between the anisotropic Dirac cones does not contribute to the RKKY oscillations. Note that, both χ_{11} and χ_{12} recover the similar form of graphene [221, 220] in the limit : $v_t = 0$, $v_x = v_y = v_F$.

Behavior of χ_{12}, as a function of R_x and v_t, is depicted in Fig. 6.3(b). Here also the period of oscillation increases with the increment of v_t, similar to χ_{11}. This feature can be understood from Eq.(6.20) where the argument of Meijer G-function is proportional to v_t. We also explore the long distance ($k_F^{'}R_x \gg 1$) and short distance ($k_F^{'}R_x \ll 1$) limit of χ_{12} employing asymptotic behavior of Meijer G-function. We find,

$$\lim_{y\to 0}\tilde{M}(y) = \frac{2y^2}{3\sqrt{\pi}}\,, \tag{6.21}$$

$$\lim_{y\to \infty}\tilde{M}(y) = \frac{[3\pi - 10\cos(2y) - 8y\sin(2y)]}{8\sqrt{\pi}y}\,. \tag{6.22}$$

Employing the above limits, we obtain the following analytical forms of RKKY exchange interaction as

$$\lim_{k_F^{'}R_x\to\infty}\chi_{12}(R_x) = \frac{\chi_{12}^L}{R_x^3}[3\pi - 5\cos(2k_F^{'}R_x) - 4k_F^{'}R_x\sin(2k_F^{'}R_x)]\,, \tag{6.23}$$

$$\lim_{k_F^{'}R_x\to 0}\chi_{12}(R_x) = \frac{\chi_{12}^S}{R_x^3}\left[1 + \frac{16(k_F^{'}R_x)^3}{9\pi}\right]\,, \tag{6.24}$$

with $\chi_{12}^L = 1/8\pi^2\sqrt{v_F^2 - v_t^2}$ and $\chi_{12}^S = 3/16\pi\sqrt{v_F^2 - v_t^2}$.

The oscillatory behavior of χ_{11} and χ_{12} as a function of v_t is clearly visible from Figs. 6.3[(c)-(d)]. They exhibit similar features for χ_{11} and χ_{12} with the variation of v_t as in both cases the period of oscillation depends on the tilting parameter. It is evident that due to R_x^{-3} dependency (see Eq.(6.14) and Eq.(6.20)), amplitude of both χ_{11} and χ_{12} become vanishingly small as one gradually enhances the distance between the two magnetic impurities.

It is important to note that, even without the tilting parameter, the Fermi surface is anisotropic due to the anisotropy in Fermi velocities ($v_x \neq v_y$). Effect of this anisotropy, in the absence of tilting ($v_t = 0$), on RKKY exchange interaction is presented in Fig. 6.4. It is evident that the effect of such simple anisotropic Fermi surface on susceptibility (χ_{11} and χ_{12}) is negligibly small. This may be a

possible way to distinguish between these two kind of anisotropies ($v_t = 0$ and $v_t \neq 0$) by measuring the RKKY interaction.

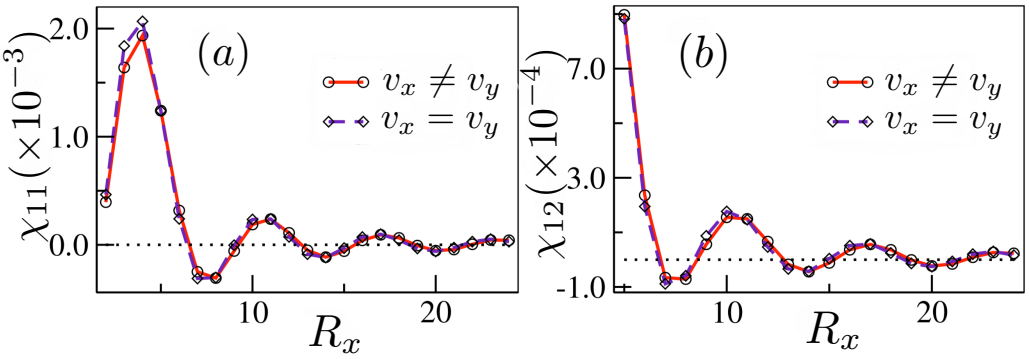

Figure 6.4: The behavior of the suscepibilities χ_{11} and χ_{12} are illustrated as a function of R_x with $v_t = 0$ for both anisotropic Fermi velocities and isotropic counterpart in panel (a) and (b) respectively. The value of the other parameters are chosen as $R_y = 0$, $E_F^{(0)} = 0.5$.

6.4.2 Impurities are aligned parallel to the tilt axis

Here, we present the analytical form of the susceptibility in the limit $R_x \to 0$ *i.e.,* when the two magnetic impurities are situated along the tilt axis. This has been illustrated by golden and dark green arrows in Fig. 6.2. We proceed in the similar way as in the previous subsection and obtain

$$\begin{aligned}\chi_{11} &= -\frac{1}{\pi R_y^3 v_F}\int_{-\infty}^{z_F} dz z^2 \Bigg[-\cos\left(K_y R_y - \frac{v_t}{v_F} z\right)^2 J_0(z) Y_0(z) \\ &\quad + \frac{v_t^2}{v_F^2}\sin\left(K_y R_y - \frac{v_t}{v_F} z\right)^2 J_1(z) Y_1(z)\Bigg], \end{aligned} \tag{6.25}$$

where, $z = E v_F R_y/(v_F^2 - v_t^2)$ and $z_F = E_F v_F R_y/(v_F^2 - v_t^2)$.

$$\begin{aligned}\chi_{12} &= -\frac{1}{\pi R_y^3 v_F}\int_{-\infty}^{z_F} dz z^2 \Bigg[\cos\left(K_y R_y - \frac{v_t}{v_F} z\right)^2 J_1(z) Y_1(z) \\ &\quad - \frac{v_t^2}{v_F^2}\sin\left(K_y R_y - \frac{v_t}{v_F} z\right)^2 J_0(z) Y_0(z)\Bigg]. \end{aligned} \tag{6.26}$$

The explicit analytical form of both χ_{11} and χ_{12}, after performing the integration over energy, are very messy and not possible to write in a compact form. Rather, we present our results for them in Fig. 6.5 both as a function of R_y and v_t. We note that Fig. 6.5(a) is almost identical to Fig. 6.5(b) and Fig. 6.5(c) is to Fig. 6.5(d). This feature can be attributed to the fact that the Hamiltonian is written

in two atomic basis (two sublattice indices) of borophene (tilted Graphene), which do not couple directly to the magnetic moments. Such feature is in complete contrast to the case of topological insulator [226, 228] in which the actual spin degree of freedom of the surface states directly couples to the impurity spin moment.

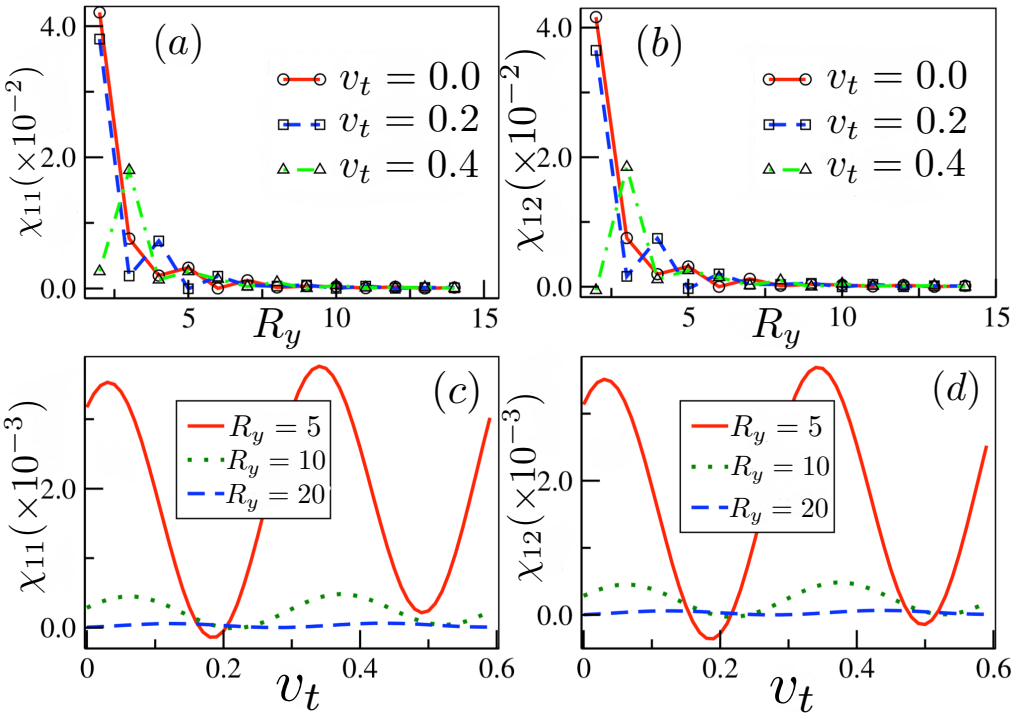

Figure 6.5: The behavior of the suscepibilities χ_{11} and χ_{12} is illustrated as a function of R_y in panels (a) and (b), and as a function of v_t in panels (c) and (d) respectively. The value of the other parameters are chosen as $v_F = 1.0$, $R_x = 0$, $E_F^{(0)} = 0.5$.

We observe that the period of oscillation is almost constant with v_t, as can be seen from Fig 6.5(c). In this particular limit of $R_x \to 0$, the interference among the Dirac fermions from different Dirac points in the Brillouin zone plays a crucial rule in determining the oscillatory nature of RKKY exchange interaction. From Eqs.[(6.25)-(6.26)], one can note that the period of oscillation depends both on K_y and v_t. As the tilting angles (velocity) lie in opposite directions for the two Dirac points $\mathbf{K}$ and $\mathbf{K}'$, the effect of tilting on RKKY exchange interaction, nullifies each other due to destructive interference. Hence, the period of oscillation does not vary with the enhancement of v_t. The latter behavior indicates that the interference between the anisotropic Dirac cones dominates over the effect of Fermi level in determining the overall period of oscillation. Nevertheless, the amplitude of RKKY oscillation decreases with the degree of tilting v_t due to the lowering of the Fermi level (see Eq.(6.5)). Although DOS increases with the tilting parameter, however near the Dirac points DOS is negligbly small and hence it contributes negligibly in determining the amplitude of oscillation, especially in the

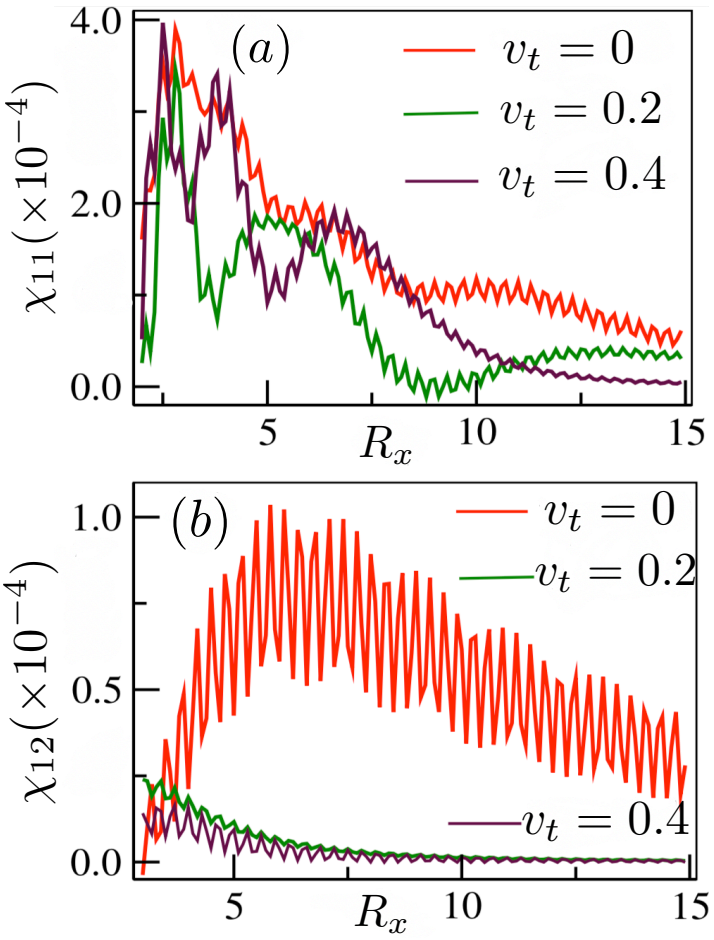

Figure 6.6: The behavior of the susceptibilities χ_{11} and χ_{12} are depicted as a function of R_x in panels (a) and (b) respectively. The value of the other parameters are chosen as $v_F = 1.0$, $E_F^{(0)} = 0.5$, $R_y = 5$ in panel (a) and $R_y = 2$ in panel (b).

long distance limit where only small momenta are important. The presence of interfence among the Dirac points enhances the oscillation frequency of both χ_{11} and χ_{12} compared to the previous case (see Figs. 6.3[(a)-(b)]). Also, the oscillatory behavior of RKKY exchange with enhanced frequency as a function of v_t, is clearly visible from Fig. 6.5(c) and Fig. 6.5(d).

6.4.3 Impurities are located in the x-y plane

In this subsection, we present our numerical results when the two magnetic impurities are placed at arbitrary positions in the x-y plane of the bulk 2D borophene sheet *i.e.*, $R_x \neq 0$ and $R_y \neq 0$. In this case, it is not possible to obtain any kind of analytical form of the susceptibility. Hence, we compute the real space Green's function by numerically integrating over momenta and energy degrees of freedom. The corresponding results for χ_{11} and χ_{12} are illustrated as a function of R_x for different values of the tilting parameter v_t with $R_y = 5$ in Fig. 6.6(a) and $R_y = 2$ in Fig. 6.6(b) respectively. It is apparent from Fig. 6.6(a) (when two magnetic impurities are placed on same atoms in the x-y

plane) that the oscillations appear very rapidly as a function of R_x and manifest weak dependence on the values of v_t. These high frequency rapid oscillations emerge due to the interference between the two Dirac cones. This has been reported earlier for other 2D Dirac systems [218, 220, 224]. The competition between the enhancement of DOS and reduction of Fermi energy with tilting parameter (see Eq.(6.5)), for arbitrarily placed impurities, results in the non-monotonic variation of amplitude of oscillation as a function of v_t in the short and intermediate distance scale. This feature can be seen from Fig. 6.6(a). However for large distance between the two impurities, only small momenta contribute to the RKKY exchange interaction and hence lowering of the Fermi level controls the amplitude, resulting in monotonic decrease of χ_{11} with tilting.

The behavior of the spin density oscillations, for two magnetic impurities placed on different atomic sites in the x-y plane, is shown in Fig. 6.6(b) choosing $R_y = 2$. There is one notable difference between Fig 6.6(a) and Fig. 6.6(b) is that in Fig 6.6(a), the oscillatory behavior associated with an envelope of the amplitude is prominent while in Fig. 6.6(b) the period is larger. As the period of oscillation is inversely proportional to the distance, for very small distance, envelope of amplitude of the RKKY exchange interaction decays (period becomes large) while the oscillations are prominent for larger distances. Moreover, for the small separation of the impurities, χ_{12} exhibits non monotonic behavior with v_t. On the other hand, for large distance ($R_x > 5$) χ_{12} decreases monotonically with the tilting parameter v_t which can again be attributed to the effect of tilting on the Fermi level and DOS.

6.5 Summary and Conclusions

To summarize, in this chapter, we have explored the effect of the tilted and anisotropic Dirac cones on the RKKY exchange interaction in the bulk of a 8-Pmmn borophene. We observe that the tilting of the Dirac cones, for specific orientation of the impurities, manifests itself with the significant reduction in the RKKY exchange interaction oscillation frequency. This feature can be an indirect signature of the degree of tilting present in tilted and anisotropic Dirac cone. We present our analytical expressions for the susceptibility, in terms of Meijer G-function, which is directly proportional to the exchange interaction strength. We consider two special cases: when two magnetic impurities are located perpendicular to the tilt axis (x axis) and along the tilt axis (y axis). In the former case, interference between the Dirac cones does not contribute to the Friedel oscillations and the period of oscillation

increases with tilting parameter. In contrast, for the impurities being along the tilt axis, interference among the Dirac cones plays the dominant role in determining the period of oscillation while the tilting parameter exhibits negligible contribution. Moreover, due to opposite orientation of tilting of the Dirac cones at the inequivalent Dirac points, the effect of tilting originating from each Dirac point on RKKY exchange interaction nullifies each other when the impurities reside along the tilt axis. However, the amplitude of oscillation decreases with the tilting parameter because of lowering of the Fermi level. We also separate out the effect of simple anisotropy ($v_x \neq v_y$) on RKKY exchange interaction in absence of tilting ($v_t = 0$) and show that such anisotropy in Fermi surface exhibits negligible effect on the response function in case of borophene. For arbitrarily placed magnetic impurities in the x-y plane (neither along nor perpendicular to the tilt axis), we evaluate our results numerically and show rapid oscillations (beating pattern) in susceptibility due to the interference between the two Dirac cones and subdominant effects arising from the tilt parameter.

As far as practical realization of our results are concerned, it may be possible to deposit magnetic adatoms such as Co or Fe on bulk borophene to study RKKY exchange interaction in it. However, these adatoms consist of outermost *s* electrons, besides the *d* electrons that act as essential magnetic moments, which can modify the exchange interaction. Moreover, one has to be careful such that the band structure does not get modified significantly by these impurities. Nevertheless, a simple molecule possessing localized magnetic moments which interact via host material atoms and does not alter the bulk band structure, can be deposited on 8-Pmmn borophene and may be a possible testbed for our theoretical predictions.

Throughout this chapter we have discussed RKKY exchange interaction in 8-Pmmn Borophene due to the presence of external magnetic impurities. There is another phenomena that takes place when a magnetic impurity is placed in a metallic host : the Kondo effect [240] which is a many-body phenomena where the scattering of conduction electrons in a metal, lying near the Fermi level, due to the magnetic impurities results in a characteristic change of electrical resistivity with temperature. The Kondo temperature T_K is defined by the energy scale below which the local magnetic moment of a magnetic impurity is screened by the conduction electron spins of the metal. When multiple impurities are present in the metal, the Kondo effect competes with RKKY interaction. Doniac [241] pointed out the difference in their scaling with the antiferromagnetic coupling J as $T_K \sim e^{-1/J}$ and $J_{RKKY} \sim J^2$ (for weak coupling J). There exists a critical point $J = J_C$ where $T_K = J_{RKKY}$. For weak coupling limit *i.e.,* in the limit of $J < J_C$, RKKY interaction becomes dominant [242].

Although we have focused on RKKY exchange interaction in 8-Pmmn Borophene as our host material, qualitatively the results should be similar for any other 2D materials having tilted Dirac cone for *e.g.* tilted graphene, organic conductor α-$(\mathrm{BEDT}-\mathrm{TTF})_2\mathrm{I}_3$ [42, 243] etc. Then χ_{11} and χ_{12} would refer to the measure of RKKY exchange interaction (in units of $J\hbar^2/4$) corresponding to impurities being placed on same sublattices and different sublattices respectively.

Here, we emphasize that 8-Pmmn borophene is ideally not a coplanar 2D Dirac material. Rather, it has a finite thickness due to the two kinds of atoms being non-coplanar. However, only those atoms located in a hexagonal manner in a buckled structure contribute to the formation of Dirac cones [39]. Therefore, the finite thickness which we have neglected in our analysis, should manifests negligible effect on the RKKY exchange interaction.

CHAPTER 7

Summary and Outlooks

In this chapter, we summarize the outcome of the thesis and discuss possible extensions of the works which are still unexplored. This thesis has been devoted to study various transport properties and magnetic exchange properties of several 2D Dirac materials and Majorana nanowire. Investigation of newly discovered 2D materials namely Silicene, Borophene etc. has attracted immense interest among experimentalists as well as theoreticians due to their possible application in diverse areas ranging from topological quantum computation to spintronics. Topological phases have been predicted in Silicene: a new generation of 2D materials. Therefore various transport properties such as thermal transport, quantum pumping are important not only for a better understanding of the materials but also to unravel the possible applications.

In this direction, in chapter 3, we have investigated thermal conductance κ by Dirac fermions in silicene NIS junction where superconductivity is induced in silicene sheet via the proximity effect. We study the behavior of TC in this set-up both for thin and thick insulating barrier limits. We show that TC exhibits $\pi/2$ periodic oscillation with respect to the barrier strength in thin barrier limit for undoped ($\mu_N = 0$) and moderately doped ($0 < \mu_N \leq \Delta$) regime where the Fermi surface mismatch between the normal and superconducting sides is significant. The oscillation becomes π periodic as a function of barrier strength in the highly doped ($\mu_N \gg \Delta$) regime where Fermi surfaces in the two sides are almost aligned. This change of periodicity ($\pi/2$ to π) in thermal response with the variation of doping concentration can be an indirect probe to identify the crossover from SAR to retro AR.

Nonetheless, TC shows conventional exponential dependence on temperature independent of doping concentration and barrier characteristics. The external electric field reduces TC monotonically in the undoped regime. However, a non-trivial interplay between band gap at Dirac points and doping concentration appears in the moderately doped case. Consequently, electric field can tune TC in the later regime. On the other hand, electric field has a negligible effect on TC when $\mu_N/\Delta \gg \lambda$. In the thick barrier limit, oscillation of TC persists both as a function of barrier thickness d as well as barrier height V_0. The latter can be tuned by an additional gate voltage applied at the insulating region. However, we show that the periodicity of TC no longer remains constant, rather becomes functions of both d and V_0. Also after a certain barrier thickness ($d \sim 0.4\lambda_F$), the amplitude of oscillations in TC decays for arbitrary V_0 in the highly doped regime.

In chapter 4, we have investigated the possibility of enhancing the CAR probability $|t_A|^2$ in silicene NSN set up by introducing thin insulating barrier I at each NS interface. It is shown that, for electrons with normal incidence, resonant CAR can be obtained in our setup by tuning the band gap in both the normal silicene regions by applying an external electric field as well as adjusting the chemical potential by additional gate voltages. We also show that $|t_A|^2$ is periodic in χ_1-χ_2 plane due to relativistic nature of Dirac fermions. On the other hand, it is also possible to attain transmission probability $|t_e|^2$ of magnitude unity in silicene NISIN junction under suitable circumstances. Owing to Dirac nature of particles, $|t_e|^2$ also exhibits periodic behavior in the space of barrier strengths χ_1 and χ_2. We then explored adiabatic quantum charge pumping through our NISIN setup and show that the behavior of pumped charge as a function of the pumping strength P is closely related to the features of CAR probability $|t_A|^2$ or transmission probability $|t_e|^2$ in the pumping parameter space. For electrons with normal incidence, large pumped charge with value close to $Q \sim 2e$ can be obtained when particular circular or elliptic pumping contour encloses the resonant CAR in χ_1-χ_2 plane. Although the major contribution to Q, in this case, arises from the dissipative part. On the other hand, large pumped charge can also be obtained with lemniscate contour when odd number of $|t_A|^2$ peaks are enclosed by each of its bubble. In contrast, pumped charge approaches to $Q \sim -e$ when various pumping contours enclose $|t_e|^2$ resonance in the same parameter space. However, pumped charge decreases monotonically as we increase the angle of incidence of the incoming electron. In experimental situation, the measurable quantity should be the angle averaged pumped charge analogous to angle averaged conductance. From our analysis, we expect that the qualitative nature of angle averaged pumped charge as a function of the pumping strength will remain similar to the $\alpha_{eL} = 0$

case. Although the quantitative value of Q will be smaller than the angle resolved case as Q decreases monotonically with α_{eL}.

In chapter 5, we have studied two terminal differential conductance of a quasi 1D FS junction where the superconductor consists of mixed singlet and triplet pairings. When the superconducting part of the NW becomes topological and $\tilde{h}$ is parallel (anti-parallel) to $\mathbf{d}$ vector ($\psi = 0(\psi = \pi)$), transport is blocked through the junction due to the absence of SFAR. On the other hand, when $\tilde{h}$ is perpendicular to $\mathbf{d}$ ($\psi = \pi/2$) differential conductance splits away from $\epsilon = 0$ due to time-reversal breaking boundary perturbation. Moreover, zero energy conductance spectra exhibits sharp transition from $4e^2/h$ to $2e^2/h$ when $\tilde{h} > \mu$ *i.e.,* , as we move into the polarized regime. Such transition between quantized conductances at zero bias demonstrates an efficient spin dependent coupling to a single MZM from the pair of MZMs, using a ferromagnetic lead.

In chapter 6, we have explored the effect of the tilted and anisotropic Dirac cones on the RKKY exchange interaction in the bulk of an 8-Pmmn borophene. We observe that the tilting of the Dirac cones, for a specific orientation of the impurities, manifests itself with a significant reduction in the RKKY exchange interaction oscillation frequency. This feature can be an indirect signature of the degree of tilting present in tilted and anisotropic Dirac cone. We present our analytical expressions for the susceptibility, in terms of Meijer G-function, which is directly proportional to the exchange interaction strength. We consider two special cases: when two magnetic impurities are located perpendicular to the tilt axis (x axis) and along the tilt axis (y axis). In the former case, interference between the Dirac cones does not contribute to the Friedel oscillations and the period of oscillation increases with the tilting parameter. In contrast, for the impurities being along the tilt axis, interference among the Dirac cones plays the dominant role in determining the period of oscillation while the tilting parameter exhibits negligible contribution. Moreover, due to the opposite orientation of the tilting of the Dirac cones at the inequivalent Dirac points, the effect of tilting originating from each Dirac point on RKKY exchange interaction nullifies each other when the impurities reside along the tilt axis. However, the amplitude of oscillation decreases with the tilting parameter because of the lowering of the Fermi level. We also separate out the effect of simple anisotropy ($v_x \neq v_y$) on RKKY exchange interaction in absence of tilting ($v_t = 0$) and show that such anisotropy in the Fermi surface exhibits negligible effect on the response function in case of borophene. For arbitrarily placed magnetic impurities in the x-y plane (neither along nor perpendicular to the tilt axis), we evaluate our results numerically and show rapid oscillations (beating pattern) in susceptibility due to the interfer-

ence between the two Dirac cones and subdominant effects arising from the tilt parameter.

Spin transport without concomitant charge counterpart is a topic of extensive research due to its own merit of having applications in spintronics. Adiabatic spin pumping, in this direction, has been proposed in normal metal-ferromagnet (NF) junction [244] using magnetization dynamics. Such novel spin pumping can be interesting to investigate in silicene and explore the connection between topological phase transition and possibility of pure spin pumping. One can also naively expect to have moderate spin pumping in ferromagnet-insulator-superconductor-insulator-ferromagnet (FISIF) junction of silicene in the polarised regime of the ferromagnetic region.

On the other hand, sureshot distinction of Majorana mode from other possible trivial zero mode is still lacking. Various heterostructure composed of the non-centrosymmetric superconductor which host Majorana modes in the topological phase can be studied to explore the possibility of the desired distinction.

Appendices

APPENDIX A

Appendix for Chapter 1

A.1 Derivation of low energy effective Hamiltonian of Silicene

We begin with the lattice Hamiltonian given by Eq.(1.8):

$$\begin{aligned} H &= -t\sum_{<i,j>\alpha}\hat{c}^{\dagger}_{i\alpha}\,\hat{c}_{j\alpha} + i\frac{\lambda_{SO}}{3\sqrt{3}}\sum_{<<i,j>>\alpha\beta}\nu_{ij}\hat{c}^{\dagger}_{i\alpha}\sigma^{z}_{\alpha\beta}\,\hat{c}_{j\beta} \\ &\quad -i\frac{2}{3}\lambda_R\sum_{<<i,j>>\alpha\beta}\mu_{ij}\hat{c}^{\dagger}_{i\alpha}(\vec{\sigma}\times\hat{d}_{ij})^{z}_{\alpha\beta}\,\hat{c}_{j\beta} \\ &\quad +el\sum_{i\alpha}\zeta_i E^{i}_{z}\hat{c}^{\dagger}_{i\alpha}\,\hat{c}_{i\alpha} \;-\mu\sum_{i\alpha}\hat{c}^{\dagger}_{i\alpha}\,\hat{c}_{i\alpha}\;. \end{aligned} \tag{A.1}$$

We now proceed to show the derivation of the low energy effective Hamiltonian. The lattice structure is shown below

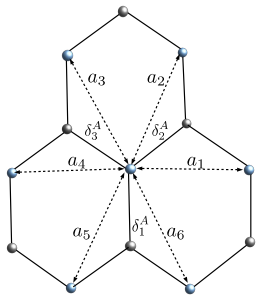

Figure A.1: Nearest neighbor and next nearest neighbor coupling are shown in silicene lattice.

We write down the nearest-neighbor (n.n) vectors $\delta_i^{A,B}$ and next nearest neighbour (n.n.n) vectors $\mathbf{a}_i$ for both sublattices. Note that, the n.n.n vectors are the same for both sublattices while the n.n vectors are different. The n.n are :

$$\delta_1^A = (0, \frac{a}{\sqrt{3}}, a_z),\ \delta_2^A = (\frac{a}{2}, -\frac{a}{\sqrt{3}}, a_z),\ \delta_3^A = (-\frac{a}{2}, -\frac{a}{\sqrt{3}}, a_z),$$
$$\delta_1^B = (0, -\frac{a}{\sqrt{3}}, -a_z),\ \delta_2^A = (-\frac{a}{2}, \frac{a}{\sqrt{3}}, -a_z),\ \delta_3^A = (\frac{a}{2}, \frac{a}{\sqrt{3}}, -a_z),$$

and the n.n.n vectors are:

$$\begin{aligned} \mathbf{a}_1 &= (a,0,0),\ \mathbf{a}_2 = \frac{a}{2}(1,\sqrt{3},0),\ \mathbf{a}_3 = \frac{a}{2}(-1,\sqrt{3},0), \\ \mathbf{a}_4 &= (-a,0,0),\ \mathbf{a}_5 = \frac{a}{2}(-1,-\sqrt{3},0),\ \mathbf{a}_6 = \frac{a}{2}(1,-\sqrt{3},0). \end{aligned} \tag{A.2}$$

The a_z component is small compared to a_x, a_y and hence neglected in the following calculation for simplicity. We also do not consider Rashba term in the Hamiltonian anymore, as λ_R is small compared to λ_{SO} and do not alter the physics near the Dirac points.

We now write the Hamiltonian in momentum space by Fourier-transforming the real space Hamiltonian and obtain

$$\begin{aligned} H &= -t \sum_{\mathbf{k},\delta^{\mathbf{A}},\alpha} A^\dagger_{\mathbf{k}\alpha} B_{\mathbf{k}\alpha} e^{-i\mathbf{k}\delta^{\mathbf{A}}} - t \sum_{\mathbf{k},\delta^{\mathbf{B}},\alpha} B^\dagger_{\mathbf{k}\alpha} A_{\mathbf{k}\alpha} e^{-i\mathbf{k}\delta^{\mathbf{B}}} \\ &+ \frac{i\lambda_{SO}}{3\sqrt{3}} \sum_{\alpha,\beta,\mathbf{a},\mathbf{k}} (\nu^A_{\mathbf{a}} e^{-i\mathbf{k}\mathbf{a}} A^\dagger_{\mathbf{k}\alpha} \sigma^z_{\alpha\beta} A_{\mathbf{k}\beta} + (\nu^B_{\mathbf{a}}) e^{-i\mathbf{k}\mathbf{a}} B^\dagger_{\mathbf{k}\alpha} \sigma^z_{\alpha\beta} B_{\mathbf{k}\beta}) \qquad \text{(A.3)} \\ &+ (elE_z - \mu) \sum_{\mathbf{k}\sigma} A^\dagger_{\mathbf{k}\sigma} A_{\mathbf{k}\sigma} - (elE_z + \mu) \sum_{\mathbf{k}\sigma} B^\dagger_{\mathbf{k}\sigma} B_{\mathbf{k}\sigma} \qquad \text{(A.4)} \end{aligned}$$

where we have used:

$$\begin{aligned} \nu^A_{\mathbf{a}_1} = \nu^A_{\mathbf{a}_3} = \nu^A_{\mathbf{a}_5} = -\nu^A_{\mathbf{a}_2} = -\nu^A_{\mathbf{a}_4} = -\nu^A_{\mathbf{a}_6} = 1, \\ \nu^B_{\mathbf{a}_1} = \nu^B_{\mathbf{a}_3} = \nu^B_{\mathbf{a}_5} = -\nu^B_{\mathbf{a}_2} = -\nu^B_{\mathbf{a}_4} = -\nu^B_{\mathbf{a}_6} = -1. \end{aligned} \tag{A.5}$$

The summations over the n.n and n.n.n vectors can be obtained as :

$$\begin{aligned}\gamma_{\mathbf{k}} &\equiv \sum_{\delta^A} e^{-i\mathbf{k}\delta^{\mathbf{A}}} = \Big(\sum_{\delta^B} e^{-i\mathbf{k}\delta^{\mathbf{B}}}\Big)^* = e^{-iak_y/\sqrt{3}} + 2e^{iak_y/2\sqrt{3}}\cos(\tfrac{ak_x}{2}),\\ \theta_{\mathbf{k}} &\equiv \sum_{\mathbf{a}} \nu^A_{\mathbf{a}} e^{-i\mathbf{k}\mathbf{a}} = -\sum_{\mathbf{a}} \nu^B_{\mathbf{a}} e^{-i\mathbf{k}\mathbf{a}} = -2i[\sin(ak_x) - 2\sin(ak_x/2)\cos(\sqrt{3}ak_y/2)]. \qquad \text{(A.6)}\end{aligned}$$

We are interested in understanding the physics near the Dirac points in the BZ which are $\mathbf{K}_\pm = (\pm\frac{4\pi}{3a}, 0)$. Therefore, we expand the Hamiltonian for small $\mathbf{k}$ around these Dirac points by chosing $k_x \to k_x \pm \frac{4\pi}{3a}$ and $k_y \to k_y$. For small k_x and k_y, we can assume $k_x a \ll 1$, $k_y a \ll 1$ and only take terms first order in $\mathbf{k}$. Hence we obtain :

$$\gamma_{\mathbf{K}_\pm+\mathbf{k}} = \frac{\sqrt{3}a}{2}(\pm k_x + ik_y),\ \theta_{\mathbf{K}_\pm+\mathbf{k}} = \mp 3\sqrt{3}i. \qquad \text{(A.7)}$$

We now define the Fermi velocity $v_F = \frac{\sqrt{3}a}{2}$ and choose our basis as $\psi = \{A_{\mathbf{k}\alpha}, B_{\mathbf{k}\alpha}\}^T$. We can write the Hamiltonian in this basis as :

$$H^s_\eta = \begin{pmatrix} \Delta^\eta_\alpha & \hbar v_{\mathrm{F}}(\eta k_x + ik_y) \\ \hbar v_{\mathrm{F}}(\eta k_x - ik_y) & -\Delta^\eta_\alpha \end{pmatrix}, \qquad \text{(A.8)}$$

This corresponds to Eq.(1.12) in the main text.

APPENDIX B

Appendix for Chapter 2

B.1 Full Rashba Hamiltonian in the helical basis

In this appendix, we show that the Hamiltonian for the Rashba spin-orbit coupled nanowire in proximity to a s-wave superconductor, $\mathcal{H}_0 + \mathcal{H}_{sc}$ given by Eq. (2.18), when written in the helical basis, gives rise to an effective p-wave like pairing. We closely follow the seminal paper by Alicea [245] and Cayao thesis [246].

$$\psi(k) = \phi_-(k)\psi_-(k) + \phi_+(k)\psi_+(k)\,, \tag{B.1}$$

where $\psi_\pm$ annihilates states in the upper/lower bands and $\phi_\pm$ are the respective normalized wavefunctions which are written as column vector having two spinor components

$$\phi_+(k) = \begin{pmatrix} \phi_+^\uparrow(k) \\ \phi_+^\downarrow(k) \end{pmatrix} = \frac{1}{\sqrt{2}} \begin{pmatrix} +\gamma_k \\ 1 \end{pmatrix}, \tag{B.2}$$

and

$$\phi_-(k) = \begin{pmatrix} \phi_-^\uparrow(k) \\ \phi_-^\downarrow(k) \end{pmatrix} = \frac{1}{\sqrt{2}} \begin{pmatrix} -\gamma_k \\ 1 \end{pmatrix}, \tag{B.3}$$

where $\gamma_k = \frac{(i\alpha k + B)}{\sqrt{B^2+\alpha^2 k^2}}$. Writing $\psi(k)$ as a two component column vector in the form

$$\phi_+(k) = \begin{pmatrix} \phi_+^{\uparrow}(k) \\ \phi_+^{\downarrow}(k) \end{pmatrix} \tag{B.4}$$

The Eq.(B.1) now becomes

$$\begin{aligned} \psi_{\uparrow}(k) &= \frac{1}{\sqrt{2}} \left[-\gamma_k \psi_-(k) + \gamma_k \psi_+(k) \right] , \\ \psi_{\downarrow}(k) &= \frac{1}{\sqrt{2}} \left[\psi_-(k) + \psi_+(k) \right] , \end{aligned} \tag{B.5}$$

We now proceed to rewrite the terms of the full Hamiltonian given by Eq.(2.18) in the helical basis given in Eq. (B.5).

Kinetic term

The kinetic Hamiltonian is given by,

$$\mathcal{H}_{kin} \, = \, \int dx \left[\psi_{\uparrow}^{\dagger}(x) \left[\xi_k \right] \psi_{\uparrow} \, + \, \psi_{\downarrow}^{\dagger}(x) \left[\xi_k \right] \psi_{\downarrow} \right] , \tag{B.6}$$

where $\xi_k = \hbar^2 k^2 / 2m - \mu$. Using Eqs. (B.5), we write each of the terms in the new basis

$$\begin{aligned} \psi_{\uparrow}^{\dagger}\psi_{\uparrow} &= \frac{1}{2} \left[\psi_-^{\dagger}(k)\psi_-(k) + \psi_+^{\dagger}(k)\psi_+(k) - \psi_+^{\dagger}(k)\psi_-(k) - \psi_-^{\dagger}(k)\psi_+(k) \right] , \\ \psi_{\downarrow}^{\dagger}\psi_{\downarrow} &= \frac{1}{2} \left[\psi_-^{\dagger}(k)\psi_-(k) + \psi_+^{\dagger}(k)\psi_+(k) + \psi_+^{\dagger}(k)\psi_-(k) + \psi_-^{\dagger}(k)\psi_+(k) \right] , \end{aligned} \tag{B.7}$$

We have used : $\gamma_k^{\dagger}\gamma_k = |\gamma_k|^2 = 1$. Now Eq. (B.6) becomes,

$$\mathcal{H}_{kin} \, = \, \int dx \, \xi_k \Big[\psi_-^{\dagger}(k)\psi_-(k) \, + \, \psi_+^{\dagger}(k)\psi_+(k) \Big] . \tag{B.8}$$

Spin-orbit term

The spin-orbit coupling term in the Hamiltonian Eq. (2.19) is

$$\mathcal{H}_{soc} \, = \, (i\alpha k) \int \, dx \left[\psi_{\uparrow}^{\dagger} \, \psi_{\downarrow} \, - \, \psi_{\downarrow}^{\dagger} \, \psi_{\uparrow} \right] . \tag{B.9}$$

Using Eqs. (B.5), we can write

$$\begin{aligned}\psi_\uparrow^\dagger\psi_\downarrow &= \frac{1}{2}\Big[-\gamma_k^\dagger\psi_-^\dagger(k)\psi_-(k) + \gamma_k^\dagger\psi_+^\dagger(k)\psi_-(k) - \gamma_k^\dagger\psi_-^\dagger(k)\psi_+(k) + \gamma_k^\dagger\psi_+^\dagger(k)\psi_+(k)\Big] \\ \psi_\downarrow^\dagger\psi_\uparrow &= \frac{1}{2}\Big[-\gamma_k\psi_-^\dagger(k)\psi_-(k) - \gamma_k\psi_+^\dagger(k)\psi_-(k) + \gamma_k\psi_-^\dagger(k)\psi_+(k) + \gamma_k\psi_+^\dagger(k)\psi_+(k)\Big] \ .\end{aligned} \tag{B.10}$$

Therefore, we obtain

$$\begin{aligned}\mathcal{H}_{SO} = \frac{i\alpha k}{2}\int dx\Big[&(\gamma_k - \gamma_k^\dagger)\psi_-^\dagger(k)\psi_-(k) + (k)(\gamma_k^\dagger - \gamma_k)\psi_+^\dagger\psi_+(k) \\ &+ (\gamma_k^\dagger + \gamma_k)\psi_+^\dagger(k)\psi_-(k) - (\gamma_k^\dagger + \gamma_k)\psi_-^\dagger(k)\psi_+(k)\Big] \ .\end{aligned} \tag{B.11}$$

Zeeman term

The Zeeman term in the Hamiltonian given by Eq. (2.19) reads,

$$\mathcal{H}_z \ = \ B\int dx\left[\psi_\uparrow^\dagger\psi_\downarrow \ + \ \psi_\downarrow^\dagger\psi_\uparrow\right] \ . \tag{B.12}$$

Using Eq. (B.10), we get

$$\begin{aligned}\mathcal{H}_Z = \frac{B}{2}\int dx\Big[&-(\gamma_k + \gamma_k^\dagger)\psi_-^\dagger(k)\psi_-(k) + (\gamma_k^\dagger + \gamma_k)\psi_+^\dagger(k)\psi_+(k) \\ &+ (\gamma_k^\dagger - \gamma_k)\psi_+^\dagger(k)\psi_-(k) - (k)(\gamma_k^\dagger - \gamma_k)\psi_-^\dagger\psi_+(k)\Big] \ .\end{aligned} \tag{B.13}$$

Kinetic, spin-orbit and Zeeman terms

We now add up all the three terms we have obtained so far and write

$$\begin{aligned}\mathcal{H}_{kin} + \mathcal{H}_{SO} + \mathcal{H}_Z = \int\frac{dx}{2}\Big\{&\psi_-^\dagger(k)\big[i\alpha k(\gamma_k - \gamma_k^\dagger) - B(\gamma_k + \gamma_k^\dagger) + 2\xi_k\big]\psi_-(k) \\ &+ \psi_+^\dagger(k)\big[i\alpha k(\gamma_k^\dagger - \gamma_k) + B(\gamma_k^\dagger + \gamma_k) + 2\xi_k\big]\psi_+(k) \\ &+ \psi_+^\dagger(k)\big[i\alpha k(\gamma_k^\dagger + \gamma_k) + B(\gamma_k^\dagger - \gamma_k)\big]\psi_-(k) \\ &+ \psi_-^\dagger(k)\big[-i\alpha k(\gamma_k^\dagger + \gamma_k) - B(\gamma_k^\dagger - \gamma_k)\big]\psi_+(k)\Big\} \ .\end{aligned} \tag{B.14}$$

Using the form of $\gamma_k = \frac{B+i\alpha k}{\sqrt{B^2+\alpha^2k^2}}$, we get the following relations:

$$\begin{aligned}\gamma_k^\dagger - \gamma_k &= \frac{-2i\alpha k}{\sqrt{B^2+\alpha^2k^2}} \\ \gamma_k^\dagger + \gamma_k &= \frac{2B}{\sqrt{B^2+\alpha^2k^2}}\,,\end{aligned} \tag{B.15}$$

Using these relations, we can write

$$\mathcal{H}_{kin} + \mathcal{H}_{SO} + \mathcal{H}_Z = \int dx \big[\varepsilon_+(k)\psi_+^\dagger(k)\psi_+(k) + \varepsilon_-(k)\psi_-^\dagger(k)\psi_-(k)\big]\,, \tag{B.16}$$

where $\varepsilon_{k,\pm} = \xi \pm \sqrt{B^2+\alpha^2k^2}$

Superconducting term

The superconducting term in the Hamiltonian given by Eq. (2.20) is

$$\mathcal{H}_{sc} = \frac{1}{2}\int dx \Big\{\Delta\Big[\psi_\uparrow^\dagger(k)\psi_\downarrow^\dagger(-k) - \psi_\downarrow^\dagger(-k)\psi_\uparrow^\dagger(k)\Big] + h.c\Big\}\,, \tag{B.17}$$

We have used fermion anti-commutation relations

$$\big\{\psi_\uparrow^\dagger(k), \psi_\downarrow^\dagger(-k)\big\} = 0\,. \tag{B.18}$$

Now, the elements of $\mathcal{H}_{sc}$ in the helical basis becomes

$$\begin{aligned}\psi_\uparrow^\dagger(k)\psi_\downarrow^\dagger(-k) &= \frac{1}{2}\Big[-\gamma_k^\dagger\psi_-^\dagger(k)\psi_-^\dagger(-k) + \gamma_k^\dagger\psi_+^\dagger(k)\psi_-^\dagger(-k) - \gamma_k^\dagger\psi_-^\dagger(k)\psi_+^\dagger(-k) + \gamma_k^\dagger\psi_+^\dagger(k)\psi_+^\dagger(-k)\Big]\,, \\ \psi_\downarrow^\dagger(-k)\psi_\uparrow^\dagger(k) &= \frac{1}{2}\Big[-\gamma_k^\dagger\psi_-^\dagger(-k)\psi_-^\dagger(k) - \gamma_k^\dagger\psi_+^\dagger(-k)\psi_-^\dagger(k) + \gamma_k^\dagger\psi_-^\dagger(-k)\psi_+^\dagger(k) + \gamma_k^\dagger\psi_+^\dagger(-k)\psi_+^\dagger(k)\Big]\end{aligned} \tag{B.19}$$

Hence we can write

$$\begin{aligned}&\psi_\uparrow^\dagger(k)\psi_\downarrow^\dagger(-k) - \psi_\downarrow^\dagger(-k)\psi_\uparrow^\dagger(k) = \\ &\frac{1}{2}\Big[-\gamma_k^\dagger\psi_-^\dagger(k)\psi_-^\dagger(-k) + \gamma_k^\dagger\psi_+^\dagger(k)\psi_-^\dagger(-k) - \gamma_k^\dagger\psi_-^\dagger(k)\psi_+^\dagger(-k) + \gamma_k^\dagger\psi_+^\dagger(k)\psi_+^\dagger(-k) \\ &+\gamma_k^\dagger\psi_-^\dagger(-k)\psi_-^\dagger(k) + \gamma_k^\dagger\psi_+^\dagger(-k)\psi_-^\dagger(k) - \gamma_k^\dagger\psi_-^\dagger(-k)\psi_+^\dagger(k) - \gamma_k^\dagger\psi_+^\dagger(-k)\psi_+^\dagger(k)\Big]\,.\end{aligned} \tag{B.20}$$

There are four combinations of the operators $\psi_\pm$ and in the following we separate them out and evaluate them individualy as :

$$\begin{aligned}\Big[\psi^\dagger_\uparrow(k)\psi^\dagger_\downarrow(-k) - \psi^\dagger_\downarrow(-k)\psi^\dagger_\uparrow(k)\Big]_{--} &= \frac{1}{2}\Big[-\gamma^\dagger_k\psi^\dagger_-(k)\psi^\dagger_-(-k) + \gamma^\dagger_k\psi^\dagger_-(-k)\psi^\dagger_-(k)\Big] \\ &= \gamma^\dagger_k\frac{1}{2}\Big[-\psi^\dagger_-(k)\psi^\dagger_-(-k) + \gamma^\dagger_{-k}\psi^\dagger_-(k)\psi^\dagger_-(-k)\Big] \\ &= \frac{1}{2}\Big[-\gamma^\dagger_k + \gamma^\dagger_{-k}\Big]\psi^\dagger_-(k)\psi^\dagger_-(-k)\,,\end{aligned} \tag{B.21}$$

where in the second term of the second equality, we have substituted k by $-k$. Similarly we find the other terms as

$$\Big[\psi^\dagger_\uparrow(k)\psi^\dagger_\downarrow(-k) - \psi^\dagger_\downarrow(-k)\psi^\dagger_\uparrow(k)\Big]_{++} == \frac{1}{2}\Big[\gamma^\dagger_k - \gamma^\dagger_{-k}\Big]\psi^\dagger_+(k)\psi^\dagger_+(-k) \tag{B.22}$$

and

$$\begin{aligned}&\Big[\psi^\dagger_\uparrow(k)\psi^\dagger_\downarrow(-k) - \psi^\dagger_\downarrow(-k)\psi^\dagger_\uparrow(k)\Big]_{+-,-+} \\ &= \frac{1}{2}\Big[\gamma^\dagger_k\psi^\dagger_+(k)\psi^\dagger_-(-k) + \gamma^\dagger_k\psi^\dagger_+(-k)\psi^\dagger_-(k) - \gamma^\dagger_k\psi^\dagger_-(k)\psi^\dagger_+(-k) - \gamma^\dagger_k\psi^\dagger_-(-k)\psi^\dagger_+(k)\Big]\,, \\ &= \frac{1}{2}\Big[2\psi^\dagger_+(k)\psi^\dagger_-(-k)\gamma^\dagger_k + 2\psi^\dagger_+(-k)\psi^\dagger_-(k)\gamma^\dagger_k\Big] \\ &= \Big[\gamma^\dagger_k + \gamma^\dagger_{-k}\Big]\psi^\dagger_+(k)\psi^\dagger_-(-k)\,,\end{aligned} \tag{B.23}$$

We have used fermionic anti-commutation relation, $\{\psi^\dagger_\alpha, \psi^\dagger_\beta\} = 0$ in the second equality, and in in the second term of the fourth equality we have substituted k by $-k$ as before.

We now obtain the following combination of γ_k :

$$-\gamma^\dagger_k + \gamma^\dagger_{-k} = \frac{2i\alpha k}{\sqrt{B^2+\alpha^2k^2}}\,, \tag{B.24}$$

$$\gamma^\dagger_k - \gamma^\dagger_{-k} = -\frac{2i\alpha k}{\sqrt{B^2+\alpha^2k^2}}\,, \tag{B.25}$$

$$\gamma^\dagger_k + \gamma^\dagger_{-k} = \frac{2B}{\sqrt{B^2+\alpha^2k^2}}\,. \tag{B.26}$$

and thus the superconducting term becomes,

$$\begin{aligned}\mathcal{H}_{sc} = \frac{1}{2}\int dx \Bigg\{ & \left[\frac{i\alpha k\Delta}{\sqrt{B^2+\alpha^2k^2}}\right]\psi_-^\dagger(k)\psi_-^\dagger(-k) \\ & + \left[\frac{-i\alpha k\Delta}{\sqrt{B^2+\alpha^2k^2}}\right]\psi_+^\dagger(k)\psi_+^\dagger(-k) \\ & + \left[\frac{2B\Delta}{\sqrt{B^2+\alpha^2k^2}}\right]\psi_+^\dagger(k)\psi_-^\dagger(-k) + h.c\Bigg\}.\end{aligned} \tag{B.27}$$

So, both intra and interband pairings have appeared in Eq. (B.27). If we negelect the upper band and only consider the lower one, we get back the superconducting Hamiltonian given in Eq.(2.24) after Fourier transforming the first term of Eq. (B.27).

APPENDIX C

Appendix for Chapter 3

C.1 Derivation of the thermal conductance formula

Here we present the outline of the derivation of the formula for tehrmal conductance (electronic contribution only). We closely follow the well-known BTK formalism[61], to derive the same in N-I-S junction. Tunneling conductance in NS junction is given by :

$$\frac{dI}{dV} = G = \frac{G_0}{2}\int_{-\frac{\pi}{2}}^{\frac{\pi}{2}} (1 + |r(eV)|^2 - |r_A(eV)|^2)\cos(\alpha)d\alpha \tag{C.1}$$

where $r(eV)$ and $r_A(eV)$ denote the reflection and Andreev reflection probability respectively, at bias V applied in the normal side of the junction. α is the angle of incidence from normal side and the factor $\frac{1}{2}$ arises due to the integration over the angular range from $-\frac{\pi}{2}$ to $\frac{\pi}{2}$. G_0 is the ballistic conductance of metallic system, and $N(eV)$ denotes the number of available channels for a sample. G_0 is constant for small bias voltage *i.e.,* $eV \ll E_F$ where E_F is the Fermi energy. This BTK formula is derived at zero temperature.

We now consider the following situation : normal side is kept at temperature $T_N = T - \delta T/2$ and the superconducting side is kept at temperature $T_S = T + \delta T/2$. We assume, in our formulation, $\delta T, V \ll T$, where T is the average temperature in the junction. Therefore, a small thermal gradient

δT is applied across the junction for thermal transport to take place.

Energy distribution of electrons that propagate from the normal metal to the NS interface is the equilibrium Fermi distribution shifted by eV : $f^{\rightarrow}(E) = f(E - eV)$. Electrons moving from the NS interface to the normal metal side, are produced in three processes : (i) electrons are reflected from the interface with probability B; (ii) holes are Andreev reflected as electrons with probability A; and (iii) quasiparticles coming from the superconductor are transmitted into the normal side with the probability $(1 - A - B)$. The energy distribution of the electrons moving into the normal metal side from NS interface is, thus, given by

$$f^{\leftarrow}(E) = A(E)[1 - f^{\rightarrow}(-E)] + B(E)f^{\rightarrow}(E) + [1 - A(E) - B(E)]f(E) \tag{C.2}$$

The heat current that flows from the normal metal into the superconductor (in one transverse mode) can be writen as

$$\begin{aligned} j_{NS} &= \int dE(E - eV)(f^{\rightarrow} - f^{\leftarrow}) \\ &= \int_{-\infty}^{\infty} dE\,[1 - B(E)]f^N(E - eV) - A(E)f^N(E + eV) - [1 - A(E) - B(E)]f^S(E) \end{aligned}$$

We expand the Fermi distribution, for small bias voltage and small temperature gradient, in the following way

$$f^N = f_{T_N}(E - eV) = f_T(E) - eV\frac{\partial f}{\partial E} + \frac{E\delta T}{2T}\frac{\partial f}{\partial T} \tag{C.3}$$

$$f^S = f_{T_S}(E) = f_T(E) - \frac{E\delta T}{2T}\frac{\partial f}{\partial T} \tag{C.4}$$

We now substitute Eq.(C.4) in Eq. (C.3) and obtain :

$$j_{NS} = \int_{-\infty}^{\infty} dE(E - eV)[1 - A(E) - B(E)]f(E) \tag{C.5}$$

Taking derivative with respect to temperature, we find the normalized thermal conductance across the junction as

$$\kappa = \int_{-\infty}^{\infty} dE[1 - A(E) - B(E)] \frac{E^2}{4T^2 \cosh(\frac{E}{2k_B T})^2} \tag{C.6}$$

where, we have used

$$\begin{aligned} f &= \frac{1}{1 + e^{-\beta E}} \\ \frac{\partial f}{\partial T} &= \frac{e^{\beta E}}{(1 + e^{\beta E})^2} \frac{E}{k_B T^2} \end{aligned} \tag{C.7}$$

We have approximated $E - eV \approx E$ in the final expression to obtain κ as no external bias has been applied. Now, the incoming electrons can have any angle of incidence and hence we have to average over the angle of incident electrons : α. We also have to keep in mind that the hole reflection angle α_h can be different from α_e and finally we obtain the required formula :

$$\begin{aligned} \kappa &= \int_0^{\infty} \int_{-\frac{\pi}{2}}^{\frac{\pi}{2}} dE d\alpha_e \left[1 - R_e - R_h \frac{\cos(\alpha_h)}{\cos(\alpha_e)}\right] \\ &\quad \cos(\alpha_e) \left[\frac{E^2}{4T^2 \cosh^2(\frac{E}{2T})}\right]. \end{aligned} \tag{C.8}$$

This is the formula used in the main text [see Eq.(4.13)]. Note that, the temperature gradient δT is small and thus we expect that phonos will not be excited in the system. Therefore, we consider only the electronic contribution to the thermal conductance (TC).

APPENDIX D

Appendix for Chapter 4

D.1 Derivation of the formula for pumped charge

An electron pump converts a periodic modulation of its characteristics, in absence of any bias voltage, into a time-independent electric current which is termed as 'pump current'. Some example of these characteristics are the charge on the device, the location of a scatterer, the magnetic flux threading the sample, gate voltage etc. Brouwer in his seminal paper[140], considered a parametric electron pump through an open system via a scattering approach. He formulated the pumped current in terms of the scattering matrix $S(\chi_1, \chi_2)$ where χ_1 and χ_2 are pumping parameters. We closely follow the derivation of pumped current given by Brouwer in Ref. [140].

The system under consideration is shown schematically in Fig. which consists of a quantum dot being coupled to two electron reservoirs (left and right) by ballistic point contacts. The two electron reservoirs are kept at the same chemical potential so that there is no net current from left reservoir to the right. There are two external parameters $\chi_1(t)$ and $\chi_2(t)$ of the dot which are varied periodically as shown in Fig. D.1a. Büttiker, Thomas, and Prêtre [139] calculated the emissivity that can be transferred by the infinitesimal change of two parameters.

For a small and slow harmonic variation of the parameter, $\chi(t) = \chi_0 + \delta\chi_\omega e^{i\omega t}$, the charge $\delta Q(l)$

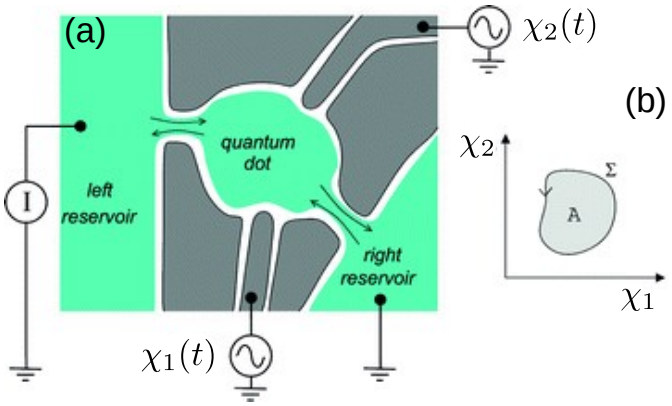

Figure D.1: (a) Schematic of an electron pump device. (b) Area enclosed by the periodic modulation of the parameters $\chi_1(t)$ and $\chi_2(t)$. This figure is adapted from Ref.**??**.

entering the cavity through contact l ($l = 1, 2$) can be written as

$$\delta Q(l,\omega) = e\frac{dn(l)}{d\chi}\delta\chi_\omega\,, \tag{D.1}$$

$$\frac{dn(l)}{d\chi} = \frac{1}{2\pi}\sum_\beta\sum_{\alpha\in l}\mathrm{Im}\,\frac{\partial S_{\alpha\beta}}{\partial\chi}S^*_{\alpha\beta}. \tag{D.2}$$

$S_{\alpha\beta}$ are the scattering matrix elements where the index α is summed from 1 to N for the contact 1 and from $N+1$ to $2N$ for the contact 2. The quantity $dn(l)/d\chi$ is called the *emissivity* into contact l [139]. The Eq. (D.2) is valid to first order in the frequency ω. After Fourier transformation we can obtain :

$$\delta Q(l,t) = e\frac{dn(l)}{d\chi}\delta\chi(t). \tag{D.3}$$

For a simultaneous small variation of two parameters χ_1 and χ_2, the emitted charge $\delta Q(l,t)$ through contact l reads ($l = 1, 2$)

$$\delta Q(l,t) = e\frac{dn(l)}{d\chi_1}\delta\chi_1(t) + e\frac{dn(l)}{d\chi_2}\delta\chi_2(t). \tag{D.4}$$

Now, we find the emmitted charge when both the parameters χ_1 and χ_2 are varied by finite amount. The total charge emitted through contact l in one period $\tau = 2\pi/\omega$ is found to be [140] :

$$Q(l,\tau) = e\int_0^\tau dt\left(\frac{dn(l)}{d\chi_1}\frac{d\chi_1}{dt} + \frac{dn(l)}{d\chi_2}\frac{d\chi_2}{dt}\right). \tag{D.5}$$

where $\frac{dn(l)}{d\chi_l}$ are given by Eq.(D.2). In one full period, the pair of parameters $\chi_1(t)$ and $\chi_2(t)$ forms a closed path in the (χ_1, χ_2) parameter space, as shown in Fig. D.1(b). This formula does not give quan-

tized pumped charge as Coulomb blockade is lifted and the system is well coupled with the reservoirs.

S-matrix for the NISIN structure of silicene as given in Eq. (4.16) reads

$$S = \begin{bmatrix} |r_e|e^{i\gamma_e} & |r_A|e^{i\gamma_h} & |t_e|e^{i\delta_e} & |t_A|e^{i\delta_h} \\ |r_A|e^{i\gamma_h} & |r_e|e^{i\gamma_e} & |t_A|e^{i\delta_h} & |t_e|e^{i\delta_e} \\ |t_e|e^{i\delta_e} & |t_A|e^{i\delta_h} & |r_e|e^{i\gamma_e} & |r_A|e^{i\gamma_h} \\ |t_A|e^{i\delta_h} & |t_e|e^{i\delta_e} & |r_A|e^{i\gamma_h} & |r_e|e^{i\gamma_e} \end{bmatrix} , \tag{D.6}$$

Using Eq.(D.5), we can write

$$Q(\tau) = \frac{e}{2\pi}\int_0^\tau dt \sum_{i=1,2}\Big[\frac{d\chi_i}{dt}\sum_\beta\sum_{\alpha\in l}\text{Im}\,\frac{\partial S_{\alpha\beta}}{\partial\chi_i}S^*_{\alpha\beta} \tag{D.7}$$

We use the following relation : $Im(\frac{\partial S_{11}}{\partial\chi_1}S^*_{11}) = \frac{\partial t}{\partial\chi_1}Im(\frac{\partial S_{11}}{\partial t}S^*_{11})$ and obtain

$$\begin{aligned} Q(\tau) = \frac{e}{\pi}\int_0^\tau dt\Big[&\{Im(\frac{\partial S_{11}}{\partial t}S^*_{11}) + Im(\frac{\partial S_{12}}{\partial t}S^*_{12}) \\ &+Im(\frac{\partial S_{13}}{\partial t}S^*_{13}) + Im(\frac{\partial S_{14}}{\partial t}S^*_{14})\} \end{aligned}$$

We now substitute the elements of the S matrix given by Eq.(D.6) in Eq.(D.8) and obtain

$$\begin{aligned} Q = \frac{e}{2\pi}\int_0^T dt[\;&- |r_A|^2(\dot\gamma_h\cos\alpha_{hL} + \dot\gamma_e\cos\alpha_{eL}) \\ &- |t_A|^2(\dot\delta_h\cos\alpha_{hR} + \dot\gamma_e\cos\alpha_{eL}) \\ &+ |t_e|^2(\dot\delta_e\cos\alpha_{eR} - \dot\gamma_e\cos\alpha_{eL}) \\ &+ \dot\gamma_e\cos\alpha_{eL}]\,, \end{aligned} \tag{D.8}$$

This is our working formula to obtain pumped charge. For normal incidence *i.e.,* $\alpha_{eL} = 0$, the last term of Eq.(D.8) consisting of the time derivative of reflection phase (γ_e) is called "*topological part* while the rest is termed as "*dissipative part*". The last term is "topological" becuase this term does not depend on scattering process amplitudes and for $\alpha_{eL} = 0$, the possible change in this term $\dot\gamma_e$ in a full period can be integer multiples of 2π. On the other hand, the rest of the terms in Eq.(4.17) are together termed as "dissipative" because their cumulative contribution prevents the perfect quantization of

pumped charge. This formula indicates that quantization of pumped charge is still possible in open quantum system.

APPENDIX E

Appendix for Chapter 5

E.1 Anti-resonance in tunneling conductance of Majorana nanowire

We here demonstrate the some analytical understanding in support of the anti-resonance shown in Fig.3 of Chapter 5. The analytical expressions of the scattering amplitudes are far from being simple. To get the clear picture of the anti-resonance of SFAR, we separated the spin space and particle-hole space to obtain the mixing in spin space and particle-hole space separately.

We write the wave functions in the most simple form :

$$\psi_{e\uparrow} = |e\uparrow >= \begin{pmatrix} a \\ b \\ 0 \\ 0 \end{pmatrix}, \ \psi_{e\downarrow} = |e\downarrow >= \begin{pmatrix} -b \\ a \\ 0 \\ 0 \end{pmatrix},$$

$$\psi_{h\uparrow} = |h\uparrow >= \begin{pmatrix} 0 \\ 0 \\ a \\ b \end{pmatrix}, \ \psi_{h\downarrow} = |h\downarrow >= \begin{pmatrix} 0 \\ 0 \\ -b \\ a \end{pmatrix}$$

$$\psi^e_{S\uparrow} = |e1 >= \begin{pmatrix} \alpha_1 \\ 0 \\ 0 \\ \beta_1 \end{pmatrix}, \ \psi^e_{S\downarrow} = |e2 >= \begin{pmatrix} 0 \\ \alpha_2 \\ \beta_2 \\ 0 \end{pmatrix},$$

$$\psi^h_{S\uparrow} = |h1 >= \begin{pmatrix} -\beta_2 \\ 0 \\ 0 \\ \alpha_2 \end{pmatrix}, \ \psi^h_{S\downarrow} = |h2 >= \begin{pmatrix} 0 \\ -\beta_1 \\ \alpha_1 \\ 0 \end{pmatrix}$$

where $a = \cos(\frac{\psi}{2}), b = \sin(\frac{\psi}{2})$

$$\alpha_1 \ = \ u_\uparrow(\theta) \ = \ \sqrt{\frac{1}{2} + \frac{\sqrt{\epsilon^2 - (\Delta_p^2 + \Delta_s^2 + 2\Delta_p\Delta_s\cos\theta)}}{2\epsilon}}$$

$$\alpha_2 \ = \ u_\downarrow(\theta) \ = \ \sqrt{\frac{1}{2} + \frac{\sqrt{\epsilon^2 - (\Delta_p^2 + \Delta_s^2 - 2\Delta_p\Delta_s\cos\theta)}}{2\epsilon}}$$

$$\beta_1 \;=\; \eta^*_{\uparrow}(\theta) v_{\uparrow}(\theta)$$
$$= \frac{\Delta_s + \Delta_p\, e^{-i\theta}}{\sqrt{\Delta_s^2+\Delta_p^2+2\Delta_p\Delta_s\cos\theta}} \sqrt{\frac{1}{2} - \frac{\sqrt{\epsilon^2-(\Delta_p^2+\Delta_s^2+2\Delta_p\Delta_s\cos\theta)}}{2\epsilon}}$$
$$\beta_2 \;=\; \eta^*_{\downarrow}(\theta) v_{\downarrow}(\theta)$$
$$= \frac{\Delta_s - \Delta_p\, e^{-i\theta}}{\sqrt{\Delta_s^2+\Delta_p^2-2\Delta_p\Delta_s\cos\theta}} \sqrt{\frac{1}{2} - \frac{\sqrt{\epsilon^2-(\Delta_p^2+\Delta_s^2-2\Delta_p\Delta_s\cos\theta)}}{2\epsilon}}$$

Now we write this Bogoliubov transformation coefficients in terms of mixing angles θ_1 and θ_2 in the particle-hole space in the following manner:

$$\alpha_1 \;=\; \cos\theta_1,\; \alpha_2 \;= \cos\theta_2$$
$$\beta_1 \;=\; \sin\theta_1,\; \beta_2 \;= \sin\theta_2$$

we have intentionally neglected any phase factor in β which do not affect the scattering amplitudes in our calculation.

The Nambu basis is chosen as $(u_{\uparrow},\, u_{\downarrow},\, v_{\uparrow},\, v_{\downarrow})^T$. So the 4-component spinors in F region can be written as a direct product of two 2-component spinor in particle-hole space and spin space. Hence,

$$|e\uparrow> = a|1> + b|2> \quad ,\; |e\downarrow> = -b|1> + a|2>$$
$$|h\uparrow> = a|3> + b|4> \quad ,\; |h\downarrow> = -b|3> + a|4>$$
$$|e1> = \alpha_1|1> + \beta_1|4> \quad ,\; |e2> = \alpha_2|2> + \beta_2|3>$$
$$|h1> = -\beta_2|1> + \alpha_2|4> \quad ,\; |h2> = -\beta_1|2> + \alpha_1|3>$$

Here, $|1>, |2>, |3>, |4>$ are the basis vectors in 4 dimension. It is important to note that "a" and "b" are the mixing in the spin space while "$\alpha_{1,2}$" and "$\beta_{1,2}$" are the mixing in the particle hole space. So there are totally 3 angles: ψ inside ferromagnet, θ_1 andθ_2 inside superconductor. The remainder work is to find all the four scattering amplitudes in terms of these angles which will help in understanding the novel anti-resonance.

It is worth mentioning that spinors inside superconductor can not be written as a direct product of two 2-component spinors because of particle-hole symmetry. Following Burset et al [203] we change the basis from $(u_\uparrow,\, u_\downarrow,\, v_\uparrow,\, v_\downarrow)^T$ to $(u_\uparrow,\, v_\downarrow,\, u_\downarrow,\, v_\uparrow)^T$ which makes it possible to write the wavefunctions as a direct product of two 2-component spinors.

Now, using continuity of wavefunction *i.e* $\psi_F(x=0) = \psi_S(x=0)$ we get,

$$\begin{aligned} |e\uparrow> + r_{\uparrow\uparrow}|e\uparrow> + r_{\uparrow\downarrow}|e\downarrow> + r^A_{\uparrow\uparrow}|h\uparrow> + r^A_{\uparrow\downarrow}|h\downarrow> \\ = c_1|e1> + c_2|e2> + d_1|h1> + d_2|h2> \end{aligned} \tag{E.1}$$

Multiplying Eq. (E.1) by $<1|,\ <2|,\ <3|,\ <4|$ from left, we obtain 4 equations:

$$\begin{aligned} (1+r_{\uparrow\uparrow})(a\times 1) - r_{\uparrow\downarrow}(b\times 1) &= c_1(1\times\alpha_1) - d_1(1\times\beta_2) \\ (1+r_{\uparrow\uparrow})(b\times 1) + r_{\uparrow\downarrow}(a\times 1) &= c_2(1\times\alpha_2) - d_2(1\times\beta_1) \\ r^A_{\uparrow\uparrow}(a\times 1) - r^A_{\uparrow\downarrow}(b\times 1) &= c_2(1\times\beta_2) + d_2(1\times\alpha_1) \\ r^A_{\uparrow\uparrow}(b\times 1) + r^A_{\uparrow\downarrow}(a\times 1) &= c_1(1\times\beta_1) + d_1(1\times\alpha_2) \end{aligned}$$

From the continuity of the derivatives *i.e* $\frac{d\psi_S}{dx}|_{x=0} - \frac{d\psi_F}{dx}|_{x=0} = k_F Z\psi_F(x=0)$, we obtain

$$\begin{aligned} & i(q_e c_1|e1> + q_e c_2|e2> - q_h d_1|h1> - q_h d_2|h2>) \\ - \quad & i(k_{e\uparrow}(1-r_{\uparrow\uparrow})|e\uparrow> - k_{e\downarrow}r_{\uparrow\downarrow}|e\downarrow> + k_{h\uparrow}r^A_{\uparrow\uparrow}|h\uparrow> + k_{h\downarrow}r^A_{\uparrow\downarrow}|h\downarrow>) \\ & = k_F Z\{(1+r_{\uparrow\uparrow})|e\uparrow> + r_{\uparrow\downarrow}|e\downarrow> + r^A_{\uparrow\uparrow}|h\uparrow> + r^A_{\uparrow\downarrow}|h\downarrow>\} \end{aligned} \tag{E.2}$$

Similarly as above, multiplying Eq. (E.2) by $<1|,\ <2|,\ <3|,\ <4|$ from left, we obtain 4 equations:

(with $Z=0$ *i.e* no barrier case for simplicity)

$$
\begin{aligned}
q_e c_1(1\times\alpha_1)+q_h d_1(1\times\beta_2) &= k_{e\uparrow}(1-r_{\uparrow\uparrow})(a\times 1)+k_{e\downarrow}r_{\uparrow\downarrow}(b\times 1)\\
q_e c_2(1\times\alpha_2)+q_h d_2(1\times\beta_1) &= k_{e\uparrow}(1-r_{\uparrow\uparrow})(b\times 1)-k_{e\downarrow}r_{\uparrow\downarrow}(a\times 1)\\
q_e c_2(1\times\beta_2)-q_h d_2(1\times\alpha_1) &= k_{h\uparrow}r^A_{\uparrow\uparrow}(a\times 1)-k_{h\downarrow}r^A_{\uparrow\downarrow}(b\times 1)\\
q_e c_1(1\times\beta_1)-q_h d_1(1\times\alpha_2) &= k_{h\uparrow}r^A_{\uparrow\uparrow}(b\times 1)+k_{h\downarrow}r^A_{\uparrow\downarrow}(a\times 1)
\end{aligned}
$$

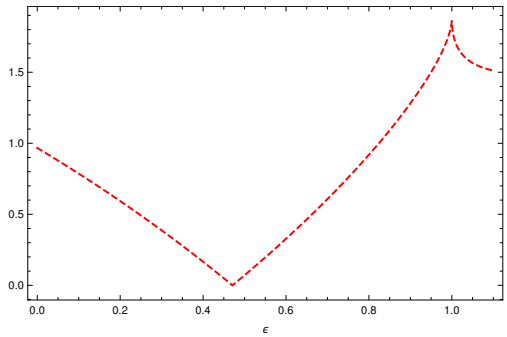

Figure E.1: "LHS" of Eq. (E.3) is drawn as a function of ϵ. Parameters used are: $\tilde{h}=1,\ \mu=0, \Delta_p=1.0,\ \Delta_s=0.0,\ U=15,\ \psi=\pi/2,\ \theta=0$

From these 8 equations, we obtain the following form of SFAR:

$$
\begin{aligned}
r^A_{\uparrow\uparrow} = \{16k_{e\uparrow}(q_e+q_h)\{(k_{e\downarrow}+q_e)(k_{h\downarrow}+q_h)\cos\theta_1\cos\theta_2\\
+(k_{h\downarrow}-q_e)(k_{e\downarrow}-q_h)\sin\theta_1\sin\theta_2\}\sin\psi\sin(\theta_1+\theta_2)\}/D
\end{aligned}
$$

where denominator D is a large exression. Vanishing of $r^A_{\uparrow\uparrow}$ gives,

$$
\tan\theta_1\tan\theta_2+\frac{(k_{e\downarrow}+q_e)(k_{h\downarrow}+q_h)}{(k_{h\downarrow}-q_e)(k_{e\downarrow}-q_h)}=0 \tag{E.3}
$$

Behaviour of "LHS" of Eq. (E.3) as a function of ϵ is shown in Fig. E.1 where we see that for the particular energy $\epsilon\simeq 0.47$, Eq. (E.3) is satisfied and $r^A_{\uparrow\uparrow}$ vanishes.

APPENDIX F

Appendix for Chapter 6

F.1 Some Useful Integrations

$$
\begin{aligned}
\int_{-\infty}^{\infty} dx \frac{e^{ix}}{\sqrt{\alpha^2 - x^2}} &= -2iK_0(-i\alpha) \\
\int_{-\infty}^{\infty} dx \frac{xe^{ix}}{\sqrt{\alpha^2 - x^2}} &= -2i\alpha K_1(-i\alpha) \\
\int_0^{\infty} dz f(\frac{z}{z0}) z^2 J_0(z) Y_0(z) &= \frac{1}{16} \\
\int_0^{\infty} dz f(\frac{z}{z0}) z^2 J_1(z) Y_1(z) &= -\frac{3}{16} \\
\int_0^{y} dz z^2 J_0(z) Y_0(z) &= -\frac{y}{2\sqrt{\pi}} M(y) \\
\int_0^{y} dz z^2 J_1(z) Y_1(z) &= -\frac{y}{2\sqrt{\pi}} \tilde{M}(y)
\end{aligned}
\tag{F.1}
$$

where, $f(\frac{z}{z0}) \to 1$ as $\frac{z}{z0} \to \infty$.
$M(y) = G^{2,0}_{1,3}\left(\begin{smallmatrix} \frac{3}{2} \\ 1,1,1,-\frac{1}{2} \end{smallmatrix} \middle| y^2 \right)$ and $\tilde{M}(y) = G^{2,1}_{2,4}\left(\begin{smallmatrix} \frac{1}{2},\frac{3}{2} \\ 1,2,0,-\frac{1}{2} \end{smallmatrix} \middle| y^2 \right)$ are the Meijer G-function.

Bibliography

[1] P. Vogt, P. D. Padova, C. Quaresima, J. Avila, E. Frantzeskakis, M. C. Asensio, A. Resta, B. Ealet, and G. L. Lay. Silicene: Compelling experimental evidence for graphenelike two-dimensional silicon. *Phys. Rev. Lett.*, 108:155501, April 2012.

[2] Baojie Feng, Osamu Sugino, Ro-Ya Liu, Jin Zhang, Ryu Yukawa, Mitsuaki Kawamura, Takushi Iimori, Howon Kim, Yukio Hasegawa, Hui Li, et al. Dirac fermions in borophene. *Phys. Rev. Lett.*, 118(9):096401, 2017.

[3] Vincent Mourik, Kun Zuo, Sergey M Frolov, SR Plissard, EPAM Bakkers, and Leo P Kouwenhoven. Signatures of majorana fermions in hybrid superconductor-semiconductor nanowire devices. *Science*, 336(6084):1003–1007, 2012.

[4] Hao Zhang *et al.* . Quantized majorana conductance. *Nature*, 556(7699):74, 2018.

[5] Motohiko Ezawa. Monolayer topological insulators: Silicene, germanene, and stanene. *J. Phys. Soc. Jpn.*, 84(12):121003, 2015.

[6] Cheng-Cheng Liu, Hua Jiang, and Yugui Yao. Low-energy effective hamiltonian involving spin-orbit coupling in silicene and two-dimensional germanium and tin. *Phys. Rev. B*, 84(19):195430, 2011.

[7] A. H. Castro Neto, F. Guinea, N. M. R. Peres, K. S. Novoselov, and A. K. Geim. The electronic properties of graphene. *Rev. Mod. Phys.*, 81:109, January 2009.

[8] Kostya S Novoselov, Andre K Geim, Sergei V Morozov, D Jiang, Y_ Zhang, Sergey V Dubonos, Irina V Grigorieva, and Alexandr A Firsov. Electric field effect in atomically thin carbon films. *Science*, 306(5696):666–669, 2004.

[9] Charles L Kane and Eugene J Mele. Quantum spin hall effect in graphene. *Phys. Rev. Lett.*, 95(22):226801, 2005.

[10] B Andrei Bernevig, Taylor L Hughes, and Shou-Cheng Zhang. Quantum spin hall effect and topological phase transition in hgte quantum wells. *Science*, 314(5806):1757–1761, 2006.

[11] B Andrei Bernevig and Shou-Cheng Zhang. Quantum spin hall effect. *Phys. Rev. Lett.*, 96(10):106802, 2006.

[12] Markus König, Steffen Wiedmann, Christoph Brüne, Andreas Roth, Hartmut Buhmann, Laurens W Molenkamp, Xiao-Liang Qi, and Shou-Cheng Zhang. Quantum spin hall insulator state in hgte quantum wells. *Science*, 318(5851):766–770, 2007.

[13] Michel Houssa, A Dimoulas, and A Molle. Silicene: a review of recent experimental and theoretical investigations. *J. Phys. Cond. Matt.*, 27(25):253002, 2015.

[14] Steven P Koenig, Rostislav A Doganov, Hennrik Schmidt, AH Castro Neto, and Barbaros Özyilmaz. Electric field effect in ultrathin black phosphorus. *Appl. Phys. Lett.*, 104(10):103106, 2014.

[15] Hui Tang and Sohrab Ismail-Beigi. First-principles study of boron sheets and nanotubes. *Phys. Rev. B*, 82(11):115412, 2010.

[16] Sajedeh Manzeli, Dmitry Ovchinnikov, Diego Pasquier, Oleg V Yazyev, and Andras Kis. 2d transition metal dichalcogenides. *Nat. Rev. Mater.*, 2(8):17033, 2017.

[17] Hui Pan, Zhenshan Li, Cheng-Cheng Liu, Guobao Zhu, Zhenhua Qiao, and Yugui Yao. Valley-polarized quantum anomalous hall effect in silicene. *Phys. Rev. Lett.*, 112(10):106802, 2014.

[18] M. Ezawa. Topological phase transition and electrically tunable diamagnetism in silicene. *Eur. Phys. J. B*, 85:363, July 2012.

[19] E Taghizadeh Sisakht, F Fazileh, MH Zare, M Zarenia, and FM Peeters. Strain-induced topological phase transition in phosphorene and in phosphorene nanoribbons. *Phys. Rev. B*, 94(8):085417, 2016.

[20] Xiaofeng Qian, Junwei Liu, Liang Fu, and Ju Li. Quantum spin hall effect in two-dimensional transition metal dichalcogenides. *Science*, 346(6215):1344–1347, 2014.

[21] B. Lalmi, H. Oughaddou, H. Enriquez, A. Kara, S. Vizzini, B. Ealet, and B. Aufray. Epitaxial growth of a silicene sheet. *Appl. Phys. Lett.*, 97:223109, December 2010.

[22] Jimin Kim, Seung Su Baik, Sae Hee Ryu, Yeongsup Sohn, Soohyung Park, Byeong-Gyu Park, Jonathan Denlinger, Yeonjin Yi, Hyoung Joon Choi, and Keun Su Kim. Observation of tunable band gap and anisotropic dirac semimetal state in black phosphorus. *Science*, 349(6249):723–726, 2015.

[23] Xiaojun Wu, Jun Dai, Yu Zhao, Zhiwen Zhuo, Jinlong Yang, and Xiao Cheng Zeng. Two-dimensional boron monolayer sheets. *ACS nano*, 6(8):7443–7453, 2012.

[24] Qing Hua Wang, Kourosh Kalantar-Zadeh, Andras Kis, Jonathan N Coleman, and Michael S Strano. Electronics and optoelectronics of two-dimensional transition metal dichalcogenides. *Nat. Nanotech.*, 7(11):699, 2012.

[25] Igor Žutić, Jaroslav Fabian, and S Das Sarma. Spintronics: Fundamentals and applications. *Rev. Mod. Phys.*, 76(2):323, 2004.

[26] Chetan Nayak, Steven H Simon, Ady Stern, Michael Freedman, and Sankar Das Sarma. Non-abelian anyons and topological quantum computation. *Rev.Mod. Phys.*, 80(3):1083, 2008.

[27] Kyozaburo Takeda and Kenji Shiraishi. Theoretical possibility of stage corrugation in si and ge analogs of graphite. *Phys. Rev. B*, 50(20):14916, 1994.

[28] Gian G Guzmán-Verri and LC Lew Yan Voon. Electronic structure of silicon-based nanostructures. *Phys. Rev. B*, 76(7):075131, 2007.

[29] C. C. Liu, W. Feng, and Y. Yao. Quantum spin hall effect in silicene and two-dimensional germanium. *Phys. Rev. Lett.*, 107:076802, August 2011.

[30] Motohiko Ezawa. A topological insulator and helical zero mode in silicene under an inhomogeneous electric field. *New J. Phys.*, 14(3):033003, 2012.

[31] Motohiko Ezawa. Photoinduced topological phase transition and a single dirac-cone state in silicene. *Phys. Rev. Lett.*, 110(2):026603, 2013.

[32] Emil Prodan. Robustness of the spin-chern number. *Phys. Rev. B*, 80(12):125327, 2009.

[33] DN Sheng, ZY Weng, L Sheng, and FDM Haldane. Quantum spin-hall effect and topologically invariant chern numbers. *Phys. Rev. Lett.*, 97(3):036808, 2006.

[34] L Sheng, DN Sheng, CS Ting, and FDM Haldane. Nondissipative spin hall effect via quantized edge transport. *Phys. Rev. Lett.*, 95(13):136602, 2005.

[35] Fan Zhang, Allan H MacDonald, and Eugene J Mele. Valley chern numbers and boundary modes in gapped bilayer graphene. *Proceedings of the National Academy of Sciences*, 110(26):10546–10551, 2013.

[36] Motohiko Ezawa. Topological kirchhoff law and bulk-edge correspondence for valley chern and spin-valley chern numbers. *Phys. Rev. B*, 88(16):161406, 2013.

[37] Antoine Fleurence, Rainer Friedlein, Taisuke Ozaki, Hiroyuki Kawai, Ying Wang, and Yukiko Yamada-Takamura. Experimental evidence for epitaxial silicene on diboride thin films. *Phys. Rev. Lett.*, 108(24):245501, 2012.

[38] Evgeni S Penev, Somnath Bhowmick, Arta Sadrzadeh, and Boris I Yakobson. Polymorphism of two-dimensional boron. *Nano Lett.*, 12(5):2441–2445, 2012.

[39] Alejandro Lopez-Bezanilla and Peter B Littlewood. Electronic properties of 8- pmmn borophene. *Phys. Rev. B*, 93(24):241405, 2016.

[40] Xiang-Feng Zhou, Xiao Dong, Artem R Oganov, Qiang Zhu, Yongjun Tian, and Hui-Tian Wang. Semimetallic two-dimensional boron allotrope with massless dirac fermions. *Phys. Rev. Lett.*, 112(8):085502, 2014.

[41] AD Zabolotskiy and Yu E Lozovik. Strain-induced pseudomagnetic field in the dirac semimetal borophene. *Phys. Rev. B*, 94(16):165403, 2016.

[42] MO Goerbig, J-N Fuchs, G Montambaux, and F Piéchon. Tilted anisotropic dirac cones in quinoid-type graphene and $\alpha - (bedt - ttf)_2 i_3$. *Phys. Rev. B*, 78(4):045415, 2008.

[43] Andrew J Mannix, Xiang-Feng Zhou, Brian Kiraly, Joshua D Wood, Diego Alducin, Benjamin D Myers, Xiaolong Liu, Brandon L Fisher, Ulises Santiago, Jeffrey R Guest, et al. Synthesis of borophenes: Anisotropic, two-dimensional boron polymorphs. *Science*, 350(6267):1513–1516, 2015.

[44] Baojie Feng, Jin Zhang, Qing Zhong, Wenbin Li, Shuai Li, Hui Li, Peng Cheng, Sheng Meng, Lan Chen, and Kehui Wu. Experimental realization of two-dimensional boron sheets. *Nat. Chem.*, 8(6):563, 2016.

[45] Ettore Majorana. Teoria simmetrica dell'elettrone e del positrone. *Il Nuovo Cimento (1924-1942)*, 14(4):171, 1937.

[46] Frank Wilczek. Majorana returns. *Nat. Phys.*, 5(9):614, 2009.

[47] Ady Stern. Non-abelian states of matter. *Nature*, 464(7286):187, 2010.

[48] Gregory Moore and Nicholas Read. Nonabelions in the fractional quantum hall effect. *Nuclear Physics B*, 360(2-3):362–396, 1991.

[49] Liang Fu and Charles L Kane. Superconducting proximity effect and majorana fermions at the surface of a topological insulator. *Phys. Rev. Lett.*, 100(9):096407, 2008.

[50] PGf de Gennes. Boundary effects in superconductors. *Rev. Mod. Phys.*, 36(1):225, 1964.

[51] Yong-Joo Doh, Jorden A van Dam, Aarnoud L Roest, Erik PAM Bakkers, Leo P Kouwenhoven, and Silvano De Franceschi. Tunable supercurrent through semiconductor nanowires. *Science*, 309(5732):272–275, 2005.

[52] Roman M Lutchyn, Jay D Sau, and S Das Sarma. Majorana fermions and a topological phase transition in semiconductor-superconductor heterostructures. *Phys. Rev. Lett.*, 105(7):077001, 2010.

[53] Yuval Oreg, Gil Refael, and Felix von Oppen. Helical liquids and majorana bound states in quantum wires. *Phys. Rev. Lett.*, 105(17):177002, 2010.

[54] S Nadj-Perge, IK Drozdov, Bogdan Andrei Bernevig, and Ali Yazdani. Proposal for realizing majorana fermions in chains of magnetic atoms on a superconductor. *Phys. Rev. B*, 88(2):020407, 2013.

[55] A Yu Kitaev. Unpaired majorana fermions in quantum wires. *Physics-Uspekhi*, 44(10S):131, 2001.

[56] Yu A Bychkov and Emmanuel I Rashba. Oscillatory effects and the magnetic susceptibility of carriers in inversion layers. *Journal of physics C: Solid state physics*, 17(33):6039, 1984.

[57] Jason Alicea. New directions in the pursuit of majorana fermions in solid state systems. *Reports on Progress in Physics*, 75(7):076501, 2012.

[58] Anindya Das, Yuval Ronen, Yonatan Most, Yuval Oreg, Moty Heiblum, and Hadas Shtrikman. Zero-bias peaks and splitting in an al-inas nanowire topological superconductor as a signature of majorana fermions. *Nat. Phys.*, 8(12):887–895, 2012.

[59] Sébastien R Plissard, Dorris R Slapak, Marcel A Verheijen, Moïra Hocevar, George WG Immink, Ilse van Weperen, Stevan Nadj-Perge, Sergey M Frolov, Leo P Kouwenhoven, and Erik PAM Bakkers. From insb nanowires to nanocubes: looking for the sweet spot. *Nano Lett.*, 12(4):1794–1798, 2012.

[60] Andrew C Potter and Patrick A Lee. Engineering a p+ ip superconductor: Comparison of topological insulator and rashba spin-orbit-coupled materials. *Phys. Rev. B*, 83(18):184520, 2011.

[61] GE Blonder, M Tinkham, and TM Klapwijk. Transition from metallic to tunneling regimes in superconducting microconstrictions: Excess current, charge imbalance, and supercurrent conversion. *Phys. Rev. B*, 25(7):4515, 1982.

[62] Kam Tuen Law, Patrick A Lee, and Tai Kai Ng. Majorana fermion induced resonant andreev reflection. *Phys. Rev. Lett.*, 103(23):237001, 2009.

[63] Chun-Xiao Liu, Jay D Sau, and S Das Sarma. Role of dissipation in realistic majorana nanowires. *Phys. Rev. B*, 95(5):054502, 2017.

[64] P Krogstrup, NLB Ziino, W Chang, SM Albrecht, MH Madsen, Erik Johnson, Jesper Nygård, CM Marcus, and TS Jespersen. Epitaxy of semiconductor–superconductor nanowires. *Nature Materials*, 14(4):400, 2015.

[65] Sasa Gazibegovic, Diana Car, Hao Zhang, Stijn C Balk, John A Logan, Michiel WA de Moor, Maja C Cassidy, Rudi Schmits, Di Xu, Guanzhong Wang, et al. Epitaxy of advanced nanowire quantum devices. *Nature*, 548(7668):434, 2017.

[66] Onder Gul, Hao Zhang, Folkert K de Vries, Jasper Van Veen, Kun Zuo, Vincent Mourik, Sonia Conesa-Boj, Michał P Nowak, David J Van Woerkom, Marina Quintero-Perez, et al. Hard superconducting gap in insb nanowires. *Nano Lett.*, 17(4):2690–2696, 2017.

[67] Hao Zhang, Önder Gül, Sonia Conesa-Boj, Michał P Nowak, Michael Wimmer, Kun Zuo, Vincent Mourik, Folkert K De Vries, Jasper Van Veen, Michiel WA De Moor, et al. Ballistic superconductivity in semiconductor nanowires. *Nat. Comm.*, 8:16025, 2017.

[68] Leonid P Rokhinson, Xinyu Liu, and Jacek K Furdyna. The fractional ac josephson effect in a semiconductor-superconductor nanowire as a signature of majorana particles. *Nat. Phys.*, 8(11):795–799, 2012.

[69] ADK Finck, DJ Van Harlingen, PK Mohseni, K Jung, and X Li. Anomalous modulation of a zero-bias peak in a hybrid nanowire-superconductor device. *Phys. Rev. Lett.*, 110(12):126406, 2013.

[70] Eduardo JH Lee, Xiaocheng Jiang, Ramón Aguado, Georgios Katsaros, Charles M Lieber, and Silvano De Franceschi. Zero-bias anomaly in a nanowire quantum dot coupled to superconductors. *Phys. Rev. Lett.*, 109(18):186802, 2012.

[71] Graham Kells, Dganit Meidan, and PW Brouwer. Near-zero-energy end states in topologically trivial spin-orbit coupled superconducting nanowires with a smooth confinement. *Phys. Rev. B*, 86(10):100503, 2012.

[72] Elsa Prada, Pablo San-Jose, and Ramón Aguado. Transport spectroscopy of n s nanowire junctions with majorana fermions. *Phys. Rev. B*, 86(18):180503, 2012.

[73] Dmitry Igorevich Pikulin, JP Dahlhaus, M Wimmer, Henning Schomerus, and CWJ Beenakker. A zero-voltage conductance peak from weak antilocalization in a majorana nanowire. *New J. of Phys.*, 14(12):125011, 2012.

[74] Falko Pientka, Graham Kells, Alessandro Romito, Piet W Brouwer, and Felix Von Oppen. Enhanced zero-bias majorana peak in the differential tunneling conductance of disordered multisubband quantum-wire/superconductor junctions. *Phys. Rev. Lett.*, 109(22):227006, 2012.

[75] Jie Liu, Andrew C Potter, KT Law, and Patrick A Lee. Zero-bias peaks in the tunneling conductance of spin-orbit-coupled superconducting wires with and without majorana end-states. *Phys. Rev. Lett.*, 109(26):267002, 2012.

[76] Eduardo JH Lee, Xiaocheng Jiang, Manuel Houzet, Ramón Aguado, Charles M Lieber, and Silvano De Franceschi. Spin-resolved andreev levels and parity crossings in hybrid superconductor–semiconductor nanostructures. *Nat. Nanotech.*, 9(1):79, 2014.

[77] Sven Marian Albrecht, AP Higginbotham, Morten Madsen, Ferdinand Kuemmeth, Thomas Sand Jespersen, Jesper Nygård, Peter Krogstrup, and CM Marcus. Exponential protection of zero modes in majorana islands. *Nature*, 531(7593):206–209, 2016.

[78] Fabrizio Nichele, Asbjørn CC Drachmann, Alexander M Whiticar, Eoin CT O'Farrell, Henri J Suominen, Antonio Fornieri, Tian Wang, Geoffrey C Gardner, Candice Thomas, Anthony T Hatke, et al. Scaling of majorana zero-bias conductance peaks. *Phys. Rev. Lett.*, 119(13):136803, 2017.

[79] Sangjun Jeon, Yonglong Xie, Jian Li, Zhijun Wang, B Andrei Bernevig, and Ali Yazdani. Distinguishing a majorana zero mode using spin-resolved measurements. *Science*, 358(6364):772–776, 2017.

[80] Chun-Xiao Liu, Jay D Sau, Tudor D Stanescu, and S Das Sarma. Andreev bound states versus majorana bound states in quantum dot-nanowire-superconductor hybrid structures: Trivial versus topological zero-bias conductance peaks. *Phys. Rev. B*, 96(7):075161, 2017.

[81] A. K. Geim and K. S. Novoselov. The rise of graphene. *Nat. Materials*, 6:183, March 2007.

[82] X. L. Qi and S. C. Zhang. Topological insulators and superconductors. *Rev. Mod. Phys.*, 83:1057, 2011.

[83] M Zahid Hasan and Charles L Kane. Colloquium: topological insulators. *Rev. Mod. Phys.*, 82(4):3045, 2010.

[84] Ayami Hattori, Sho Tanaya, Keiji Yada, Masaaki Araidai, Masatoshi Sato, Yasuhiro Hatsugai, Kenji Shiraishi, and Yukio Tanaka. Edge states of hydrogen terminated monolayer materials: silicene, germanene and stanene ribbons. *J. Phys. Cond. Matt.*, 29(11):115302, 2017.

[85] P. D. Padova *et al*. Evidence of graphene-like electronic signature in silicene nanoribbons. *Appl. Phys. Lett.*, 96:261905, June 2010.

[86] Chun-Liang Lin, Ryuichi Arafune, Kazuaki Kawahara, Noriyuki Tsukahara, Emi Minamitani, Yousoo Kim, Noriaki Takagi, and Maki Kawai. Structure of silicene grown on ag (111). *Appl. Phys. Exp.*, 5(4):045802, 2012.

[87] I. Zutić, J. Fabian, and S. Das Sarma. Spintronics: Fundamentals and applications. *Rev. Mod. Phys.*, 76:323–410, Apr 2004.

[88] Wei-Feng Tsai, Cheng-Yi Huang, Tay-Rong Chang, Hsin Lin, Horng-Tay Jeng, and Arun Bansil. Gated silicene as a tunable source of nearly 100% spin-polarized electrons. *Nat. Comm.*, 4:1500, 2013.

[89] Yangyang Wang, Jiaxin Zheng, Zeyuan Ni, Ruixiang Fei, Qihang Liu, Ruge Quhe, Chengyong Xu, Jing Zhou, Zhengxiang Gao, and Jing Lu. Half-metallic silicene and germanene nanoribbons: towards high-performance spintronics device. *Nano*, 7(05):1250037, 2012.

[90] Yangyang Wang, Ruge Quhe, Dapeng Yu, Ju Li, and Jing Lu. Silicene spintronics. *Chin. Phys. B*, 24(8):087201, 2015.

[91] S. Rachel and M. Ezawa. Giant magnetoresistance and perfect spin filter in silicene, germanene, and stanene. *Phys. Rev. B*, 89:195303, May 2014.

[92] Motohiko Ezawa. Spin valleytronics in silicene: Quantum spin hall–quantum anomalous hall insulators and single-valley semimetals. *Phys. Rev. B*, 87(15):155415, 2013.

[93] Arijit Kundu, HA Fertig, and Babak Seradjeh. Floquet-engineered valleytronics in dirac systems. *Phys. Rev. Lett.*, 116(1):016802, 2016.

[94] T. Yokoyama. Controllable valley and spin transport in ferromagnetic silicene junctions. *Phys. Rev. B.*, 87:241409(R), June 2013.

[95] Ruchi Saxena, Arijit Saha, and Sumathi Rao. Conductance, valley and spin polarizations, and tunneling magnetoresistance in ferromagnetic-normal-ferromagnetic junctions of silicene. *Phys. Rev. B*, 92(24):245412, 2015.

[96] Li Tao, Eugenio Cinquanta, Daniele Chiappe, Carlo Grazianetti, Marco Fanciulli, Madan Dubey, Alessandro Molle, and Deji Akinwande. Silicene field-effect transistors operating at room temperature. *Nat. Nanotech.*, 10(3):227–231, 2015.

[97] Michel Houssa, Bas van den Broek, Emilio Scalise, G Pourtois, VV Afanas' Ev, and Andre Stesmans. An electric field tunable energy band gap at silicene/(0001) zns interfaces. *Phys. Chem. Chem. Phys.*, 15(11):3702–3705, 2013.

[98] ND Drummond, Viktor Zolyomi, and VI Fal'Ko. Electrically tunable band gap in silicene. *Phys. Rev. B*, 85(7):075423, 2012.

[99] M. Ezawa and N. Nagaosa. Interference of topologically protected edge states in silicene nanoribbons. *Phys. Rev. B.*, 88:121401(R), September 2013.

[100] Motohiko Ezawa. Antiferromagnetic topological superconductor and electrically controllable majorana fermions. *Phys. Rev. Lett.*, 114(5):056403, 2015.

[101] C. W. J. Beenakker. Colloquium: Andreev reflection and klein tunneling in graphene. *Rev. Mod. Phys.*, 80:1337, October 2008.

[102] J. Linder and T. Yokoyama. Superconducting proximity effect in silicene: Spin-valley-polarized andreev reflection, nonlocal transport, and supercurrent. *Phys. Rev. B.*, 89:020504(R), January 2014.

[103] Y. Xu, G. Zhongxue, and S. C. Zhang. Enhanced thermoelectric performance and anomalous seebeck effects in topological insulators. *Phys. Rev. Lett.*, 112:226801, 2014.

[104] R. Lundgren, P. Laurell, and G. A. Fiete. Thermoelectric properties of weyl and dirac semimetals. *Phys. Rev. B.*, 90:165115, 2014.

[105] V. Chandrasekhar. Thermal transport in superconductor/normal-metal structures. *Supercond. Sci. Technol.*, 22:083001, 2009.

[106] P. Machon, M. Eschrig, and W. Belzig. Giant thermoelectric effects in a proximity-coupled superconductor-ferromagnet device. *New J. Phys.*, 16:073002, 2014.

[107] A. Ozaeta, P. Virtanen, F. S. Bergeret, and T. T. Heikkilä. Predicted very large thermoelectric effect in ferromagnet-superconductor junctions in the presence of a spin-splitting magnetic field. *Phys. Rev. Lett.*, 112:057001, 2014.

[108] Takehito Yokoyama, Jacob Linder, and Asle Sudbø. Heat transport by dirac fermions in normal/superconducting graphene junctions. *Phys. Rev. B*, 77(13):132503, 2008.

[109] MM Wysokiński. Temperature dependence of the zero-bias conductance in the graphene nis junction. *Acta Physica Polonica, A.*, 126, 2014.

[110] M. Salehi, M. Alidoust, Y. Rahnavard, and G. Rashedi. Thermal transport properties of graphene-based ferromagnetic/singlet superconductor/ferromagnetic junctions. *J. Appl. Phys.*, 107:123916, 2010.

[111] M. Salehi, M. Alidoust, and G. Rashedi. Signatures of d -wave symmetry on thermal dirac fermions in graphene-based f—i—d junctions. *J. Appl. Phys.*, 108:083917, 2010.

[112] AF Andreev. Thermal conductivity of the intermediate state of superconductors. *Sov. Phys. JETP*, 46, 1964.

[113] EV Bezuglyi and V Vinokur. Heat transport in proximity structures. *Phys. Rev. Lett.*, 91(13):137002, 2003.

[114] Subhro Bhattacharjee, Moitri Maiti, and K Sengupta. Theory of tunneling conductance of graphene normal metal-insulator-superconductor junctions. *Phys. Rev. B*, 76(18):184514, 2007.

[115] C. W. J. Beenakker. Specular andreev reflection in graphene. *Phys. Rev. Lett.*, 97:067007, August 2006.

[116] A Bardas and D Averin. Peltier effect in normal-metal–superconductor microcontacts. *Phys. Rev. B.*, 52(17):12873, 1995.

[117] S. Bhattacharjee and K. Sengupta. Tunneling conductance of graphene nis junctions. *Phys. Rev. Lett.*, 97:217001, November 2006.

[118] Surajit Sarkar, Arijit Saha, and Suhas Gangadharaiah. Tunneling conductance in normal-insulator-superconductor junctions of silicene. *Superlattices and Microstructures*, 123:436–446, 2018.

[119] Dmitri K Efetov, L Wang, C Handschin, KB Efetov, J Shuang, R Cava, T Taniguchi, K Watanabe, J Hone, CR Dean, et al. Specular interband andreev reflections at van der waals interfaces between graphene and nbse 2. *Nat. Phys.*, 12(4):328–332, 2016.

[120] J. Linder and A. Sudbø. Dirac fermions and conductance oscillations in s- and d-wave superconductor-graphene junctions. *Phys. Rev. Lett.*, 99:147001, October 2007.

[121] H. W. Kim *et al*. Nanoscale control of phonon excitations in graphene. *Nat. Comm.*, 6:7528, 2015.

[122] Hubert B Heersche, Pablo Jarillo-Herrero, Jeroen B Oostinga, Lieven M. K. Vandersypen, and Alberto F Morpurgo. Bipolar supercurrent in graphene. *Nature*, 446(7131):56–59, 2007.

[123] Jae-Hyun Choi, Gil-Ho Lee, Sunghun Park, Dongchan Jeong, Jeong-O Lee, H-S Sim, Yong-Joo Doh, and Hu-Jong Lee. Complete gate control of supercurrent in graphene p-n junctions. *Nat. Comm.*, 4:2525, 2013.

[124] Victor E Calado, Srijit Goswami, Gaurav Nanda, Mathias Diez, Anton R Akhmerov, Kenji Watanabe, Takashi Taniguchi, Teun M Klapwijk, and Lieven M. K. Vandersypen. Ballistic josephson junctions in edge-contacted graphene. *Nat. Nanotechnol.*, 10:761, 2015.

[125] Wu Shi, Jianting Ye, Yijin Zhang, Ryuji Suzuki, Masaro Yoshida, Jun Miyazaki, Naoko Inoue, Yu Saito, and Yoshihiro Iwasa. Superconductivity series in transition metal dichalcogenides by ionic gating. *Sci. Rep.*, 5:12534, 2015.

[126] ME Dávila, Lede Xian, S Cahangirov, Angel Rubio, and G Le Lay. Germanene: a novel two-dimensional germanium allotrope akin to graphene and silicene. *New J. Phys.*, 16(9):095002, 2014.

[127] Feng-feng Zhu, Wei-jiong Chen, Yong Xu, Chun-lei Gao, Dan-dan Guan, Can-hua Liu, Dong Qian, Shou-Cheng Zhang, and Jin-feng Jia. Epitaxial growth of two-dimensional stanene. *Nat. Mat.*, 14(10):1020, 2015.

[128] T. P. Kaloni, G. Schreckenbach, M. S. Freund, and U. Schwingenschlögl. Current developments in silicene and germanene. *Phys. Status Solidi RRL*, 10(2):133, 2016.

[129] T. P. Kaloni, N. Singh, and U. Schwingenschlögl. Prediction of a quantum anomalous hall state in co-decorated silicene. *Phys. Rev. B*, 89:035409, 2014.

[130] G Falci, Denis Feinberg, and FWJ Hekking. Correlated tunneling into a superconductor in a multiprobe hybrid structure. *Europhys. Lett.*, 54(2):255, 2001.

[131] G Bignon, M Houzet, F Pistolesi, and F. W. J. Hekking. Current-current correlations in hybrid superconducting and normal-metal multiterminal structures. *Europhys. Lett.*, 67(1):110, 2004.

[132] S. Russo, M. Kroug, T. Klapwijk, and A. Morpurgo. Experimental observation of bias-dependent nonlocal andreev reflection. *Phys. Rev. Lett.*, 95(2):027002, 2005.

[133] P. C. Zimansky and V. Chandrasekhar. Nonlocal correlations in normal-metal superconducting systems. *Phys. Rev. Lett.*, 97(23):237003, 2006.

[134] J. Brauer, F. Hübler, M. Smetanin, D. Beckmann, and H. v. Löhneysen. Nonlocal transport in normal-metal/superconductor hybrid structures: Role of interference and interaction. *Phys. Rev. B*, 81:024515, 2010.

[135] Ganesh C Paul, Surajit Sarkar, and Arijit Saha. Thermal conductance by dirac fermions in normal-insulator-superconductor junction of silicene. *Phys. Rev. B*, 94:155453, 2016.

[136] Patrik Recher, Eugene V. Sukhorukov, and Daniel Loss. Andreev tunneling, coulomb blockade, and resonant transport of nonlocal spin-entangled electrons. *Phys. Rev. B*, 63(16):165314, Apr 2001.

[137] A. Levy Yeyati, F. S. Bergeret, A. Martin-Rodero, and T. M. Klapwijk. Entangled andreev pairs and collective excitations in nanoscale superconductors. *Nat. Phys.*, 3:455, 2007.

[138] DJ Thouless. Quantization of particle transport. *Phys. Rev. B*, 27(10):6083, 1983.

[139] M Büttiker, H Thomas, and A Prêtre. Current partition in multiprobe conductors in the presence of slowly oscillating external potentials. *Z. Phys. B*, 94(1-2):133–137, 1994.

[140] PW Brouwer. Scattering approach to parametric pumping. *Phys. Rev. B.*, 58(16):R10135, 1998.

[141] PW Brouwer. Rectification of displacement currents in an adiabatic electron pump. *Phys. Rev. B*, 63(12):121303, 2001.

[142] Mykhaylo Moskalets and M Büttiker. Floquet scattering theory of quantum pumps. *Phys. Rev. B*, 66(20):205320, 2002.

[143] Mykhaylo Moskalets and Markus Büttiker. Adiabatic quantum pump in the presence of external ac voltages. *Phys. Rev. B*, 69(20):205316, 2004.

[144] Arijit Kundu, Sumathi Rao, and Arijit Saha. Quantum charge pumping through a superconducting double barrier structure in graphene. *Phys. Rev. B*, 83(16):165451, 2011.

[145] Q Niu. Towards a quantum pump of electric charges. *Phys. Rev. Lett.*, 64(15):1812, 1990.

[146] IL Aleiner and AV Andreev. Adiabatic charge pumping in almost open dots. *Phys. Rev. Lett.*, 81(6):1286, 1998.

[147] TA Shutenko, IL Aleiner, and BL Altshuler. Mesoscopic fluctuations of adiabatic charge pumping in quantum dots. *Phys. Rev. B*, 61(15):10366, 2000.

[148] O Entin-Wohlman, Amnon Aharony, and Y Levinson. Adiabatic transport in nanostructures. *Phys. Rev. B*, 65(19):195411, 2002.

[149] O Entin-Wohlman and Amnon Aharony. Quantized adiabatic charge pumping and resonant transmission. *Phys. Rev. B*, 66(3):035329, 2002.

[150] R. Benjamin and C. Benjamin. Quantum spin pumping with adiabatically modulated magnetic barrier's. *Phys. Rev. B*, 69:085318, 2004.

[151] C. Benjamin and R. Citro. Nonlocal pure spin current injection via quantum pumping and crossed andreev reflection. *Phys. Rev. B*, 72:085340, 2005.

[152] Sourin Das and Sumathi Rao. Effects of interaction on an adiabatic quantum electron pump. *Phys. Rev. B*, 71(16):165333, 2005.

[153] Shamik Banerjee, Anamitra Mukherjee, Sumathi Rao, and Arijit Saha. Adiabatic charge pumping through a dot at the junction of n quantum wires. *Phys. Rev. B*, 75(15):153407, 2007.

[154] A. Agarwal and D. Sen. Equation of motion approach to non-adiabatic quantum charge pumping. *J. Phys. Cond. Matt.*, 19:046205, 2007.

[155] A. Agarwal and D. Sen. Nonadiabatic charge pumping in a one-dimensional system of noninteracting electrons by an oscillating potential. *Phys. Rev. B*, 76:235316, 2007.

[156] Rakesh P Tiwari and M Blaauboer. Quantum pumping in graphene with a perpendicular magnetic field. *Appl. Phys. Lett.*, 97(24):243112, 2010.

[157] R. Zhu and H. Chen. Quantum pumping with adiabatically modulated barriers in graphene. *Appl. Phys. Lett.*, 95:122111, September 2009.

[158] J. Splettstoesser, M. Governale, and J. König. Adiabatic charge and spin pumping through quantum dots with ferromagnetic leads. *Phys. Rev. B*, 77:195320, 2008.

[159] S. Rojek, M. Governale, and J. König. Spin pumping through quantum dots. *Phys. Status Solidi B*, 251:1912, 2014.

[160] M Switkes, CM Marcus, K Campman, and AC Gossard. An adiabatic quantum electron pump. *Science*, 283(5409):1905–1908, 1999.

[161] PJ Leek, MR Buitelaar, VI Talyanskii, CG Smith, David Anderson, GAC Jones, Jiang Wei, and DH Cobden. Charge pumping in carbon nanotubes. *Phys. Rev. Lett.*, 95(25):256802, 2005.

[162] Susan K Watson, RM Potok, CM Marcus, and V Umansky. Experimental realization of a quantum spin pump. *Phys. Rev. Lett.*, 91(25):258301, 2003.

[163] MR Buitelaar, V Kashcheyevs, PJ Leek, VI Talyanskii, CG Smith, D Anderson, GAC Jones, J Wei, and DH Cobden. Adiabatic charge pumping in carbon nanotube quantum dots. *Phys. Rev. Lett.*, 101(12):126803, 2008.

[164] Francesco Giazotto, Panayotis Spathis, Stefano Roddaro, Subhajit Biswas, Fabio Taddei, Michele Governale, and Lucia Sorba. A josephson quantum electron pump. *Nat. Phys.*, 7(11):857–861, 2011.

[165] MD Blumenthal, B Kaestner, L Li, S Giblin, TJBM Janssen, M Pepper, D Anderson, G Jones, and DA Ritchie. Gigahertz quantized charge pumping. *Nat. Phys.*, 3(5):343–347, 2007.

[166] Elsa Prada, Pablo San-Jose, and Henning Schomerus. Quantum pumping in graphene. *Phys. Rev. B*, 80(24):245414, 2009.

[167] M Alos-Palop and M Blaauboer. Adiabatic quantum pumping in normal-metal–insulator–superconductor junctions in a monolayer of graphene. *Phys. Rev. B*, 84(7):073402, 2011.

[168] R Citro, F Romeo, and N Andrei. Electrically controlled pumping of spin currents in topological insulators. *Phys. Rev. B*, 84(16):161301, 2011.

[169] M. Alos-Palop, R. P. Tiwari, and M. Blaauboer. Adiabatic quantum pumping through surface states in 3d topological insulators. *New. J. Phys.*, 14:113003, 2012.

[170] J. E. Avron, A. Elgart, G. M. Graf, and L. Sadun. Optimal quantum pumps. *Phys. Rev. Lett.*, 87:236601, Nov 2001.

[171] Y. Levinson, O. Entin-Wohlman, and P. Wölfle. Pumping at resonant transmission and transferred charge quantization. *Physica A*, 302:335–344, 2001.

[172] Arijit Saha, Diego Rainis, Rakesh P Tiwari, and Daniel Loss. Quantum charge pumping through fractional fermions in charge density modulated quantum wires and rashba nanowires. *Phys. Rev. B*, 90(3):035422, 2014.

[173] M. Gibertini, R. Fazio, M. Polini, and F. Taddei. Topological pumping in class-d superconducting wires. *Phys. Rev. B*, 88:140508(R), October 2013.

[174] Pouyan Ghaemi, Shinsei Ryu, Taylor L Hughes, et al. Competing adiabatic thouless pumps in enlarged parameter spaces. *Phys. Rev. B*, 94(23):235160, 2016.

[175] Ganesh C Paul and Arijit Saha. Quantum charge pumping through resonant crossed andreev reflection in a superconducting hybrid junction of silicene. *Phys. Rev. B*, 95(4):045420, 2017.

[176] Surajit Sarkar, Arijit Saha, and Suhas Gangadharaiah. Tunneling conductance in normal-insulator-superconductor junctions of silicene. *Superlattices and Microstructures*, 123:436–446, 2018.

[177] A. Kundu, S. Rao, and A. Saha. Resonant tunneling through superconducting double barrier structures in graphene. *Phys. Rev. B*, 82:155441, October 2010.

[178] J. Cayssol. Crossed andreev reflection in a graphene bipolar transistor. *Phys. Rev. Lett.*, 100:147001, April 2008.

[179] Manas Ranjan Sahu, Pratap Raychaudhuri, and Anindya Das. Andreev reflection near the dirac point at the graphene-nbse_2 junction. *Phys. Rev. B*, 94:235451, Dec 2016.

[180] CWJ Beenakker. Search for majorana fermions in superconductors. *Annu. Rev. Condens. Matter Phys.*, 4(1):113–136, 2013.

[181] Steven R Elliott and Marcel Franz. Colloquium: Majorana fermions in nuclear, particle, and solid-state physics. *Rev. Mod. Phys.*, 87(1):137, 2015.

[182] CJ Bolech and Eugene Demler. Observing majorana bound states in p-wave superconductors using noise measurements in tunneling experiments. *Phys. Rev. Lett.*, 98(23):237002, 2007.

[183] Karsten Flensberg. Tunneling characteristics of a chain of majorana bound states. *Phys. Rev. B*, 82(18):180516, 2010.

[184] Michael Wimmer, AR Akhmerov, JP Dahlhaus, and CWJ Beenakker. Quantum point contact as a probe of a topological superconductor. *New J. Phys.*, 13(5):053016, 2011.

[185] Dmitry Bagrets and Alexander Altland. Class d spectral peak in majorana quantum wires. *Phys. Rev. Lett.*, 109(22):227005, 2012.

[186] MT Deng, S Vaitiekėnas, Esben Bork Hansen, Jeroen Danon, M Leijnse, Karsten Flensberg, Jesper Nygård, P Krogstrup, and Charles M Marcus. Majorana bound state in a coupled quantum-dot hybrid-nanowire system. *Science*, 354(6319):1557–1562, 2016.

[187] Elsa Prada, Ramón Aguado, and Pablo San-Jose. Measuring majorana nonlocality and spin structure with a quantum dot. *Phys. Rev. B*, 96(8):085418, 2017.

[188] Jorge Cayao, Pablo San-Jose, Annica M Black-Schaffer, Ramón Aguado, and Elsa Prada. Majorana splitting from critical currents in josephson junctions. *Phys. Rev. B*, 96(20):205425, 2017.

[189] Michael Hell, Karsten Flensberg, and Martin Leijnse. Distinguishing majorana bound states from localized andreev bound states by interferometry. *Phys. Rev. B*, 97(16):161401, 2018.

[190] Ernst Bauer and Manfred Sigrist. *Non-centrosymmetric superconductors: introduction and overview*, volume 847. Springer Science & Business Media, 2012.

[191] Sungkit Yip. Noncentrosymmetric superconductors. *Annu. Rev. Condens. Matter Phys.*, 5(2):15–33, 2014.

[192] Manfred Sigrist and Kazuo Ueda. Phenomenological theory of unconventional superconductivity. *Rev. Mod. Phys.*, 63(2):239, 1991.

[193] KV Samokhin, ES Zijlstra, and SK Bose. Cept 3 si: An unconventional superconductor without inversion center. *Phys. Rev. B*, 69(9):094514, 2004.

[194] AB Karki, YM Xiong, I Vekhter, D Browne, PW Adams, DP Young, KR Thomas, Julia Y Chan, H Kim, and R Prozorov. Structure and physical properties of the noncentrosymmetric superconductor mo_3al_2c. *Phys. Rev. B*, 82(6):064512, 2010.

[195] M. Mondal, B. Joshi, S. Kumar, A. Kamlapure, S. C. Ganguli, A. Thamizhavel, S. S. Mandal, S. Ramakrishnan, and P. Raychaudhuri. Andreev bound state and multiple energy gaps in the noncentrosymmetric superconductor bipd. *Phys. Rev. B.*, 86:094520, 2012.

[196] Tomoya Kawai, Hiroshi Muranaka, Marie-Aude Measson, Tetsuya Shimoda, Yusuke Doi, Tatsuma D Matsuda, Yoshinori Haga, Georg Knebel, Gérard Lapertot, Dai Aoki, et al. Magnetic and superconducting properties of cetx3 (t: transition metal and x: Si and ge) with noncentrosymmetric crystal structure. *J. Phys. Soc. Jap.*, 77(6):064716–064716, 2008.

[197] K Izawa, Y Kasahara, Y Matsuda, K Behnia, T Yasuda, R Settai, and Y Onuki. Line nodes in the superconducting gap function of noncentrosymmetric cept 3 si. *Phys. Rev. Lett.*, 94(19):197002, 2005.

[198] Yuri L Zuev, Valentina A Kuznetsova, Ruslan Prozorov, Matthew D Vannette, Maxim V Lobanov, David K Christen, and James R Thompson. Evidence for s-wave superconductivity in noncentrosymmetric re 3 w from magnetic penetration depth measurements. *Phys. Rev. B*, 76(13):132508, 2007.

[199] J Chen, L Jiao, JL Zhang, Y Chen, L Yang, M Nicklas, F Steglich, and HQ Yuan. Evidence for two-gap superconductivity in the non-centrosymmetric compound lanic2. *New J. Phys.*, 15(5):053005, 2013.

[200] M Nishiyama, Yoshihiko Inada, and Guo-qing Zheng. Spin triplet superconducting state due to broken inversion symmetry in li 2 pt 3 b. *Phys. Rev. Lett.*, 98(4):047002, 2007.

[201] Ganesh C Paul, Arijit Saha, and Sourin Das. Spin-selective coupling to majorana zero modes in mixed singlet and triplet superconducting nanowires. *Phys. Rev. B*, 97(20):205446, 2018.

[202] Carsten Honerkamp and Manfred Sigristt. Andreev reflection in unitary and non-unitary triplet states. *Journal of low temperature physics*, 111(5):895–915, 1998.

[203] P. Burset, F. Keidel, Y. Tanaka, N. Nagaosa, and B. Trauzettel. Transport signatures of superconducting hybrids with mixed singlet and chiral triplet states. *Phys. Rev. B*, 90(8):085438, 2014.

[204] Ganesh C Paul, Paramita Dutta, and Arijit Saha. Transport and noise properties of a normal metal–superconductor–normal metal junction with mixed singlet and chiral triplet pairings. *J. Phys. Cond. Matt.*, 29(1):015301, 2016.

[205] Ganesh C Paul, Paramita Dutta, and Arijit Saha. Effects due to unconventional pairing in transport through a normal metal-superconductor-normal metal hybrid junction. In *AIP Conf. Proc.*, volume 1832, page 110013, 2017.

[206] L Hofstetter, A Geresdi, Martin Aagesen, Jesper Nygård, C Schönenberger, and S Csonka. Ferromagnetic proximity effect in a ferromagnet–quantum-dot–superconductor device. *Phys. Rev. Lett.*, 104(24):246804, 2010.

[207] Alexander Altland and Martin R Zirnbauer. Nonstandard symmetry classes in mesoscopic normal-superconducting hybrid structures. *Phys. Rev. B*, 55(2):1142, 1997.

[208] Andreas P Schnyder, Shinsei Ryu, Akira Furusaki, and Andreas WW Ludwig. Classification of topological insulators and superconductors in three spatial dimensions. *Phys. Rev. B*, 78(19):195125, 2008.

[209] Jan Carl Budich and Eddy Ardonne. Topological invariant for generic one-dimensional time-reversal-symmetric superconductors in class diii. *Phys. Rev. B*, 88(13):134523, 2013.

[210] James J He, Tai Kai Ng, Patrick A Lee, and Kam Tuen Law. Selective equal-spin andreev reflections induced by majorana fermions. *Phys. Rev. Lett.*, 112(3):037001, 2014.

[211] Hao-Hua Sun, Kai-Wen Zhang, Lun-Hui Hu, Chuang Li, Guan-Yong Wang, Hai-Yang Ma, Zhu-An Xu, Chun-Lei Gao, Dan-Dan Guan, Yao-Yi Li, et al. Majorana zero mode detected with spin selective andreev reflection in the vortex of a topological superconductor. *Phys. Rev. Lett.*, 116(25):257003, 2016.

[212] Kostya S Novoselov, Andre K Geim, SVb Morozov, Da Jiang, MIc Katsnelson, IVa Grigorieva, SVb Dubonos, Firsov, and AA. Two-dimensional gas of massless dirac fermions in graphene. *Nature*, 438(7065):197, 2005.

[213] Melvin A Ruderman and Charles Kittel. Indirect exchange coupling of nuclear magnetic moments by conduction electrons. *Phys. Rev.*, 96(1):99, 1954.

[214] Tadao Kasuya. Electrical resistance of ferromagnetic metals. *Prog. of Theor. Phys.*, 16(1):58–63, 1956.

[215] K Yosida. K. yosida, phys. rev. 106, 893 (1957). *Phys. Rev.*, 106:893, 1957.

[216] Saeed Saremi. Rkky in half-filled bipartite lattices: Graphene as an example. *Phys. Rev. B*, 76(18):184430, 2007.

[217] L Brey, HA Fertig, and S Das Sarma. Diluted graphene antiferromagnet. *Phys. Rev. Lett.*, 99(11):116802, 2007.

[218] Annica M Black-Schaffer. Rkky coupling in graphene. *Phys. Rev. B*, 81(20):205416, 2010.

[219] Eugene Kogan. Rkky interaction in graphene. *Phys. Rev. B*, 84(11):115119, 2011.

[220] M Sherafati and S Satpathy. Rkky interaction in graphene from the lattice green's function. *Phys. Rev. B*, 83(16):165425, 2011.

[221] M Sherafati and S Satpathy. Analytical expression for the rkky interaction in doped graphene. *Phys. Rev. B*, 84(12):125416, 2011.

[222] Bruno Uchoa, TG Rappoport, and AH Castro Neto. Kondo quantum criticality of magnetic adatoms in graphene. *Phys. Rev. Lett.*, 106(1):016801, 2011.

[223] Moslem Zare, Fariborz Parhizgar, and Reza Asgari. Topological phase and edge states dependence of the rkky interaction in zigzag silicene nanoribbon. *Phys Rev. B*, 94(4):045443, 2016.

[224] SK Firoz Islam, Paramita Dutta, AM Jayannavar, and Arijit Saha. Probing decoupled edge states in a zigzag phosphorene nanoribbon via rkky exchange interaction. *Phys. Rev. B*, 97(23):235424, 2018.

[225] Houjian Duan, Shuai Li, Shi-Han Zheng, Zhenlong Sun, Mou Yang, and Rui-Qiang Wang. Anisotropic rkky interaction and modulation with mechanical strain in phosphorene. *New J. of Phys.*, 19(10):103010, 2017.

[226] Qin Liu, Chao-Xing Liu, Cenke Xu, Xiao-Liang Qi, and Shou-Cheng Zhang. Magnetic impurities on the surface of a topological insulator. *Phys. Rev. Lett.*, 102(15):156603, 2009.

[227] Rudro R Biswas and Alexander V Balatsky. Impurity-induced states on the surface of three-dimensional topological insulators. *Phys. Rev. B*, 81(23):233405, 2010.

[228] Jia-Ji Zhu, Dao-Xin Yao, Shou-Cheng Zhang, and Kai Chang. Electrically controllable surface magnetism on the surface of topological insulators. *Phys. Rev. Lett.*, 106(9):097201, 2011.

[229] Alexander A. Zyuzin and Daniel Loss. Rkky interaction on surfaces of topological insulators with superconducting proximity effect. *Phys. Rev. B*, 90:125443, Sep 2014.

[230] Hao-Ran Chang, Jianhui Zhou, Shi-Xiong Wang, Wen-Yu Shan, and Di Xiao. Rkky interaction of magnetic impurities in dirac and weyl semimetals. *Phys. Rev. B*, 92(24):241103, 2015.

[231] V. Kaladzhyan, A. A. Zyuzin, and P. Simon. Rkky interaction on the surface of three-dimensional dirac semimetals. *Phys. Rev. B*, 99:165302, Apr 2019.

[232] Mahroo Shiranzaei, Hosein Cheraghchi, and Fariborz Parhizgar. Effect of the rashba splitting on the rkky interaction in topological-insulator thin films. *Phys Rev. B*, 96(2):024413, 2017.

[233] Ganesh C Paul, SK Firoz Islam, and Arijit Saha. Fingerprints of tilted dirac cones on the rkky exchange interaction in 8-pmmn borophene. *Phys. Rev. B*, 99(15):155418, 2019.

[234] Philip Richard Wallace. The band theory of graphite. *Phys. Rev.*, 71(9):622, 1947.

[235] Cristina Bena and Steven A Kivelson. Quasiparticle scattering and local density of states in graphite. *Phys. Rev. B*, 72(12):125432, 2005.

[236] Philip Phillips. *Advanced solid state physics*. Cambridge University Press, 2012.

[237] Piers Coleman. *Introduction to many-body physics*. Cambridge University Press, 2015.

[238] CS Meijer. *On the G-function*. North-Holland, 1946.

[239] Jerry L Fields. The asymptotic expansion of the meijer g-function. *Mathematics of Computation*, pages 757–765, 1972.

[240] Jun Kondo. Resistance minimum in dilute magnetic alloys. *Progress of theoretical physics*, 32(1):37–49, 1964.

[241] S Doniach. The kondo lattice and weak antiferromagnetism. *Physica B*, 91:231–234, 1977.

[242] Andrej Schwabe, Daniel Gütersloh, and Michael Potthoff. Competition between kondo screening and indirect magnetic exchange in a quantum box. *Phys. Rev Lett.*, 109(25):257202, 2012.

[243] Shinya Katayama, Akito Kobayashi, and Yoshikazu Suzumura. Pressure-induced zero-gap semiconducting state in organic conductor α-(bedt-ttf) 2i3 salt. *J. Phys. Soc. of Japan*, 75(5):054705, 2006.

[244] Yaroslav Tserkovnyak, Arne Brataas, and Gerrit E. W. Bauer. Spin pumping and magnetization dynamics in metallic multilayers. *Phys. Rev. B*, 66:224403, Dec 2002.

[245] Jason Alicea. Majorana fermions in a tunable semiconductor device. *Phys. Rev. B*, 81(12):125318, 2010.

[246] Jorge Cayao. Hybrid superconductor-semiconductor nanowire junctions as useful platforms to study majorana bound states. *arXiv preprint arXiv:1703.07630*, 2017.